Delft University of Technology

Engineering the Kitaev chain

Bordin, A.

DOI
10.4233/uuid:f85b1055-fe65-4924-9a42-b342f4435fd8

Publication date
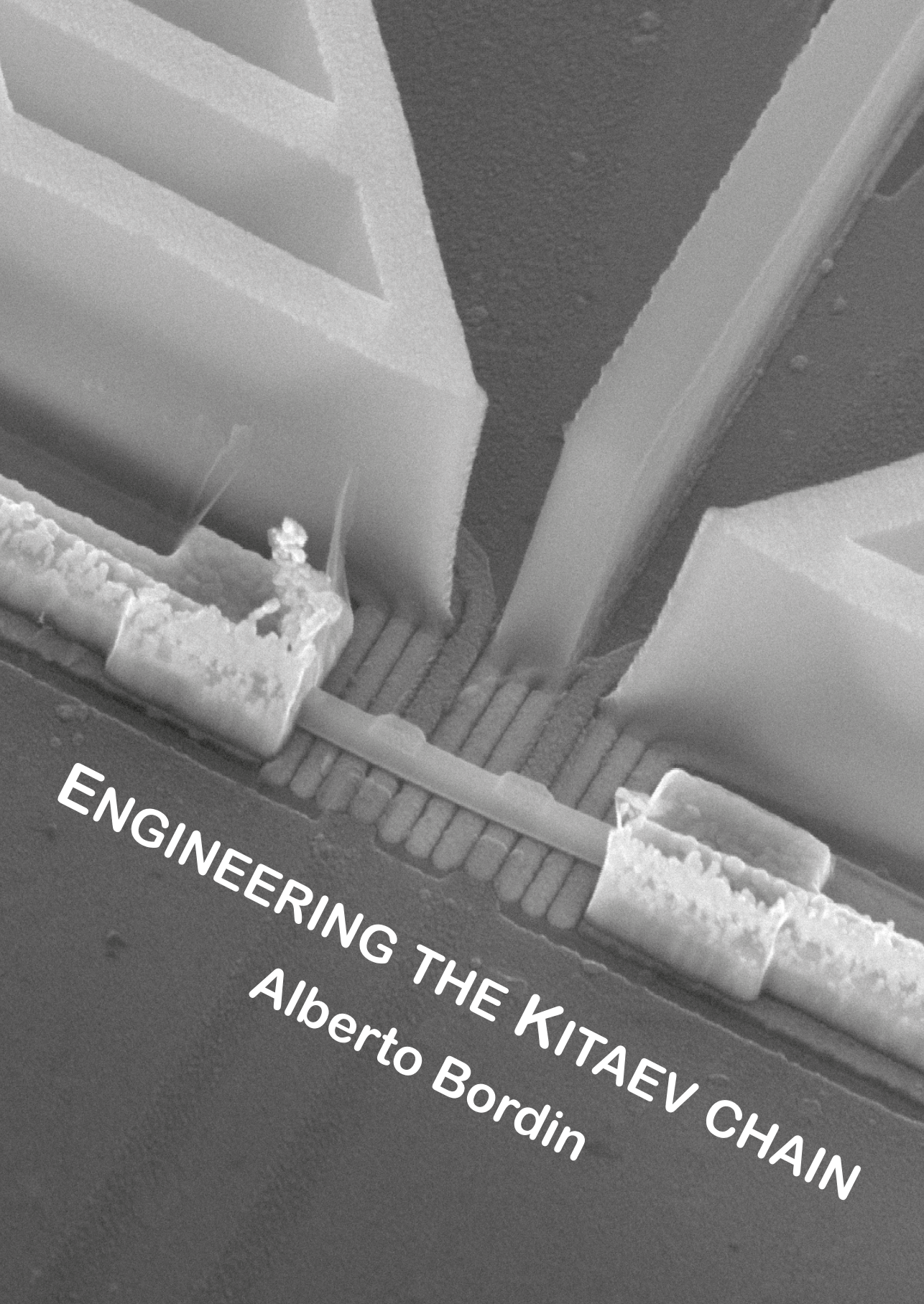2025

Document Version
Final published version

Important note
To cite this publication, please use the final published version (if applicable).
Please check the document version above.

ENGINEERING THE KITAEV CHAIN

Alberto Bordin

ENGINEERING THE KITAEV CHAIN

ENGINEERING THE KITAEV CHAIN

Dissertation

for the purpose of obtaining the degree of doctor
at Delft University of Technology,
by the authority of the Rector Magnificus prof. dr. ir. T. H. J. J. van der Hagen,
chair of the Board of Doctorates,
to be defended publicly on
Monday 13 January 2025 at 12:30 PM

by

Alberto BORDIN

Master of Science in Physics,
Scuola Normale Superiore & University of Pisa, Italy,
born in London, United Kingdom.

This dissertation has been approved by the promotors.

Composition of the doctoral committee:

Rector Magnificus,	chairperson
Prof. dr. ir. L. P. Kouwenhoven,	Delft University of Technology, promotor
Dr. C. K. Andersen,	Delft University of Technology, copromotor

Independent members:

Prof. dr. ir. R. Hanson	Delft University of Technology
Dr. S. Conesa Boj	Delft University of Technology
Prof. dr. C. W. J. Beenakker	Leiden University
Prof. dr. G. Katsaros	Institute of Science and Technology Austria
Prof. dr. G. A. Steele	Delft University of Technology, reserve member

Alle mie maestre e ai miei maestri

CONTENTS

SUMMARY

Nanotechnology enables the study of various quantum phenomena on real hardware. For instance, semiconducting and superconducting nanostructures can define single-electron transistors, quantum dots, Josephson junctions, and many other examples of quantum devices. It's a wonderful sandbox.

In this thesis, we exploit such a technology to bring the Kitaev chain model to life. The Kitaev Hamiltonian, discussed in the second chapter of this dissertation, describes a chain of N fermionic sites coupled by a standard tunneling and a more exotic superconducting pairing. It is one of the simplest models able to bring the concept of topology into condensed matter physics. Proposed more than twenty years ago, it attracted many experimental groups around the world, due to the promise of realizing a topologically protected qubit. This would be encoded into the Majorana bound states predicted to appear at the ends of the chain. However, such a qubit was never made, due to the difficulty of reproducing the Kitaev model with realistic, hence imperfect, materials.

Here, we demonstrate that engineering Kitaev chains with state-of-the-art materials is possible, by compensating imperfections with fine tuning. As opposed to top-down approaches, this requires building the chain site-by-site and tuning carefully each of them. In this work, each site is represented by a semiconducting quantum dot, while short semiconducting-superconducting hybrids mediate the inter-dot couplings. First, we describe minimal arrays of two quantum dots, show how to control every term of the Kitaev Hamiltonian, and detect the appearance of Majorana bound states. Then, we generalize the tuning procedure to three-site Kitaev chain devices. We also study the additional complications caused by multiple superconductors on the same device.

The main downside of a few-site Kitaev chain is the lack of topological protection. Nevertheless, we demonstrate that its Majorana bound states already exhibit partial protection (against some parameter perturbations), which increases substantially from two- to three-site chains. In the outlook, we propose to generalize the techniques described here to realize a rudimentary Majorana qubit and scale up to even longer Kitaev chains, whose partial protection evolves into topological as N grows.

SAMENVATTING

Nanotechnologie maakt het mogelijk om verschillende kwantumfenomenen op echte hardware te bestuderen. Bijvoorbeeld, halfgeleider- en supergeleider-nanostructuren kunnen enkel-elektrontransistoren, kwantumstippen, Josephson-juncties en vele andere voorbeelden van kwantumapparaten definiëren. Het is een fascinerende speelplaats.

In dit proefschrift maken we gebruik van deze technologie om het Kitaev-ketenmodel tot leven te brengen. De Kitaev-Hamiltoniaan, besproken in het tweede hoofdstuk van dit proefschrift, beschrijft een keten van N fermionische locaties die gekoppeld zijn door een standaard tunnelkoppeling en een meer exotische supergeleidende koppeling. Het is een van de eenvoudigste modellen die het concept van topologie in de vaste stof fysica introduceren. Het model werd meer dan twintig jaar geleden voorgesteld en trok sindsdien veel experimentele onderzoeksgroepen over de hele wereld aan, vanwege de belofte om een topologisch-beschermde qubit te realiseren. Deze qubit zou worden gecodeerd in de Majorana toestanden die naar verwachting aan de uiteinden van de keten verschijnen. Echter, een dergelijke qubit is nooit gerealiseerd vanwege de moeilijkheid om het Kitaev-model met realistische, en dus onvolmaakte, materialen te reproduceren.

Hier tonen we aan dat het mogelijk is om Kitaev-ketens te construeren met state-of-the-art materialen door imperfecties te compenseren met nauwkeurige kalibratie. In tegenstelling tot top-down benaderingen vereist dit het opbouwen van de keten locatie-voor-locatie en het zorgvuldig kalibreren van elke locatie. In dit werk wordt elke locatie vertegenwoordigd door een halfgeleidende kwantumstip, terwijl korte halfgeleidende-supergeleidende hybriden de koppelingen tussen de stippen mediëren. Eerst beschrijven we minimale reeksen van twee kwantumstippen, laten we zien hoe elke term van de Kitaev-Hamiltoniaan kan worden gecontroleerd en detecteren we het verschijnen van Majorana-gebonden toestanden. Vervolgens generaliseren we de afstelprocedure naar ketens met drie locaties. We bestuderen ook de extra complicaties die worden veroorzaakt door meerdere supergeleiders op hetzelfde apparaat.

Het belangrijkste nadeel van een Kitaev-keten met slechts enkele locaties is het gebrek aan topologische bescherming. Desondanks tonen we aan dat de Majorana toestanden al een gedeeltelijke bescherming vertonen (tegen sommige parameterperturbaties), die aanzienlijk toeneemt van ketens met twee naar drie locaties. In de vooruitblik stellen we voor om de hier beschreven technieken te generaliseren om een rudimentaire Majorana-qubit te realiseren en op te schalen naar nog langere Kitaev-ketens, waarvan de gedeeltelijke bescherming evolueert naar topologische bescherming naarmate N toeneemt.

RIASSUNTO

La nanotecnologia consente lo studio di vari fenomeni quantistici su hardware reale. Ad esempio, nanostrutture semiconduttrici e superconduttrici possono definire transistor a singolo elettrone, quantum dots, giunzioni di Josephson e molti altri esempi di dispositivi quantistici. È un meraviglioso contesto per la sperimentazione.

In questa tesi, sfruttiamo la nanotecnologia per dare vita alla catena di Kitaev. La Hamiltoniana da lui proposta, discussa nel secondo capitolo di questa tesi, descrive una catena di N siti fermionici accoppiati attraverso un normale tunneling e un più esotico accoppiamento superconduttivo. Si tratta di uno dei modelli più semplici in grado di introdurre il concetto di topologia in fisica della materia. Proposto più di vent'anni fa, ha attratto numerosi gruppi sperimentali in tutto il mondo grazie alla promessa di realizzare un qubit protetto topologicamente. Questo qubit sarebbe codificato nei fermioni di Majorana previsti alle estremità della catena. Tuttavia, un tale qubit non è mai stato realizzato, a causa della difficoltà di riprodurre il modello di Kitaev con materiali realistici, e quindi imperfetti.

In questa tesi dimostriamo che è possibile realizzare catene di Kitaev utilizzando i materiali odierni, compensando le imperfezioni con una calibrazione precisa. Diversamente dagli approcci top-down, ciò richiede la costruzione della catena sito per sito e la calibrazione accurata di ciascuno di essi. In questo lavoro, ogni sito è rappresentato da un quantum dot semiconduttore, mentre brevi ibridi semiconduttore-superconduttore mediano l'accoppiamento tra siti vicini. Inizialmente descriviamo array minimi di due quantum dots, mostriamo come controllare ogni termine dell'Hamiltoniana di Kitaev e rileviamo la comparsa di fermioni di Majorana. Successivamente, generalizziamo la procedura di calibrazione a catene di Kitaev composte da tre siti. Studiamo anche le complicazioni aggiuntive causate dalla presenza di più superconduttori nello stesso dispositivo.

Il principale svantaggio di una catena di Kitaev con pochi siti è la mancanza di protezione topologica. Tuttavia, in questo lavoro dimostriamo che i suoi fermioni di Majorana mostrano già una protezione parziale (da alcune perturbazioni dei parametri), che aumenta significativamente passando da catene a due siti a quelle a tre siti. Nelle conclusioni, proponiamo di generalizzare le tecniche descritte qui per realizzare un rudimentale Majorana qubit e scalare verso catene di Kitaev più lunghe, la cui protezione parziale diventa topologica con l'aumentare di N.

Resumen

L a nanotecnología permite el estudio de varios fenómenos cuánticos en hardware real. Por ejemplo, las nanoestructuras semiconductoras y superconductoras pueden definir transistores de electrón único, puntos cuánticos, uniones de Josephson y muchos otros ejemplos de dispositivos cuánticos. Es un maravilloso campo de experimentación.

En esta tesis, aprovechamos esta tecnología para dar vida al modelo de la cadena de Kitaev. El hamiltoniano de Kitaev, discutido en el segundo capítulo de esta tesis, describe una cadena de N sitios fermiónicos acoplados mediante un término de túnel estándar y un acoplamiento superconductivo más exótico. Es uno de los modelos más simples capaces de introducir el concepto de topología en la física de la materia condensada. Propuesto hace más de veinte años, ha atraído a numerosos grupos experimentales de todo el mundo debido a la promesa de realizar un cúbit protegido topológicamente. Este cúbit estaría codificado en los estados ligados de Majorana que se supone que aparezcan en los extremos de la cadena. Sin embargo, este cúbit nunca se ha logrado debido a la dificultad de reproducir el modelo de Kitaev con materiales realistas, y por tanto imperfectos.

Aquí, demostramos que es posible crear cadenas de Kitaev utilizando los materiales de última generación, compensando las imperfecciones mediante una calibración precisa. A diferencia de los enfoques convencionales que buscan implementar el sistema como un conjunto preensamblado, este método requiere montar la cadena sitio tras sitio y ajustar cuidadosamente cada elemento. En este trabajo, cada sitio está representado por un punto cuántico semiconductor, mientras que segmentos híbridos semiconductor-superconductor median los acoplamientos entre los sitios. Primero, describimos conjuntos mínimos de dos puntos cuánticos, mostramos cómo controlar cada término del hamiltoniano de Kitaev y detectamos la aparición de los estados ligados de Majorana. Luego, generalizamos el procedimiento de ajuste a dispositivos con cadenas de Kitaev de tres sitios. También estudiamos las complicaciones adicionales causadas por la presencia de múltiples superconductores en el mismo dispositivo.

La principal desventaja de una cadena de Kitaev con pocos sitios es la falta de protección topológica. No obstante, demostramos que sus estados ligados de Majorana ya exhiben una protección parcial (frente a algunas perturbaciones de los parámetros), la cual aumenta significativamente al pasar de cadenas de dos sitios a cadenas de tres sitios. En el último capítulo, proponemos generalizar las técnicas descritas aquí para realizar un cúbit de Majorana rudimentario y escalar hacia cadenas de Kitaev más largas, cuya protección parcial evoluciona a una protección topológica a medida que N crece.

1

INTRODUCTION

fatti non foste a viver come bruti,
ma per seguir virtute e canoscenza".

Dante Alighieri, *Inferno*, XXVI, 119-120

[you were not made to live your lives as brutes,
but to be followers of worth and knowledge.]

1

cosa serve? [What's the purpose of it?] – my father asks, every time I attempt to explain to him a bit of my research. This short chapter begins by trying to answer my father's question, addressing the *why* underneath the research presented in this dissertation, before introducing, briefly, the *how*.

THE DREAM: COMBINING QUANTUM INFORMATION AND TOPOLOGY

The research presented in this dissertation is motivated by the fascinating idea of combining quantum information with the concept of topology.

Quantum information is the use of objects that behave according to quantum mechanics to perform information tasks, such as computations, simulations, communications, and cryptography (Nielsen and Chuang, 2010). In its simplest form, it relies on storing information into *quantum bits* (qubits), which are the quantum analog of classical bits. While bits are either 0 or 1, qubits can be in any superposition $\alpha |0\rangle + \beta |1\rangle$, where $|0\rangle$, $|1\rangle$ are quantum states and α, β are complex numbers (normalized such that $|\alpha|^2 + |\beta|^2 = 1$). The possibility of superposition is one of the key qubit features, but it comes at the price of being delicate. Due to unavoidable couplings to the environment, a qubit prepared in the state $|1\rangle$ may decay into $|0\rangle$ over a characteristic lifetime indicated as T_1. Similarly, the imaginary components of the α and β coefficients may get lost over a characteristic T_2 coherence time. These T_1 and T_2 times are typically very short. For instance, even the latest 105-qubit processor created by Google (Acharya et al., 2024), arguably the best quantum processor to date, reports an average physical qubit lifetime of just $T_1 = 68\,\mu s$ and a coherence time $T_2 = 89\,\mu s$. To overcome this limitation, it is possible to use multiple physical qubits to encode one better-performing logical qubit, using quantum error correction techniques (Shor, 1995; Steane, 1996; Gottesman, 1997; Terhal, 2015). However, this comes with a significant overhead: for instance, the Google team could encode a logical qubit with lifetime $T_1 = 291\,\mu s$ using 101 of their physical qubits (Acharya et al., 2024).

An alternative to the large overhead given by quantum error correction is having better qubits to start with. The mathematical concept of *topology* studies the objects that are not affected by small perturbations. If it were possible to store quantum information in a topological object, then this would be intrinsically protected from decay and decoherence. A first proposal of this kind was put forward by Kitaev (1997; 2003) and then refined into a second, simpler, proposal: the Kitaev chain (2001). This model stores in-
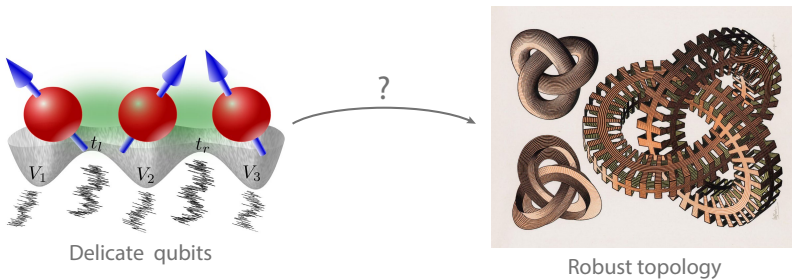

Delicate qubits

Robust topology

Figure 1.1: Image credits to Russ (2019) and Escher (1965).

formation into exotic quasiparticles known as Majorana bound states (Majorana, 1937). Eventually, if such Majoranas are spatially separated and an energy gap ensures protection from small perturbations, then the quantum information is topologically protected and fault-tolerant by nature (Kitaev, 2001, 2003).

TWO DECADES OF OBSESSIVE RESEARCH

The pioneering ideas of Kitaev quickly developed into the concept of topological quantum computation (Freedman et al., 2002; Nayak et al., 2008) and sparked particular interest in the search for Majorana bound states (Alicea, 2012). Interestingly, even the surface codes, arguably the most popular quantum correction architectures (Acharya et al., 2024), have a topological origin (Dennis et al., 2002; Kitaev, 2003; Fowler et al., 2012) and were eventually able to simulate topological systems using 2D arrays of either superconducting qubits (Satzinger et al., 2021) or Rydberg atoms (Semeghini et al., 2021). More recently, even some of the characteristic properties of Majorana bound states, such as the protection against local perturbations and the non-Abelian exchange statistics, were simulated using superconducting quantum processors (Mi et al., 2022; Andersen et al., 2023).

Here, rather than trying to simulate Majoranas with ordinary qubits, we are trying to realize them directly at a hardware level. While simulated Majoranas are limited by the quantum simulator lifetime (Mi et al., 2022), hardware Majoranas carry the hope of building a topological quantum memory with longer life and coherence times than any other qubit architecture on the market (Kitaev, 2001). This promise motivated an obsessive search for Majorana bound states in condensed matter systems for more than two decades (Kouwenhoven, 2024). The first decade was dominated by theoretical work (Nayak et al., 2008; Alicea, 2012; Leijnse and Flensberg, 2012b; Beenakker, 2013), while the second one brought tremendous advances in the material science (Chang et al., 2015; Aseev et al., 2018; Badawy et al., 2019; Heedt et al., 2021). In between the two decades, the theoretical realization that semiconductor-superconductor hybrid nanowires could potentially implement an effective Kitaev chain model (Lutchyn et al., 2010; Oreg et al., 2010) brought enormous attention to the field. The subsequent experimental observations (Mourik et al., 2012; Albrecht et al., 2016; Deng et al., 2016) gave the illusion that the technology was ready to deliver. However, the community eventually recognized that disorder in such systems is a profound limiting factor for the Lutchyn-Oreg approach. This disorder includes inhomogeneities, charge impurities, and other imperfections (Prada et al., 2020; Pan and Das Sarma, 2020). For instance, careful estimation of the impurity density in state-of-the-art semiconductors (Ahn et al., 2021) and of its impact (Woods et al., 2021) shows that even the best materials have too many impurities – by orders of magnitude – to realize the Lutchyn-Oreg proposal (Ahn et al., 2021). This understanding, together with the retraction of two high-impact papers (Zhang et al., 2021; Gazibegovic et al., 2022), created an avalanche effect that destroyed the field at the end of the second decade. For most of the community, the Lutchyn-Oreg approach is dead. Worldwide, there are only two notable groups still pursuing it: one is Microsoft Quantum (Aghaee et al., 2023, 2024) and the other is in Beijing (Jiang et al., 2022; Gao et al., 2024); besides substantial investments by both groups in improving the materials, their recent claims are not always free from controversy (Hess et al., 2023).

A new paradigm: engineering the Kitaev chain site by site

Ahn et al. (2021) are clear: state-of-the-art materials are too disordered to sustain any topological phase. Then, the only possibilities to go forward are either improving the current materials, changing materials, or changing strategy. Here, we opt for the latter. Figure 1.2 compares the Lutchyn-Oreg strategy (panel a) with our new paradigm (panel b), which is introduced in detail in the next chapter. In essence, the Lutchyn-Oreg recipe is a top-down approach that requires a (quasi) one-dimensional nanowire in contact with a superconductor and a few bottom gates to tune the electrochemical potential. If there is a sufficiently large external magnetic field, the potential is appropriately tuned and the disorder is low enough, then a topological phase with one Majorana bound state at each end should appear. Our strategy, first proposed by Sau and Das Sarma (2012), Leijnse and Flensberg (2012a), and Fulga et al. (2013), is instead a bottom-up approach that consists of engineering the N-site Kitaev chain Hamiltonian site after site. Instead of relying on the perfection of existing materials, we are creating a *metamaterial*, i.e. an artificial lattice, where every portion is tuned independently. The downside of this new approach is the more complicated nanofabrication it requires, the time-demanding tuning of the devices, and the fact that few-sites Kitaev chains are not topologically protected. However, the benefit of bottom-up Kitaev chains is, finally, overcoming the problem of material disorder and demonstrating – unambiguously and reproducibly – the presence of Majoranas. Besides requiring fine-tuning of the device, few-sites Kitaev chain Majorana bound states are real Majoranas (Leijnse and Flensberg, 2012a) and, thus, they can be used to create a qubit (Tsintzis et al., 2024). The more sites are added to the chain, the more its Majoranas are protected from local perturbations (Sau and Das Sarma, 2012), eventually reaching true topological protection in the long-chain limit.
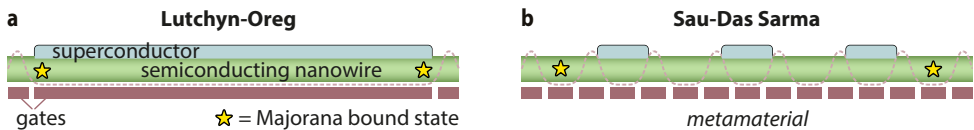
Figure 1.2: **a.** Effective Kitaev chain architecture proposed by Lutchyn et al. (2010) and Oreg et al. (2010). **b.** Schematic of a (4-site) Kitaev chain engineered with a bottom-up approach, adapted from Sau and Das Sarma (2012). Dashed lines illustrate the potential profile defined by the electrostatic gates.

This dissertation presents the results of this change of paradigm, following the key experiments enabling and demonstrating the appearance of Majorana bound states in few-site Kitaev chains.

- Chapter 2 contains a theoretical introduction to Kitaev chains, Majorana bound states and Majorana qubits. It is followed by a more practical guide introducing one-by-one all the ingredients we use to build a Kitaev chain in practice.

- Chapters 3 to 6 show the realization of elementary Kitaev chains with two or three sites. They are arranged as a rhyme:
  -Chapter 3 demonstrates the ingredients of a 2-site Kitaev Hamiltonian;
  -Chapter 4 puts them together, realizing a 2-site Kitaev chain hosting Majoranas;
  -Chapter 5 demonstrates the ingredients of a 3-site Kitaev Hamiltonian;
  -Chapter 6 puts them together, realizing a 3-site Kitaev chain hosting Majoranas.

- Chapter 7 is a bonus. It leverages the same 3-site chain device geometry used in chapter 6 but for a different purpose: controlling, studying, and improving a supercurrent transistor.

- Chapter 8 concludes the dissertation. It shows ongoing progress and the next steps towards Majorana qubits and topological protection.

Overall, this metamaterial approach to Kitaev chains may still seem foolish for what it promises. It involves great patience and hard work and may never deliver a ground-breaking technology. Among all the quantum platforms in development, it is hard to predict if topological quantum computing will ever have any technological relevance. In full disclosure, the scientific community is not even sure if quantum computing itself is ever going to be of any use: the supremacy of quantum over classical computing is still a conjecture (Bernstein and Vazirani, 1993; Aaronson and Chen, 2017). We should be grateful if, at the end of the day, there will be any quantum speed-up at all. Eventually, it may happen and it may be a significant leap forward for human technology.

Nevertheless, that is not the only reason for doing what we are doing. The initial question – *A cosa serve?* – can be interpreted in two ways. If you are only concerned about the potential *use* of our research, we might not have a satisfactory answer, but if you are interested in the *meaning* of it, we can reveal that our reward is already here. In truth, we are not doing what we are doing because it's useful, but because it's beautiful. We do it for an urge to deepen our understanding, to create something new, to see something no human has ever seen before, as Dante Alighieri suggests in the epigraph of this chapter. Here, the Kitaev chain physics offers an unbelievable playground, combining many different aspects of materials, science, and technology: semiconductors and superconductors, nanowires and thin films, cryogenics and nanofabrication, Josephson Junctions, quantum dots and Andreev bound states, spin combinations and spin-orbit coupling, just to name a few. The ensemble is so rich that new discoveries are almost guaranteed.

If you only care about quantum technologies, we cannot promise that you will ever benefit from any (topological) quantum computer. But it is very likely that, sooner or later, some of the new phenomena we discover will turn useful as well. Maybe that is the fate of chapter 7, in this dissertation almost by accident, which provides a new understanding and control of Josephson junctions. It is natural to deploy such knowledge to develop better supercurrent transistors and superconducting diodes (Seoane Souto et al., 2022). Could they enable viable dissipation-less electronics to suppress the overwhelming energy consumption and environmental pollution of big data centers? Who knows.

2

THEORY

Per correr miglior acque alza le vele
omai la navicella del mio ingegno,
che lascia dietro a sé mar sì crudele;

e canterò di quel secondo regno
dove l'umano spirito si purga
e di salire al ciel diventa degno.

Dante Alighieri, *Purgatorio*, I, 1-6

[To course across more kindly waters now
my talent's little vessel lifts her sails,
leaving behind herself a sea so cruel;

and what I sing will be that second kingdom,
in which the human soul is cleansed of sin,
becoming worthy of ascent to Heaven.]

*This chapter introduces the theoretical concepts underlying the experiments discussed in
the following chapters. Conceptually, it is divided into two parts. First, we introduce our
target Hamiltonian and discuss it from a purely abstract point of view. Secondly, we intro-
duce one by one all the elements that are necessary to realize such Hamiltonian in practice.*

2.1. THE KITAEV CHAIN

T he main goal of this thesis is to engineer in a real system the following toy model:

$$H_N = \sum_{n=1}^{N} \mu_n c_n^\dagger c_n + \sum_{n=1}^{N-1} \left(t_n c_n^\dagger c_{n+1} + \Delta_n c_n^\dagger c_{n+1}^\dagger + h.c. \right). \tag{2.1}$$

This Hamiltonian was originally proposed by Alexei Kitaev (2001) and later adapted by Sau and Das Sarma (2012); it models a one-dimensional chain of N sites, hence known as the Kitaev chain. Every site can host one fermion, described by the creation and annihilation operators $c_n^\dagger$ and c_n and with on-site energy μ_n. The terms t_n and Δ_n are responsible for the coupling between neighboring sites: t_n corresponds to the hopping of a single fermion and Δ_n corresponds to the creation of two fermions into a pair of neighboring sites. While the energies μ_n are always real numbers – they are indeed in the diagonal of the Hamiltonian matrix – the t_n and Δ_n are in general complex numbers (their conjugates also appear in the Hamiltonian under $h.c.$). For instance, Δ_n corresponds to the creation while Δ_n^* corresponds to the annihilation of a pair of fermions. Not all of the $2(N-1)$ complex phases ϕ_{t_n} and ϕ_{Δ_n} of $t_n = |t_n| e^{i\phi_{t_n}}$ and $\Delta_n = |\Delta_n| e^{i\phi_{\Delta_n}}$ are observable; N of them can be absorbed with a gauge transformation such as

$$c_n \mapsto c_n \cdot \exp\left(i\phi_{\Delta_{N-1}} + \sum_{m=n}^{N-1} i\phi_{t_m} \right) \tag{2.2}$$

but the remaining $N-2$ phases are not trivial. Therefore, complex phases are not a concern for minimal Kitaev chains of just two sites, but become relevant for any longer ones, as discussed in the experiment of chapter 6.

The Kitaev chain model is summarized in figure 2.1, highlighting the role of the μ_n, t_n, and Δ_n terms. Finally, it is important to stress that there is no summation over the spin degree of freedom in the Kitaev Hamiltonian. So any spin degeneracy should be removed in order to engineer equation 2.1 in a realistic system.
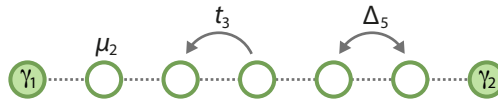
Figure 2.1: **Schematic illustration of a Kitaev chain with seven sites.** For every n between 1 and 7, μ_n represents the on-site energy, t_n corresponds to the hopping of a single fermion between neighboring sites and Δ_n to the creation (or annihilation) of a pair of fermions into neighboring sites. γ_1 and γ_2 represent Majorana modes that might appear at each end of the chain.

The beauty and relevance of the Kitaev chain model lie in the possibility of hosting a pair of exotic quasiparticles, known as Majorana fermions, Majorana bound states, Majorana zero modes, or simply Majoranas. The next section shows what they are, why they are useful, and how they can appear at the two ends of the Kitaev chain.

2.1.1. MAJORANA STATES

HALF ELECTRONS

Majorana states were first introduced by Ettore Majorana nearly a century ago as a change of basis for the electron and positron operators (Majorana, 1937). Here, we can follow Majorana's original idea, rewriting the fermionic creation and annihilation operators as the sum of their real and imaginary parts, which we define as the Majorana operators γ_1 and γ_2:

$$
\begin{aligned}
c^\dagger &= \frac{1}{2}\left(\gamma_1 - i\gamma_2\right) \\
c &= \frac{1}{2}\left(\gamma_1 + i\gamma_2\right)
\end{aligned}
\tag{2.3}
$$

It follows from the definition that such Majorana states always come in pairs:

$$1 \text{ fermion} \longrightarrow 2 \text{ Majorana states}$$
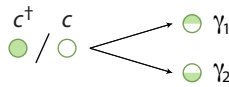
Furthermore, inverting the equations 2.3 shows that Majorana operators are equal superposition of electrons and holes

$$
\begin{aligned}
\gamma_1 &= c + c^\dagger \\
i\gamma_2 &= c - c^\dagger
\end{aligned}
\tag{2.4}
$$

which brings as a consequence the following properties:

$$
\begin{aligned}
&\text{(i)} \quad \gamma_k = \gamma_k^\dagger \\
&\text{(ii)} \quad \gamma_k^2 = 1 \\
&\text{(iii)} \quad \{\gamma_1, \gamma_2\} = 0
\end{aligned}
\tag{2.5}
$$

with $k \in \{1, 2\}$. The (ii) property is what motivates the choice of the $\frac{1}{2}$ coefficient in equations 2.3; other popular choices include 1 as in (Majorana, 1937) and $\frac{1}{\sqrt{2}}$. The (i) property, instead, means that a Majorana particle is its own antiparticle. It also implies that Majorana states have zero energy and zero charge. This has important consequences from a practical point of view. First, we know exactly where to look for Majorana modes in the energy spectrum. Secondly, the fact that Majorana states have zero charge makes them immune to Coulomb interactions. This makes them interesting candidates for storing quantum information into something that is decoupled from the charge noise in the environment. Finally, the (iii) property is actually very general: it holds for any pair of Majorana operators γ_a and γ_b (with $a \neq b$), even if they originate from different fermions, as it can be easily verified using the anticommutation rules of fermionic operators.

It follows that we can define a new fermion from *any* pair of Majorana states

$$
\begin{aligned}
c_{\text{new}}^\dagger &\equiv \frac{1}{2}\left(\gamma_a - i\gamma_b\right) \\
c_{\text{new}} &\equiv \frac{1}{2}\left(\gamma_a + i\gamma_b\right)
\end{aligned}
$$

where the anticommutation rules can be easily verified using the properties (ii) and (iii):

$$\left\{c_{\text{new}}^{\dagger}, c_{\text{new}}^{\dagger}\right\} = \{c_{\text{new}}, c_{\text{new}}\} = 0, \qquad \left\{c_{\text{new}}^{\dagger}, c_{\text{new}}\right\} = 1.$$

From one fermion, we can define a pair of Majoranas, and from *any* pair of Majorana states, we can define a fermion. The circle is closed.
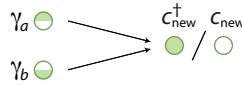
So far, it is unclear how this Majorana story can be useful at all. Majorana states are chargeless, but the electrons they define are definitely not. So how can such electrons be protected from charge noise? Indeed, if the two Majoranas defining one electron overlap, then viewing them as two Majoranas or as one electron is just a matter of mathematical taste, it has no physical consequence. So, what's the point? The critical observation is that Coulomb interactions are *local* interactions. If two Majoranas overlap, charge noise can affect the electron they define. However, if the Majoranas are isolated and far apart, the resulting non-local electron is protected from local charge noise. In general, the system is safeguarded against local perturbations, as no reasonable addition to the Hamiltonian can involve an isolated γ_a or γ_b; such terms do not conserve charge parity (Kitaev, 2001). Perturbations would instead require terms $\propto \gamma_a \gamma_b$, which are inherently non-local.

In summary, the key is finding a way to spatially separate the two Majorana states. To see how this is possible, let's consider again the Kitaev chain model.

THE DOMINO GAME
Let's compare the following two pictures where we view the Kitaev chain in the Majorana basis. In figure 2.2 the Majoranas are paired site by site, while figure 2.3 couples Majorana states from neighboring sites.

Figure 2.2: **Trivial Kitaev chain.** Majorana states are paired site by site.
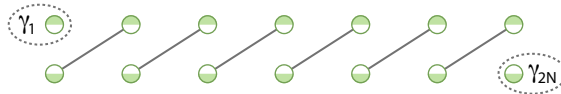
Figure 2.3: **Non-trivial Kitaev chain.** Pairing Majorana operators from neighboring sites would leave two un-paired Majorana modes at each end of the chain. This situation is non-trivial and is referred to as the "topo-logical" Kitaev chain (Lutchyn et al., 2010; Oreg et al., 2010; Alicea et al., 2011).
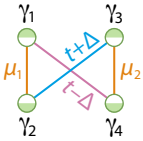
This second situation presents two isolated Majorana modes, γ_1 and γ_{2N}, one at each end of the chain. Together, they define one protected non-local fermion.

POOR MAN'S MAJORANA STATES

To see how to construct the situation of figure 2.3, let's consider the minimal cell consisting of just two sites. We can explicitly write the two-site Kitaev chain Hamiltonian in terms of the Majorana operators, starting from the μ_1-term:

$$c_1^\dagger c_1 = \frac{1}{2}\left(\gamma_1 - i\gamma_2\right)\frac{1}{2}\left(\gamma_1 + i\gamma_2\right) = \frac{1}{2} + \frac{i}{2}\gamma_1\gamma_2 \qquad (2.6)$$

where we used the properties (ii) and (iii) to arrive at the final expression. Ignoring the constants, the μ_1-term is simply replaced by $i\gamma_1\gamma_2$. In a similar way, we can compute the $i\gamma_2\gamma_3$ and $i\gamma_1\gamma_4$ pairing operators and see that they correspond to the $t+\Delta$ and $t-\Delta$ combinations:

$$\begin{aligned}
i\gamma_1\gamma_2 &\sim c_1^\dagger c_2 \longrightarrow \mu_1 \quad \text{(and analogously for } \mu_2\text{)}\\
-i\gamma_2\gamma_3 &= c_1^\dagger c_2 + c_2^\dagger c_1 + c_1^\dagger c_2^\dagger + c_2 c_1 \longrightarrow t+\Delta\\
i\gamma_1\gamma_4 &= c_1^\dagger c_2 + c_2^\dagger c_1 - c_1^\dagger c_2^\dagger - c_2 c_1 \longrightarrow t-\Delta
\end{aligned} \qquad (2.7)$$

Figure 2.4: **Graph representation of Majorana couplings.**

It is especially practical to visualize Majorana couplings as in figure 2.4. Since the two-site Kitaev chain Hamiltonian is reduced to

$$H_2 = \frac{1}{2}\left(\mu_1 + \mu_2\right) + \frac{i}{2}\left[\mu_1\gamma_1\gamma_2 + \mu_2\gamma_3\gamma_4 - (t+\Delta)\gamma_2\gamma_3 + (t-\Delta)\gamma_1\gamma_4\right], \qquad (2.8)$$

the graph representation of figure 2.4 is an equivalent description of the Hamiltonian. The weight of every arc represents the strength of the corresponding coupling. If any of the couplings is 0, then we don't even draw the corresponding arc.

In this framework, it is easy to find out how to realize the desired scheme of figure 2.3: we just need to set

$$\begin{cases} \mu_1 = \mu_2 = 0 \\ \quad t = \Delta \end{cases} \qquad (2.9)$$

and we get two unpaired Majorana states (figure 2.5a). We stress that such Majoranas are perfectly uncoupled and do not overlap, as long as equations 2.8 and 2.9 hold. Of course, this is a delicate scenario and that is the reason why these two-site chain Majorana modes are known as *poor man's Majoranas* (Leijnse and Flensberg, 2012a). Equation 2.9 is regarded as the poor man's Majorana *sweet spot.* Here, the non-local electron defined by the Majoranas has indeed zero energy and zero charge. But as soon as we detune from the sweet spot, this is no longer true. Nevertheless, poor man's Majoranas retain partial protection against detuning of the on-site energies μ_n, as can be seen in figure 2.5. At the sweet spot (panel a), the γ_1 and γ_4 are uncoupled. When $t \neq \Delta$ (panel c) they are obviously coupled. But if only one μ is detuned from 0 (say μ_1 without loss of generality) then one of the two Majoranas is still isolated (panel b). Since Majorana states always come in pairs, there must be another unpaired Majorana. This would be part of the $\{\gamma_1, \gamma_2, \gamma_3\}$ cluster which forms one fermion plus one unpaired Majorana state $\tilde{\gamma}$.
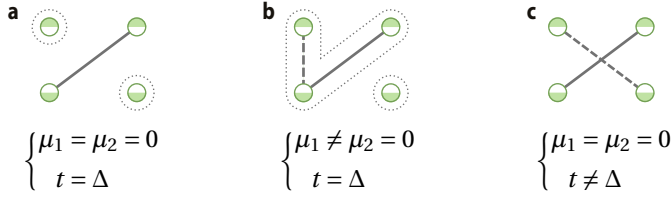
Figure 2.5: Minimal Kitaev chain model with **a**. Two unpaired Majoranas. **b.** A cluster of three coupled Majoranas, which is equivalent to one fermion plus one delocalized Majorana state, together with an isolated Majorana state in site 2. **c.** No unpaired Majorana states.

Note that γ_4 and $\tilde{\gamma}$ have a partial spatial overlap, yet they are uncoupled and therefore retain zero energy and zero charge. If both μ_1 and μ_2 differ from zero then the graph becomes fully connected, meaning that all Majoranas are paired up. As a consequence, the corresponding electrons are no longer bound to zero energy. It turns out that their energy split quadratically as a function of μ_1 and μ_2 (Leijnse and Flensberg, 2012a):

$$E_\pm = \pm\frac{\mu_1\mu_2}{2t}\left[1+\mathcal{O}\left(\frac{\mu_{1,2}}{t}\right)\right]. \tag{2.10}$$

In contrast, if $t \neq \Delta$ the electron energies split linearly as a function of their difference:

$$E_\pm = \pm(t-\Delta). \tag{2.11}$$

Both statements can be easily verified by diagonalizing the two-site Kitaev chain Hamiltonian, which reads as follows in the Nambu basis $\left\{c_1, c_2, c_1^\dagger, c_2^\dagger\right\}$:

$$H_2 = \begin{pmatrix} \mu_1 & t & 0 & \Delta \\ t & \mu_2 & -\Delta & 0 \\ 0 & -\Delta & -\mu_1 & -t \\ \Delta & 0 & -t & -\mu_2 \end{pmatrix} \tag{2.12}$$

In summary, two-site Kitaev chains are a great example of how to spatially separate two Majorana states and, surprisingly, they retain partial protection at the sweet spot: no single μ detuning can couple the two unpaired Majoranas (figure 2.5b) and even with simultaneous detuning of both on-site energies there is protection to linear order fluctuations (equation 2.10). The main issue is leaving the sweet spot via $t \neq \Delta$ (equation 2.11): the only way to overcome it is to build longer chains.

SCALING UP THE CHAIN
Let's consider figure 2.5c and add one more site to the chain to get figure 2.6a. Here there are unpaired Majorana states even if $t_1 \neq \Delta_1$. Indeed, if a three-site chain is tuned to the following condition, there is no detuning of a single parameter that could couple the two edge Majorana states:

$$\begin{cases} \mu_1 = \mu_2 = \mu_3 = 0 \\ t_1 = \Delta_1 \\ t_2 = \Delta_2 \end{cases} \tag{2.13}$$
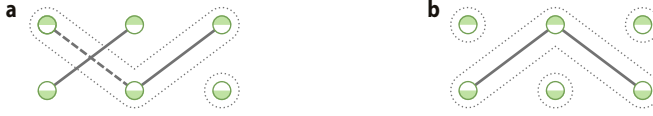
Figure 2.6: **a.** Three-site Kitaev chain with $\mu_1 = \mu_2 = \mu_2 = 0$ and $t_2 = \Delta_2$, but $t_1 \neq \Delta_1$, having two unpaired Majorana states. **b.** Three-site chain with $\mu_1 = \mu_2 = \mu_2 = 0$, $t_1 = \Delta_1$ and $t_2 = -\Delta_2$, having four degenerate Majorana states.

However, the price to pay is sensitivity to phase. For instance, if all phases are zero but $\phi_{\Delta_2} = \pi$ as in figure 2.6b, then we can get four unpaired Majorana states, which are too many: since any pair could define one fermion, any perturbation could make the quantum information stored into one Majorana pair to leak into the other one. At this π point, there is no protection against perturbations.

As shown by the gauge transformation 2.2, all the t_n and one of the Δ_n can be chosen to be real, while the remaining $N-2$ parameters are in general complex.[1] This also reduces the generality of the graph representation of Majorana pairings, which is accurate only if all Hamiltonian terms are real. In that case, the N-site chain Hamiltonian can be written as follows (Kitaev, 2001):

$$H_N = \frac{1}{2} \sum_{n=1}^{N} \mu_n + \frac{i}{2} \sum_{n=1}^{N} \mu_n \gamma_{2n-1} \gamma_{2n} + \frac{i}{2} \sum_{n=1}^{N-1} \left[-(t_n - \Delta_n) \gamma_{2n} \gamma_{2n+1} + (t_n + \Delta_n) \gamma_{2n-1} \gamma_{2n+2} \right],$$

but if any of the phases are complex, then the Hamiltonian form gets more complicated in the Majorana basis. With complex phases, it's more natural to go back to Nambu basis $\left\{ c_1, c_2, c_3, c_1^\dagger, c_2^\dagger, c_3^\dagger \right\}$ and study the three-site chain spectrum as a function of the phase, here included in Δ_2 without loss of generality:

$$H_3 = \begin{pmatrix} \mu_1 & t_1 & 0 & 0 & \Delta_1 & 0 \\ t_1 & \mu_2 & t_2 & -\Delta_1 & 0 & \Delta_2 \\ 0 & t_2 & \mu_2 & 0 & -\Delta_2 & 0 \\ 0 & -\Delta_1 & 0 & -\mu_1 & -t_1 & 0 \\ \Delta_1 & 0 & -\Delta_2^* & -t_1 & -\mu_2 & -t_2 \\ 0 & -\Delta_2^* & 0 & 0 & -t_2 & -\mu_3 \end{pmatrix} \tag{2.14}$$

Figure 2.7a shows the phase dependence of the three-site chain spectrum. There is always a zero energy mode, but at $\phi_{\Delta_2} = \pi$ the energy gap to the first excited state is closed: here there are two degenerate zero energy fermions, exactly as predicted by figure 2.6b. We note that having a fully real Hamiltonian doesn't solve the phase issue: by varying the absolute value of Δ_2 down to negative values, the gap is closed when $t_2 = -\Delta_2$ (figure 2.7b). So, in any case, some sort of phase control is needed in order to safely store quantum information in the zero energy modes, away from the π-phase points.

---

[1]It was shown that a truly one-dimensional chain with only Rashba-type spin-orbit coupling and magnetic field along the chain is supposed to have real inter-dot couplings, meaning that the only allowed phases are 0 and π (Sau and Das Sarma, 2012). Unfortunately, real-life systems are not perfectly one-dimensional and the field is never perfectly aligned. One should make sure to have a thin enough chain and small enough out-of-axis field components to have negligible imaginary parts; we don't know how feasible this is. Moreover, not even having all the t_n and Δ_n real would remove the necessity of phase control since π phases are the detrimental ones, as shown in the following. So, for maximum generality, we keep considering $N-2$ complex phases, unless otherwise specified.
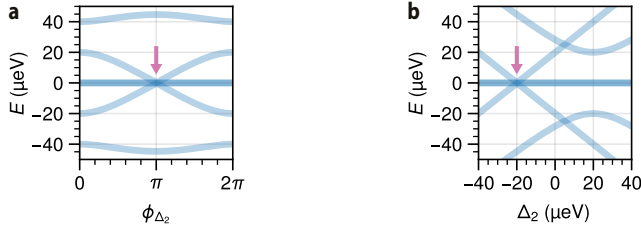
Figure 2.7: Three-site Kitaev chain spectrum with $\mu_1 = \mu_2 = \mu_2 = 0$, $t_1 = \Delta_1 = 10\,\mu\text{eV}$ and $t_2 = 20\,\mu\text{eV}$ as a function of **a.** the phase ϕ_{Δ_2} (with $|\Delta_2| = 20\,\mu\text{eV}$) or **b.** Δ_2 itself as a real number. In both panels, the pink arrow highlights the point where $t_2 = -\Delta_2$ as in figure 2.6b. At this point, the spectrum is gapless. To make the degeneracies visible, we display the spectral lines with some transparency. We remind that in the Nambu basis the spectrum is symmetrized with respect to zero energy and, therefore, it is artificially doubled (the Hamiltonian is indeed $2N \times 2N$ instead of $N \times N$). The line at zero energy looks darker because it corresponds to 2 degenerate eigenvalues, although it represents a single fermionic mode; when $t_2 = -\Delta_2$ (pink arrows) it corresponds to 4 eigenvalues, i.e. 2 degenerate fermionic modes.

Provided some sort of phase control, the benefits of scaling up the chain are remarkable. This is highlighted in figure 2.8 where the two-site chain spectrum as a function of t is shown next to the three-site chain spectrum as a function of t_1. For the two-site chain, there is only one point – the poor man's Majorana sweet spot – hosting zero-energy modes. Instead, the three-site chain shows one persistent zero energy mode for the full range. We note that this is true for all phases but π, where the zero energy modes might be two (figure 2.9).
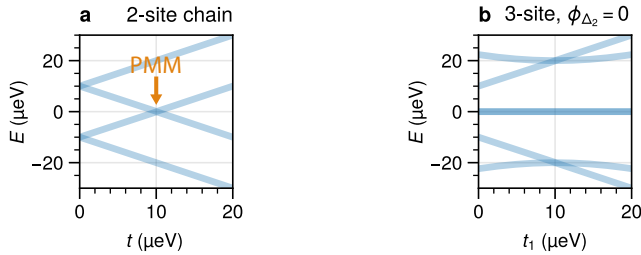
Figure 2.8: Comparison between two- and three-site Kitaev chains as a function of t_1. The poor man's Majorana (PMM) sweet spot is highlighted in panel **a** with an orange arrow. $\mu_n = 0\ \forall n$, $\Delta = \Delta_1 = t_2 = \Delta_2 = 10\,\mu\text{eV}$.
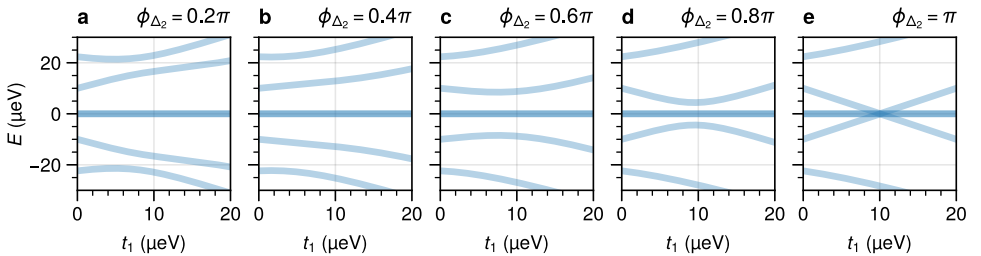
Figure 2.9: Three-site chain spectrum as a function of t_1 for various phases. $\mu_n = 0\ \forall n$, $\Delta_1 = t_2 = |\Delta_2| = 10\,\mu\text{eV}$.

The protection of zero-energy modes is a direct consequence of the chain's length and energy gap. To appreciate the latter, let's compare the following two scenarios. Panel a of

Figure 2.10: **a.** Three-site Kitaev chain with $\mu_n = t_n = \Delta_n = 0 \ \forall n$: there is no protection of the three zero-energy fermions. **b.** Here $t_n = \Delta_n \neq 0 \ \forall n$. There is one protected fermion localized in sites 1 and 3.

figure 2.10 represents a three-site Kitaev chain Hamiltonian with all parameters set to 0. Here there are six unpaired Majorana modes, defining three zero-energy fermions. The system is gapless, so any perturbation would couple the degenerate fermions. Panel b, instead, represents a Kitaev Hamiltonian tuned to satisfy equation 2.13 ($t_n = \Delta_n \neq 0 \ \forall n$). Here γ_1 and γ_6 can be coupled by small perturbations only through virtual excitations of the intermediate states of energies $2t_1$ and $2t_2$. In general, the same reasoning applies to chains of any length N. We list below the leading-order perturbation terms for few-site Kitaev chains calculated with the time-independent perturbation theory (Sakurai and Napolitano, 2020, chapter 5):

- $[N=2] \quad (\Delta - t) + \frac{\mu_1 \mu_2}{2t} + \dots$

- $[N=3] \quad \frac{(\Delta_1 - t_1)\mu_3}{2t_2} + \frac{\mu_1(\Delta_2 - t_2)}{2t_1} + \frac{\mu_1\mu_2\mu_3}{4t_1 t_2} + \frac{\mu_1(\Delta_1 - t_1)(\Delta_2 - t_2)}{4t_1^2} + \frac{(\Delta_1 - t_1)(\Delta_2 - t_2)\mu_3}{4t_2^2} + \dots$

- $[N=4] \quad \frac{(\Delta_1 - t_1)(\Delta_3 - t_3)}{2t_2} + \dots + \frac{\mu_1\mu_2\mu_3\mu_4}{8t_1 t_2 t_3} + \dots$

- $[N=5] \quad \frac{(\Delta_1 - t_1)(\Delta_3 - t_3)\mu_5}{4t_2 t_4} + \frac{(\Delta_1 - t_1)\mu_3(\Delta_4 - t_4)}{4t_2 t_3} + \frac{\mu_1(\Delta_2 - t_2)(\Delta_4 - t_4)}{4t_1 t_3} + \dots + \frac{\mu_1\mu_2\mu_3\mu_4\mu_5}{16t_1 t_2 t_3 t_4} + \dots$

- $[N=6] \quad \frac{(\Delta_1 - t_1)(\Delta_3 - t_3)(\Delta_5 - t_5)}{4t_2 t_4} + \dots + \frac{\mu_1\mu_2\mu_3\mu_4\mu_5\mu_6}{32t_1 t_2 t_3 t_4 t_5} + \dots$

(for brevity, we omit terms that are not leading-order nor all-μ from $N = 4$ onwards). Looking closely at the above expansions, we can appreciate several properties and trends. First of all, the $[N=2]$ terms reproduce as expected the predictions of equations 2.11 and 2.10. Secondly, the $(\Delta - t)$ term of the two-site chain is the only one without the denominator: any Kitaev chain with $N > 2$ is protected by an energy gap. Furthermore, the all-μ terms suggest an exponential scaling proportional to $(2t)^{-(N-1)}$. And, finally, the first terms of every line suggest a scaling proportional to $(2t)^{-\lfloor (N-1)/2 \rfloor}$ (where $\lfloor x \rfloor$ denotes the smallest integer $\leq x$) which predicts an even-odd effect: scaling up the chain from even to odd Ns should have a relatively bigger effect than the other way around (Leumer et al., 2020; Ezawa, 2024). This is again due to the fact that Majoranas come in pairs and odd-N chains must have unpaired Majoranas if all μ_n are exactly zero.

All the trends listed here are confirmed by the simulations shown in figure 2.11, where $\mu_n \approx 0$ and $t_n \approx \Delta_n \approx t \ \forall n$. Uncorrelated Gaussian noise with standard deviations δt and $\delta\mu$ is included into every t_n and μ_n respectively. Panel a, where $\delta t = \delta\mu = 1\,\mu eV$, shows a clear even-odd effect and a scaling roughly $\propto 10^{-N/2}$. While panel b, where $\delta t = 0.1\,\mu eV$ so that the noise on the on-site energies can dominate, shows a scaling roughly $\propto 10^{-N}$ and no appreciable even-odd effect. In both cases, the scaling is exponential.

2
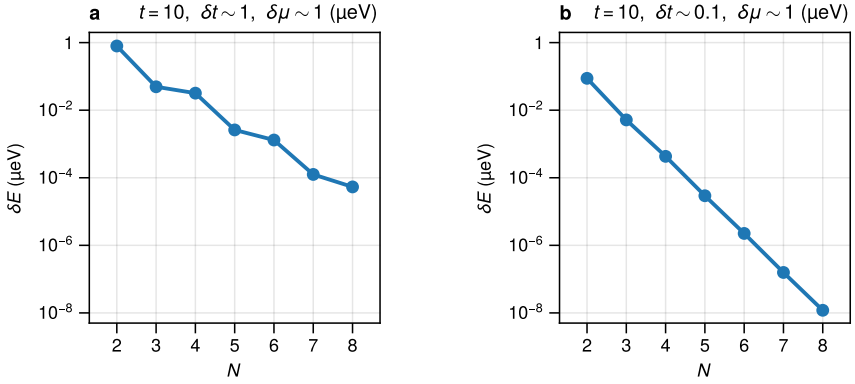
Figure 2.11: **Exponential scaling of Majorana protection against small perturbations on μ_n and $(t_n - \Delta_n)$.** Both panels start from a configuration where $\mu_n = 0$ and $t_n = \Delta_n = 10\mu eV \ \forall n$. Every t_n is independently perturbed with a random Gaussian noise of sigma δt. Similarly, independent Gaussian noises with sigma $\delta\mu$ are added to every μ_n. For every N, we plot the average energy of the smallest positive eigenvalue across 10000 random noise configurations (in other words, $2\delta E$ is the average energy splitting of the edge Majorana states due to perturbations of the Hamiltonian). **a.** $\delta t = \delta\mu = 1\mu eV$. Scaling the chain from even to odd N brings a relatively larger benefit than the other way around. The energy is roughly $\propto 10^{-N/2}$ **b.** $\delta t = 0.1\mu eV$, $\delta\mu = 1\mu eV$. There is no clear-even odd effect and the energy is roughly $\propto 10^{-N}$

Finally, it is crucial to note that, thanks to this exponential scaling, the $t_n \approx \Delta_n$ requirement can be relaxed completely for long chains. For instance, in the $N \to \infty$ limit, with uniform parameters ($\mu_n = \mu$, $t_n = t$, $\Delta_n = 0 \ \forall n$),

$$\begin{cases} |\mu| < 2t \\ \Delta \neq 0 \end{cases}$$

is a sufficient condition for hosting unpaired Majoranas at the chain ends (Kitaev, 2001). And, even with non-uniform parameters, matching the signs of real t_n and Δ_n couplings site by site

$$\begin{cases} \text{sign}(t_n\Delta_n) = \text{sign}(t_{n+1}\Delta_{n+1}) \\ |\mu_{n+1}| < \max(|t_n|, |\Delta_n|) \end{cases}$$

is also a sufficient condition for unpaired Majorana states at the chain ends (Sau and Das Sarma, 2012). For finite N systems, the exponential scaling ensures the possibility of getting nearly degenerate edge states, arbitrarily close to zero energy, already with reasonably short chains.

2.2. MAJORANA QUBITS

This section completes the abstract introduction to Kitaev chains, but is not essential for the understanding of the rest of the thesis so that busy readers can skip it with no harm. This section is written for the reader wondering how to actually store quantum information into Majorana modes. We describe here how to define a Majorana qubit and how to leverage the Majorana exchange statistics to engineer several qubit gates.

2.2.1. HOW TO STORE QUANTUM INFORMATION INTO MAJORANA MODES

To build a quantum computer, the very first requirement is to be able to hold information in well-defined quantum states (DiVincenzo, 1997). Furthermore, the Hilbert space describing such a system should have (at least) two dimensions, to allow for non-trivial operations. Hence, the minimal quantum object supporting this ability is a two-level system – a *qubit* (DiVincenzo, 2000). We refer to such two levels with the labels $|0\rangle_L$ and $|1\rangle_L$.

Having a Kitaev chain hosting Majorana bound states, a natural way to define two levels is using the Fock states $\{|0\rangle, |1\rangle\}$ describing the occupation of the non-local fermion defined by γ_1 and γ_{2N}:

$$|0\rangle_L \equiv |0\rangle \quad \text{zero fermions}$$
$$|1\rangle_L \equiv |1\rangle \quad \text{one fermion}$$

Notice that $|0\rangle$ and $|1\rangle$ have the same (zero) energy, therefore a $|1\rangle$ state cannot decay into a $|0\rangle$ via, for instance, the spontaneous emission of a photon, as would happen in most non-degenerate two-level systems. They are also protected from perturbations and charge noise, so they look ideal for quantum information storage. The problem is that such $|0\rangle$ and $|1\rangle$ do not form a proper qubit, because of two important issues:

1. In closed condensed matter systems, the number of fermions is conserved. So it wouldn't be possible to perform any operations on such two states.

2. Having many fermionic modes in a quantum processor would create ordering issues since swapping any two fermions gives a minus sign.

Let's see in the following how both concerns can be addressed. First of all, in condensed matter systems coupled to superconductors, it's not the fermion number to be conserved but just its parity. This partially relaxes the first issue. This is true also for the Kitaev chain Hamiltonian, which doesn't conserve the total number of electrons, but it does conserve the parity (the $\Delta_n c_n^\dagger c_{n+1}^\dagger$ and $\Delta_n^* c_{n+1} c_n$ terms can create and annihilate pairs of electrons). To circumvent this parity constraint, it is sufficient to add one extra ancillary Kitaev chain to account for the total parity conservation. For instance, having a system with N Kitaev chains encoding $|x_1\rangle, |x_2\rangle, \dots |x_N\rangle$ fermionic states, an additional Kitaev chain storing $|x_1 \oplus x_2 \oplus \dots x_N\rangle$ would keep the total parity constant (here each of the x_n is either 0 or 1 and $\oplus$ denotes the addition modulo 2, alias the XOR boolean operation).

The second issue is more subtle. To understand it, let's consider in figure 2.12 a representative quantum computation circuit from (Nielsen and Chuang, 2010, page 220). Here, the *swap* gate used last to exchange the first and the last qubit would, for instance, introduce a minus sign to the system wavefunction. Even the other two-qubit gates ("S"
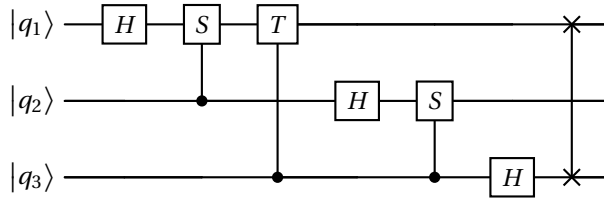
Figure 2.12: Example of a quantum computing circuit including "H" (*Hadamard*), "S", "T" and *swap* gates. This specific circuit implements a quantum Fourier transform on the three input qubits $|q_1\rangle$, $|q_2\rangle$ and $|q_3\rangle$ (Nielsen and Chuang, 2010, page 220).

and "T") should be implemented taking possible fermion exchanges into account. In general, the circuit model exemplified in figure 2.12 and heavily used in quantum computing literature is not meant to take care of the qubit ordering.

Technically, fermionic modes and ordinary qubits are two different models of quantum computation (Lloyd, 1998). Nevertheless, their computational power is equivalent: every fermionic gate can be simulated with $\mathcal{O}(\log N)$ qubit gates and N qubits can be simulated with $2N$ fermions (Bravyi and Kitaev, 2002). The logarithmic slowdown of fermion simulation might suggest that fermionic modes have slightly more computational power than qubits. However, for realistic systems where fermionic interactions are local, it is even possible to simulate local fermionic gates with a constant rather than a logarithmic slowdown (Bravyi and Kitaev, 2002). So, fermionic modes do not seem to have any real computational advantage (or disadvantage) compared to ordinary qubits.

As a final remark, the attentive reader might have noticed that $2N$ fermions might be unnecessarily too many to simulate N qubits. $N+1$ parity-preserving fermions define a 2^N-dimensional Hilbert space (for each parity sector), so, in principle, they should suffice to simulate N qubits. However, having a single extra fermion to take care of the total parity conservation requires the physical implementation of various gates to be different for a different N (Nayak et al., 2008). It is more practical to take care of the parity conservation qubit by qubit, encoding each of them as a pair of fermions (Leijnse and Flensberg, 2012b):

$$
\begin{aligned}
|0\rangle_L &\equiv |00\rangle \quad \text{zero fermions} \\
|1\rangle_L &\equiv |11\rangle \quad \text{two fermions}
\end{aligned}
\tag{2.15}
$$

where we restricted ourselves to the even-parity sector without loss of generality (if the parity is odd, $|0\rangle_L \equiv |10\rangle$, $|1\rangle_L \equiv |01\rangle$ works analogously). Finally, we note that this encoding trivially removes the ordering issue as well, since a pair of fermions is a boson. The definition 2.15 is a valid qubit encoding.

2.2.2. HOW TO OPERATE MAJORANA QUBITS

Storing quantum information into Majorana modes is a remarkable achievement by itself. On top of that, coupling bare Kitaev chains with other quantum computing systems, such as spin qubits or superconducting qubits, could already bring several benefits. For example, spin-qubits can be very fast, due to strong qubit-qubit interactions (Stano and Loss, 2022), but typical coherence times are short compared, for instance, to supercon-

ducting qubits (Kjaergaard et al., 2020). Creating a hybrid spin-Kitaev quantum processor could combine the strengths of each platform, having both fast two-qubit operations and long-lived memories.

On the other side, finding ways to implement single- and two-qubit gates with topologically protected Majorana modes has the potential to realize fault-tolerant quantum computation (Kitaev, 2003), which is an even bigger achievement. To see whether or not this can be realized, let's first study what happens when two Majoranas are exchanged, a process known as *braiding*.

BRAIDING

Let's first consider a two-dimensional system, where the Majorana exchange statistics is easier to derive, and then extend the result to Kitaev chains. 1D and 2D Majorana systems are closely related and their connection is extensively discussed in Alicea's review (2012). For both dimensionalities, the essential Hamiltonian ingredient for the emergence of Majorana modes is a superconducting-like term proportional to the momentum. In Kitaev chains, this comes from the $\Delta c_n^\dagger c_{n+1}^\dagger$ term, which is Fourier-transformed into $-i\Delta \sin k$ in momentum space. For 2D systems, a $i\Delta (k_x + i k_y)$ term provides the same result. This is why both systems are often referred to as p-wave superconductors. For further details see (Alicea, 2012).

Let's then consider a 2D p-wave superconductor inside a magnetic field perpendicular to the plane, and follow Ivanov's reasoning (2001) to derive the exchange statistics. Here, four vortices can trap one Majorana each, as shown in figure 2.13. The superconducting phase ϕ is single-valued everywhere apart from the branch cuts illustrated in red, where ϕ jumps by 2π. The key point is observing that if the electron phase jumps by $\Delta\phi$, this is equivalent to rotating the electron creation and annihilation operators by $\Delta\phi/2$ (Ivanov, 2001), so that a 2π shift on the electron wavefunction translates into a π shift on the Majorana operators. If we exchange the vortices hosting γ_1 and γ_2 clockwise
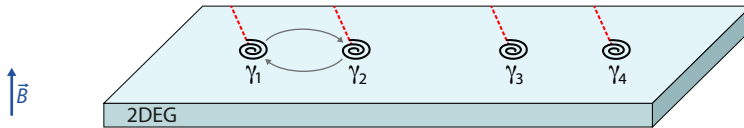
Figure 2.13: 2D topological superconductor immersed in an external magnetic field perpendicular to the plane. Each vortex hosts a single Majorana mode.

as in figure 2.13, then γ_1 would cross a branch cut while γ_2 would not. This implies the following transformation:

$$\gamma_1 \longmapsto -\gamma_2$$
$$\gamma_2 \longmapsto \gamma_1$$

And it is easy to verify that the following braiding operator B_{12} realizes such a mapping, acting on each Majorana via $\gamma_i \longmapsto B_{12}\gamma_i B_{12}^\dagger$:

$$B_{12} = \frac{1}{\sqrt{2}} \left(1 + \gamma_1 \gamma_2\right)$$

Notice that the braiding operator affects only γ_1 and γ_2, while leaving all other Majorana modes unmodified [this property is what makes the choice of the operator unique (Leijnse and Flensberg, 2012b)]. So we can extend the same reasoning to any pair of neighboring Majorana operators and get analogous expressions for B_{23} and B_{34}. With these operators, we can finally calculate how the exchange of Majoranas affects the qubit states $|0\rangle_L$ and $|1\rangle_L$:

$$B_{12} |00\rangle = \frac{1+i}{\sqrt{2}} |00\rangle$$
$$B_{12} |11\rangle = \frac{1-i}{\sqrt{2}} |11\rangle$$

(2.16)

Under the action of B_{12}, both states get a phase factor that is neither $+1$ nor -1, which means that Majorana modes are neither bosons nor fermions: they are *anyons* (Wilczek, 1982). The action of B_{23} is even more striking since it can create a superposition:

$$B_{23} |00\rangle = \frac{1}{\sqrt{2}} (|00\rangle + i |11\rangle)$$
$$B_{23} |11\rangle = \frac{1}{\sqrt{2}} (|00\rangle - i |11\rangle)$$

(2.17)

Using these expressions, it's immediate to verify such braiding operations do not commute: $B_{23}B_{12} \neq B_{12}B_{23}$. Majorana modes are *non-abelian* anyons.

The anionic exchange statistics wouldn't be possible in three dimensions. In 3D, a double exchange of particles is topologically equivalent to the identity, so the only possible particles are either fermions or bosons. In one and two dimensions this doesn't need to be the case (Leinaas and Myrheim, 1977). Indeed, a double braid of Majoranas is not the identity, but flips the sign of both Majorana operators since each of them would need to cross exactly one of the branch cuts of figure 2.13. The identity is reached with a quadruple braid:

$$B_{12}^2 = \gamma_1 \gamma_2 \qquad B_{12}^4 = 1$$

(2.18)

Notice that the non-abelian nature wouldn't be possible without a degenerate ground state: all operations on a one-dimensional ground state are trivial.[2] Here, instead, braiding operations are rotating the two-dimensional ground state, i.e. they are implementing single-qubit gates! Now that we have shown how Majorana braiding works in 2D systems, we return to the Kitaev model and extend these results to such a platform. The most natural proposal (Alicea et al., 2011) involves *networks* of Kitaev chains since they are essentially 2D (see for instance figure 2.15). Here, the key ingredient is being able to physically move the Majorana modes. This can be achieved by acting on the μ_n parameters: for instance, starting from a Kitaev chain with $\mu_n = 0$ and $t_n = \Delta_n \; \forall n$, setting $\mu_1 \gg t_1$ would transfer γ_1 from the first to the second site, as shown in figure 2.14. With this principle, B_{12} and B_{23} can be implemented using T-junctions of Kitaev chains, as shown in figures 2.15–2.16 and rigorously proven in the supplementary material of (Alicea et al., 2011). An experimental demonstration of the figure 2.14 principle is shown in chapter 6.

---

[2]Formally: all one-dimensional representations of the braiding group (of any group, actually) are abelian.

Figure 2.14: **Shuttling Majorana modes by acting on the onsite energies**. Here, topological Kitaev chain sections with $\mu_n = 0\ \forall n$ are depicted with a green background. Unpaired Majorana bound states are indicated with full circles. Setting $\mu_1 \gg t_1, \Delta_1$ transfers the leftmost unpaired Majorana from the first to the second site. This is a consequence of the perturbation shown in figure 2.5b: as μ_1 exceeds the inter-dot couplings, the unpaired Majorana is left on the second site.
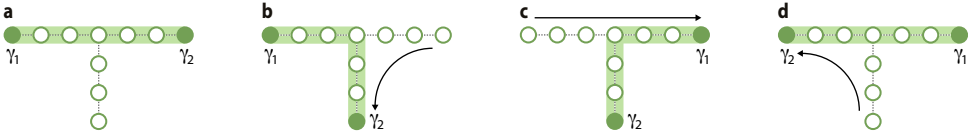
Figure 2.15: B_{12} **braiding sequence using a Kitaev chain T-junction.** γ_2 is first transferred to the additional leg, then γ_1 is shuttled to the right and, finally, γ_2 is transferred to the left. All transfers are performed by acting solely on the on-site chemical potentials μ_n (Alicea et al., 2011).
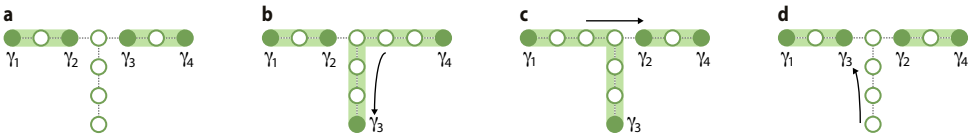
Figure 2.16: B_{23} **braiding sequence using a Kitaev chain T-junction.** γ_3 is first parked in the additional leg, then γ_2 is shuttled to the right and, finally, γ_3 is transferred to the left. Again, all transfers are performed by acting solely on the on-site chemical potentials μ_n.

Finally, we signal the existence of braiding protocols that do not require to physically move the Majorana modes but rely instead on measuring the fermion parity of pairs of Majoranas (Bonderson et al., 2008). This is known as *measurement-based braiding.*

UNIVERSAL QUANTUM COMPUTATION

Realistic quantum computers can suffer from either random errors or calibration errors. Decoherence is an example of a random error, while a calibration error could be aiming at rotating a qubit by 90° and instead rotating it by 90.01°. Long Kitaev chains are protected from decoherence, and braiding gates implement perfect rotations, as long as the unpaired Majorana modes are kept far apart during the exchanges. Braids are discrete: a quasi-particle is either taken around another or is not, and this does not depend on the details of the exchanging path (Nayak et al., 2008). We say that braiding gates are *topologically protected,* a computational model based on them is known as *topological quantum computation* and is fault-tolerant by nature (Freedman et al., 2002). So it is crucial to understand which gates can be realized via braiding and whether or not they suffice for *universal* quantum computation, i.e. whether they can implement *any* unitary transformation on a set of qubits (up to an arbitrarily small precision and an overall irrelevant phase).

To find out which qubit rotations the braiding gates are implementing, we can calculate the matrix elements of the $\gamma_a \gamma_b$ products (where $a \neq b$) and find out that they are equal to the Pauli matrices in the $\{|0\rangle_L, |1\rangle_L\}$ basis:

$$\begin{aligned}
\sigma_z &= -i\gamma_1\gamma_2 = -i\gamma_3\gamma_4 \\
\sigma_x &= -i\gamma_2\gamma_3 \\
\sigma_y &= +i\gamma_1\gamma_3
\end{aligned} \tag{2.19}$$

With these expressions, it is straightforward to identify the braiding gates with $\frac{\pi}{2}$ rotations, also shown in figure 2.17.

$$\begin{aligned}
B_{12} &= e^{-i\frac{\pi}{4}\sigma_z} = B_{34} \\
B_{23} &= e^{-i\frac{\pi}{4}\sigma_x}
\end{aligned} \tag{2.20}$$

Consistently with equation 2.18, it is trivial to see here that a double braid is not the identity and that a quadruple braid is.
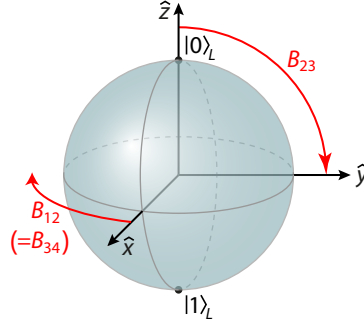
Figure 2.17: **Bloch sphere rotations induced by braiding operations.**

B_{12}, B_{23} and their combinations generate all the $\frac{\pi}{2}$ rotations of the Bloch sphere around the $\hat{x}$, $\hat{y}$ and $\hat{z}$ axes, but this gate set is obviously not universal. To make matters worse, such qubit rotations belong to the Clifford group, which is known to be efficiently simulable on a classical computer according to the Gottesman–Knill theorem (Gottesman, 1997). In summary, topological quantum computation with Majorana modes is not universal, and it can be simulated efficiently. Is braiding of any use at all?

It turns out that we are not missing many gates to get a universal set. The $\{H, T, \text{CNOT}\}$ gate set is known to be universal (Nielsen and Chuang, 2010, page 189):

$$H = \frac{1}{\sqrt{2}}\begin{pmatrix} 1 & 1 \\ 1 & -1 \end{pmatrix} \qquad T = \begin{pmatrix} 1 & 0 \\ 0 & e^{i\frac{\pi}{4}} \end{pmatrix} \qquad \text{CNOT} = \begin{pmatrix} 1 & 0 & 0 & 0 \\ 0 & 1 & 0 & 0 \\ 0 & 0 & 0 & 1 \\ 0 & 0 & 1 & 0 \end{pmatrix} \tag{2.21}$$

where H ("*Hadamard*") and T are single-qubit gates, while CNOT is a two-qubit gate in the $\{|00\rangle_L, |01\rangle_L, |10\rangle_L, |11\rangle_L\}$ basis. The Hadamard gate can be realized with braiding

via $H = \frac{1}{\sqrt{2}}\left(B_{12}^2 + B_{23}^2\right)$. The T gate, instead, is a $\frac{\pi}{4}$ rotation around the $\hat{z}$ axis (up to a global phase), so it can't be implemented with braiding operations: to realize it, non-topological operations are certainly needed. The CNOT situation is slightly more delicate. Within the natural qubit encoding of equation 2.15 ($|0\rangle_L = |00\rangle$, $|1\rangle_L = |11\rangle$), Bravyi demonstrated a *no-entanglement rule*: it is impossible to create two-qubit entanglement with topologically protected operations starting from $|00\rangle_L \equiv |0000\rangle$ (Bravyi, 2006). Since the CNOT is an entangling gate (for instance CNOT $(|0\rangle_L + |1\rangle_L) \otimes |0\rangle_L = |00\rangle_L + |11\rangle_L$) then it can't be realized within this encoding using braiding gates only. One approach to circumvent this *no-entanglement rule* is choosing a different encoding: Georgiev was indeed able to construct a CNOT gate using braiding operations only by encoding two qubits into six Majoranas instead of eight, however, this construction might be hard to extend to systems with more qubits (Georgiev, 2006). Another approach is to maintain the natural encoding of equation 2.15 and rely on a combination of topological and non-topological gates to implement both the T and the CNOT (Bravyi, 2006).

Even if not all the qubit gates can be implemented with braiding operations, a combination of topological and non-topological gates can be beneficial compared to a fully non-topological scheme. A reduced amount of non-protected operations can substantially simplify the error correction process since it's easier to protect from fewer error sources (Bravyi and Kitaev, 2005). Typical quantum error correction schemes can converge only if all the gate errors are below a small threshold, estimated to be between $\sim 10^{-6}$ and $\sim 10^{-2}$ depending on the qubit encoding architecture (Aharonov and Ben-Or, 1997; Knill et al., 1998; Raussendorf and Harrington, 2007). In comparison, Bravyi could construct protocols allowing for an error threshold as high as 14% by combining Majorana topological operations with a few noisy ones. He implemented a procedure known as *magic state distillation* (Bravyi and Kitaev, 2005; Bravyi, 2006).

There are various ways to complement topological operations with noisy ones in order to achieve universal quantum computation. One of the most natural ones involves bringing two unpaired Majoranas temporarily close to each other, breaking the topological protection on purpose. This splits the zero energy modes and, therefore, makes them evolve freely; the right evolution time implements the T gate (Freedman et al., 2006). Such scheme plus topological operations plus the ability to measure the joint fermion parity of four Majoranas is sufficient to achieve universality (Bravyi, 2006). For other proposals involving superconducting islands, we refer to Plugge et al. (2016, 2017) and Karzig et al. (2017).

UNIVERSAL TOPOLOGICAL QUANTUM COMPUTATION

It is unfortunate that Majorana braiding is not universal by itself. Moreover, we remark that *all* the Majorana braiding gates, including the CNOT (Georgiev, 2006), belong to the Clifford group and, vice-versa, the whole Clifford group is generated by braiding gates (Litinski and von Oppen, 2018). So *any* computation implemented with Majorana braiding can be efficiently simulated on a classical computer (Gottesman, 1997). It is a suspicious coincidence: we are engineering topology – something described by a discrete number of classes – into quantum objects, and we are getting what can be simulated efficiently on a classical computer – something built with discrete units. Is this lack of universality a limit of Majoranas or a more fundamental limitation of topology?

We recall that the richness of the braiding gates originates from the ground-state degeneracy. A singly degenerate ground state leads to abelian exchange statistics. In the Majorana case, doubly degenerate ground states are leading to non-abelian exchange statistics able to engineer Clifford gates. Then it is no surprise that higher dimensional systems, such as the $\mathbb{Z}_3$ parafermions, can actually support universal topological quantum computation (Alicea and Fendley, 2016). Majoranas are also known as *Ising anyons*, due to the relation to the $\mathbb{Z}_2$ group (Chiu et al., 2016), while the $\mathbb{Z}_3$ parafermions are closely related to the so-called *Fibonacci anyons*, which are the simplest known non-abelian model capable of topological universal quantum computation (Nayak et al., 2008).

non-degenerate ground state $\rightarrow$ operations are trivial (hence abelian)

doubly-degenerate ground state $\rightarrow$ non-abelian anyons, but only Clifford operations

higher degeneracy $\rightarrow$ universal quantum computation (with anyons)

In summary, we started by reviewing the simple Kitaev chain toy model, discussed the Poor Man's Majoranas appearing in a minimal two-site chain, and showed the exponential benefits of scaling it up. We went on to discuss the possible storage of quantum information and how to implement several topologically protected qubit gates via Majorana braiding. With the addition of a few non-topological operations, it is even possible to achieve universal quantum computation, yielding a record-high quantum error correction threshold. Finally, we concluded by mentioning that all of this might be just a stepping stone towards even more exotic and more powerful non-abelian anyons such as the $\mathbb{Z}_3$ parafermions.

ow that we have introduced the Kitaev chain toy model from a purely abstract point of view, we turn our attention to the proposal of a physical realization. Following the Kitaev Hamiltonian terms one by one, we introduce and discuss, from a theoretical point of view, all the ingredients that can implement the Kitaev chain in practice.

2.3. QUANTUM DOTS

To realize an N-site chain, it is natural to think of an array of quantum dots (QDs). In particular, semiconducting QDs can confine a few electrons into well-defined orbitals, thereby acting as artificial atoms (Kouwenhoven et al., 2001). If the QD energy levels are separated enough ($\Delta E \gg k_B T$), then the low-energy spectrum is equivalent to $\mu c^\dagger c$ – the first term of the Kitaev Hamiltonian. The QD energy spectrum can be measured with metallic leads and controlled by metallic gates (figure 2.18a,b). Gates are coupled capacitively (C_G), while the leads are weakly coupled to the QD via tunneling barriers, modeled as a capacitor ($C_{S/D}$) in parallel with a resistor ($R_{S/D} \sim 1-1000\,\mathrm{k\Omega}$).
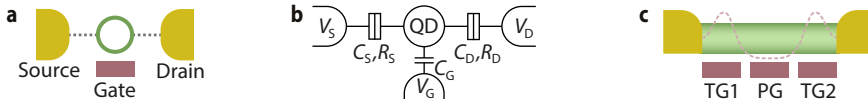
Figure 2.18: **a, b.** Schematic and circuit diagram of a quantum dot tunnel coupled to metallic contacts (source and drain) and capacitively coupled to one gate. **c.** Illustration of a realistic quantum dot confined in a semiconducting nanowire by several gates (here TG1, PG, and TG2).

Within the constant-interaction model (Van Houten et al., 1992; Hanson et al., 2007), the energy of a QD with N electrons amounts to

$$E(N) = \frac{\left[-e\left(N - N_0\right) + \sum_i C_i V_i\right]^2}{2C} + \sum_{n=1}^{N} E_n \tag{2.22}$$

where $C = \sum_i C_i$ and C_i and V_i are, respectively, the capacitances and the voltages of the nearby metallic parts. In the simple case of figure 2.18b, $C = C_S + C_D + C_G$, but more terms might be needed in case of more gates, leads or other metallic parts (figure 2.18c). It is meaningful to distinguish the first and the second terms of equation 2.22. The former encompasses all the electrostatic contributions, while the latter comes from the solution of Schrödinger's equation for a particle in a box, yielding the atom-like energy levels E_n (Kouwenhoven et al., 1997). The level spacing $\Delta E_n \equiv E_n - E_{n-1}$ has an order of magnitude of $\sim \frac{h^2}{m^* L^2}$ in the few-electrons regime, where h is the Planck constant, m^* is the effective mass and L is the characteristic length scale of the QD. It follows that semiconductors with a low effective mass have less stringent confinement requirements for resolving the level spacing. Popular III-V semiconductors such as GaAs, InAs, and InSb fall in this category, yielding a level spacing of $\sim 10\,\mathrm{meV}$ ($\sim k_B \cdot 100\,\mathrm{K}$) for $L \sim 100\,\mathrm{nm}$, a spacial resolution comfortably within state-of-the-art nanofabrication capabilities. Finally, we note that the N-dependence of the level spacing strongly depends on the dimensionality: for 1D boxes $\Delta E_n \propto N$, for 2D ones is constant, while $\Delta E_n \propto \frac{1}{\sqrt[3]{N}}$ in 3D. These simple calculations do not consider degeneracies ($E_n = 0$) such as the spin-degeneracy or further

ones due to possible additional symmetries (Tarucha et al., 1996). Due to degeneracies and geometric imperfections, realistic QDs have a non-monotonic $E_{\text{add}}(N)$; still, for QDs with comparable width, height, and depth, the $\frac{1}{\sqrt[3]{N}}$ trend is visible and stresses the importance of achieving the few-electrons regime to resolve the level spacing.

Using equation 2.22, we can calculate the electrochemical potential $\mu(N)$, i.e. the energy cost of the Nth electron,

$$\mu(N) \equiv E(N) - E(N-1) = \frac{e^2}{C}\left(N - N_0 - \frac{1}{2}\right) - \frac{e}{C}\sum_i C_i V_i + E_N \qquad (2.23)$$

and the addition energy, i.e. the difference between adding two consecutive electrons,

$$E_{\text{add}}(N) \equiv \mu(N) - \mu(N-1) = \frac{e^2}{C} + \Delta E_n \qquad (2.24)$$

Equation 2.23 highlights a key capability for our Kitaev chain purposes. By varying the gate voltage V_G, we can continuously control the electrochemical potential:

$$\mu = \frac{C_G}{C} e V_G + \text{constant.} \qquad (2.25)$$

The proportionality constant $\frac{C_G}{C}$ is denoted as the *lever arm* α. Finally, the last equation (2.24) pinpoints the distinction between the classical and quantum contributions: besides the level spacing ΔE_n, adding each electron requires an additional *charging energy* $E_c \equiv \frac{e^2}{C}$.[3] The addition energy is never zero due to the finite E_c; in particular, this energy cost may forbid the transport of electrons from source to drain for low voltage bias $\Delta V \equiv V_S - V_D$ if $|e\Delta V| < E_c$. This transport blockade due to electrostatics is known as *Coulomb blockade*, while the current peaks appearing whenever $\left|\mu(N)\right| < e\Delta V$ are known as *Coulomb peaks*.
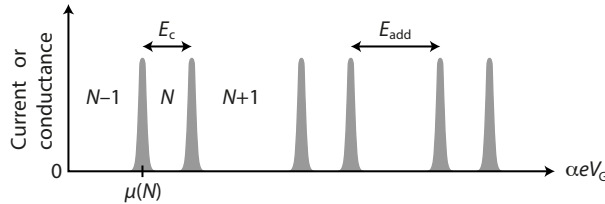
Figure 2.19: Illustration of Coulomb peaks for an odd N. Due to spin degeneracy, they appear in pairs separated by E_c. The vertical axis might display either the measured source to drain current I (for a low bias $\Delta V \ll E_c/e$) or its derivative at zero bias: the conductance $G \equiv \left.\frac{dI}{d\Delta V}\right|_{\Delta V=0}$.

As shown in figure 2.19, the Coulomb peaks appear in pairs separated by $E_{\text{add}} = E_c$ due to the spin degeneracy. Each pair corresponds to one atom-like orbital. In principle, it is also possible to observe Coulomb peaks grouped in quartets, sextets, and so on, in case of orbital degeneracies, either due to coincidences or further symmetries (Tarucha et al., 1996).

---

[3]We note that other authors define the charging energy as $E_c \equiv \frac{e^2}{2C}$.
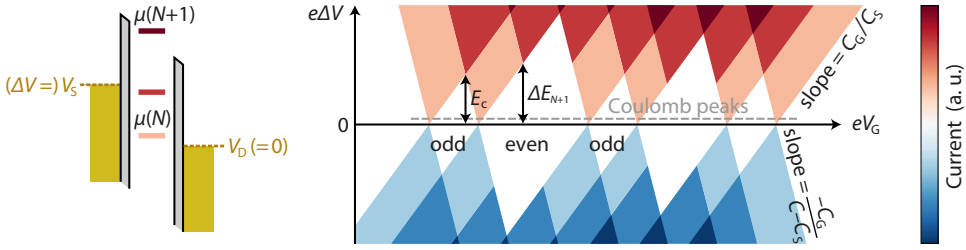
Figure 2.20: **Coulomb diamonds**. The source to drain current is measured as a function of V_G and the voltage bias ΔV. The Coulomb peaks correspond to the current peaks at $|e\Delta V| \ll E_c$. The schematic on the left shows that at a bias higher than the level spacing ΔE_n, transport can occur via multiple energy levels, resulting in a higher current.

At higher bias ΔV, the electron transport looks like figure 2.20, where the Coulomb peaks evolve into *Coulomb diamonds* as a function of V_G and ΔV. Here, the unit of the horizontal axis depends on the lever arm α, but the unit of the vertical axis doesn't: a voltage bias ΔV provides an electron energy $e\Delta V$, with no need of additional proportionality constants. This observation permits the extraction of the lever arm from a Coulomb diamond measurement. For instance, setting $V_D = 0$ (and thus $\Delta V = V_S$), makes the Coulomb diamond slopes equal to $\frac{C_G}{C_S}$ and $\frac{-C_G}{C-C_S}$, with which is easy to verify the following equation for the lever arm:

$$\frac{1}{\alpha} = \left| \frac{1}{\text{positive slope}} \right| + \left| \frac{1}{\text{negative slope}} \right| \tag{2.26}$$

Finally, note that when the energy bias $e\Delta V$ is higher than the level spacing ΔE_n, it is possible to transport electrons also via the higher energy levels without paying the E_c energy cost, as shown in the schematic on the left of figure 2.20. As a result, the ΔE_n show up at the edges of even diamonds in the form of current steps.

2.3.1. ZEEMAN SPLITTING

Degeneracies are detrimental for Kitaev chain purposes. We remind that the Hamiltonian of equation 2.1 considers a spinless chain, with no summation over the spin degree of freedom. This is essential: if we doubled the Kitaev Hamiltonian, any unpaired Majorana would get a counterpart and thus recombine into a trivial local fermion.

The spin degeneracy can be lifted with an external magnetic field B. This creates a Zeeman splitting $E_Z = g\mu_B B$, where μ_B is the Bohr magneton and the proportionality constant g is called g-factor.[4] To lift the spin degeneracy in practice, it is sufficient to achieve $E_Z \gg k_B T (\sim 4\,\mu\text{eV}$ in a standard dilution refrigerator with $T \sim 50\,\text{mK})$. This requirement is not so stringent: with a g-factor of 2 it demands $B \gg 40\,\text{mT}$; with the high g-factor of InSb (≈ 50) it requires $B \gg 1.5\,\text{mT}$.

The g-factor can be extracted experimentally by monitoring the Coulomb peaks as a function of B, as shown in figure 2.21. Here, it looks like a few lines "bounce" against each

---

[4]We note that many authors indicate with E_Z the Zeeman energy acquired by a single spin $E_Z = \frac{g}{2}\mu_B B\sigma$, where $\sigma = +1$ for spin up and $\sigma = -1$ for spin down. Here, for consistency with most references, we chose to indicate with E_Z the energy splitting between the two spins, hence gaining a factor of 2.
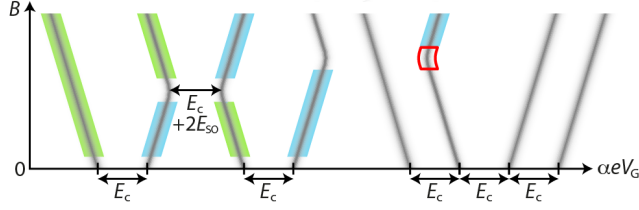
Figure 2.21: Representative illustration of Coulomb peak dependence on the external magnetic field. Non-degenerate levels are highlighted in green (spin-down) and blue (spin-up). The red contour shows that the elbows are curved.

other. This happens whenever $E_Z = \Delta E_n$, as it becomes more favorable to first fill the spin-down of the next orbital. When $E_{add} - E_c \gg k_B T$, the degeneracy is lifted, the spin is well-defined and highlighted in figure 2.21 in green (spin-down) and blue (spin-up). The degeneracy is not lifted for the lines of the rightmost quartet due to an additional orbital degeneracy. This example shows that accidental degeneracies can be spotted from the measurement illustrated in figure 2.21 by the presence of consecutive parallel lines.

Finally, the red contour highlights that the lines are curved whenever the spin polarization changes. It is due to spin-mixing caused by spin-orbit coupling (SOC).

2.3.2. SPIN-ORBIT COUPLING

The spin-orbit interaction couples the spin degree of freedom with the momentum $\vec{k}$. It is naturally present in all atoms, where it produces a (small) shift to the energy levels, and it is also present in bare semiconductors in the Rashba form

$$H_{SO} = \alpha_R \vec{\sigma} \times \vec{k} \tag{2.27}$$

or Dresselhaus form

$$H_{SO} = \alpha_D \left[\sigma_x k_x (k_y^2 - k_z^2) + \sigma_y k_y (k_z^2 - k_x^2) + \sigma_z k_z (k_x^2 - k_y^2) \right] \tag{2.28}$$

where $\vec{\sigma} = (\sigma_x, \sigma_y, \sigma_z)$ is the vector of Pauli matrices acting on the spinor $\begin{pmatrix} \psi_\uparrow(\vec{r}) \\ \psi_\downarrow(\vec{r}) \end{pmatrix}$ and α_R and α_D are proportionality constants.

In semiconducting QDs, the SOC can couple opposite spins from different orbitals. The elbow curvature highlighted in red in figure 2.21 comes from the avoided crossing of such levels, which can be used to estimate the SOC strength (Nadj-Perge et al., 2012). Indeed, the second and third resonances of figure 2.21 are separated by the sum of the charging energy and the repulsion due to SOC: $E_c + 2E_{SO}$.

Since $2E_{SO}$ can be much smaller than the charging energy, it is practical to measure it directly, from the high bias transport as a function of B shown in figure 2.22. We note that, in general, the amplitude of the avoided crossings might vary from level to level, due to the orbital component of SOC. In particular, this level-dependent E_{SO} might differ from the Rashba or Dresselhaus SOC strength in the bulk of the semiconductor, nevertheless, it gives the correct ballpark number (Nadj-Perge et al., 2012).
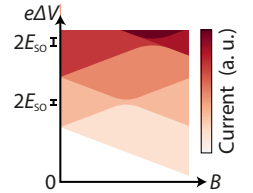
Figure 2.22: E_{SO} estimation from the high-bias transport.

2.3.3. DOUBLE QDs

So far, we reviewed how one QD can confine electrons into isolated energy levels, realizing $\mu_n c_n^\dagger c_n$ and controlling the electrochemical potential μ via equation 2.25. We also showed how the spin-degeneracy can be lifted with a finite magnetic field. It remains to show how to combine multiple quantum dots to create a chain.

TG1 PG1 TG2 PG2 TG3
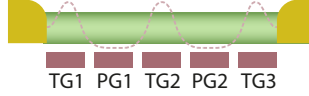
Figure 2.23: Schematic of a double quantum dot defined on a semiconducting nanowire by three tunnel-barrier ("T") gates and controlled by two plunger ("P") gates.

Figure 2.23 illustrates a chain of two QDs defined on a semiconducting nanowire deposited on a gate array. Here, the "T" gates create tunneling barriers, while the "P" gates are dedicated to the control of the chemical potential of both QDs: μ_1 and μ_2. Figure 2.24 shows a few examples of *charge stability diagrams*, which report the Coulomb peaks of both QDs as a function of V_{PG1} and V_{PG2}. The charge occupations define a checkerboard pattern, which might turn into a honeycomb pattern (panel c) in case of a finite capacitive cross-coupling (van der Wiel et al., 2002).
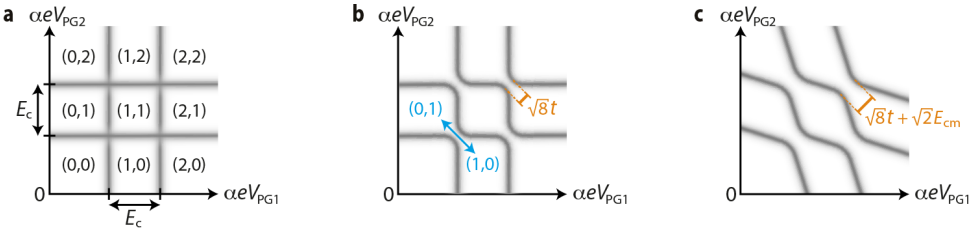
Figure 2.24: **Charge stability diagrams of double quantum dots. a.** The vertical and horizontal grey lines depict the Coulomb peaks of the first and second QD respectively. The numbers in parenthesis indicate the charge occupations of the two dots (N_1, N_2). **b.** A small tunneling rate t couples the regions with the same total charge, turning the crossing points into avoided crossings of amplitude $\sqrt{8}t$. **c.** In the case of a finite cross-coupling, where V_{PG1} affects μ_2 and vice-versa, the charge degeneracy lines appear skewed and the amplitude of the avoided crossings is augmented by the mutual charging energy E_{cm} (times $\sqrt{2}$) that each dot acquires when one charge is added to the other.

The architecture of figure 2.23 can be scaled to more than two QDs. It was demonstrated using either nanowires (Mu et al., 2021), carbon nanotubes (Grove-Rasmussen et al., 2008) or two-dimensional electron gases (Zajac et al., 2016), proving the feasibility of the $\sum_n \mu_n c_n^\dagger c_n$ term for a Kitaev chain of several sites. On top of that, an array of QDs can also implement the second term of the Kitaev Hamiltonian, $\sum_n t_n c_n^\dagger c_{n+1} + h.c.$, since the tunnel-coupling of neighboring QDs can be modeled by a hopping amplitude t_n (van der Vaart et al., 1995). Such a hopping term also manifests in the charge stability diagrams of figure 2.24b,c in the form of avoided crossings of amplitude $\sqrt{8}t$, where $2t$ is the energy difference between the bonding and anti-bonding of the two hybridized charge occupations (see for instance the blue arrow in panel b) and the additional $\sqrt{2}$ comes from the 45° tilt in the charge stability diagram.

At this stage, there is only one remaining term to complete the Kitaev Hamiltonian: $\sum_n \Delta_n c_n^\dagger c_{n+1}^\dagger + h.c.$ However, this cannot be found in QDs. Even considering semiconductors in general, it is hard to imagine any $c_i^\dagger c_j^\dagger$ mechanism able to pair electrons, since they naturally repel each other due to Coulomb interactions. There is a need for something else.

2.4. SUPERCONDUCTIVITY

In superconductors, there is an effective attractive interaction between electrons. In conventional superconductors, this is provided by electron-phonon scattering (Fröhlich, 1950), but it can have a different origin for more exotic superconducting states. In any case, such attractive interaction can condense the free electrons into a sea of *Cooper pairs* (Cooper, 1956). In the following, we don't discuss in detail all the wonderful properties of superconductivity, which include zero resistance and perfect diamagnetism (Tinkham, 2004), but rather focus on how this attractive pairing provides the $c_i^\dagger c_j^\dagger$ coupling needed for the Kitaev chain.

Most of the common superconductors available in the laboratory, such as Al, In, Nb, Pb, Sn, Ti, and many others, are well described by the Bardeen-Cooper-Schrieffer (BCS) microscopic theory of superconductivity (1957) with the following Hamiltonian:

$$H_{\text{BCS}} = \sum_{\vec{k},\sigma} \varepsilon_{\vec{k}} c_{\vec{k}\sigma}^\dagger c_{\vec{k}\sigma} + \sum_{\vec{k},\vec{k}'} U_{\vec{k}\vec{k}'} c_{\vec{k}\uparrow}^\dagger c_{-\vec{k}\downarrow}^\dagger c_{-\vec{k}'\downarrow} c_{\vec{k}'\uparrow} \tag{2.29}$$

where $\vec{k}$ and $\vec{k}'$ are electron momenta, $\sigma \in \{\uparrow, \downarrow\}$ is the spin, $\varepsilon_{\vec{k}} = \frac{\hbar^2 \vec{k}^2}{2m^*} - \mu_F$ is the electron energy with respect to the Fermi energy (μ_F) and $U_{\vec{k}\vec{k}'} < 0$ is the attractive interaction between electrons. Using a mean-field approximation (Bogoljubov, 1958; Valatin, 1958), the BCS Hamiltonian can be simplified to

$$H_{\text{B}} = \sum_{\vec{k},\sigma} \varepsilon_{\vec{k}} c_{\vec{k}\sigma}^\dagger c_{\vec{k}\sigma} - \sum_{\vec{k}} \left(\Delta_{\vec{k}} c_{\vec{k}\uparrow}^\dagger c_{-\vec{k}\downarrow}^\dagger + h.c. \right) + \text{constant} \tag{2.30}$$

Here, the $\Delta_{\vec{k}}$ pairing comes from the average of the attractive coupling U times the expectation value of the $c_{\vec{k}'\uparrow}^\dagger c_{-\vec{k}'\downarrow}^\dagger$ factor:

$$\Delta_{\vec{k}} \equiv -\sum_{\vec{k}'} U_{\vec{k}\vec{k}'} \left\langle c_{\vec{k}'\uparrow}^\dagger c_{-\vec{k}'\downarrow}^\dagger \right\rangle \tag{2.31}$$

Since U is negative, $\Delta_{\vec{k}}$ is positive. The Hamiltonian 2.30 has the advantage of being block-diagonal, and can be fully diagonalized as follows:

$$H_{\text{B}} = \sum_{\vec{k}} E_{\vec{k}} \left(b_{\vec{k}\uparrow}^\dagger b_{\vec{k}\uparrow} + b_{-\vec{k}\downarrow}^\dagger b_{-\vec{k}\downarrow} \right) + \text{constant} \tag{2.32}$$

$$\text{where} \quad E_{\vec{k}} \equiv \sqrt{\varepsilon_{\vec{k}}^2 + \Delta_{\vec{k}}^2} \quad \text{and} \quad \begin{cases} b_{\vec{k}\uparrow} = u_{\vec{k}} c_{\vec{k}\uparrow} - v_{\vec{k}} c_{-\vec{k}\downarrow}^\dagger \\ b_{-\vec{k}\downarrow} = u_{\vec{k}} c_{-\vec{k}\downarrow} + v_{\vec{k}} c_{\vec{k}\uparrow}^\dagger \end{cases} \tag{2.33}$$

$$\text{with} \quad \left|u_{\vec{k}}\right|^2 = \frac{1}{2}\left(1 + \frac{\varepsilon_{\vec{k}}}{E_{\vec{k}}}\right) \quad \text{and} \quad \left|u_{\vec{k}}\right|^2 + \left|v_{\vec{k}}\right|^2 = 1 \tag{2.34}$$

The b operators correspond to a new kind of quasiparticles – the *bogoliubons* – which are a mixture of electrons and holes. The coefficients $u_{\vec{k}}$ and $v_{\vec{k}}$ are, respectively, their electron-like and hole-like components.[5] They are shown in figure 2.25a as a function of the momentum. In the same figure, panels b and c show the energy spectrum of electrons, holes, and bogoliubons. Whereas panel d shows the bogoliubon density of states, which is gapped and diverges at $\pm\Delta$. We remind that, in order to appreciate such energy gap and the so-called *coherence peaks* of the density of states experimentally, $k_B T \ll \Delta$ is required. Common BCS superconductors, including the already mentioned ones, have $\Delta/k_B \sim 1K$.
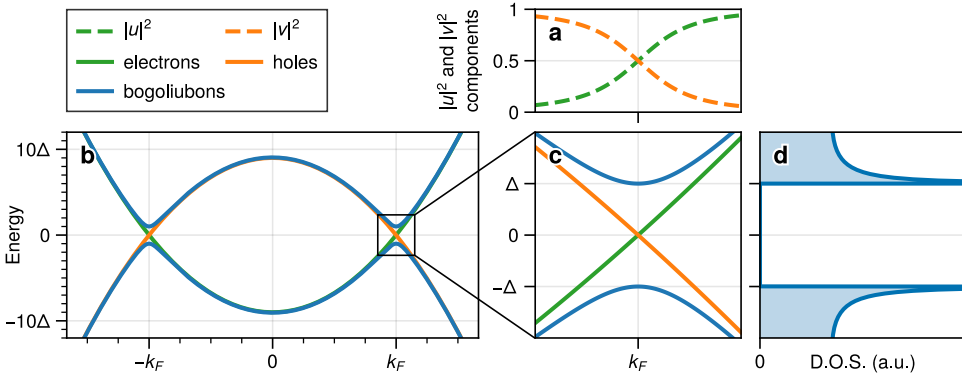
Figure 2.25: Numerical calculations of the u and v components (panel a), the energy spectrum with respect to the Fermi energy (panels b and c), and the bogoliubon density of states (panel d). Calculations are performed with a momentum-independent energy gap $\Delta_{\vec{k}} \equiv \Delta \sim 0.1\mu_F$. The 3D density of states shown in panel d is calculated using the numerical derivative of the bogoliubon spectrum. The Fermi momentum k_F is defined by $\frac{\hbar^2 k_F^2}{2m^*} = \mu_F$.

The target $\sum_n \Delta_n c_n^\dagger c_{n+1}^\dagger$ term of the Kitaev Hamiltonian and the $\sum_{\vec{k}} \Delta_{\vec{k}} c_{\vec{k}\uparrow}^\dagger c_{-\vec{k}\downarrow}^\dagger$ electron-hole coupling term of equation 2.30 are very similar. It remains to figure out how to match the summation indices while combining superconductivity with the semiconducting quantum dots described earlier. This is the focus of the following sections.

2.4.1. JOSEPHSON JUNCTIONS
A prime example showing how superconducting properties can be exported into other materials is represented by Josephson junctions. They are formed by connecting two superconductors S_1 and S_2 via a weak link: like an insulating layer (SIS junction), a constriction (ScS), or a normal conductor (SNS). We are particularly interested in the

---

[5]In general, $u_{\vec{k}}$ and $v_{\vec{k}}$ are complex numbers, although there is a gauge arbitrariness in this case, which is the rationale for plotting their squares here. There is a sole constraint on the phase difference between $u_{\vec{k}}$ and $v_{\vec{k}}$: it must match the $\Delta_{\vec{k}}$ phase. If $\Delta_{\vec{k}}$ is real then both $u_{\vec{k}}$ and $v_{\vec{k}}$ can be chosen to be real, as was done in Bogoliubov's original work (1958). For more details on the phase see (Tinkham, 2004, page 61).

latter since it can be formed by semiconducting-superconducting heterostructures (figure 2.26c). Here, Cooper pairs from the superconductors may diffuse into the semiconductor via the so-called *proximity effect*, making it (weakly) superconducting as well (Tinkham, 2004, page 197).
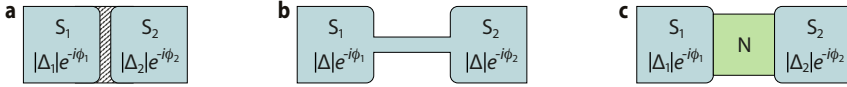
Figure 2.26: Illustrations of SIS, ScS, and SNS Josephson junctions.

Without going into the details of Josephson junction theory, for which we refer to Tinkham (2004, chapter 6), here we only mention the two Josephson relations (Josephson, 1962), which are essential for the understanding of chapters 6 and 7:

$$I_s = I_c \sin \Delta\phi \tag{2.35}$$

$$\frac{d(\Delta\phi)}{dt} = \frac{2eV}{\hbar} \tag{2.36}$$

where $\Delta\phi \equiv \phi_2 - \phi_1$ is the phase difference between the two superconductors.

The first relation predicts that the weak link can sustain a finite *supercurrent* I_s, which may be as large as the *critical current* I_c. Supercurrent means current with zero resistance, while, if a current $I > I_c$ is forced through the weak link, the junction returns to the normal-conductor state and becomes resistive. Equation 2.35 holds precisely only for ideal SIS junctions at zero temperature. Finite temperature fluctuations can cause the junction to switch prematurely to the normal state (Tinkham, 2004, page 207) at a *switching current* $I_{sw} < I_c$. And realistic SNS junctions might deviate from the ideal sinusoidal behavior of the *current-phase relationship* (CPR) of equation 2.35.

The second Josephson relation (equation 2.36) matters when a finite voltage bias V is applied across the junction. It predicts a precession of the phase $\Delta\phi$ which is rather fast: $V = 1\,\mu V$ yields $\frac{d(\Delta\phi)}{dt} = 3\,\text{GHz}$.

2.4.2. ANDREEV BOUND STATES

The supercurrent through a Josephson junction might be carried by Andreev bound states (ABSs) as illustrated in figure 2.27a. ABSs can be seen in a simple toy model as arising from resonant *Andreev reflection*, which is the reflection of an electron into a hole at the interface between a normal conductor and a superconductor (Andreev, 1964). Andreev reflection is made possible by the creation (or annihilation) of a Cooper pair

Figure 2.27: Illustrations of **a.** Supercurrent carried by an ABS via resonant Andreev reflection **b.** An ABS formed in a (semi-)conductor coupled to a single superconductor.

into the superconductor. This enables the supercurrent flow by continuously destroying Cooper pairs from S_1 and creating them into S_2 (figure 2.27a). The resonant condition mandates that the sum of the phases acquired during the reflections and the electron (or hole) traveling in the normal conductor equals zero (mod 2π). A bound state is formed when the resonant condition is met and the quasi-particles are confined (we come back to the importance of such confinement later on). This can also happen with one superconductor only, as shown in figure 2.27b where normal reflections replace the Andreev reflection with the second superconductor. Here, Cooper pairs are continuously formed and destroyed at the interface, yielding an effective pairing Γ between the electrons in the normal conductor. To formalize this intuition, we consider the following model.

A SIMPLE MODEL: THE ATOMIC LIMIT

If a single spin-degenerate level of energy ξ is weakly coupled to a superconductor, the ABS Hamiltonian can be written as follows

$$H_{\text{ABS}} = \sum_\sigma \xi c_\sigma^\dagger c_\sigma + \Gamma \left(c_\uparrow^\dagger c_\downarrow^\dagger + h.c. \right) \tag{2.37}$$

with further additions in the case of a finite charging energy and Zeeman field. It takes the following form in the $\{|0\rangle, |\uparrow\downarrow\rangle, |\downarrow\rangle, |\uparrow\rangle\}$ basis with the $|\uparrow\downarrow\rangle \equiv c_\uparrow^\dagger c_\downarrow^\dagger |0\rangle$ ordering convention:

$$H_{\text{ABS}} = \begin{pmatrix} 0 & \Gamma & 0 & 0 \\ \Gamma & 2\xi + E_c & 0 & 0 \\ 0 & 0 & \xi - \frac{E_Z}{2} & 0 \\ 0 & 0 & 0 & \xi + \frac{E_Z}{2} \end{pmatrix} \tag{2.38}$$

The Hamiltonian 2.38 – already diagonal for the odd $\{|\downarrow\rangle, |\uparrow\rangle\}$ subspace – can be diagonalized in the even $\{|0\rangle, |\uparrow\downarrow\rangle\}$ subspace with a Bogoliubov transformation. This yields the even eigenstates

$$\begin{cases} |S-\rangle = u|0\rangle - v|\uparrow\downarrow\rangle \\ |S+\rangle = v|0\rangle + u|\uparrow\downarrow\rangle \end{cases} \quad \text{of energies} \quad E_{S\pm} = \xi + \frac{E_c}{2} \pm \sqrt{\left(\xi + \frac{E_c}{2}\right)^2 + \Gamma^2} \tag{2.39}$$

$$\text{where} \quad |u|^2 = \frac{1}{2}\left[1 + \frac{\xi + \frac{E_c}{2}}{\left(\xi + \frac{E_c}{2}\right)^2 + \Gamma^2}\right] \quad \text{and} \quad |u|^2 + |v|^2 = 1 \tag{2.40}$$

which resemble the BCS bogoliubons (equations 2.33 and 2.34), with the substitutions $\epsilon_{\vec{k}} \mapsto \xi + \frac{E_c}{2}$ and $\Delta_{\vec{k}} \mapsto \Gamma$. However, as opposed to the BCS bogoliubons, the eigenstates of equation 2.39 do not correspond to single-particle excitations, since the Hamiltonian 2.38 is written for a many-body basis. Adding a single particle to the ABS implies switching the eigenstate parity from even to odd (or vice-versa) and requires a supply of the corresponding energy difference (Lee et al., 2013). Therefore, to get the single-particle ABS spectrum it is sufficient to calculate the difference between the $E_{S\pm}$ even eigenvalues and the $\xi \pm \frac{E_Z}{2}$ odd ones, yielding

$$E_{\text{ABS}} = \pm \left[\frac{E_c}{2} \pm \frac{E_Z}{2} - \sqrt{\left(\xi + \frac{E_c}{2}\right)^2 + \Gamma^2} \right] \tag{2.41}$$

This is calculated in figure 2.28b-d for three values of Γ (at $E_Z = 0$, for simplicity). In particular, panel b sets $\Gamma = 0$, losing all superconducting properties and recovering the Coulomb diamond of a standard QD. Note that there are two charge degeneracy points at $\xi + \frac{E_c}{2} = \pm \frac{E_c}{2}$. Here, the ground state parity switches from even to odd and back to even, as shown in section 2.3. As Γ is increased, E_{S-} is lowered, and for $\Gamma \geq \frac{E_c}{2}$ the parity switches disappear (panel d): here, $|S-\rangle$ is the many-body ground state for any ξ. The Γ dependence of the ground state parity is summarized in panel a, for the E_Z dependence we refer to (Lee et al., 2013).
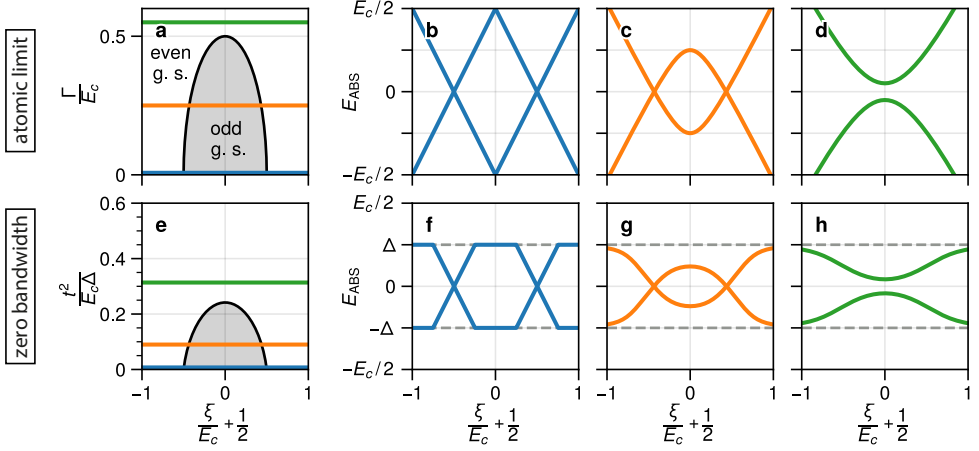
Figure 2.28: **Comparison between the atomic limit (first row) and the zero-bandwidth approximation (second row) of the Anderson impurity model.** The first column shows the many-body ground-state parity, and the others show the single-particle excitation spectra for $\Gamma \in \{0, 0.25, 0.55\}$, $t \in \{0, 0.15, 0.28\}$, $E_Z = 0$, $E_c = 1$, $\Delta = 0.25$.

THE ANDERSON IMPURITY MODEL

The Hamiltonian 2.38 can be formally derived – see for instance (Bauer et al., 2007) or (Meng et al., 2009) – from the *Anderson impurity model* (Anderson, 1961), which considers an impurity tunnel-coupled to a metallic lead. In our case, the lead is a superconductor described by the BCS Hamiltonian of equation 2.30. The Anderson model of an impurity coupled to a BCS superconductor reads as follows:

$$H_{\text{Anderson}} = H_{\text{I}} + H_t + H_{\text{B}}$$
$$H_{\text{I}} = \sum_\sigma \left(\xi + \frac{E_Z}{2}\sigma_z \right) c_\sigma^\dagger c_\sigma + E_c c_\uparrow^\dagger c_\uparrow c_\downarrow^\dagger c_\downarrow$$
$$H_t = \sum_\sigma t d_\sigma^\dagger c_\sigma + h.c. \tag{2.42}$$
$$H_{\text{B}} = \sum_{\vec{k},\sigma} \varepsilon_{\vec{k}} d_{\vec{k}\sigma}^\dagger d_{\vec{k}\sigma} - \sum_{\vec{k}} \left(\Delta_{\vec{k}} d_{\vec{k}\uparrow}^\dagger d_{-\vec{k}\downarrow}^\dagger + h.c. \right)$$

where we used $d^\dagger$ and d for the creation and annihilation operators in the superconductor in order to distinguish them from the impurity ones ($c^\dagger$ and c). The d and c operators come together only in the tunnel-coupling H_t proportional to the parameter t. The

impurity Hamiltonian H_I comprises a single-level energy ξ, a Zeeman splitting E_Z and possibly a finite charging energy E_c. Thus, it can model either a magnetic impurity (like transition-metal adatoms on a superconducting surface), a defect in the crystal lattice or a quantum dot.

The crucial feature is having some sort of confinement, yielding a localized orbital of energy ξ. Looking at the naive picture of figure 2.27b, we stress the importance of confinement in all directions, also the ones parallel to the S-N interface. Otherwise, instead of the Andreev bound states discussed here, we would get Andreev *bands*, with an energy dispersion depending on the momentum parallel to the S-N interface. For this reason, it is natural to picture ABSs as quantum dot orbitals coupled to a superconductor. This motivates the usage of E_Z and E_c as the ABS Zeeman energy and charging energy, respectively (in the same spirit, μ is sometimes used in place of ξ, for instance, in chapter 3). Nevertheless, we stress that the ABS Zeeman and charging energies might be significantly different compared to an uncoupled QD due to, respectively, g-factor renormalization (Antipov et al., 2018) and an increase of the capacitance. For instance, chapters 4 and 6 report $g_{QD} \sim 45$ and $g_{ABS} \sim 20$; chapters 3 and 7 report $E_c^{QD} \sim 2-4\,\mathrm{meV}$ while considering E_c^{ABS} to be negligible ($\ll 1\,\mathrm{meV}$).

The numbers matter, and with them also the validity of the Hamiltonian 2.38. Such a simple effective Hamiltonian is known as the *atomic limit* of the Anderson model and is a good approximation as long as $\Gamma, E_c, E_{ABS} \ll \Delta$ (Meng et al., 2009). The two models are connected by $\Gamma = \pi t^2 \rho_0$, where ρ_0 is the normal-state density of states at the Fermi energy. However, realistic devices could have $E_c \sim \Delta$ or even larger, which would make the atomic limit completely ungrounded for most of the parameter space shown, for instance, in figure 2.28a, especially where $\Gamma \sim E_c$. To address such a broad parameter space, we can utilize a different approximation of the Anderson model: the zero-bandwidth one.

ZERO-BANDWIDTH APPROXIMATION

The raw Anderson impurity model of equation 2.42 is hard to solve. The spectrum can be calculated numerically with advanced techniques such as the Numerical Renormalization Group (NRG) (Bauer et al., 2007) or quantum Monte Carlo simulations (Siano and Egger, 2004), but these techniques are computationally heavy and out of the scope of this manuscript. A simpler approach involves approximating the BCS superconductor with a single pair of energy levels, dropping the summation over $\vec{k}$. This corresponds to approximating the BCS density of states (figure 2.25d) as a pair of coherence peaks with zero bandwidth (ZBW): the density of states is set to zero both inside and outside the gap. Within this approximation, the Anderson model is greatly simplified:

$$H_{\mathrm{Anderson}} \approx H_I + H_t + H_{\mathrm{ZBW}}$$
$$H_{\mathrm{ZBW}} = -\Delta d_\uparrow^\dagger d_\downarrow^\dagger + h.c. \tag{2.43}$$

It consists of a 16×16 matrix which can be separated into even and odd subspaces and diagonalized. Again, the single-particle ABS spectrum is the difference between the even and odd eigenvalues. It is shown in figure 2.28f-h for different selections of the tunnel amplitude t. As opposed to the atomic limit case, here we can appreciate that the ABS spectrum is bound to the parent gap Δ, as shown in experimental data (Lee et al., 2013).

In conclusion, the ZBW approximation is a good compromise between computational speed and accuracy for a wide parameter range, as proven by the qualitative comparison with experimental data and the quantitative comparison with NRG calculations (Žitko and Pavešić, 2022). For $\Gamma, E_c \ll \Delta$, where the atomic limit is valid and preferable due to its simple analytical solution, the spectrum calculated with the two approximations is identical, with the following simple correspondence:

$$\Gamma = \frac{t^2}{\Delta} \tag{2.44}$$

2.4.3. CROSSED ANDREEV REFLECTION

Now that ABSs have been introduced, we show how they can mediate the Δ_n pairing between neighboring QDs. Figure 2.29 shows an ABS connecting two quantum dots. If
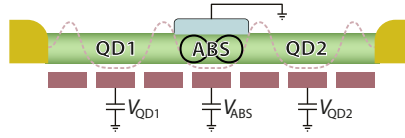
Figure 2.29: Illustration of an ABS (∞ symbol) tunnel-coupled to two QDs.

the ABS is in the even ground state $|S-\rangle = u|0\rangle - v|\uparrow\downarrow\rangle$, then, with amplitude proportional to v, it can donate one of the two electrons to either of the neighboring QDs and then, with u, it can return to the even ground state by donating the remaining electron to the other QD. Creating an electron into both QDs is exactly what the $\Delta_n c_n^\dagger c_{n+1}^\dagger$ term does. Note that since the first electron can be donated to either the left or the right QD, this process is proportional to $2uv$. Both sequences are shown on the left of figure 2.30.

The reversed process, instead, can fill the $u|0\rangle$ component of the ABS, taking one electron from either QD and, eventually, going back to the $|S-\rangle$ ground state into the $v|\uparrow\downarrow\rangle$ component. This process is also proportional to $2uv$ and realizes $\Delta^* c_{n+1} c_n$. Both the direct and the reversed process are denoted here as *crossed Andreev reflection* (CAR), since c_n destroys an electron from the nth site and c_{n+1} can be viewed as creating a hole in the $(n+1)^{\text{th}}$ one. Analogously, $c_n^\dagger$ and $c_{n+1}^\dagger$ destroy a hole and create an electron.
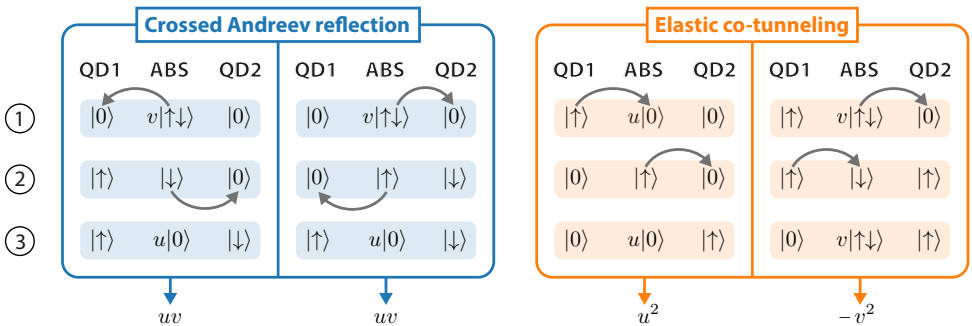
Figure 2.30: Schematic illustration of the two CAR paths and two ECT ones mediate by one ABS.

2.4.4. ELASTIC CO-TUNNELING

Besides the Δ_n terms, ABSs can also realize tunneling $t_n c_n^\dagger c_{n+1}$ between neighboring QDs. Strikingly, the dependence on the u and v components is completely different from the CAR case. As the right side of figure 2.29 shows, one electron can be transferred from QD1 to QD2 in two ways: it can either directly tunnel from QD1 to the ABS and then to QD2 or it can involve a second electron tunneling first from the ABS to QD2 and then fill the void from QD1 to the ABS. The first option involves, twice, the u component of the ABS, while the second path involves only the v one. It turns out that the two paths interfere destructively so that the total t_n amplitude mediated by the ABS is proportional to $u^2 - v^2$ (Liu et al., 2022; Bordin et al., 2023). The origin of the destructive interference is the fermionic exchange statistics involving the two electrons used by the v path. A simple proof is reported in appendix A.

In synthesis, following the results of figure 2.30 and the calculation reported in chapter 6, the Δ_n and t_n amplitudes have the following dependence on the ABS components:

$$\Delta_n \propto \left(\frac{uv}{E_\uparrow} + \frac{uv}{E_\downarrow} \right) \exp\left(i\phi_n\right) \qquad t_n \propto \frac{u^2}{E_\uparrow} - \frac{v^2}{E_\downarrow} \tag{2.45}$$

where $E_\uparrow$ and $E_\downarrow$ are the ABS excitation energies for the two different spin components. Such denominators are due to the intermediate states used in step ② of figure 2.30. One path excites the ABS from the $|S-\rangle$ to the $|\uparrow\rangle$ state, while the other relies on the $|\downarrow\rangle$ one. Since the ABS excitation requires the corresponding energy cost, these are second-order processes involving a virtual occupation of the ABS. Hence, we refer to the effective t_n processes as *elastic co-tunneling* (ECT). The *"co-"* reminds us of the second order, while the *"elastic"* reminds us of the energy conservation requirement: the QD1 and QD2 energy levels must be aligned.

CAR is also a second-order process, but the QD energy levels must be anti-aligned to create or destroy Cooper pairs at zero energy. Hence, both QDs must be at zero energy for CAR and ECT to coexist.

Finally, we note that the radically different dependence of CAR and ECT on the ABS chemical potential ξ is crucial for Kitaev chain purposes. Figure 2.31 super-imposes the CAR and ECT signals for the simple situation where $E_c = E_Z = 0$, so that $E_\uparrow = E_\downarrow \equiv E_{ABS}$ (the finite-field case is discussed further on and in chapter 3). At $\xi = 0$, ECT is suppressed by the destructive interference, whereas for large $|\xi|$, is CAR to be suppressed faster than ECT: this ensures the existence of crossing points (brown) where $|t_n| = |\Delta_n|$, as prescribed in section 2.1.1. In addition, we note that the left crossing point realizes $t_n = |\Delta_n|$ while the right one produces $t_n = -|\Delta_n|$. Such sign freedom can be used to tune the relative phase between t_n and Δ_n for long Kitaev chains (Liu et al., 2024b).
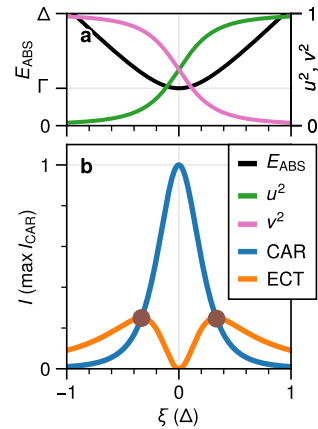
Figure 2.31: ξ dependence of **a.** the ABS energy, u^2 and v^2, **b.** the CAR- and ECT-induced currents.

2.5. THE KITAEV CHAIN IN PRACTICE

Figure 2.32 summarizes how all the ingredients introduced in this chapter come together to realize the Kitaev chain Hamiltonian. The μ_n, t_n, and Δ_n terms are implemented, respectively, by an array of QDs coupled by ECT and CAR. As shown in the previous section, CAR and ECT are balanced by tuning the ABSs residing in the hybrid regions of the device. Finally, the Zeeman splitting E_Z must be larger than the temperature broadening and the inter-dot couplings t_n and Δ_n to ensure an effectively spinless Hamiltonian, as prescribed by Kitaev (2001).

However, a potential issue arises when the QDs are spin-polarized: can CAR and ECT coexist simultaneously? ECT preserves the spin, while CAR couples opposite spins via the $v|\uparrow\downarrow\rangle$ component of the ABS. They are seemingly incompatible. The issue can be solved using non-collinear quantization axes for neighboring QDs (Leijnse and Flensberg, 2012a), enabling finite $\langle\uparrow|t_n c_n^\dagger c_{n+1}|\downarrow\rangle$ and $\langle\uparrow|\Delta_n c_n^\dagger c_{n+1}^\dagger|\uparrow\rangle$ amplitudes. This could be achieved using micromagnets to locally polarize every QD (Bordoloi et al., 2022) along different directions (Jardine et al., 2021). A practical alternative is relying on the spin-orbit coupling to possibly flip the spins as the electrons travel from one QD to the next. SOC is naturally present in our devices, as discussed in section 2.3.2, and is strong enough to enable a substantial spin precession so that the spin-fliping probability is of the same order of magnitude as the spin-preserving one (G. Wang et al., 2022a; Q. Wang et al., 2023). With SOC, CAR and ECT can coexist for any QD spin selection: the Kitaev chain Hamiltonian implementation is complete.

$$H_N = \sum_{n=1}^{N} \mu_n c_n^\dagger c_n + \sum_{n=1}^{N-1} \left(t_n c_n^\dagger c_{n+1} + \Delta_n c_n^\dagger c_{n+1}^\dagger + h.c. \right)$$

Figure 2.32: Summary of the Kitaev chain recipe.

More details are reported in the appendices:

- Appendix B reports the nanofabrication recipes used for the Kitaev chain devices of the following chapters.

- Appendix C presents a sequence of measurements illustrating how to tune a Kitaev chain from scratch: from the basic device characterization to the full implementation of figure 2.32's concept.

FURTHER READING

This pedagogical introduction to Kitaev chains was inspired by Kitaev's seminal work (2001) and the subsequent realistic proposals (Sau and Das Sarma, 2012; Leijnse and Flensberg, 2012a; Fulga et al., 2013). To complete the picture, we list here the main works that contributed to the first realizations of Kitaev chains in recent years, to their understanding, and proposed further developments towards the first Majorana qubits.

The pioneering experimental work in Delft (Wang et al., 2022a; chapters 3 and 4) triggered a booming theoretical effort in many places around the globe, including Lund (Tsintzis et al., 2022, 2024; Seoane Souto et al., 2023, 2024; Samuelson et al., 2024; Svensson and Leijnse, 2024; Benestad et al., 2024; Nitsch et al., 2024), Delft (Liu et al., 2022, 2023, 2024a,b; Torres Luna et al., 2024; Miles et al., 2024; Bozkurt et al., 2024; Pan et al., 2024), Budapest (Boross et al., 2019; Széchenyi and Pályi, 2020; Boross and Pályi, 2024; Kocsis et al., 2024), Madrid (Pino et al., 2024; Cayao and Aguado, 2024; Alvarado et al., 2024), Beijing (Liu et al., 2024c), Paris (Gómez-León et al., 2024) and Basel (Luethi et al., 2024a,b).

New experiments are mostly from Delft, but already on two different platforms: InSb-Al hybrid nanowires (chapters 5 and 6; Koch et al., 2023; Zatelli et al., 2024; van Driel et al., 2024b) and InSbAs-Al 2DEGs (Wang et al., 2023; ten Haaf et al., 2024a,b; van Driel et al., 2024a). New efforts are being developed in Budapest (Kürtössy et al., 2022) and Wien.

3

TUNABLE CROSSED ANDREEV REFLECTION AND ELASTIC CO-TUNNELING IN HYBRID NANOWIRES

A short superconducting segment can couple attached quantum dots via elastic cotunneling (ECT) and crossed Andreev reflection (CAR). Such coupled quantum dots can host Majorana bound states provided that the ratio between CAR and ECT can be controlled. Metallic superconductors have so far been shown to mediate such tunneling phenomena, albeit with limited tunability. Here we show that Andreev bound states formed in semiconductor–superconductor heterostructures can mediate CAR and ECT over mesoscopic length scales. Andreev bound states possess both an electron and a hole component, giving rise to an intricate interference phenomenon that allows us to tune the ratio between CAR and ECT deterministically. We further show that the combination of intrinsic spin-orbit coupling in InSb nanowires and an applied magnetic field provides another efficient knob to tune the ratio between ECT and CAR and optimize the amount of coupling between neighboring quantum dots.

T he Kitaev chain is a prime example of condensed-matter toy models exhibiting a topological superconducting phase (Kitaev, 2001). Practical proposals to construct an artificial Kitaev chain require a set of quantum dots (QDs) separated by narrow superconducting segments (Sau and Das Sarma, 2012; Leijnse and Flensberg, 2012a; Fulga et al., 2013). Such QDs interact via two mechanisms: crossed Andreev reflection (CAR) and elastic co-tunneling (ECT). In CAR, electrons from two separate QDs tunnel into the superconductor forming a Cooper pair; or in its reversed process, a Cooper pair is split into two electrons, tunneling to different QDs (see schematic in Fig. 3.1a) (Recher et al., 2001; Beckmann et al., 2004; Russo et al., 2005). ECT occurs when a single electron tunnels between the two QDs via the superconductor (see schematic in Fig. 3.1b). The balance between CAR- and ECT-induced couplings is crucial for observing poor man's Majorana zero modes at the boundaries of a two-site Kitaev chain (Leijnse and Flensberg, 2012a), recently observed by Dvir et al. (2023). Furthermore, precise control over the interplay between CAR and ECT is crucial for achieving high-fidelity entanglement generation through Cooper-pair splitting (Choi et al., 2000; Recher et al., 2001). Moreover, this control can serve as an efficient mechanism for coupling spin-qubits over longer length scales beyond those achievable through exchange coupling (Leijnse and Flensberg, 2013; Hassler et al., 2015; González Rosado et al., 2021; Spethmann et al., 2022, 2024).

Semiconductor-superconductor hybrids are the primary platform to study CAR and ECT (Hofstetter et al., 2009, 2011; Das et al., 2012; Schindele et al., 2012) due to their unique ability to form quantum dots (QDs) in semiconductors and effectively couple them to superconductors. These hybrids enable the formation of Andreev-bound states (ABS), where a confined semiconducting level is tunnel-coupled to a superconductor. An important characteristic of ABSs is their ability to transition smoothly from electron-like to hole-like excitations through electrostatic gating (Schindele et al., 2014; Danon et al., 2020; Ménard et al., 2020). ABSs can further replace metallic superconductors in facilitating CAR and ECT processes between adjacent quantum dots (QDs) (Fülöp et al., 2015). It is predicted that the interplay between the electron and hole components of an ABS plays a crucial role in controlling CAR and ECT phenomena (Liu et al., 2022). Furthermore, the presence of an external magnetic field impacts the energy of ABSs through Zeeman splitting (Lee et al., 2013), thereby influencing the amplitudes of CAR and ECT. Notably, in the presence of spin-orbit coupling, the dependence of these amplitudes on the magnetic field direction becomes anisotropic (G. Wang et al., 2022a; Q. Wang et al., 2023).

Scaling the Kitaev chain from the two-QD system discussed by Dvir et al. (2023) to many QD, requires a deterministic control of the CAR and ECT coupling between neighboring QD. The interplay of CAR and ECT and the ABS mediating them provides the means to achieve such control. To this date, this interplay has never been demonstrated.

In this work, we report on the gate tunability of CAR and ECT in hybrid semiconductor-superconductor heterostructures. In particular, both processes are correlated with the presence of ABSs in the hybrid. By comparing experimental data and our theoretical model, we further show that the observed CAR and ECT amplitudes, respectively, result from constructive and destructive interference of tunneling paths. The interference pat-

tern is linked to the charge of the mediating Andreev bound state and can be controlled via tuning the hybrid's chemical potential. Finally, we report on the magnetic field dependence of CAR and ECT. We show how the CAR and ECT interference patterns are modified through the interplay of the orientation of the magnetic field, the direction of the spin-orbit coupling, the energy of the ABS and its spin-splitting.

3.1. CORRELATION BETWEEN ABSS AND CAR/ECT
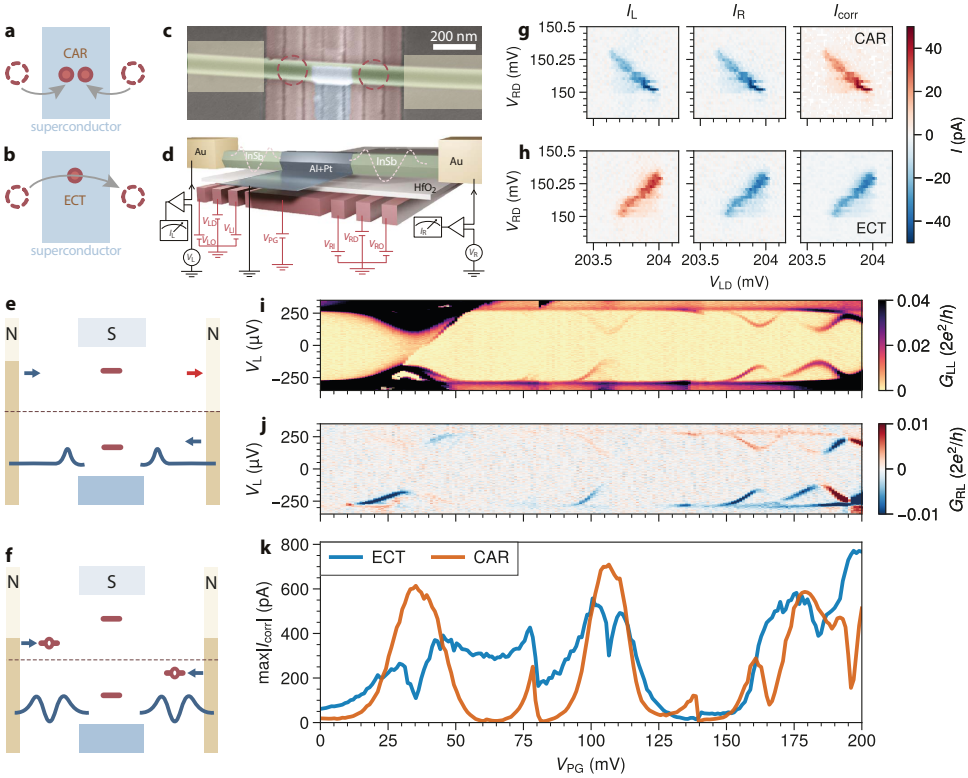
Figure 3.1: Correlation between ABSs and CAR/ECT processes. a.,b. Illustration of the ECT (a) and CAR (b) processes. **c.** Scanning electron micrograph of device A. **d.** Schematic illustration of our devices and experimental setup. An InSb nanowire (green) is coated by a thin Al shell (blue, Al+Pt for device A), on top of seven finger gates (red). Two Cr/Au leads (yellow) are attached to both sides of the wire. **e.** Spectroscopy configuration: yellow bars depict voltage bias in normal (N) contacts while blue rectangles represent the superconductor (S). Blue curves sketch the desired voltage profile defined with the gates; voltage barriers are not to scale. **f.** Configuration with QDs: applying low voltages on V_{LO}, V_{LI} and V_{RI}, V_{RO} forms a QD on the left and right side of the superconducting segment. **g., h.** Measurement of the ECT-induced current (g) and the CAR-induced current (h), as in Wang et al. (2022a), around a charge degeneracy point. **i.** G_{LL} as a function of V_L and V_{PG} when setting the gates in the tunneling spectroscopy configuration. **j.** G_{RL} as a function of V_L and V_{PG} in the same settings of panel (b). G_{LL} and G_{RL} are calculated by taking the numerical derivative after applying a Savitzky-Golay filter of window length 11 and polynomial order 1 to the measured I_L and I_R currents, respectively. **k.** CAR- and ECT-induced currents as a function of V_{PG} measured using the $N \leftrightarrow N + 1$ transition in both QDs. The values of V_{LI} and V_{RI} were kept constant during measurements of panels (b-c) and (e).

Fig. 3.1c shows a scanning electron microscope image of device A, while in Fig. 3.1d we show a schematic illustration of the device and the measurement circuit. An InSb nanowire is deposited on pre-fabricated metallic gates (separated from the nanowire by a thin dielectric layer). Using the shadow lithography technique (Heedt et al., 2021; Borsoi et al., 2021), a thin superconducting layer is deposited on top of the middle segment of the nanowire. Normal contacts are then fabricated on each side of the device. Details of the fabrication are described in Supplementary Information. The chemical potential of the semiconducting-superconducting hybrid is controlled by the plunger gate underneath (V_{PG}). The bare nanowire segments on both sides of the hybrid are regulated by three finger gates each. To measure the spectrum of the hybrid segment using tunnel spectroscopy, we create a single tunnel barrier on each side, as depicted in Fig. 3.1e. In contrast, to establish QDs on either side of the hybrid segment, we further reduce the voltage applied to the gates adjacent to the normal leads. This is done while maintaining the voltages applied to the gates neighboring the hybrid segment at fixed levels, as illustrated in Fig. 3.1f. The chemical potential of the QDs is controlled by the middle finger gates on the left and right bare nanowire segments (V_{LD} and V_{RD}).

Transport measurements are carried out by applying DC voltage biases on the left and the right contacts (V_L, V_R) and measuring the resulting DC currents on both sides (I_L, I_R). Local ($G_{LL} = dI_L/dV_L$, $G_{RR} = dI_R/dV_R$) and nonlocal ($G_{RL} = dI_R/dV_L$, $G_{LR} = dI_L/dV_R$) conductances were obtained as numerical derivatives of the DC currents unless otherwise specified. All measurements are conducted in a dilution refrigerator with a measured electron temperature of ~ 50 mK. We characterize the QDs by measuring the gate-dependent and magnetic-field-dependent transport through them and focus in the remainder of this paper on two charge transitions of each QD: from N to $N+1$ electrons and $N+1$ to $N+2$ electron where N is a small even integer (see Fig. 3.5).

The experiments described in Wang et al. (2022a) and Dvir et al. (2023) were primarily conducted using the device displayed in Fig. 3.1c. In Wang et al. (2022a), the focus was on investigating spin precession in CAR and ECT for a fixed value of the plunger gate (V_{PG}). The values for the tunnel gates were consistent with the settings used in this research. In contrast, Dvir et al. (2023) utilized barrier gates set to a more transparent configuration to boost effective coupling between the formed QDs. The phenomena reported here were measured using four devices, three of them discussed in this manuscript and in the supplementary information (see Fig. 3.6 for scanning electron imaging of the three devices).

We begin by describing our measurement method for CAR and ECT, the focus of this manuscript. Since the hybrid segment supports both processes, we turn to the applied bias to distinguish between them (Hofstetter et al., 2011). The CAR- and ECT-induced currents (I_{CAR} and I_{ECT}) are measured using a method introduced in our previous work (Wang et al., 2022a). In CAR, electrons exhibit a correlated flow, moving either inwards toward the hybrid segment to form a Cooper pair or outwards when a Cooper pair is broken. This correlation is facilitated by applying the same bias to both the right and left leads. To measure the CAR-induced currents at a specific value of V_{PG}, we apply a fixed bias of $V_L = V_R = 70\,\mu V$ to both leads and scan V_{LD} and V_{RD} within a range of approximately 1 mV around the charge degeneracy point of each dot. In Fig. 3.1g, we present the measured I_L and I_R currents alongside the correlated current $I_{corr} \equiv \text{sgn}(I_L I_R)\sqrt{|I_L I_R|}$.

We observe a current feature that maximizes along a diagonal with a negative slope, indicating opposite chemical potentials of the two QDs. CAR-induced currents occur when V_{LD} and V_{RD} satisfy the condition that the chemical potentials of both QDs have equal magnitudes but opposite signs with respect to the Fermi energy (shown schematically in Fig. 3.1f), consistent with the observation.

In ECT electrons enter the device through one lead and exit through the other, requiring an anti-symmetric bias configuration. To measure the amount of ECT-induced currents, we thus repeat the procedure described above when applying anti-symmetric bias on both leads: $V_L = -V_R = 70\,\mu V$. Fig. 3.1h shows the ECT-induced current, displaying a current feature with a positive diagonal, consistent with both QDs being resonant with each other.

We emphasize that we only measure current when both QDs are within the bias window. The absence of a subgap current through a single QD indicates that the charging energy of the QDs is sufficient to suppress electron-hole correlation on the QDs.

In this manuscript, as in Wang et al. (2022a), the maximum of I_{corr} is taken as a proxy of the CAR strength $I_{CAR} \equiv \max(I_{corr})$, and minus the minimum of I_{corr} is taken as a proxy of the ECT strength $I_{ECT} \equiv -\min(I_{corr})$. For every CAR and ECT measurement, we make sure that the bias voltages V_L and V_R are smaller than the ABS energy.

We now turn our attention to the spectrum of the hybrid semiconducting-superconducting segment. To measure tunnel spectroscopy, we form a single tunnel barrier on each side of this segment, as shown schematically in Fig. 3.1e. Fig. 3.1i shows that at low values of V_{PG}, the spectrum features a hard superconducting gap. Increasing V_{PG} leads to the formation of discrete ABSs under the superconducting film appearing as electron-hole symmetric sub-gap peaks. These peaks also appear in the nonlocal conductance (Fig. 3.1j), indicating that the ABSs extend throughout the hybrid segment (Rosdahl et al., 2018).

Next, to measure currents induced by CAR and ECT (I_{CAR} and I_{ECT}), we form a QD on each side of the hybrid segment as explained above. Fig. 3.1k shows the dependence of I_{CAR} and I_{ECT} on V_{PG} when both QDs are tuned to the $N \leftrightarrow N+1$ transition (see Fig. 3.7 for data involving $N+1 \leftrightarrow N+2$ transitions and the discussion of the effect of Pauli spin blockade). Both currents respond strongly to changes in V_{PG}, suggesting that they originate from processes that involve the hybrid segment. I_{CAR}, in particular, reaches peak currents at V_{PG} values where ABSs in the hybrid segment reach a minimal energy. In regions of V_{PG} far from ABSs, I_{CAR} and I_{ECT} are suppressed. These observations hold for all devices we measured (see Fig. 3.8 for another example).

3.2. GATE DEPENDENCE OF CAR AND ECT AT ZERO FIELD

To understand the role of ABSs in mediating CAR- and ECT-induced currents, we consider a model with two QDs on each side of a single ABS confined in the central hybrid segment, as shown in Fig. 3.2a,b. Considering only one orbital state in each QD, this reduces to a simple three-site model (Domínguez and Yeyati, 2016; Liu et al., 2022; Tsintzis et al., 2022). For simplicity, we treat the ABS as one pair of semiconducting states tunnel-coupled to the superconductor in the atomic limit (Bauer et al., 2007), simplifying the general expressions derived in by Liu et al. (2022) (see Supplementary Information for details). Andreev reflection at the semiconductor-superconductor interface hybridizes
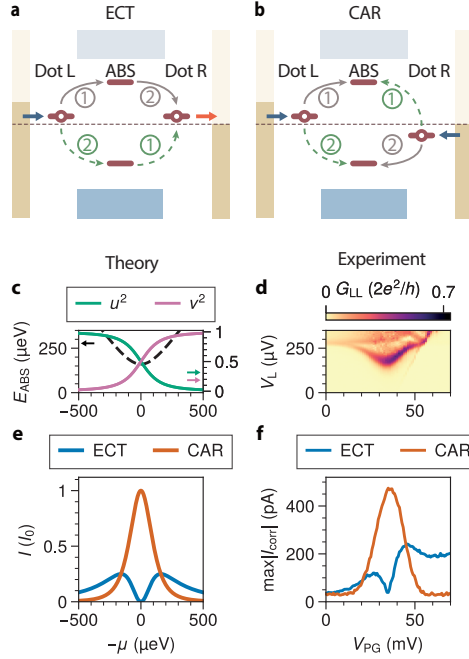
Figure 3.2: **Detailed study of CAR and ECT through an ABS. a.** Two possible paths for ECT: an electron hops from the left QD to the center ABS, followed by an escape from the ABS to the right QD (solid gray arrow), and the processes in the opposite order (dashed green arrow). **b.** Two possible paths for CAR: an electron from the left QD enters the ABS followed by another electron arriving from the right QD (solid gray arrow) and the same processes in reversed order (dashed green arrow). **c.** E_{ABS}, and u, v as a function of μ calculated in the atomic limit, where $E_{ABS} = \sqrt{\Gamma^2 + \mu^2}$ with $\Gamma = 160\,\mu eV$ (Bauer et al., 2007). μ and V_{PG} are related via $\mu = -e\alpha(V_{PG} - V_0)$ where α is the gate lever arm and $V_0 = 35\,mV$ is an offset. Comparing data to theory, we estimate $\alpha \sim 0.01$. **d.** G_{LL} as a function of V_L and V_{PG} showing a single ABS. **e.** A toy-model calculation of the transmission probability as a function of μ. **f.** A high-resolution measurement of CAR and ECT amplitudes while tuning V_{PG}. The background noise level is ~30 pA (see Supplementary methods).

the two electronic states with even charge occupation, $|0\rangle$ and $|2\rangle$, with hybridization rate Γ. The ground state of the ABS is a spin singlet of the form $|S\rangle = u|0\rangle - v|2\rangle$, where $u, v > 0$ are the normalized superposition coefficients determined by Γ and μ, the chemical potential of the electronic level before hybridization. Positive μ results in $u > v$ and negative μ leads to $u < v$ (Bauer et al., 2007). The excited states of the ABS form a doublet $|D\uparrow\rangle, |D\downarrow\rangle$ where $\uparrow / \downarrow$ indicates, in the absence of spin-orbit coupling, the spin state of the single electron occupying the ABS (see the Supplementary Information for general spin-orbit-coupled scenarios).

Under zero external magnetic field, the doublet states are degenerate and the energy difference between $|S\rangle$ and $|D\rangle$ is E_{ABS}, which reaches a minimum around $\mu = 0$ (Fig. 3.2c) (Bauer et al., 2007). An excitation from the ground state of the ABS to an excited state is said to be a Bogoliubov quasiparticle, having an electron-like part u and a hole-like part v in superposition. The effective charge of the ABS is defined as the net charge character of this excitation, $-e(u^2 - v^2)$, where $e > 0$ is the elementary charge (Schindele et al., 2014;

Danon et al., 2020; Ménard et al., 2020). This quantity ranges from $-e$ (electron-like) to $+e$ (hole-like).

We consider both CAR and ECT as coherent second-order processes that involve the virtual occupation of an ABS doublet as the intermediate state. ECT can take place through two paths. The first, marked in grey in Fig. 3.2a, involves the occupation of the ABS by adding an electron from one lead with a hopping amplitude proportional to u, followed by emptying of the ABS via ejection of the electron to the other lead, with an amplitude also proportional to u. The second, marked by the dashed green arrow in Fig. 3.2a, occurs in the opposite order: an ABS is excited to $|D\rangle$ by accepting a hole from one lead, with an amplitude proportional to v, and then relaxes to $|S\rangle$ by ejecting a hole to the other lead, also with an amplitude proportional to v. As presented in Liu et al. (2022) and briefly here in Supplementary Information, these two paths interfere destructively due to fermion exchange statistics and the ECT-induced current, I_{ECT}, is:

$$I_{ECT} = I_0 \left| \frac{u^2 - v^2}{E_{ABS}/\Gamma} \right|^2 \tag{3.1}$$

where I_0 is a proportionality constant given by $I_0 = \frac{e}{\hbar} \cdot \frac{t_L^2 t_R^2}{\Gamma^2 \gamma_{DL}}$ and depends on the coupling between the QDs and the ABS (t_L and t_R) as well as the lifetime of QDs due to coupling to the leads (γ_{DL}) in the limit of electron temperature and tunnel couplings much smaller than bias voltage. Strikingly, the destructive interference results in a suppression of I_{ECT} near $\mu = 0$ where $u^2 = v^2 = \frac{1}{2}$ (Fig. 3.2e).

The process of CAR, depicted in Fig. 3.2b, can take place via two paths as well. In the first path (marked by the dashed green arrow), an electron from the left lead populates the ABS with an amplitude proportional to u, followed by emptying of the ABS via accepting an electron from the right lead, with an amplitude proportional to v. In the second path, the roles of the left and right QDs are reversed. The two paths interfere constructively, yielding

$$I_{CAR} = I_0 \left| \frac{2uv}{E_{ABS}/\Gamma} \right|^2 \tag{3.2}$$

where I_{CAR} is the CAR-induced current, shown in Fig. 3.2e. The term uv is significant only when $|\mu|$ is small, leading to the peak in I_{CAR} around $\mu = 0$ (Fig. 3.2e). This is also where ECT is diminished, allowing CAR to dominate over ECT. Far away from ABS charge neutrality, ECT decays slower than CAR and becomes the dominant coupling mechanism, as it does not require electron-hole conversion to take place. The distinct dependencies of CAR/ECT on μ thus enable us to tune the relative strengths between them via electrostatic gating.

To study our model experimentally, we focus on the range of V_{PG} values between 0 and 70 mV where a single ABS dominates the subgap spectrum (Fig. 3.2d). The ABS reaches a minimum around $V_{PG} = 35$ mV and merges with the superconducting gap below $V_{PG} = 10$ mV and above $V_{PG} = 60$ mV. Fig. 3.2f shows I_{CAR} and I_{ECT} measured in the same V_{PG} range with higher resolution in V_{PG} than Fig. 3.1k. As predicted, I_{CAR} features a narrow peak centered around the ABS energy minimum. I_{ECT} is non-zero in a wider range of V_{PG} values and, as predicted, shows a dip when the ABS energy is minimal. We interpret this suppression as resulting from the destructive interference of the

two ECT paths. We emphasize that this quantum mechanical interference is distinct from the cancellation between electron and hole currents as observed in three-terminal spectroscopy of hybrid nanowires (Ménard et al., 2020; Pöschl et al., 2022). Note that, contrary to our theoretical model, I_{ECT} is not fully suppressed when $v > u$. This could be due to other ABSs at higher V_{PG} that contribute to I_{ECT} or higher V_{PG} increasing tunneling rates via gate cross-coupling. Similar observations of the V_{PG} dependence reported here are reproduced in two more devices (Fig. 3.8 and Fig. 3.9).

3.3. GATE DEPENDENCE OF CAR AND ECT AT FINITE FIELD
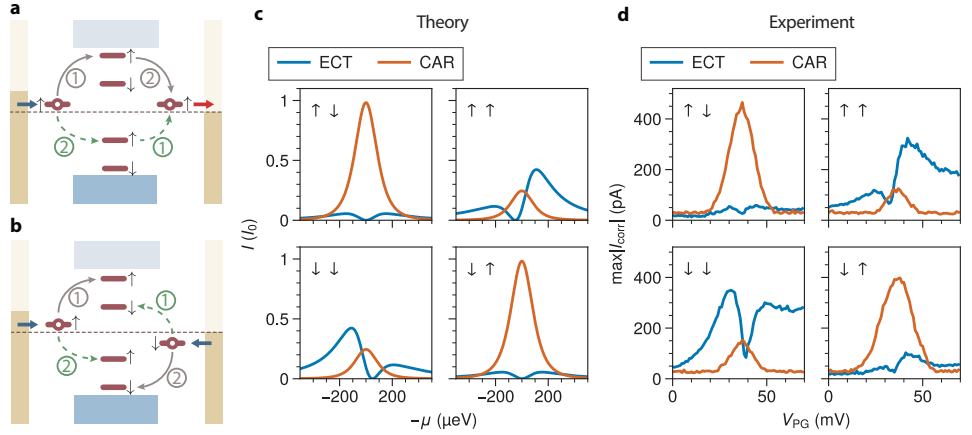
Figure 3.3: **CAR and ECT mediated by spin-polarized ABS. a.** ECT process mediated by a spin-polarized ABS between QDs in the ↑↑ spin configuration. **b.** CAR process mediated by spin-polarized ABS between QDs in the ↑↓ spin configuration. **c.** Calculation of the transmission probability of ECT and CAR via an atomic-limit ABS as a function μ at the four possible spin configurations of the QDs. Spin-orbit coupling is included in the calculation as a small spin-flipping factor ($\sigma = 0.2$) to allow for opposite-spin ECT and same-spin CAR (see Supplementary Information for model details). Other model parameters are $\Gamma = 160\,\mu eV$ and $E_Z = 100\,\mu eV$ **d.** A high-resolution CAR and ECT amplitudes while tuning V_{PG} with $\vec{B} = 80\,mT$ (applied along the nanowire direction) at the four possible spin configurations of the QDs.

Application of a Zeeman field lifts the Kramers' degeneracy of the ABS and the QDs. The spin splitting of the QDs makes their charge transitions spin-polarized: the addition energy from N to $N+1$ electrons becomes lower (spin-down, ↓), and that from $N+1$ to $N+2$ becomes higher (spin-up, ↑) (Hanson et al., 2007). We thus control the spins of the electrons participating in CAR and ECT by selecting the corresponding charge transitions (Wang et al., 2022a). The odd states of the ABS split in energy, leading to two possible excitations from the ground state $|S\rangle$: either to $|D\downarrow\rangle$ with an energy $E_\downarrow = E_{ABS} - E_Z/2$, or to $|D\uparrow\rangle$ with an energy $E_\uparrow = E_{ABS} + E_Z/2$, where E_Z is the Zeeman splitting of the ABS (Lee et al., 2013).

   Fig. 3.3a shows schematically the process of ECT in the presence of a Zeeman field when both QDs are tuned to the ↑ transition. Again, this process can take place via two paths. In the first path (marked in grey), an ↑ electron from one lead populates the $|D\uparrow\rangle$ state of the ABS. Then the ABS is emptied by emitting an ↑ electron to the other lead

through the QD. In the second process (marked by the dashed green arrow), a hole from one lead hops into the ABS, exciting it into the $|D\downarrow\rangle$ state. The ABS then relaxes by emitting a hole to the other lead. The energies of the intermediate states in the two paths, $|D\uparrow\rangle$ and $|D\downarrow\rangle$, are split and the interference pattern is thus modified. The ECT-induced current is now of the form:

$$I_{\text{ECT}}^{\uparrow\uparrow} \propto \left| \frac{u^2}{E_\uparrow} - \frac{v^2}{E_\downarrow} \right|^2 \tag{3.3}$$

Since $E_\downarrow < E_\uparrow$, ECT is stronger when the ABS is hole-like (large v) as seen in the $\uparrow\uparrow$ panel of Fig. 3.3c. Analogously, the ECT is higher when the ABS is electron-like ($u > v$) and both QDs are tuned to the $\downarrow$ transition.

CAR-induced currents are also modified by the Zeeman splitting of the ABS doublet state. CAR takes place in two paths involving both levels (shown schematically in Fig. 3.3b). In one path (marked by the dashed green arrow), the ABS occupies the $|D\downarrow\rangle$ state by receiving a $\downarrow$ electron from one lead and is emptied by receiving an $\uparrow$ electron from the other lead. In the second path (marked in grey), the order is reversed and the ABS passes through the $|D\uparrow\rangle$ state. The probability for the CAR process is now:

$$I_{\text{CAR}}^{\uparrow\downarrow} \propto \left| \frac{uv}{E_\downarrow} + \frac{uv}{E_\uparrow} \right|^2 \tag{3.4}$$

This probability peaks at the ABS energy minimum, as seen in the relevant panel of Fig. 3.3c. Note that the expected CAR peak remains symmetric in μ, in contrast to ECT. Fig. 3.3d shows the measured I_{CAR} and I_{ECT} under the application of $|\vec{B}| = 80\,\text{mT}$ along the nanowire direction, sufficient to fully spin-polarize the QDs ($E_{\text{Zeeman}}^{\text{QD}} \approx 200\,\mu\text{eV}$) and split the energy of the ABS ($E_Z \approx 100\,\mu\text{eV}$, see Refs. (Mazur et al., 2022; Wang et al., 2022a)). Spin-orbit coupling in the nanowire allows for spin-flipping processes — equal-spin CAR and opposite-spin ECT — to take place (Wang et al., 2022a), allowing us to measure ECT and CAR in all possible spin configurations. I_{CAR} is symmetric around the ABS energy minimum and is generally larger for opposite-spin than equal-spin configurations. I_{ECT} in the $\uparrow\uparrow$ spin configuration is large when the ABS is hole-like ($v > u$) and is suppressed when it is electron-like (large u). The destructive interference dip is shifted from the ABS minimum towards lower V_{PG}. The opposite trend is observed in the $\downarrow\downarrow$ spin configuration: I_{ECT} is slightly larger when the ABS is electron-like, and the interference dip is shifted towards higher values of V_{PG}. I_{ECT} in the opposite-spins configuration is nearly symmetric around the ABS minimum and is generally suppressed with respect to I_{ECT} in the equal-spin configuration. Thus, all of the qualitative predictions of the model (Liu et al., 2022) are verified in the measurements.

3.4. CAR AND ECT DEPENDENCE ON FIELD DIRECTION

So far, we have discussed the dependence of CAR and ECT magnitudes as a function of the ABS charge at zero and finite Zeeman field. In the following, we report on the dependence of CAR and ECT on the direction of the applied magnetic field $\vec{B}$, at fixed V_{PG}. We measure a second device, B, with a longer superconducting segment ($\approx 350\,\text{nm}$, much larger than the superconducting coherence length in the Al film) and no Pt layer on top of the Al. The schematic in Fig. 3.4h indicates the angles θ and φ defining the

3
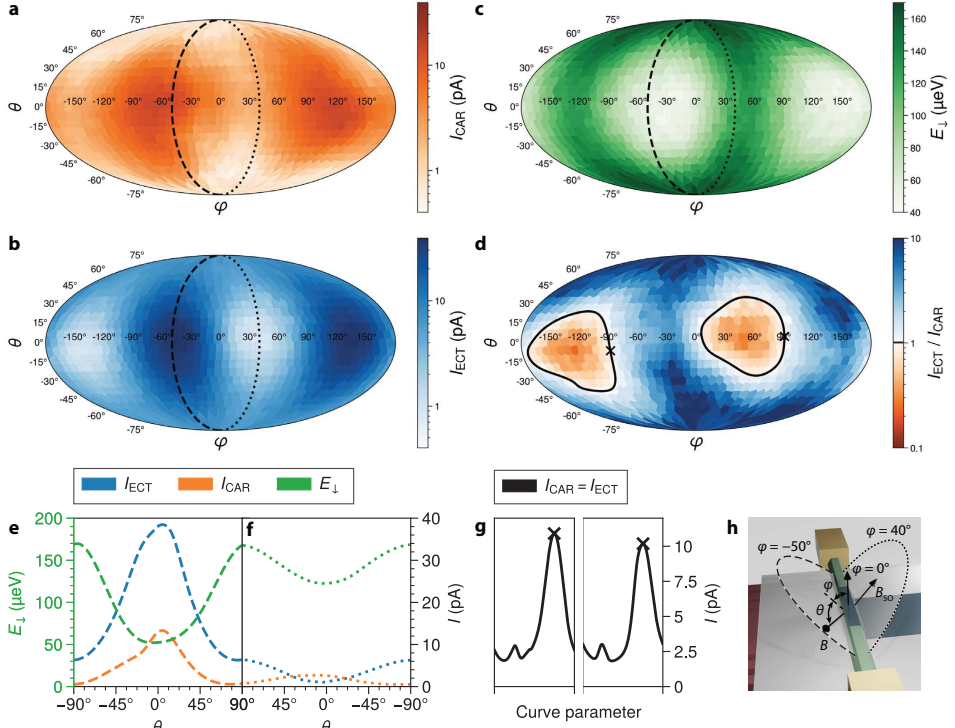
Figure 3.4: **Tuning CAR and ECT with magnetic field orientation. a-d.** Spherical plots: the center of every colored tile corresponds to a specific magnetic field orientation. Each panel is taken at fixed V_{PG} and $|\vec{B}| = 80\,\text{mT}$. $V_{PG} = 475\,\text{mV}$ in panel c, while $V_{PG} = 480\,\text{mV}$ in a, b and d. The QD spin configuration is $\downarrow\uparrow$ for all panels. See Fig. 3.10 for data corresponding to other spin configurations. **a.** CAR-induced current as a function of magnetic field direction, extracted with the same method detailed in Fig. 3.1g,h and used in the rest of the paper. **b.** ECT-induced current as a function of magnetic field orientation. **c.** Energy of the lowest-energy ABS extracted from local tunneling spectroscopy as a function of magnetic field orientation. **d.** Ratio of the ECT and CAR currents from panels b and a. Continuous lines highlight the locus of points where $I_{CAR} = I_{ECT}$; among them, the points with maximum current are marked with crosses. **e.** Interpolation of data shown in panels a–c along the $\varphi = -50°$ meridian. **f.** Interpolation of data shown in panels a–c along the $\varphi = +40°$ meridian. **g.** I_{CAR} along the $I_{CAR} = I_{ECT}$ curves shown in panel d. Negative-φ points are parameterized and plotted on the left, positive-φ points on the right. **h.** Schematic defining θ and φ: $\theta = \pm 90°$ is the direction parallel to the nanowire. $\theta = \varphi = 0°$ is the direction perpendicular to the substrate.

field direction of $\vec{B}$. The QDs are set to the $\downarrow\uparrow$ spin configuration and V_{PG} is selected such that ECT is stronger than CAR when the field is parallel to the nanowire (see Fig. 3.10 for the other spin configurations). In Fig. 3.4, panels a and b show I_{CAR} and I_{ECT} when the angle of $\vec{B}$ is varied over a sphere. Panel c shows the energy of the lowest ABS at a similar V_{PG} (see Supplementary methods and Fig. 3.11 for analysis details). All three quantities are anisotropic and CAR and ECT amplitudes are overall negatively correlated to $E_\downarrow$ across the plotted globes, as expected for virtual tunneling processes. Below, we examine the rotational dependence of CAR and ECT along two exemplary meridians of the globe (dashed and dotted lines in panels a to c) in order to separate anisotropy due

to ABS energy from that caused by spin.

As discussed above, CAR and ECT amplitudes are inversely proportional to the ABS energy. This effect is highly visible in Fig. 3.4e, where we plot $E_\downarrow$, I_{CAR} and I_{ECT} along the meridian with $\varphi = -50°$ (dashed line in Fig. 3.4a-c). Here, $E_\downarrow$ is significantly modulated between ~ 170 µeV and ~ 50 µeV and, accordingly, both I_{CAR} and I_{ECT} increase drastically at the energy minimum. In contrast, very different pattern can be obtained when we rotate the magnetic field along the meridian of $\varphi = 40°$ (dotted line in Fig. 3.4a-c). Fig. 3.4f shows that, along this meridian, $E_\downarrow$ changes by a small amount. As before, I_{CAR} is enhanced where $E_\downarrow$ is minimal. However, I_{ECT} varies in the opposite way and becomes completely suppressed around $\theta = 0$ (perpendicular to the nanowire axis). This suppression is generic across various V_{PG} values and, therefore, not explained by either the energy or the charge of the ABS. We attribute the reduction of opposite-spin ECT along this specific direction to spin blockade (Wang et al., 2022a). When the QDs select opposite spins, spin precession due to spin-orbit coupling enables the presence of some I_{ECT} (Liu et al., 2022). However, if the applied $\vec{B}$ is parallel to the effective spin-orbit field $\vec{B}_{SO}$, no spin precession occurs and, therefore, ECT is suppressed between QDs with opposite spins (Hofmann et al., 2017; Wang et al., 2018). The observation of this type of spin blockade reveals the orientation of the spin-orbit field. Compared to prior works measuring the spin-orbit field direction in hybrid nanowires via superconducting gap size anisotropy, the method presented here using spin conservation to detect $\vec{B}_{SO}$ direction is less prone to other effects such as orbital depairing and g-factor anisotropy (Fig. 3.12).

With these two effects in mind, we summarize the angle dependence of CAR and ECT over the entire sphere as follows. First, there exists one special $\vec{B}$ direction along which equal-spin CAR and opposite-spin ECT are strongly suppressed (see Fig. 3.10 for other spin combinations). We interpret this as a spin-blockade effect and its direction as that of the spin-orbit field. Away from this blockaded direction, multiple factors compete to influence the amplitudes of CAR and ECT, such as the angle between $\vec{B}$ and $\vec{B}_{SO}$ and the energy of the mediating ABS.

This combination of anisotropic ABS energy and spin-orbit coupling makes the $\vec{B}$ direction dependence of CAR and ECT very rich, enabling further tuning of their relative amplitudes. Fig. 3.4d shows the ratio between I_{ECT} and I_{CAR} as a function of $\vec{B}$ orientation. Here, due to the aforementioned influence of the ABS charge, I_{ECT} is larger than I_{CAR} on most of the sphere. However, since ECT is suppressed along a specific direction, the ratio between I_{ECT} and I_{CAR} can be inverted. Such tunability allows for $I_{CAR} = I_{ECT}$, the sweet spot essential for the realization of Poor Man's Majoranas in a minimal Kitaev chain (Leijnse and Flensberg, 2012a; Dvir et al., 2023). Fig. 3.4d shows with continuous lines the locus of points where $\frac{I_{ECT}}{I_{CAR}} = 1$ and Fig. 3.4g reports the corresponding current values, highlighting with crosses the points where $I_{CAR}(= I_{ECT})$ is maximal. It is therefore evident that the $\vec{B}$ dependence of CAR and ECT not only enables the tuning to the $I_{CAR} = I_{ECT}$ sweet spot, but also allows optimization of their strengths.

3.5. Conclusion

In summary, we have measured ECT- and CAR-induced currents mediated by ABSs formed in a proximitized InSb nanowire. We show that the amplitudes of both processes depend on the charge of the ABSs, and are thus highly tunable via electrostatic gating. Particularly, we show that ECT is significantly suppressed when the ABS is charge-neutral due to destructive interference originating from fermionic exchange statistics. Furthermore, we examine how the interference pattern and the balance between ECT and CAR are shifted when the applied magnetic field spin-polarizes the QDs and splits the energy of the ABS. Finally, we measure how the magnetic field orientation modifies both the energy of the ABS and the effect of spin-orbit coupling, adding another independent knob to tune CAR and ECT. These results demonstrate deterministic control of the relative amplitudes of CAR and ECT, forming the foundation of realizing an artificial Kitaev chain (Dvir et al., 2023).

Author contributions
GW, GPM, NvL, AB, FZ, and DvD fabricated the devices. GW, TD, SLDtH, AB, and DX performed the electrical measurements. TD and GW designed the experiment. AB, GW, and TD analyzed the data. AB, TD, and LPK prepared the manuscript with input from all authors. TD and LPK supervised the project. CXL developed the theoretical model with input from MW. SG, GB, and EPAMB performed InSb nanowire growth.

Data Availability and Code Availability
Raw data presented in this work, the data processing/plotting code, and the code used for the theory calculations are available at https://doi.org/10.5281/zenodo.7395016.

3.6. SUPPLEMENTARY INFORMATION

3.6.1. THEORETICAL MODEL

In this section, we show analytically how to obtain the CAR/ECT couplings/currents based on our theoretical model. The calculation is based on Liu et al. (2022), but specialized to the atomic limit.

The model Hamiltonian for the dot-hybrid-dot system is

$$H = H_{\text{dot}} + H_{\text{hybrid}} + H_{\text{tunnel}} \tag{3.5}$$

We first introduce the Hamiltonian for two quantum dots, H_{dot}:

$$H_{\text{dot}} = \varepsilon_L d_{L\eta}^\dagger d_{L\eta} + \varepsilon_R d_{R\sigma}^\dagger d_{R\sigma} \tag{3.6}$$

Here, $\varepsilon_{L/R}$ are the dot energies relative to the Fermi energy, and $d_{L\eta}, d_{R\sigma}$ denote the spin-polarized dot levels in the presence of a large magnetic field. Note that no summation is taken over the spin indices η and σ.

Next, H_{hybrid} describes the hybrid segment with two Andreev bound states. In general, we can write down its Hamiltonian in diagonalized form using Bogoliubov quasi-particle operators γ_+ and γ_-:

$$H_{\text{hybrid}} = E_+ \gamma_+^\dagger \gamma_+ + E_- \gamma_-^\dagger \gamma_- \tag{3.7}$$

More concretely, we consider a superconducting-atomic-limit model (Bauer et al., 2007) under weak spin-orbit coupling compared to the Zeeman field. This means we use the pseudospin labels $+, -$ instead of $\uparrow, \downarrow$ but treat the spin-splitting between the two as approximately E_Z. We also set the charging energy of the ABS to zero, as it is strongly screened by the grounded Al film in the experiment. Using electron annihilation operators a_+, a_-, the atomic-limit Hamiltonian is

$$H_{\text{hybrid}} \approx \mu \left(a_+^\dagger a_+ + a_-^\dagger a_- \right) + \frac{E_Z}{2} \left(a_+^\dagger a_+ - a_-^\dagger a_- \right) + \Gamma a_+^\dagger a_-^\dagger + \text{H.c.} \tag{3.8}$$

This model can be solved exactly. The ABS energies are

$$E_\pm \approx \sqrt{\mu^2 + \Gamma^2} \pm \frac{E_Z}{2}, \tag{3.9}$$

where μ is the chemical potential in the hybrid segment, which is controlled by the plunger gate voltage V_{PG} in the experimental device, Γ is the superconducting coupling strength and E_Z is the Zeeman spin splitting. The corresponding wavefunctions of the ABSs are

$$\gamma_+ = u a_+ + v a_-^\dagger, \quad \gamma_- = v a_+ - u a_-, \tag{3.10}$$

where $u^2 = 1 - v^2 = \frac{1}{2} \left(1 + \frac{\mu}{\sqrt{\mu^2 + \Gamma^2}} \right)$ are the BCS coherence factors characterizing the electron and hole components of the ABSs.

Finally, H_{tunnel} is the tunnel Hamiltonian between the dots and the hybrid segment:

$$H_{\text{tunnel}} = \sum_{a=L,R} t_a \left[\left(\cos\theta_a a_+^\dagger - \sin\theta_a a_-^\dagger \right) d_{a\uparrow} + \left(\sin\theta_a a_+^\dagger + \cos\theta_a a_-^\dagger \right) d_{a\downarrow} \right]$$
$$+ \text{H.c.} \tag{3.11}$$

Here we only consider the scenario where the spin-orbit field ($\propto \sigma_y$) is perpendicular to the globally applied magnetic field ($\propto \sigma_z$). In particular, $\theta_R = -\theta_L = k_{so}L/2$ describes the spin precession in the hybrid region due to spin-orbit interaction, where $k_{so} = m\alpha_R/\hbar^2$ is the spin-orbit wave-vector and L is the length of the hybrid segment. In the weak spin-orbit interaction regime ($k_{so}L/2 \ll 1$), the ABS of γ_+ is mainly spin-up, but it can also accommodate spin-down QD electrons with amplitude $\sim \sin(k_{so}L/2)$. Similar pictures hold for γ_- as well. Note that although we include both $\uparrow$ and $\downarrow$ in H_{tunnel} for dots, in the calculation, we only include one spin species depending on the choice of η and σ in H_{dot}, as the experimental measurements are spin-polarized.

In the tunneling regime $t_{L/R} \ll \Gamma$, the effective Hamiltonian of the coupled quantum dots can be obtained using the perturbation theory as below

$$H_{\text{eff}} = H_{\text{dot}} - H_{\text{tunnel}} \frac{1}{H_{\text{hybrid}}} H_{\text{tunnel}} + O(H_{\text{tunnel}}^3)$$
$$\approx H_{\text{dot}} - \Gamma_{\eta\sigma}^{\text{ECT}} d_{L\eta}^\dagger d_{R\sigma} - \Gamma_{\eta\sigma}^{\text{CAR}} d_{L\eta} d_{R\sigma} + h.c., \tag{3.12}$$

where $\Gamma_{\eta\sigma}^{\text{CAR}}$ and $\Gamma_{\eta\sigma}^{\text{ECT}}$ are the spin-selective CAR and ECT couplings between quantum dots. Interestingly, as shown in Liu et al. (2022) and explained in the main text of this work, the strengths of the effective couplings can be extracted from the resonant current measured in a three-terminal setup, that is

$$I_{\text{CAR/ECT}}^{\max} \propto \left| \Gamma_{\eta\sigma}^{\text{CAR/ECT}} \right|^2. \tag{3.13}$$

In the $\uparrow\uparrow$ channel, from Eq. (3.12), the CAR coupling is

$$\Gamma_{\uparrow\uparrow}^{\text{CAR}} / t_L t_R = -\left(-\sin\theta_L \cos\theta_R \frac{uv}{E_+} - \sin\theta_R \cos\theta_L \frac{(-u)v}{E_-} \right)$$
$$+ \left(-\sin\theta_R \cos\theta_L \frac{uv}{E_+} - \sin\theta_L \cos\theta_R \frac{(-u)v}{E_-} \right)$$
$$= -\sin(\theta_R - \theta_L) \left(\frac{uv}{E_+} + \frac{uv}{E_-} \right)$$
$$= -\sin(k_{so}L) \left(\frac{uv}{E_+} + \frac{uv}{E_-} \right), \tag{3.14}$$

which gives

$$I_{\uparrow\uparrow}^{\text{CAR}} = I_0 \cdot \sigma \cdot \left| \frac{uv}{E_+} + \frac{uv}{E_-} \right|^2, \tag{3.15}$$

where $\sigma = \sin^2(k_{so}L)$ is the flipping rate due to spin-orbit interaction, and $I_0 = et_L^2 t_R^2/(\hbar \Gamma^2 \gamma_{DL})$. Similarly,

$$
\begin{aligned}
\Gamma_{\uparrow\uparrow}^{\text{ECT}}/t_L t_R &= \left(\cos\theta_L \cos\theta_R \frac{u^2}{E_+} + \sin\theta_L \sin\theta_R \frac{(-u)^2}{E_-} \right) \\
&\quad - \left(\cos\theta_L \cos\theta_R \frac{v^2}{E_-} + \sin\theta_L \sin\theta_R \frac{v^2}{E_+} \right) \\
&= \cos(k_{so}L) \left(\frac{u^2}{E_+} - \frac{v^2}{E_-} \right) - \sin^2(k_{so}L/2) \frac{2E_Z}{E_+ E_-}
\end{aligned}
\tag{3.16}
$$

giving

$$
I_{\uparrow\uparrow}^{\text{ECT}} \approx I_0 \cdot (1-\sigma) \cdot \left| \frac{u^2}{E_+} - \frac{v^2}{E_-} \right|^2.
\tag{3.17}
$$

Here, the ECT current in Eq. (3.17) shows a destructive interference between two virtual paths. In the first path, an electron first hops from the right dot into the hybrid before it hops out to the left ($\propto u^2$). In the second path, an electron first escapes from the hybrid segment to the left dot, leaving behind a hole-like ABS excitation, which is later annihilated when a second electron jumps in from the right dot ($\propto -v^2$). The minus sign responsible for the destructive interference stems from fermionic statistics when switching the order of two hopping events. In contrast, the CAR current in Eq. (3.15) shows a constructive interference pattern. Because the CAR process is proportional to uv instead of u^2 or v^2, an additional minus sign in the ABS wavefunctions (see Eq. (3.10)) cancels the minus sign from fermionic statistics, yielding a constructive interference between the two virtual paths. A similar analysis and calculation gives the current in the $\uparrow\downarrow$ channel:

$$
\begin{aligned}
I_{\uparrow\downarrow}^{\text{CAR}} &= I_0 \cdot (1-\sigma) \cdot \left| \frac{uv}{E_+} + \frac{uv}{E_-} \right|^2, \\
I_{\uparrow\downarrow}^{\text{ECT}} &= I_0 \cdot \sigma \cdot \left| \frac{\mu}{E_+ E_-} \right|^2.
\end{aligned}
\tag{3.18}
$$

The currents in the remaining channels are readily obtained using the following symmetry relation (Liu et al., 2022):

$$
\begin{aligned}
I_{\downarrow\uparrow}^{\text{CAR}}(E_Z) &= I_{\uparrow\downarrow}^{\text{CAR}}(E_Z), \\
I_{\downarrow\uparrow}^{\text{ECT}}(E_Z) &= I_{\uparrow\downarrow}^{\text{ECT}}(E_Z), \\
I_{\downarrow\downarrow}^{\text{CAR}}(E_Z) &= I_{\uparrow\uparrow}^{\text{CAR}}(E_Z), \\
I_{\downarrow\downarrow}^{\text{ECT}}(E_Z) &= I_{\uparrow\uparrow}^{\text{ECT}}(-E_Z).
\end{aligned}
\tag{3.19}
$$

In the absence of Zeeman field and when the dot occupancy is tuned at the transition of N to $N+1$, currents from all four spin channels are allowed, yielding the total current

$$I^{\text{CAR}} = \sum_{\eta,\sigma=\uparrow,\downarrow} I^{\text{CAR}}_{\eta\sigma}(E_Z=0) = 2 \cdot I_0 \cdot \left| \frac{2uv}{E} \right|^2,$$

$$I^{\text{ECT}} = \sum_{\eta,\sigma=\uparrow,\downarrow} I^{\text{ECT}}_{\eta\sigma}(E_Z=0) = 2 \cdot I_0 \cdot \left| \frac{u^2-v^2}{E} \right|^2, \tag{3.20}$$

where $E = \sqrt{\mu^2 + \Gamma^2}$.

3.6.2. Methods

Device fabrication
Fig. 3.1d shows a device schematic and the electrical circuit used to measure it. Scanning electron microscope images of reported devices are shown in Fig. 3.6. For device A, InSb nanowires were deposited on pre-fabricated metallic gates, separated from the nanowire by a 20 nm layer of HfO$_2$ dielectric. Using the shadow lithography technique (Heedt et al., 2021; Borsoi et al., 2021), an 8 nm layer of Al was deposited on top of the middle segment of the nanowire, followed by a 2 Å layer of Pt and an additional 20 nm of AlO$_x$ capping layer. Normal Cr/Au contacts were later fabricated using standard e-beam lithography. Full details of the fabrication can be found in the Supplementary Information of Mazur et al. (2022). For devices B and C, no additional Pt layer was used. For device C only, a double dielectric layer was used: 10 nm of Al$_2$O$_3$ followed by 10 nm of HfO$_2$.

Data processing
Transport was measured by applying DC voltage biases on the left and the right leads (V_L, V_R) and measuring the resulting DC currents on both sides (I_L, I_R). Local ($G_{\text{LL}} = dI_L/dV_L$, $G_{\text{RR}} = dI_R/dV_R$) and nonlocal ($G_{\text{RL}} = dI_R/dV_L$, $G_{\text{LR}} = dI_L/dV_R$) conductances were obtained as numerical derivatives of the DC currents after applying a Savitzky-Golay filter, unless otherwise specified. The $E_\downarrow$ energy of Fig. 3.4c and E_{gap} values of Fig. 3.12 are extracted from $I_R(V_R)$ tunnel spectroscopy measurements by detecting where $|I_R|$ exceeds a 5% threshold of its value far outside the superconducting gap (see data repository for details and Fig. 3.11 for comparison between conductance spectroscopy and $E_\downarrow$ thus extracted). All measurements were conducted in a dilution refrigerator with a measured electron temperature of ~ 50 mK.

Extraction of CAR and ECT amplitudes
ECT-induced currents are measured with fixed voltage biases such that $V_L \neq V_R$. Due to energy conservation, ECT-induced currents arise when V_{LD} and V_{RD} fulfill the condition that the chemical potentials of both QDs are aligned and within the bias window. The ECT-induced current is detected as correlated current flowing from one lead to the other. Similarly, CAR-induced currents are measured with fixed voltage biases such that $V_L \neq -V_R$. CAR-induced current arises when the QD chemical potentials are equal in magnitude with an opposite sign with respect to the Fermi energy (shown schematically

in Fig. 3.1f). CAR currents flow jointly from the leads to the superconductor or vice-versa. For each CAR and ECT measurement, V_{LD} and V_{RD} are swept around a charge degeneracy point of each dot. We measure I_L and I_R and calculate the correlated current $I_{corr} \equiv \text{sign}(I_L I_R)\sqrt{|I_L I_R|}$. In this manuscript, as in Wang et al. (2022a), the maximum of I_{corr} is taken as a proxy of the CAR strength $I_{CAR} \equiv \max(I_{corr})$, and minus the minimum of I_{corr} is taken as a proxy of the ECT strength $I_{ECT} \equiv -\min(I_{corr})$. Notice that in the absence of CAR or ECT signal, $\max(I_{corr})$ and $-\min(I_{corr})$ give the background noise. Background noise level is $\sim 30\,\text{pA}$ for device A and $\sim 1\,\text{pA}$ for devices B and C. We note that, instead of taking the bare maximum and minimum of I_{corr}, averaging procedures can improve the signal-to-noise ratio (Wang et al., 2023), although come at the price of having to set an arbitrary threshold. Every CAR data point in Fig. 3.2f and 3.3d is taken from a V_{LD}-V_{RD} sweep with symmetric biases, while every ECT data point is taken from a subsequent V_{LD}-V_{RD} sweep with anti-symmetric biases. Every data point of Fig. 3.4a-b comes from a single V_{LD}-V_{RD} sweep with finite $V_L > 0$ while $V_R = 0$; in this case, positive μ_{LD} allows for CAR and negative μ_{LD} allows for ECT. For every CAR and ECT measurement, we make sure that the bias voltages V_L and V_R are smaller than the ABS energy. I_{CAR}, I_{ECT} and $E_\downarrow$ values along specific lines shown in Fig. 3.4e-f are extracted from a spherical interpolation of Fig. 3.4a-c data. The interpolation is performed using the `scipy` implementation of a smooth bivariate spline approximation in spherical coordinates. Code generating all plots is available in the linked repository.

3.7. EXTENDED DATA
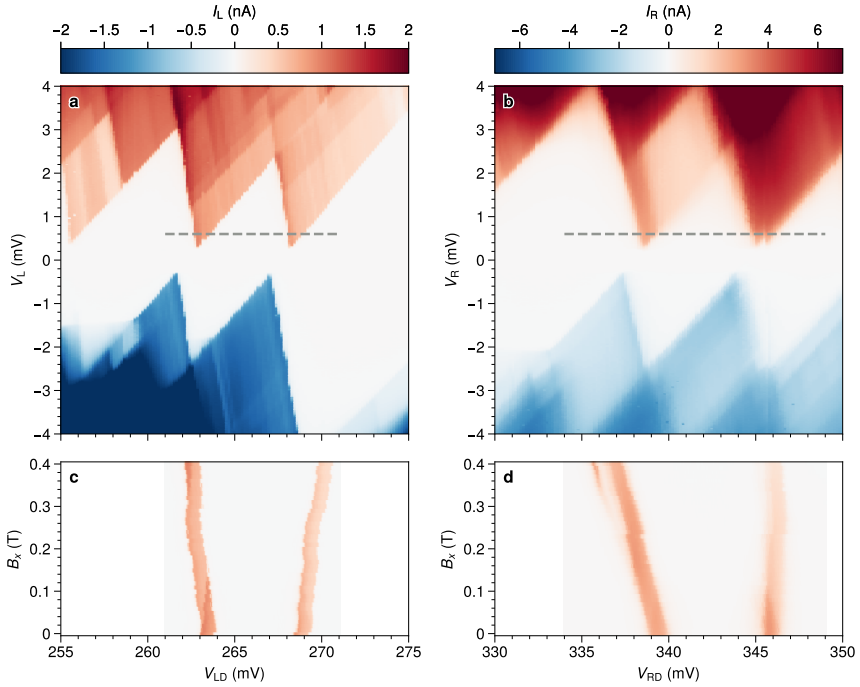
Figure 3.5: **QD characterization in device A. a.** Coulomb blockade diamonds of the left QD, from which we estimate the charging energy to be $E_c = 2.15$ meV and lever arm $\alpha = 0.4$. **b.** Coulomb blockade diamonds of the right QD. We estimate $E_c = 2.3$ meV and $\alpha = 0.35$. In both QDs, no sub-gap current is visible, indicating QDs are weakly coupled to S and retain their charge eigenstates. Dashed lines highlight a 600 μV voltage bias set for panels c and d. **c.** Current through the left QD at $V_L = 600$ μV measured against gate voltage and magnetic field along the nanowire, B_x. Spin-degenerate orbitals Zeeman-split in opposite directions. We estimate a g-factor of $g = 40$. **d.** Current through the right QD at $V_R = 600$ μV. $g = 46$.
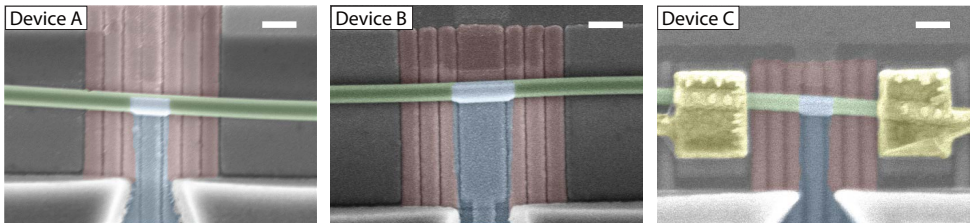
Figure 3.6: **False-colored SEM images of measured devices.** Green is nanowire, blue is Al (Al+Pt for device A), red are bottom gates, and yellow are Au contacts. Devices A and B were imaged prior to Au contact deposition. Scale bars are 200 nm. The hybrid segments are respectively 220, 350 and 200 nm long. The short devices A and C host isolated ABSs with visible destructive interference of ECT (Fig. 3.2 and 3.9). The long device B was used for the dependence of CAR and ECT on magnetic field direction (Fig. 3.4), since more spin precession due to spin-orbit coupling is expected for longer devices.
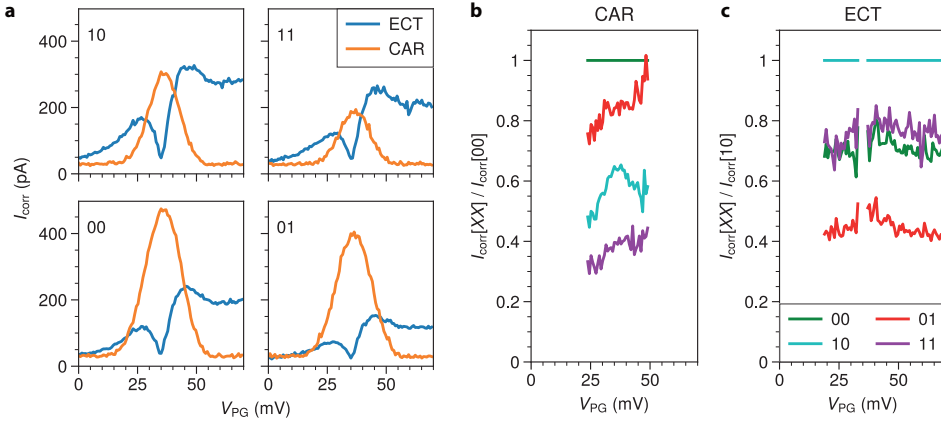
Figure 3.7: **Pauli spin blockade at** $\vec{B} = 0$**. a.** V_{PG} dependence of CAR and ECT using four charge degeneracy points corresponding to one pair of spin-degenerate levels in each QD. Bias voltages are the same as described in the main text. Since there is no magnetic field, they are here denoted '00', '01', '10', '11', instead of '↓↓', '↓↑', '↑↓', '↑↑' to avoid confusion. The '00' data displayed in the bottom left plot is the same as Fig. 3.2f. All four charge degeneracy points show the same, characteristic curve shapes: single-peaked for CAR and double-peaked for ECT. For the bias polarities used here, Pauli spin blockade reduces the overall magnitude of CAR in the '11' charge degeneracy and that of ECT in the '01' charge degeneracy (Wang et al., 2022a). **b.** CAR magnitudes divided by that of the '00' charge degeneracy point. CAR-induced currents smaller than 50 pA are excluded from the plot to avoid division by small numbers. **c.** ECT magnitudes divided by that of the '10' charge degeneracy point. ECT-induced currents smaller than 50 pA are excluded from the plot to avoid division by small numbers. Panels b and c show that the ratios of CAR and ECT magnitudes relative to the non-spin-blockaded process are roughly constant as a function of V_{PG}. Thus, although Pauli spin blockade is not part of the theoretical model, its effect is mainly an overall scaling of the CAR amplitude relative to ECT and does not alter the V_{PG} dependence of them each.

3
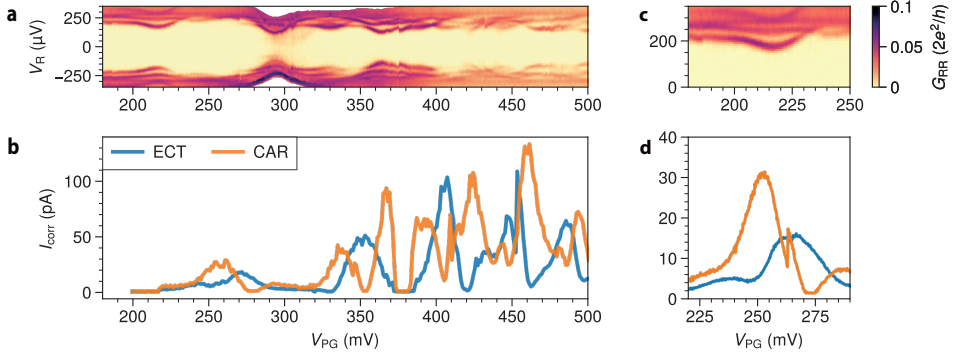
Figure 3.8: **Correlation between ABS and CAR/ECT processes in device B. a.** Local spectroscopy of device B, measured with standard lock-in techniques. The voltage bias V_R is corrected for a series resistance of 105 kΩ to take into account a fridge line resistance of 2.9 kΩ and a current meter resistance of 102 kΩ. Data is taken at $B = B_x = 100$ mT. **b.** CAR and ECT magnitudes as a function of V_{PG}. As opposed to what is presented for device A in Fig. 3.1, the values of V_{LI} and V_{RI} are not the same for the measurements shown in panels a and b. This results in a shift of ~ 40 mV of the ABS positions with respect to V_{PG}, due to cross-coupling between neighboring gates. Data is taken at $B = 0$. **c.** Zoom in of panel a around the first ABS. To compensate for the gate shift mentioned above, the plotted V_{PG} ranges differ by 40 mV for easier comparison. **d.** High-resolution measurement of CAR and ECT magnitudes for the first ABS. The effect of a gate jump can be seen at $V_{PG} \approx 260$ mV. An ECT dip, signature of destructive interference, is visible at $V_{PG} = 250$ mV, although it is less pronounced than what is observed for device A in Fig. 3.2. A weaker interference might be due to the presence of multiple ABSs (a second ABS is visible in panel c with a minimum energy at $V_{PG} \approx 245$ mV). The smaller semiconducting level spacing likely results from device B being longer than device A: the hybrid sections are 350 nm and 200 nm long, respectively.
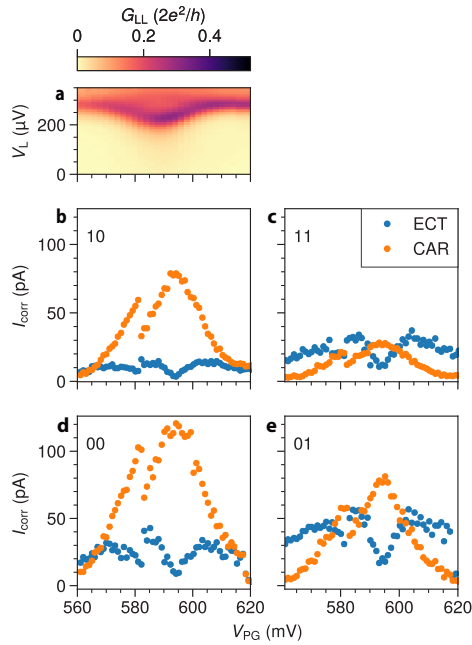
Figure 3.9: **ECT interference in another device (device C). a.** Local spectroscopy of device C, measured as in Fig. 3.2d. **b–e.** CAR and ECT magnitudes as a function of V_{PG} for four charge degeneracy points. Destructive interference of ECT is visible at $V_{PG} = 595\,\text{mV}$. The discontinuity visible in all plots at $V_{PG} = 582\,\text{mV}$ is attributed to a gate jump.
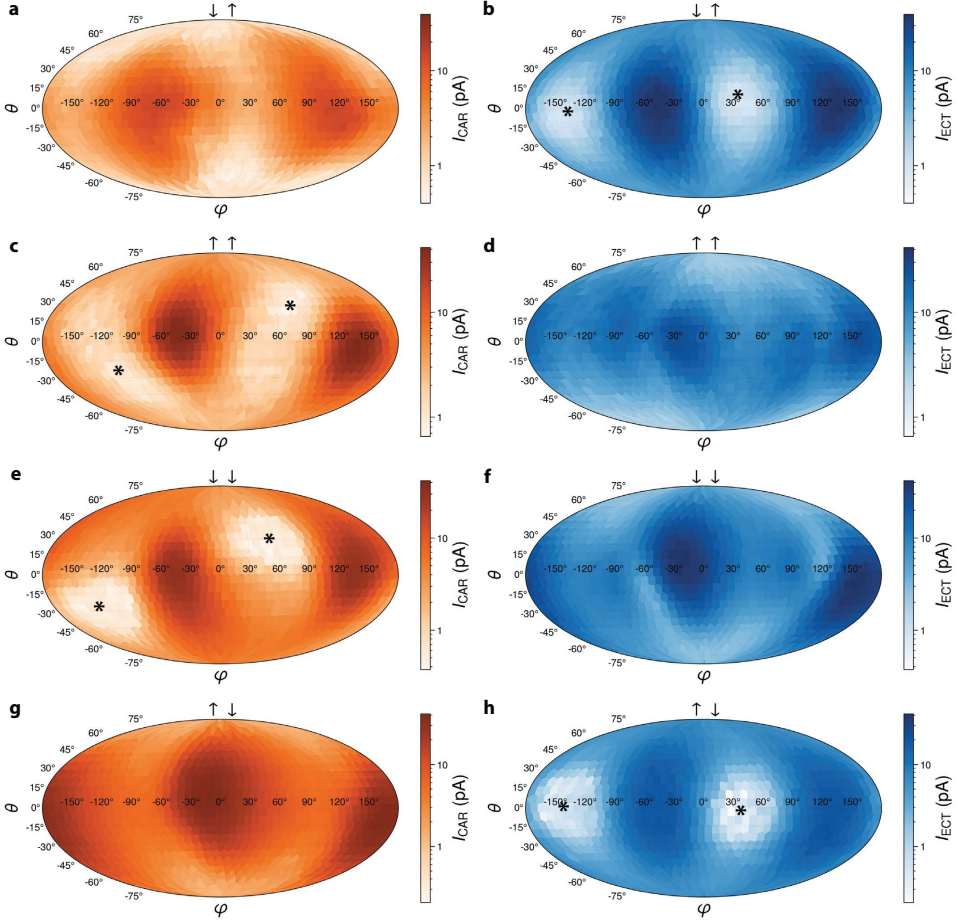
Figure 3.10: **CAR and ECT dependence on field direction for other spin selections in device B.** Spherical plots as in Fig. 3.4a-b when the QDs select other spin configurations (the ↓↑ configuration is reported here again in panels a and b as in the main text for easier comparison). When opposite spins are selected, ECT is suppressed along a single direction. While, when the QDs select ↑↑ or ↓↓ spins, it is the CAR-induced current to be suppressed along a single magnetic field direction. We interpret the suppression direction as the orientation of the spin-orbit field $\vec{B}_{SO}$ and highlight it with star marks. We remark that the suppression direction, as well as the enhancement direction, is slightly different among plots. The origin of this discrepancy is not yet fully understood. Following the discussion regarding the ABS charge, we speculate that it could be caused by more than one ABS mediating ECT and CAR. Concretely, the ABS most responsible for ECT could have a slightly different spin-orbit direction than the one mediating CAR.
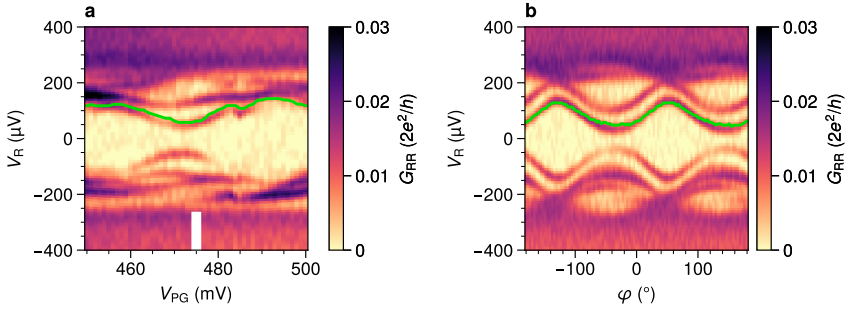
Figure 3.11: **Comparison between tunnel spectroscopy and extracted** $E_\downarrow$. **a.** Local tunnel spectroscopy of device B as a function of V_{PG} around the values used in Fig. 3.4a-c, measured using a lock-in. $|\vec{B}| = 80$ mT, applied perpendicular to the nanowire ($\theta = 0°$) and with $\varphi = -180°$. Green: extracted $E_\downarrow$ values using the same method as in Fig. 3.4c. As in that panel, the calculation is done using measured currents, in this case simultaneously acquired as the lock-in conductance. The white bar marks the V_{PG} value at which panel b data is taken. **b.** Idem, as a function of field angle φ.
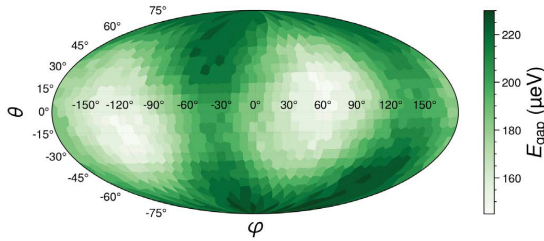
Figure 3.12: **Superconducting gap dependence on magnetic field direction.** Local tunneling spectroscopy as in Fig. 3.4c but at a negative superconducting gate: $V_{PG} = -500$ mV. Since no ABSs are present at this V_{PG} value, this is a direct measurement of the hybrid superconducting gap as a function of magnetic field orientation. $|\vec{B}| = 150$ mT. Notably, the direction along which the gap is reduced the most is different from that along which the ABS of Fig. 3.4c reaches its energy minimum. The gap-suppression direction in this strongly coupled regime (Mazur et al., 2022) is likely where orbital depairing in the Al film is the strongest, considering the size of $|\vec{B}|$ and that it is the angle that maximizes the flux incident on the Al-covered facets. Superficially, previous work on hybrid nanowires has also observed maximal gap suppression along similar angles and interpreted it as the measured spin-orbit direction (Bommer et al., 2019). However, the analysis there relied on the superconducting film made of NbTiN experiencing almost no orbital depairing along all magnetic field directions. The same interpretation is not valid in the case of Al here and, thus, gap spectroscopy cannot be used to measure the effect of spin-orbit coupling. Therefore, using CAR and ECT to measure the spin-orbit direction is less prone to complications by orbital effects compared to gap-size spectroscopy.

4

REALIZATION OF
A MINIMAL KITAEV CHAIN
IN COUPLED QUANTUM DOTS

Majorana bound states constitute one of the simplest examples of emergent non-Abelian excitations in condensed matter physics. A toy model proposed by Kitaev shows that such states can arise at the ends of a spinless p-wave superconducting chain (Kitaev, 2001). Practical proposals for its realization (Sau and Das Sarma, 2012; Leijnse and Flensberg, 2012a) require coupling neighboring quantum dots in a chain via both electron tunneling and crossed Andreev reflection (Recher et al., 2001). While both processes have been observed in semiconducting nanowires and carbon nanotubes (Hofstetter et al., 2009; Herrmann et al., 2010; Das et al., 2012; Schindele et al., 2012), crossed-Andreev interaction was neither easily tunable nor strong enough to induce coherent hybridization of dot states. Here, we demonstrate the simultaneous presence of all necessary ingredients for an artificial Kitaev chain: two spin-polarized quantum dots in an InSb nanowire strongly coupled by both elastic co-tunneling and crossed Andreev reflection. We fine-tune this system to a sweet spot where a pair of Poor Man's Majorana states is predicted to appear. At this sweet spot, the transport characteristics satisfy the theoretical predictions for such a system, including pairwise correlation, zero charge, and stability against local perturbations. While the simple system presented here can be scaled to simulate a full Kitaev chain with an emergent topological order, it can also be used imminently to explore relevant physics related to non-Abelian anyons.

4

ngineering Majorana bound states in condensed matter systems is an intensively pursued goal, both for their exotic non-Abelian exchange statistics and for potential applications in building topologically protected qubits (Kitaev, 2001, 2003; Nayak et al., 2008). The most investigated experimental approach looks for Majorana states at the boundaries of topological superconducting materials, made of hybrid semiconducting-superconducting heterostructures (Mourik et al., 2012; Deng et al., 2016; Fornieri et al., 2019; Ren et al., 2019; Vaitiekėnas et al., 2020). However, the widely-relied-upon signature of Majorana states, zero-bias conductance peaks, is by itself unable to distinguish topological Majorana states from other trivial zero-energy states induced by disorder and smooth gate potentials (Kells et al., 2012; Prada et al., 2012; Pikulin et al., 2012; Liu et al., 2017; Vuik et al., 2019; Pan and Das Sarma, 2020). Both problems disrupting the formation or detection of a topological phase originate from a lack of control over the microscopic details of the electron potential landscape in these heterostructure devices.

In this work, we realize a minimal Kitaev chain (Kitaev, 2001) using two quantum dots (QDs) coupled via a short superconducting-semiconducting hybrid (Sau and Das Sarma, 2012). By controlling the electrostatic potential on each of these three elements, we overcome the challenge imposed by random disorder potentials. At a fine-tuned sweet spot where Majorana states are predicted to appear, we observe end-to-end correlated conductance that signals emergent Majorana properties such as zero charge and robustness against local perturbations. We note that these Majorana states in a minimal Kitaev chain are *not* topologically protected and have been dubbed "Poor Man's Majorana" (PMM) states (Leijnse and Flensberg, 2012a).

4.1. Realization of a minimal Kitaev chain

The elementary building block of the Kitaev chain is a pair of spinless electronic sites coupled simultaneously by two mechanisms: elastic co-tunneling (ECT) and crossed Andreev reflection (CAR). Both processes are depicted in Fig. 4.1a. ECT involves a single electron hopping between two sites with an amplitude t. CAR refers to two electrons from both sites tunneling back and forth into a common superconductor with an amplitude Δ (not to be confused with the superconducting gap size), forming and splitting Cooper-pairs (Recher et al., 2001). To create the two-site Kitaev chain, we utilize two spin-polarized QDs where only one orbital level in each dot is available for transport. In the absence of tunneling between the QDs, the system is characterized by a well-defined charge state on each QD: $|n_{\rm LD}\, n_{\rm RD}\rangle$, where $n_{\rm LD}, n_{\rm RD} \in \{0, 1\}$ are occupations of the left and right QD levels. The charge on each QD depends only on its electrochemical potential $\mu_{\rm LD}$ or $\mu_{\rm RD}$, schematically shown in Fig. 4.1b.

In the presence of inter-dot coupling, the eigenstates of the combined system become superpositions of the charge states. ECT couples $|10\rangle$ and $|01\rangle$, resulting in two eigenstates of the form $\alpha|10\rangle + \beta|01\rangle$ (Fig. 4.1c), both with odd combined charge parity. These two bonding and anti-bonding states differ in energy by $2t$ when both QDs are at their charge degeneracy, i.e., $\mu_{\rm LD} = \mu_{\rm RD} = 0$. Analogously, CAR couples the two even states $|00\rangle$ and $|11\rangle$ to produce bonding and anti-bonding eigenstates of the form $u|00\rangle + v|11\rangle$, preserving the even parity of the original states. These states differ in energy by 2Δ when $\mu_{\rm LD} = \mu_{\rm RD} = 0$ (Fig. 4.1d). If the amplitude of ECT is stronger than CAR
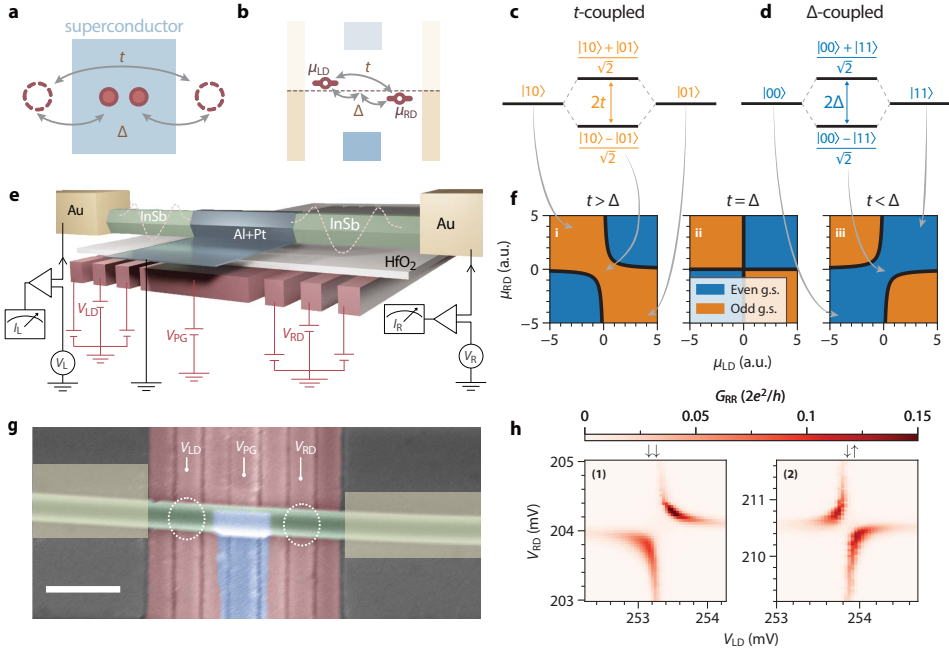
Figure 4.1: **Coupling quantum dots through elastic co-tunneling (ECT) and crossed Andreev reflection (CAR). a.** Illustration of the basic ingredients of a Kitaev chain: two QDs simultaneously coupled via ECT with amplitude t and via CAR with amplitude Δ through the superconductor in between. **b.** Energy diagram of a minimal Kitaev chain. Two QDs with gate-controlled chemical potentials are coupled via both ECT and CAR. The two ohmic leads enable transport measurements from both sides. **c.** Energy diagram showing that coupling the $|01\rangle$ and $|10\rangle$ states via ECT leads to a bonding state $(|10\rangle - |01\rangle)/\sqrt{2}$ and anti-bonding state $(|10\rangle + |01\rangle)/\sqrt{2}$. **d.** Same showing how CAR couples $|00\rangle$ and $|11\rangle$ to form the bonding state $(|00\rangle - |11\rangle)/\sqrt{2}$ and anti-bonding state $(|00\rangle + |11\rangle)/\sqrt{2}$. **e.** Illustration of the N-QD-S-QD-N device and the measurement circuit. Dashed potentials indicate QDs defined in the nanowire by finger gates. **f.** Charge stability diagram of the coupled-QD system, in the cases of $t > \Delta$ (i), $t = \Delta$ (ii), and $t < \Delta$ (iii). Blue marks regions in the (μ_{LD}, μ_{RD}) plane where the ground state is even and orange where the ground state is odd. **g.** False-colored scanning electron microscopy image of the device, prior to the fabrication of the normal leads. InSb nanowire is colored green. QDs are defined by bottom finger gates (in red) and their locations are circled. The gates controlling the two QD chemical potentials are labeled by their voltages, V_{LD} and V_{RD}. The central thin Al/Pt film, in blue, is grounded. The proximitized nanowire underneath is gated by V_{PG}. Two Cr/Au contacts are marked by yellow boxes. The scale bar is 300 nm. **h.** Right-side zero-bias local conductance G_{RR} in the (V_{LD}, V_{RD}) plane when the system is tuned to $t > \Delta$ (1) and $t < \Delta$ (2). The arrows mark the spin polarization of the QD levels. The DC bias voltages are kept at zero, $V_L = V_R = 0$, and an AC excitation of 6 μV RMS is applied on the right side.

($t > \Delta$), the odd bonding state has lower energy than the even bonding state near the joint charge degeneracy $\mu_{LD} = \mu_{RD} = 0$ (see Methods for details). The system thus features an odd ground state in a wider range of QD potentials, leading to a charge stability diagram shown in Fig. 4.1f(i) (van der Wiel et al., 2002). The opposite case of CAR dominating over ECT, i.e., $t < \Delta$, leads to a charge stability diagram shown in Fig. 4.1f(iii), where the even ground state is more prominent. Fine-tuning the system such that $t = \Delta$ equalizes the two avoided crossings, inducing an even-odd degenerate ground state at $\mu_{LD} = \mu_{RD} = 0$ (Fig. 4.1f(ii)). This degeneracy gives rise to two spatially separated PMMs,

each localized at one QD (Leijnse and Flensberg, 2012a).

Fig. 4.1e illustrates our coupled QD system and the electronic measurement circuit. An InSb nanowire is contacted on two sides by two Cr/Au normal leads (N). A 200 nm-wide superconducting lead (S) made of a thin Al/Pt film covering the nanowire is grounded and proximitizes the central semiconducting segment. The chemical potential of the proximitized semiconductor can be tuned by gate voltage V_{PG}. This hybrid segment shows a hard superconducting gap accompanied by discrete, gate-tunable Andreev bound states (Fig. 4.5). Two QDs are defined by finger gates underneath the nanowire. Their chemical potentials μ_{LD}, μ_{RD} are linearly tuned by voltages on the corresponding gates V_{LD}, V_{RD}. Bias voltages on the two N leads, V_L, V_R, are applied independently and currents through them, I_L, I_R, are measured separately. Transport characterization shows charging energies of 1.8 meV on the left QD and 2.3 meV on the right (Fig. 4.5). Standard DC+AC lock-in technique allows measurement of the full conductance matrix:

$$G = \begin{pmatrix} G_{LL} & G_{LR} \\ G_{RL} & G_{RR} \end{pmatrix} = \begin{pmatrix} \frac{dI_L}{dV_L} & \frac{dI_L}{dV_R} \\ \frac{dI_R}{dV_L} & \frac{dI_R}{dV_R} \end{pmatrix}. \tag{4.1}$$

Measurements were conducted in a dilution refrigerator in the presence of a magnetic field $B = 200$ mT applied approximately along the nanowire axis. The combination of Zeeman splitting E_Z and orbital level spacing allows single-electron QD transitions to be spin-polarized. Two neighboring Coulomb resonances correspond to opposite spin orientations, enabling the QD spins to be either parallel ($\uparrow\uparrow$ and $\downarrow\downarrow$) or anti-parallel ($\uparrow\downarrow$ and $\downarrow\uparrow$). We report on two devices, A in the main text and B in Extended Data (Fig. 4.11 and Fig. 4.12). A scanning electron microscope image of Device A is shown in Fig. 4.1g.

Transport measurements are used to characterize the charge stability diagram of the system. In Fig. 4.1h(1), we show G_{RR} as a function of QD voltages V_{LD}, V_{RD} when both QDs are set to spin-down ($\downarrow\downarrow$). The measured charge stability diagram shows avoided crossing which indicates the dominance of ECT. In Fig. 4.1h(2), we change the spin configuration to $\downarrow\uparrow$. The charge stability diagram now develops the avoided crossing of the opposite orientation, indicating the dominance of CAR for QDs with anti-parallel spins. This is, to our knowledge, the first verification of the prediction that spatially separated QDs can coherently hybridize via CAR coupling to a superconductor (Choi et al., 2000). Thus, we have introduced all the necessary ingredients for a two-site Kitaev chain.

4.2. TUNING THE RELATIVE STRENGTH OF CAR AND ECT

Majorana states in long Kitaev chains are present under a wide range of parameters due to topological protection (Kitaev, 2001). Strikingly, even a chain consisting of only two sites can host a pair of PMMs despite a lack of topological protection, if the fine-tuned sweet spot $t = \Delta$ and $\mu_{LD} = \mu_{RD} = 0$ can be achieved (Leijnse and Flensberg, 2012a). This, however, is made challenging by the above-mentioned requirement to have both QDs spin-polarized. If spin is conserved, ECT can only take place between QDs with $\downarrow\downarrow$ or $\uparrow\uparrow$ spins, while CAR is only allowed for $\uparrow\downarrow$ and $\downarrow\uparrow$. Rashba spin-orbit coupling in InSb nanowires solves this dilemma (Sau and Das Sarma, 2012; Liu et al., 2022; Wang et al., 2022a), allowing finite ECT even in anti-parallel spin configurations and CAR between QDs with equal spins.

A further challenge is to make the two coupling strengths equal for a given spin combination. Refs. (Liu et al., 2022; Wang et al., 2022a; Bordin et al., 2023) show that both CAR and ECT in our device are virtual transitions through intermediate Andreev bound states residing in the short InSb segment underneath the superconducting film. Thus, varying V_{PG} changes the energy and wavefunction of said Andreev bound states and thereby t, Δ. We search for the V_{PG} range over which Δ changes differently than t and look for a crossover in the type of charge stability diagrams.
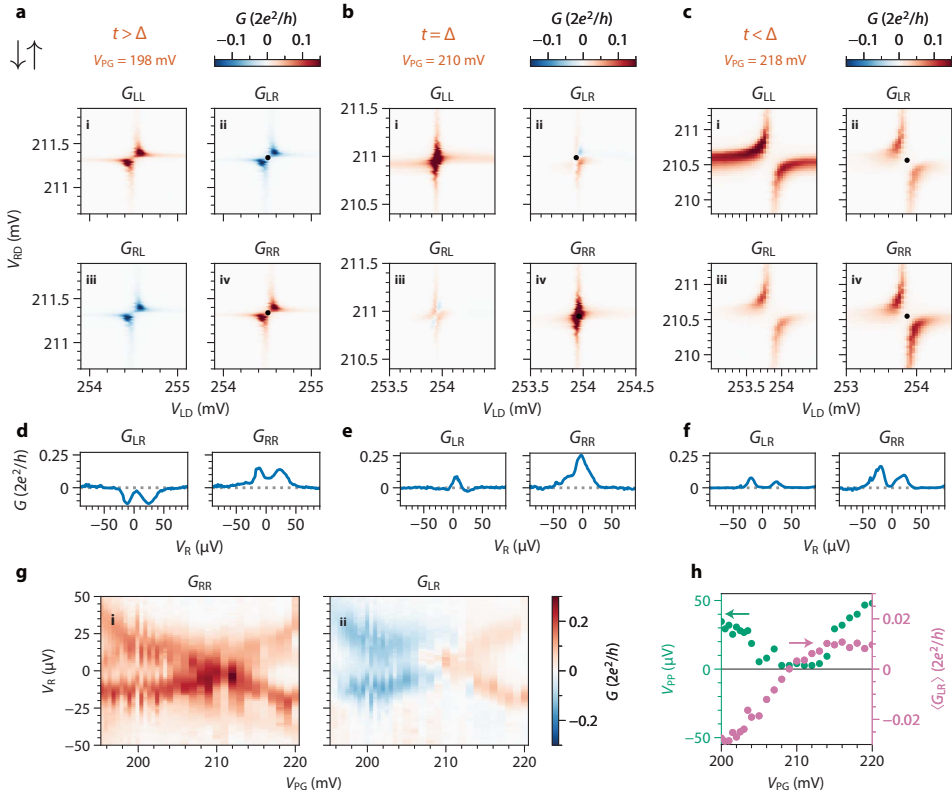
Figure 4.2: **Tuning the relative strength of CAR and ECT for the ↓↑ spin configuration. a-c.** Conductance matrices measured with $V_{PG} = (198, 210, 218)$ mV, respectively. **d-f.** G_{LR} and G_{RR} as functions of V_R when V_{LD}, V_{RD} are set to the center of each charge stability diagram in panels a to c, indicated by the black dots in the corresponding panels above them. **g.** Local (G_{RR}) and nonlocal (G_{LR}) conductance as a function of V_R and V_{PG} while keeping $\mu_{LD} \approx \mu_{RD} \approx 0$, showing the continuous crossover from $t > \Delta$ to $t < \Delta$. **h.** Green dots: peak-to-peak distance (V_{PP}) between the positive- and negative-bias segments of G_{RR}, showing the closing and re-opening of QD avoided crossings. Purple dots: average G_{LR} ($\langle G_{LR} \rangle$) as a function of V_{PG}, showing a change in the sign of the nonlocal conductance.

Fig. 4.2a-c shows the resulting charge stability diagrams for the ↓↑ spin configuration at different values of V_{PG}. The conductance matrix $G(V_L = 0, V_R = 0)$ at $V_{PG} = 198$ mV is shown in Fig. 4.2a. The local conductance on both sides, G_{LL} and G_{RR}, exhibit level repulsion indicative of $t > \Delta$. We emphasize that ECT can become stronger than CAR even

though the spins of the two QD transitions are anti-parallel due to the electric gating mentioned above. The dominance of ECT over CAR can also be seen in the negative sign of the nonlocal conductance, G_{LR} and G_{RL}. During ECT, an electron enters the system through one dot and exits through the other, resulting in negative nonlocal conductance. CAR, in contrast, causes two electrons to enter or leave both dots simultaneously, producing positive nonlocal conductance (Beckmann and Löhneysen, 2006). The residual finite conductance in the center of the charge stability diagram can be attributed to level broadening due to finite temperature and dot-lead coupling (see Fig. 4.14). In Fig. 4.2d, we show the conductance spectrum measured as a function of V_R, with V_{LD} and V_{RD} tuned to $\mu_{LD} \approx \mu_{RD} \approx 0$ (black dots in panels c(ii, iv)). A pair of conductance peaks or dips is visible on either side of zero energy.

Fig. 4.2c shows G at $V_{PG} = 218\,\mathrm{mV}$ (the G_{RR} component is also used for Fig. 4.1h(2)). Here, all the elements of G exhibit CAR-type avoided crossings. The spectrum shown in panel f, obtained at the joint charge degeneracy point (black dots in panels c(ii, iv)), similarly has two conductance peaks surrounding zero energy. The measured nonlocal conductance is positive as predicted for CAR. The existence of both $t > \Delta$ and $t < \Delta$ regimes, together with continuous gate tunability, allows us to approach the $t \approx \Delta$ sweet spot. This is shown in panel b, taken with $V_{PG} = 210\,\mathrm{mV}$. Here, G_{RR} and G_{LL} exhibit no avoided crossing while G_{LR} and G_{RL} fluctuate around zero, confirming that CAR and ECT are in balance. Accordingly, the spectrum in panel e confirms the even and odd ground states are degenerate and transport can occur at zero excitation energy via the appearance of a zero-bias conductance peak. The crossover from the $t > \Delta$ regime to the $t < \Delta$ regime can be seen across multiple QD resonances (Fig. 4.13).

To show that gate-tuning of the t/Δ ratio is indeed continuous, we repeat charge stability diagram measurements (Fig. 4.7) and bias spectroscopy at more V_{PG} values. As before, each bias sweep is conducted while keeping both QDs at charge degeneracy. Fig. 4.2g shows the resulting composite plot of G_{RR} (i) and G_{LR} (ii) vs bias voltage and V_{PG}. The X-shaped conductance feature indicates a continuous evolution of the excitation energy, with a linear zero-energy crossing agreeing with predictions in Leijnse and Flensberg (2012a). Following the analysis described in Methods, we extract the peak spacing and average nonlocal conductance in Fig. 4.2h in order to visualize the continuous crossover from $t > \Delta$ to $t < \Delta$.

4.3. POOR MAN'S MAJORANA SWEET SPOT

Next, we study the excitation spectrum in the vicinity of the $t = \Delta$ sweet spot. The predicted zero-temperature experimental signature of the PMMs is a pair of quantized zero-bias conductance peaks on both sides of the devices. These zero-bias peaks are persistent even when one of the QD levels deviates from charge degeneracy (Leijnse and Flensberg, 2012a). We focus on the $\uparrow\uparrow$ spin configuration since it exhibits higher t, Δ values when they are equal (see Fig. 4.8). Fig. 4.3a shows the charge stability diagram measured via I_R under fixed $V_L = 0, V_R = 10\,\mu\mathrm{V}$. No level repulsion is visible, indicating $t \approx \Delta$. Panel b(i) shows the excitation spectrum when both dots are at charge degeneracy. The spectra on both sides show zero-bias peaks accompanied by two side peaks. The values of t, Δ can be read directly from the position of the side peaks, which correspond to the anti-bonding excited states at energy $2t = 2\Delta \approx 25\,\mu\mathrm{eV}$. The height of the observed zero-
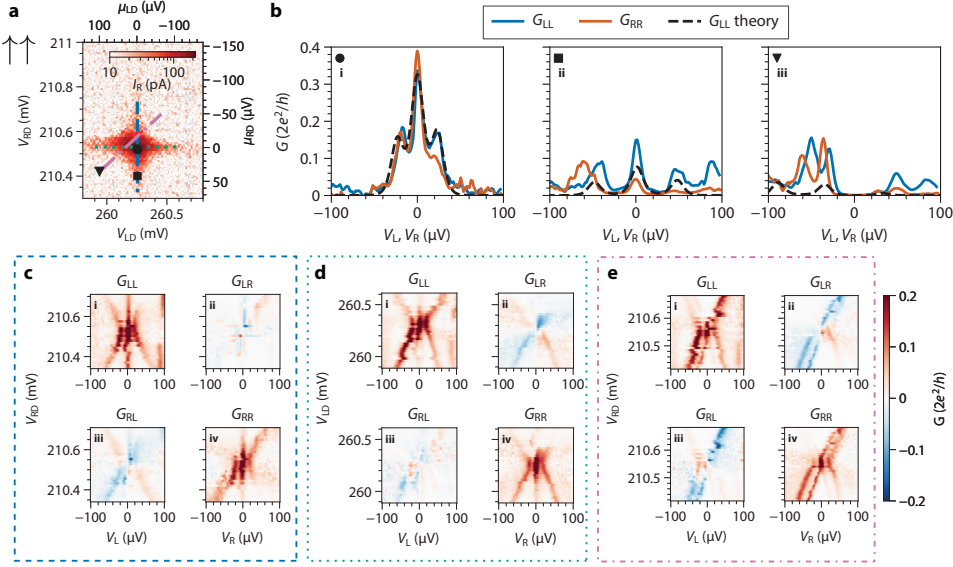
Figure 4.3: **Conductance spectroscopy at the $t = \Delta$ sweet spot for the $\uparrow\uparrow$ spin configuration. a.** I_R vs V_{LD}, V_{RD} under $V_L = 0, V_R = 10\,\mu\text{V}$. The spectra in panel b are taken at values of V_{LD}, V_{RD} marked by corresponding symbols. The gate vs bias sweeps are taken along the dashed, dotted, dash-dot lines in panels c,d,e respectively. Data are taken with fixed $V_{PG} = 215.1\,\text{mV}$. **b.** Spectra taken under the values of V_{LD}, V_{RD} marked in panel a. The dashed lines are theoretical curves calculated with $t = \Delta = 12\,\mu\text{eV}$, $\Gamma_L = \Gamma_R = 4\,\mu\text{eV}$, $T = 45\,\text{mK}$ and at QD energies converted from V_{LD}, V_{RD} using measured lever arms (see Methods for details). **c, d.** G as a function of the applied bias and V_{RD} (c) or V_{LD} (d), taken along the paths indicated by the dashed blue line and the dotted green line in panel a, respectively. **e.** G as a function of the applied bias and along the diagonal indicated by the dashed-dotted pink line in panel a. This diagonal represents $500\,\mu\text{V}$ of change in V_{LD} and $250\,\mu\text{V}$ of change in V_{RD}.

bias peaks is 0.3 to $0.4 \times 2e^2/h$, likely owing to a combination of tunnel broadening and finite electron temperature (Fig. 4.6). Fig. 4.3b(ii) shows the spectrum when the right QD is moved away from charge degeneracy while μ_{LD} is kept at 0. The zero-bias peaks persist on both sides of the device, as expected for a PMM state. In contrast, tuning both dots away from charge degeneracy, shown in Fig. 4.3b(iii), splits the zero-bias peaks.

In Fig. 4.3c,d, we show the evolution of the spectrum when varying V_{RD} and V_{LD}, respectively. The vertical feature appearing in both G_{LL} and G_{RR} shows correlated zero-bias peaks in both QDs, which persist when one QD potential departs from zero. This crucial observation demonstrates the robustness of PMMs against local perturbations. The excited states disperse in agreement with the theoretical predictions (Leijnse and Flensberg, 2012a). Nonlocal conductance, on the other hand, reflects the local charge character of a bound state on the side where current is measured (Gramich et al., 2017; Danon et al., 2020; Ménard et al., 2020). Near-zero values of G_{LR} in panel c and G_{RL} in panel d are consistent with the prediction that the PMM mode on the unperturbed side remains an equal superposition of an electron and a hole and, therefore, chargeless.

Finally, when varying the chemical potential of both dots simultaneously (panel e), we see that the zero-bias peaks split away from zero energy. This splitting is not lin-

ear, in contrast to the case when $\Delta \neq t$ (see Fig. 4.9). The profile of the peak splitting is consistent with the predicted quadratic protection of PMMs against chemical potential fluctuations (Leijnse and Flensberg, 2012a). This quadratic protection is expected to develop into topological protection in a long-enough Kitaev chain (Sau and Das Sarma, 2012).

4.4. DISCUSSION

To facilitate comparison with data, we develop a transport model (see Methods) and plot in Fig. 4.4a-c the calculated conductance matrices as functions of excitation energy, ω, vs μ_{RD} (panel a), μ_{LD} (panel b), and $\mu \equiv \mu_{LD} = \mu_{RD}$ (panel c). These conditions are an idealization of those in Fig. 4.3 (a more realistic simulation of the experimental conditions is presented in Fig. 4.10). The numerical simulations capture the main features appearing in the experiments discussed above.
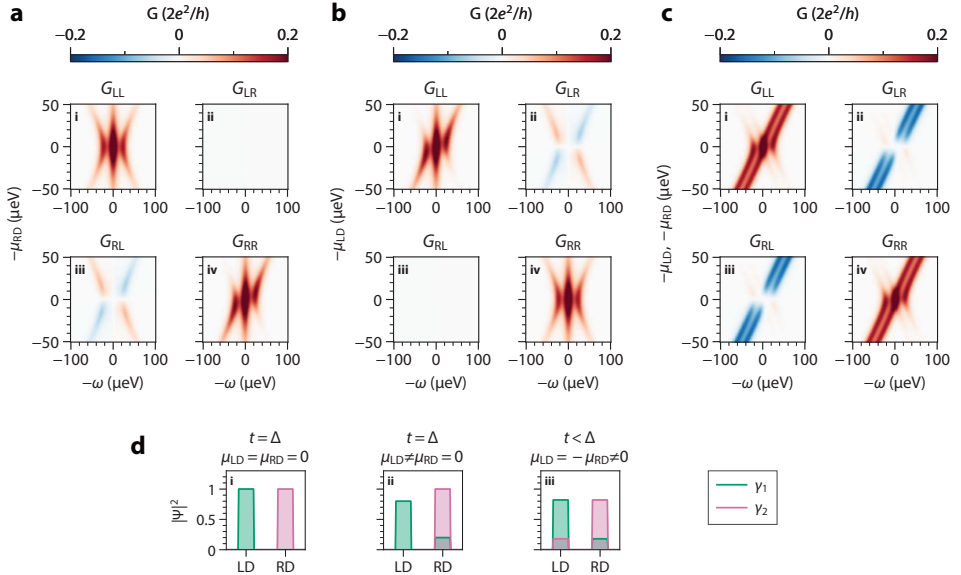
Figure 4.4: **Calculated conductance and Majorana localization. a.** Numerically calculated G as a function of energy ω and μ_{RD} at the $t = \Delta$ sweet spot. **b.** Numerically calculated G as a function of ω and μ_{LD} at the $t = \Delta$ sweet spot. **c.** Numerically calculated G as a function of ω and μ_{RD}, μ_{LD} along the diagonal corresponding to $\mu_{LD} = \mu_{RD}$ at $t = \Delta$. All of the numerical curves use the same value of $t, \Delta, \Gamma_L, \Gamma_R$ as those in Fig. 4.3. **d.** Illustrations of the localization of two zero-energy solutions for the following set of parameters: $t = \Delta$, $\mu_{LD} = \mu_{RD} = 0$ (sub-panel i), $t = \Delta$, $\mu_{RD} = 0$, $\mu_{LD} > 0$ (sub-panel ii), $t < \Delta$, $\mu_{LD} = -\mu_{RD} = \sqrt{\Delta^2 - t^2}$ (sub-panel iii).

Particle-hole symmetry ensures that zero-energy excitations in this system always come in pairs. These excitations can extend over both QDs or be confined to one of them. In Fig. 4.4d we show the calculated spatial extent of the zero-energy excitations for three scenarios. The first, in Fig. 4.4d(i), illustrates Fig. 4.3b(i) and shows that the sweet-spot zero-energy solutions are two PMMs, each localized on a different QD. The second sce-

nario in Fig. 4.4d(ii), illustrating Fig. 4.3b(ii), is varying μ_{LD} while keeping $\mu_{RD} = 0$. This causes some of the wavefunction localized on the perturbed left side, γ_1, to leak into the right QD. Since the right-side γ_2 excitation has no weight on the left, it does not respond to this perturbation and remains fully localized on the right QD. As the theory confirms (Leijnse and Flensberg, 2012a), it stays a zero-energy PMM state. Since Majorana excitations always come in pairs, the excitation on the left QD must also remain at zero energy. This provides an intuitive understanding of the remarkable stability of the zero-energy modes at the sweet spot in Fig. 4.3c,d when moving one of the QDs' chemical potentials away from zero. Finally, zero-energy solutions can be found away from the sweet spot, $t \neq \Delta$, as illustrated in Fig. 4.4d(iii). These zero-energy states are only found when both QDs are off-resonance and none of them are localized Majorana states, extending over both QDs and exhibiting no gate stability. Measurements under these conditions are shown in Fig. 4.9, where zero-energy states can be found in a variety of gate settings (panels a, c therein).

4.5. CONCLUSION

In summary, we realize a minimal Kitaev chain where two QDs in an InSb nanowire are separated by a hybrid semiconducting-superconducting segment. Compared to past works, our approach solves three challenges: strong hybridization of QDs via CAR, simultaneous coupling of two single spins via both ECT and CAR, and continuous tuning of the coupling amplitudes. This is made possible by the two QDs as well as the middle Andreev bound state mediating their couplings all being discrete, gate-tunable quantum states. The result is the creation of a new type of nonlocal states that host Majorana-type excitations at a fine-tuned sweet spot. The zero-bias peaks at this spot are robust against variations of the chemical potential of one QD and quadratically protected against simultaneous perturbations of both. This discrete and tunable way of assembling Kitaev chains shows good agreement between theory and experiment by avoiding the most concerning problems affecting the continuous nanowire experiments: disorder, smooth gate potentials, and multi-subband occupation (Pan and Das Sarma, 2021). The QD-S-QD platform discussed here opens up a new frontier to the study of Majorana physics. In the long term, this approach can generate topologically protected Majorana states in longer chains (Sau and Das Sarma, 2012). A shorter term approach is to use PMMs as an immediate playground to study fundamental non-Abelian statistics, e.g., by fusing neighboring PMMs in a device with two such copies.

4

AUTHOR CONTRIBUTIONS

GW, GPM, NvL, AB, JW, DvD, FZ fabricated the devices. GW, TD, SLDtH, AB, and XL performed the electrical measurements. TD and GW designed the experiment with inputs from FM and analyzed the data. GW, TD, and LPK prepared the manuscript with input from all authors. TD and LPK supervised the project. CXL developed the theoretical model and performed numerical simulations with input from GW, TD, and MW. SG, GB, and EPAMB performed InSb nanowire growth.

COMPETING INTERESTS

The authors declare no competing interests.

DATA AVAILABILITY AND CODE AVAILABILITY

Raw data presented in this work, the data processing/plotting code, and the code used for the theory calculations are available at https://zenodo.org/record/6594170.

4.6. METHODS

4.6.1. DEVICE FABRICATION
The nanowire hybrid devices presented in this work were fabricated on pre-patterned substrates, using the shadow-wall lithography technique described in Heedt et al. (2021) and Borsoi et al. (2021). Nanowires were deposited onto the substrates using an optical micro-manipulator setup. 8 nm of Al was grown at a mix of 15° and 45° angles with respect to the substrate. Subsequently, Device A was coated with 2 Å of Pt grown at 30°. No Pt was deposited for Device B. Finally, all devices were capped with 20 nm of evaporated AlO_x. Details of the substrate fabrication, the surface treatment of the nanowires, the growth conditions of the superconductor, the thickness calibration of the Pt coating and the ex-situ fabrication of the ohmic contacts can be found in Mazur et al. (2022). Devices A and B also slightly differ in the length of the hybrid segment: 180 nm for A and 150 nm for B.

4.6.2. TRANSPORT MEASUREMENT AND DATA PROCESSING
We have fabricated and measured six devices with similar geometry. Two of them showed strong hybridization of the QD states by means of CAR and ECT. We report on the detailed measurements of Device A in the main text and show qualitatively similar measurements from Device B in Fig. 4.11 and Fig. 4.12. All measurements on Device A were done in a dilution refrigerator with base temperature 7 mK at the cold plate and electron temperature of 40~50 mK at the sample, measured in a similar setup using an NIS metallic tunnel junction. Unless otherwise mentioned, the measurements on Device A were conducted in the presence of a magnetic field of 200 mT approximately oriented along the nanowire axis with a 3° offset. Device B was measured similarly in another dilution refrigerator under $B = 100$ mT along the nanowire with 4° offset.

Fig. 4.1e shows a schematic depiction of the electrical setup used to measure the devices. The middle segment of the InSb nanowire is covered by a thin Al shell, kept grounded throughout the experiment. On each side of the hybrid segment, we connect the normal leads to a current-to-voltage converter. The amplifiers on the left and right sides of the device are each biased through a digital-to-analog converter that applies DC and AC biases. The total series resistance of the voltage source and the current meter is less than 100 Ω for Device A and 1.11 kΩ for Device B. Voltage outputs of the current meter are read by digital multimeters and lock-in amplifiers. When DC voltage V_L is applied, V_R is kept grounded and vice versa. AC excitations are applied on each side of the device with different frequencies (17 Hz on the left and 29 Hz on the right for Device A, 19 Hz on the left and 29 Hz on the right for Device B) and with amplitudes between 2 and 6 μV RMS. In this manner, we measure the DC currents I_L, I_R and the conductance matrix G in response to applied voltages V_L, V_R on the left and right N leads, respectively. The conductance matrix is corrected for voltage divider effects (see Martinez et al. (2021) for details) taking into account the series resistance of sources and meters and in each fridge line (1.85 kΩ for Device A and 2.5 kΩ for Device B), except for the right panel of Fig. 4.1h and Fig. 4.2d. There, the left half of the conductance matrix was not measured and correction is not possible. We verify that the series resistance is much smaller than the device resistance and the voltage divider effect is never more than ~10% of the signal.

4.6.3. CHARACTERIZATION OF QDS AND THE HYBRID SEGMENT

To form the QDs described in the main text, we pinch off the finger gates next to the three ohmic leads, forming two tunnel barriers in each N-S junction. V_{LD} and V_{RD} applied on the middle finger gates on each side accumulate electrons in the QDs. We refer to the associated data repository for the raw gate voltage values used in each measurement. See Fig. 4.5a-f for results of the dot characterizations.

Characterization of the spectrum in the hybrid segment is done using conventional tunnel spectroscopy. In each uncovered InSb segment, we open up the two finger gates next to the N lead and only lower the gate next to the hybrid to define a tunnel barrier. The results of the tunnel spectroscopy are shown in Fig. 4.5g,h and the raw gate voltages are available in the data repository.

4.6.4. DETERMINATION OF QD SPIN POLARIZATION

Control of the spin orientation of QD levels is done via selecting from the even vs odd charge degeneracy points following the method detailed in Hanson et al. (2007). At the charge transition between occupancy $2n$ and $2n + 1$ (n being an integer), the electron added to or removed from the QD is polarized to spin-down ($\downarrow$, lower in energy). The next level available for occupation, at the transition between $2n + 1$ and $2n + 2$ electrons, has the opposite polarization of spin-up ($\uparrow$, higher in energy). To ensure the spin polarization is complete, the experiment was conducted with $E_Z \approx 400\,\mu eV > |eV_L|, |eV_R|$ (see Fig. 4.5 for determination of the spin configuration). In the experiment data, a change in the QD spin orientation is visible as a change in the range of V_{LD} or V_{RD}.

4.6.5. CONTROLLING ECT AND CAR VIA ELECTRIC GATING

Liu et al. (2022) describe a theory of mediating CAR and ECT transitions between QDs via virtual hopping through an intermediate Andreev bound state. Our manuscript Bordin et al. (2023) experimentally verifies the applicability of this theory to our device. To summarize the findings here, we consider two QDs both tunnel-coupled to a central Andreev bound state in the hybrid segment of the device. The QDs have excitation energies lower than that of the Andreev bound state and thus transition between them is second-order. The wavefunction of an Andreev bound state consists of a superposition of an electron part, u, and a hole part, v. Both theory and experiment conclude that the values of t and Δ depend strongly and differently on u, v. Specifically, CAR involves converting an incoming electron to an outgoing hole and thus depends on the values of u and v jointly as $|uv|^2$. ECT, however, occurs over two parallel channels (electron-to-electron and hole-to-hole) and its coupling strength depends on u, v independently as $\left|u^2 - v^2\right|^2$. As the composition of u, v is a function of the chemical potential of the middle Andreev bound state, the CAR to ECT ratio is strongly tunable by V_{PG}. We thus look for a range of V_{PG} where Andreev bound states reside in the hybrid segment, making sure that the energies of these states are high enough so as not to hybridize with the QDs directly (Fig. 4.5). Next, we sweep V_{PG} to find the crossover point between t and Δ as described in the main text.

4.6.6. ADDITIONAL DETAILS ON THE MEASUREMENT OF THE COUPLED QD SPECTRUM

The measurement of the local and nonlocal conductance shown in Fig. 4.2g was conducted in a series of steps. First, the value of V_{PG} was set, and a charge stability diagram was measured as a function of V_{LD} and V_{RD}. Representative examples of such diagrams are shown in Fig. 4.7. Second, each charge stability diagram was inspected and the joint charge degeneracy point ($\mu_{LD} = \mu_{RD} = 0$) was selected manually (V_{LD}^0, V_{RD}^0). Lastly, the values of V_{LD} and V_{RD} were set to those of the joint degeneracy point and the local and nonlocal conductance were measured as a function of V_R.

The continuous transition from $t > \Delta$ to $t < \Delta$ is visible in Fig. 4.2g via both local and nonlocal conductance. G_{RR} shows that level repulsion splits the zero-energy resonance peaks both when $t > \Delta$ (lower values of V_{PG}) and when $t < \Delta$ (higher values of V_{PG}). The zero-bias peak is restored in the vicinity of $t = \Delta$, in agreement with theoretical predictions (Leijnse and Flensberg, 2012a). The crossover is also apparent in the sign of G_{LR}, which changes from negative ($t > \Delta$) to positive ($t < \Delta$).

To better visualize the transition between the ECT- and CAR-dominated regimes, we extract V_{PP}, the separation between the conductance peaks under positive and negative bias voltages, and plot them as a function of V_{PG} in Fig. 4.2h. When tuning V_{PG}, the peak spacing decreases until the two peaks merge at $V_{PG} \approx 210\,mV$. Further increase of V_{PG} leads to increasing V_{PP}. In addition, to observe the change in sign of the nonlocal conductance, we follow $\langle G_{LR} \rangle$, the value of G_{LR} averaged over the bias voltage V_R between -100 and $100\,\mu V$ at a given V_{PG}. We see that $\langle G_{LR} \rangle$ turns from negative to positive at $V_{PG} \approx 210\,mV$, in correspondence to a change in the dominant coupling mechanism.

Fig. 4.3c-e presents measurements where the conductance was measured against applied biases along some paths within the charge stability diagram (panel a). Prior to each of these measurements, a charge stability diagram was measured and inspected, based on which the relevant path in the (V_{LD}, V_{RD}) plane was chosen. Following each bias spectroscopy measurement, another charge stability diagram was measured and compared to the one taken before to check for potential gate instability. In case of noticeable gate drifts between the two, the measurement was discarded and the process was repeated. The values of μ_{LD} and μ_{RD} required for theoretical curves appearing in panel b were calculated by $\mu_i = \alpha_i(V_i - V_i^0)$ where $i = LD, RD$ and α_i is the lever arm of the corresponding QD. The discrepancy between the spectra measured with G_{LL} and G_{RR} likely results from gate instability, since they were not measured simultaneously. Finite remaining G_{LR} in panel c and G_{RL} in panel d most likely result from small deviations of μ_{LD}, μ_{RD} from zero during these measurements.

4.6.7. MODEL OF THE PHASE DIAGRAMS IN FIG. 4.1F

To calculate the ground state phase diagram in Fig. 4.1f, we write the Hamiltonian in the many-body picture, with the four basis states being $|00\rangle, |11\rangle, |10\rangle, |01\rangle$:

$$H_{\mathrm{mb}} = \begin{pmatrix} 0 & \Delta & 0 & 0 \\ \Delta & \varepsilon_L + \varepsilon_R & 0 & 0 \\ 0 & 0 & \varepsilon_L & t \\ 0 & 0 & t & \varepsilon_R \end{pmatrix} \tag{4.2}$$

in block-diagonalized form. The two 2×2 matrices yield the energy eigenvalues separately for the even and odd subspaces:

$$E_{o,\pm} = \frac{\varepsilon_L + \varepsilon_R}{2} \pm \sqrt{\left(\frac{\varepsilon_L - \varepsilon_R}{2}\right)^2 + t^2} \tag{4.3}$$

$$E_{e,\pm} = \frac{\varepsilon_L + \varepsilon_R}{2} \pm \sqrt{\left(\frac{\varepsilon_L + \varepsilon_R}{2}\right)^2 + \Delta^2} \tag{4.4}$$

The ground state phase transition occurs at the boundary $E_{o,-} = E_{e,-}$. This is equivalent to

$$\varepsilon_L \varepsilon_R = t^2 - \Delta^2 \tag{4.5}$$

4.6.8. TRANSPORT MODEL IN FIG. 4.3 AND FIG. 4.4

We describe in this section the model Hamiltonian of the minimal Kitaev chain and the method we use for calculating the differential conductance matrices when the Kitaev chain is tunnel-coupled to two external N leads.

The effective Bogoliubov-de-Gennes Hamiltonian of the double-QD system is

$$H = \varepsilon_L c_L^\dagger c_L + \varepsilon_R c_R^\dagger c_R + t c_L^\dagger c_R + t c_R^\dagger c_L + \Delta c_L c_R + \Delta c_R^\dagger c_L^\dagger$$
$$= \frac{1}{2}\Psi^\dagger \begin{pmatrix} \varepsilon_L & t & 0 & -\Delta \\ t & \varepsilon_R & \Delta & 0 \\ 0 & \Delta & -\varepsilon_L & -t \\ -\Delta & 0 & -t & -\varepsilon_R \end{pmatrix} \Psi, \tag{4.6}$$

where $\Psi = (c_L, c_R, c_L^\dagger, c_R^\dagger)^\top$ is the Nambu spinor, $\varepsilon_{L/R}$ is the level energy in dot-L/R relative to the superconducting Fermi surface, t and Δ are the ECT and CAR amplitudes. Here we assume t and Δ to be real without loss of generality (Leijnse and Flensberg, 2012a). The presence of both t and Δ in this Hamiltonian implies breaking spin conservation during QD-QD tunneling via either spin-orbit coupling (as done in the present experiment) or non-collinear magnetization between the two QDs (as proposed in Leijnse and Flensberg (2012a)). Without one of them, equal-spin QDs cannot recombine into a Cooper pair, leading to vanishing Δ, while opposite-spin QDs cannot support finite t. The exact values of t and Δ depend on the spin-orbit coupling strength and we refer to Liu et al. (2022) for a detailed discussion.

To calculate the differential conductance for the double-QD system, we use the S-matrix method (Datta, 2005). In the wide-band limit, the S matrix is

$$S(\omega) = \begin{pmatrix} s_{ee} & s_{eh} \\ s_{he} & s_{hh} \end{pmatrix} = 1 - iW^\dagger \left(\omega - H + \frac{1}{2}iWW^\dagger\right)^{-1} W, \tag{4.7}$$

where $W = \text{diag}\{\sqrt{\Gamma_L}, \sqrt{\Gamma_R}, -\sqrt{\Gamma_L}, -\sqrt{\Gamma_R}\}$ is the tunnel matrix, with Γ_α being the tunnel coupling strength between dot-α and lead-α. The zero-temperature differential conductance is given by

$$G^0_{\alpha\beta}(\omega) = dI_\alpha/dV_\beta = \frac{e^2}{h}\left(\delta_{\alpha\beta} - |s^{\alpha\beta}_{ee}(\omega)|^2 + |s^{\alpha\beta}_{he}(\omega)|^2\right), \qquad (4.8)$$

where $\alpha, \beta = L/R$. Finite-temperature effect is included by a convolution between the zero-temperature conductance and the derivative of Fermi-Dirac distribution, i.e.,

$$G^T(\omega) = \int dE \frac{G^0(E)}{4k_B T \cosh^2[(E-\omega)/2k_B T]}. \qquad (4.9)$$

The theoretical model presented above uses five input parameters to calculate the conductance matrix under given $\mu_{LD}, \mu_{RD}, V_L, V_R$. The input parameters are: $t, \Delta, \Gamma_L, \Gamma_R, T$. To choose the parameters in Fig. 4.3b(i), we fix the temperature to the measured value $T = 45\,\text{mK}$ and make the simplification $t = \Delta$, $\Gamma \equiv \Gamma_L = \Gamma_R$. This results in only two free parameters t, Γ, which we manually choose and compare with data. While oversimplified, this approach allows us to obtain a reasonable match between theory and data taken at $\mu_{LD} = \mu_{RD} = 0$ without the risk of overfitting. To obtain the other numerical curves shown in Fig. 4.3, we keep the same choice of t, Γ and vary $\mu_{LD}, \mu_{RD}, V_L, V_R$ along various paths in the parameter space. Similarly, to model the data shown in Fig. 4.9, we keep $T = 45\,\text{mK}$ and Γ the same as in Fig. 4.3. The free parameters to be chosen are thus t and Δ. The theory panels are obtained with the same t, Δ, and only $\mu_{LD}, \mu_{RD}, V_L, V_R$ are varied in accordance with the experimental conditions.

Finally, we comment on the physical meaning of the theory predictions in Fig. 4.4a-c. Tuning μ_{RD} leads to symmetric G_{LL} and asymmetric G_{RR}, as well as zero G_{LR} and finite G_{RL} with an alternating pattern of positive and negative values. As discussed in the main text, these features, also seen in the measurements, stem from the local charge of the system: keeping $\mu_{LD} = 0$ maintains zero local charge on the left dot, while varying μ_{RD} creates finite local charge on the right dot. The complementary picture appears when varying μ_{LD} in panel b. The asymmetry in both G_{LL} and G_{RR} and the negative nonlocal conductance when tuning simultaneously $\mu_{LD} = \mu_{RD}$ are also captured in the numerical simulation in panel c. We note that while there is a qualitative agreement between the features in Fig. 4.4c and Fig. 4.3e, they were obtained under nominally different conditions. As mentioned, the theoretical curve follows $\mu_{LD} = \mu_{RD}$, while the experimental curve was taken through a path along which V_{LD} changed twice as much as V_{RD}, although the lever arms of both QDs are similar. In Fig. 4.4c, we calculate the conductance along a path reproducing the experimental conditions. We speculate that the discrepancy between Fig. 4.3e and Fig. 4.4c could arise from some hybridization between the left QD and the superconducting segment as seen in Fig. 4.5.

4.7. Extended Data
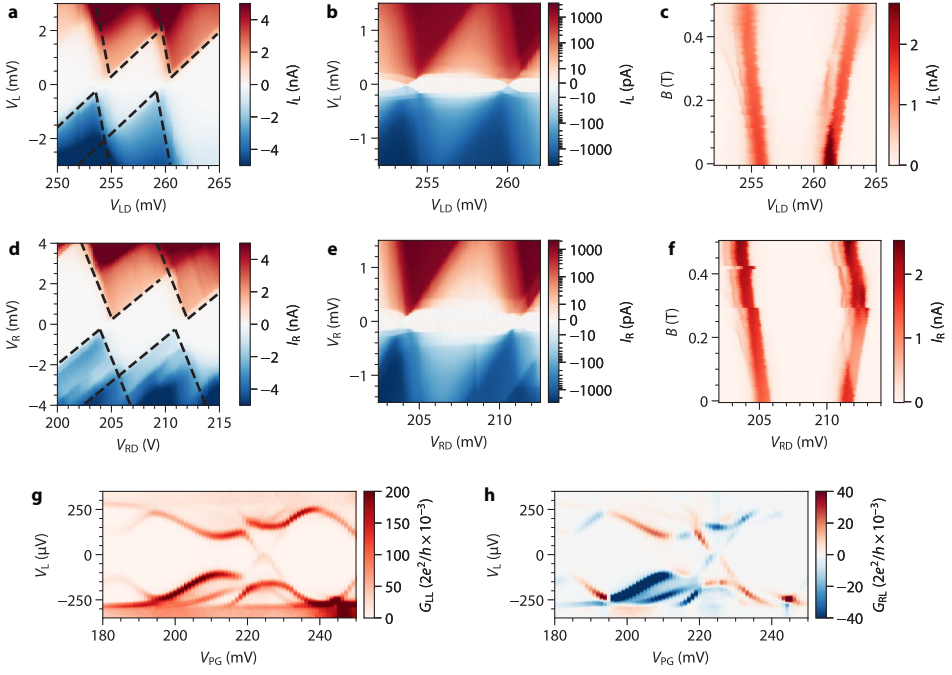
Figure 4.5: **Characterization of the QDs. a.** Coulomb blockade diamonds of the left QD when the right QD is off-resonance. I_L is measured as a function of V_L, V_{LD}. The data is overlaid with a constant interaction model (Kouwenhoven et al., 2001) with 1.8 meV charging energy and gate lever arm of 0.32. **b.** A high-resolution scan of **a** with a symmetric-logarithmic color scale to show the presence of a small amount of Andreev current at sub-gap energies. This is due to the left QD being weakly proximitized by local Andreev coupling to Al. **c.** Field dependence of the Coulomb resonances. I_L is measured as a function of V_{LD} and B with a constant $V_L = 600\,\mu V$. The resonances of opposite spin polarization evolve in opposite directions with a g-factor of ~ 35, translating to Zeeman energy of $400\,\mu eV$ at $B = 200\,mT$. **d-f.** Characterization of the right QD, as described in the captions of panels a-c. The overlaid model in **d** has charging energy 2.3 meV and gate lever arm of 0.33. No sub-gap transport is detectable in **e.** B dispersion in **f** corresponds to $g = 40$. **g, h.** Bias spectroscopy results of the proximitized InSb segment under the thin Al/Pt film. I_L, I_R are measured as a function of V_L, V_{PG}. G_{LL}, G_{RL} are obtained by taking the numerical derivative of I_L, I_R along the bias direction after applying a Savitzky-Golay filter of window length 15 and order 1. The sub-gap spectrum reveals discrete, gate-dispersing Andreev bound states. The presence of nonlocal conductance correlated with the sub-gap states shows that these Andreev bound states extend throughout the entire hybrid segment, coupling to both left and right N leads (Ménard et al., 2020). Parts of this dataset are also presented in Mazur et al. (2022) (Reproduced under the terms of the CC-BY Creative Commons Attribution 4.0 International license (https://creativecommons.org/licenses/by/4.0). Copyright 2022, The Authors, published by Wiley-VCH).
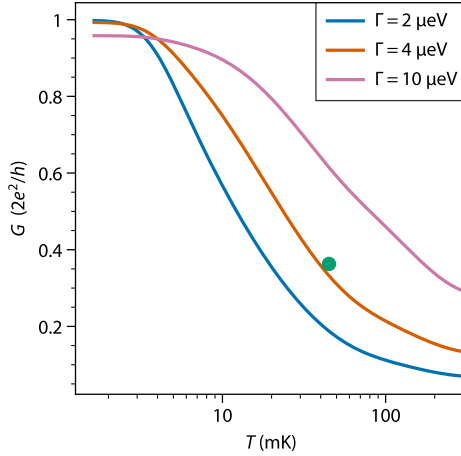
Figure 4.6: **Theoretical temperature dependence of the height of Majorana zero-bias conductance peaks.** The height of the Majorana zero-bias peaks is only quantized to $2e^2/h$ at zero temperature. At finite electron temperature T, the peak height is generally lower, with the exact value depending on T and tunnel broadening Γ_L, Γ_R due to coupling between QDs and N leads. The local zero-bias conductance G_{LL} at the sweet spot ($t = \Delta, \mu_{LD} = \mu_{RD} = 0$) is calculated and shown in this plot as a function of T, using the parameters presented in Fig. 4.3: $t = \Delta = 12\,\mu eV$. Three curves are calculated assuming three different values of tunnel coupling $\Gamma = \Gamma_L = \Gamma_R$. The orange curve assumes a Γ value that matches the experimentally observed peak width (both of the zero-bias peaks and of generic QD resonant peaks at other conductance features), showing that conductance approaching quantization would only be realized at electron temperatures $< 5\,\text{mK}$, unattainable in our dilution refrigerator. The blue curve, calculated with lower $\Gamma = 2\,\mu eV$, shows even lower conductance. Increasing Γ would not lead to conductance quantization either, since the zero-bias peaks would merge with the conductance peaks arising from the excited states (pink curve). The green dot marks the experimentally measured electron temperature and peak height (averaged between the values obtained on the left and right leads).
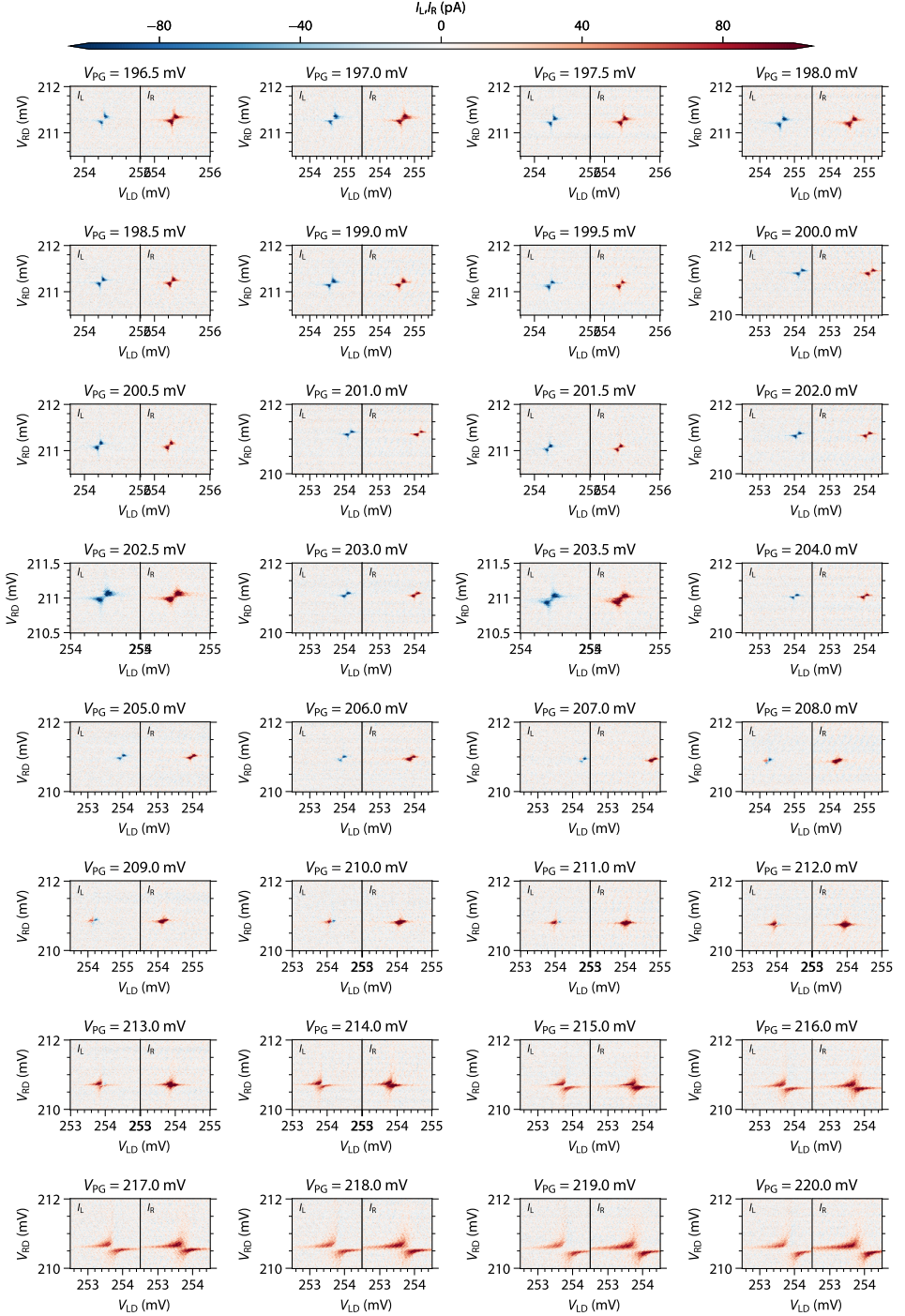
Figure 4.7: **Evolution of the charge stability diagram for the ↓↑ spin configuration.** Each panel shows I_L (nonlocal) and I_R (local) as functions of V_{LD}, V_{RD} measured under fixed biases $V_L = 0$, $V_R = 10\,\mu V$. V_{PG} is tuned from 196.5 mV, showing signatures of the $t > \Delta$ in both local and nonlocal currents, to 220 mV, featuring the opposite $t < \Delta$ regime.
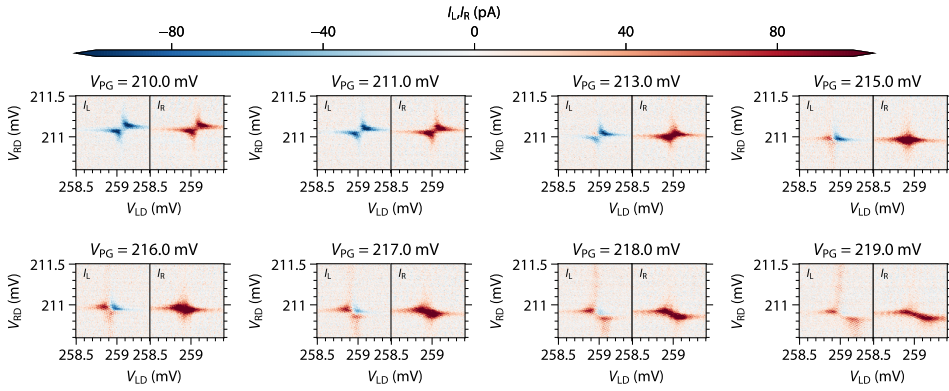
Figure 4.8: **Evolution of the charge stability diagram for the ↑↑ spin configuration.** Each panel shows I_L (nonlocal) and I_R (local) as functions of V_{LD}, V_{RD} measured under fixed biases $V_L = 0$, $V_R = 10\mu V$. V_{PG} is tuned from 210 mV, showing signatures of the $t > \Delta$ in both local and nonlocal currents, to 219 mV, featuring the opposite $t < \Delta$ regime.
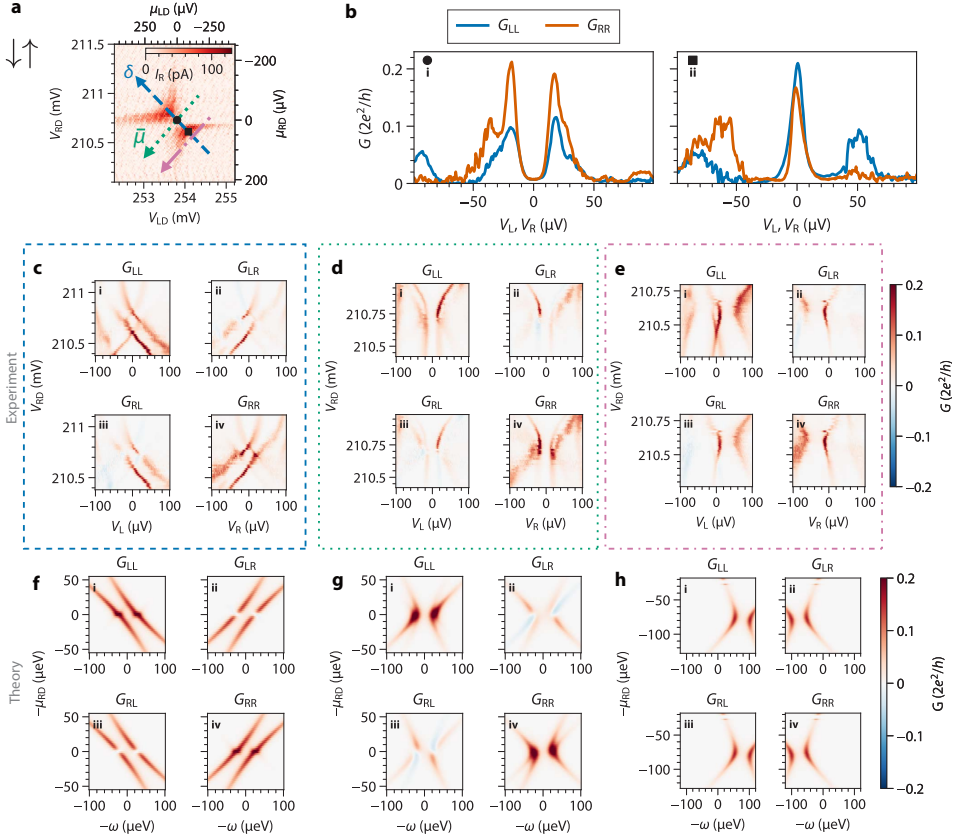
Figure 4.9: **Conductance spectroscopy when** $t < \Delta$. **a.** I_R vs μ_{LD}, μ_{RD} with $V_R = 10\mu V$. The evolution of the spectrum with the chemical potential is taken along the dashed, dashed-dotted and dotted lines in panels b,c,d, respectively. Data taken at the $\downarrow\uparrow$ spin configuration with fixed $V_{PG} = 218\,mV$. **b.** Local conductance spectroscopy taken at gate setpoints marked by corresponding symbols in panel a. Insets mark schematically the spectrum of the QDs in the absence (brown dots) and the presence (grey lines) of hybridization via CAR and ECT. **c.** Conductance matrix as a function of bias and V_{LD}, taken along the dashed blue line in panel a, i.e., varying the detuning between the QDs $\delta = (\mu_{LD} - \mu_{RD})/2$ while keeping the average chemical potential $\bar{\mu} = (\mu_{LD} + \mu_{RD})/2$ close to 0. **d.** Conductance matrix as a function of bias and V_{LD}, taken along the dotted green line in panel a, keeping the detuning between the QDs around 0. **e.** Conductance matrix as a function of bias and V_{LD}, taken along the dashed-dotted pink line in panel a, keeping roughly constant non-zero detuning between the QDs. **f, g, h.** Numerically calculated G as a function of energy ω and μ_{LD}, μ_{RD} along the paths shown in panel a. All of the numerical curves assume the same parameters as those in Fig. 4.3, except with $\Delta = 23\mu eV$ and $t = 6\mu eV$.
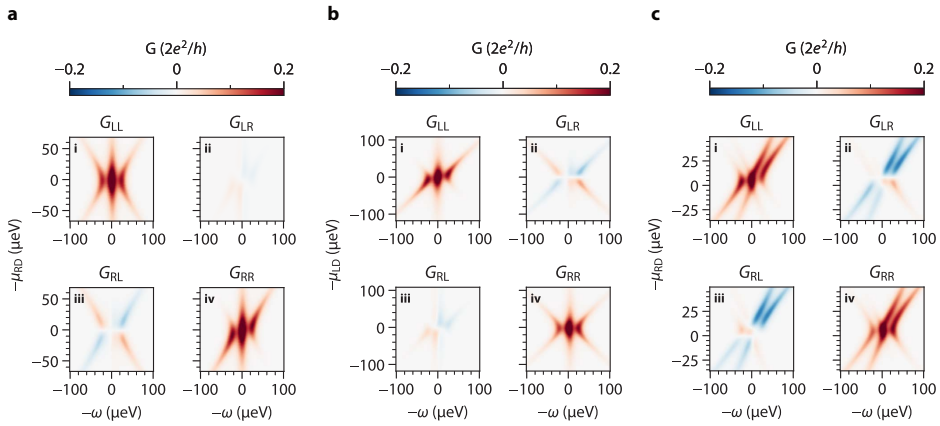
Figure 4.10: **Calculated conductance matrices at the $t = \Delta$ sweet spot a.** Numerically calculated G as a function of energy ω and μ_{LD}, μ_{RD} along the path shown in Fig. 4.3c. The presence of finite G_{LR} and asymmetric G_{RL} result from a slight deviation from the $\mu_{LD} = 0$ condition which is depicted in Fig. 4.4a. These features appear in the experimental data shown in Fig. 4.3c. **b.** Numerically calculated G as a function of energy ω and μ_{LD}, μ_{RD} along the path shown in Fig. 4.3d. The presence of finite G_{RL} and asymmetric G_{LR} result from a slight deviation from the $\mu_{RD} = 0$ condition which is depicted in Fig. 4.4b. These features appear in the experimental data shown in Fig. 4.3d. **c.** Numerically calculated G as a function of energy ω and μ_{LD}, μ_{RD} along the path shown in Fig. 4.3e. Since the path does not obey $\mu_{LD} = \mu_{RD}$, the calculated spectral lines do not follow parallel trajectories, in slight disagreement with the experimental data. The conversion from V_{LD}, V_{RD} to μ_{LD}, μ_{RD} is done as explained in the Methods section with the measured lever-arms of both QDs.

4
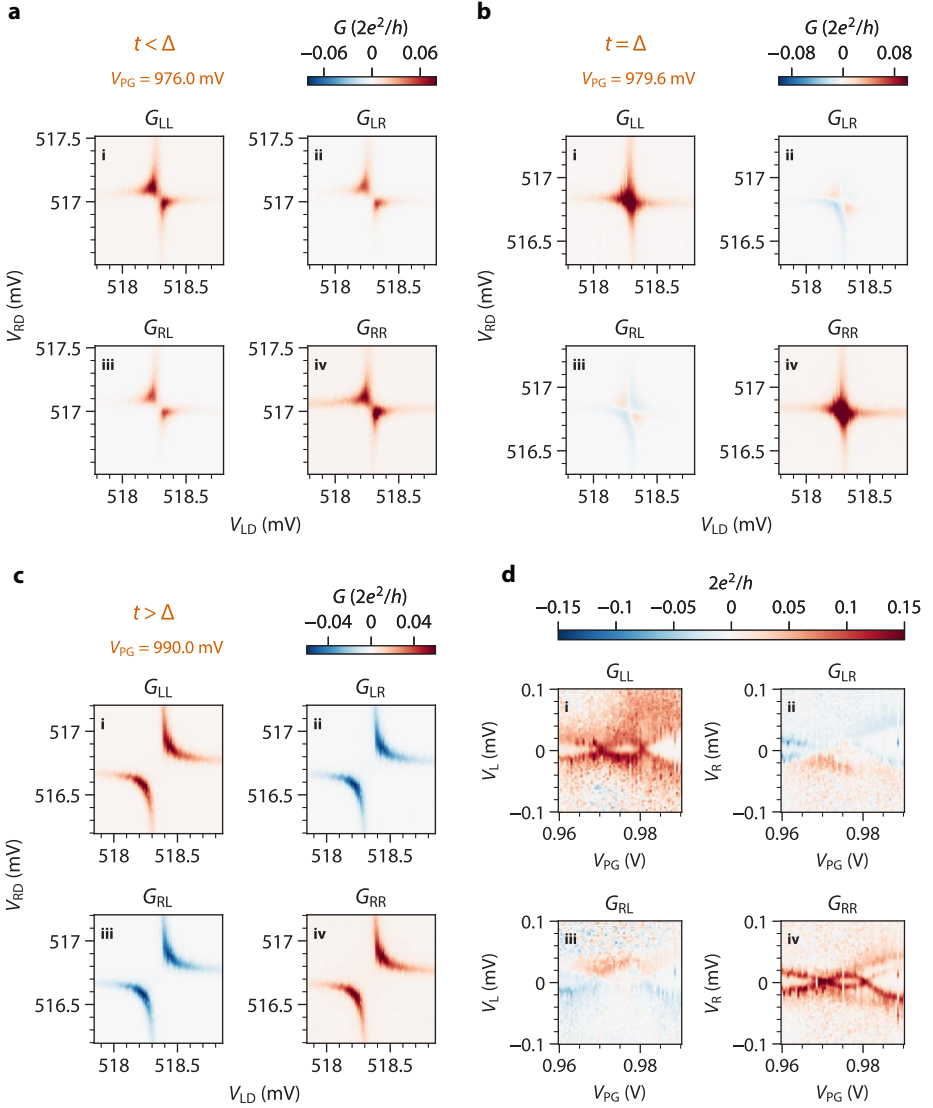
Figure 4.11: **Reproduction of the main results with Device B. a-c.** Conductance matrices measured at V_{PG} = (976, 979.6, 990) mV, respectively. **d.** Conductance matrix as a function of V_L, V_R and V_{PG} while keeping $\mu_{LD} \approx \mu_{RD} \approx 0$. This device shows two continuous crossovers from $t > \Delta$ to $t < \Delta$ and again to $t > \Delta$.
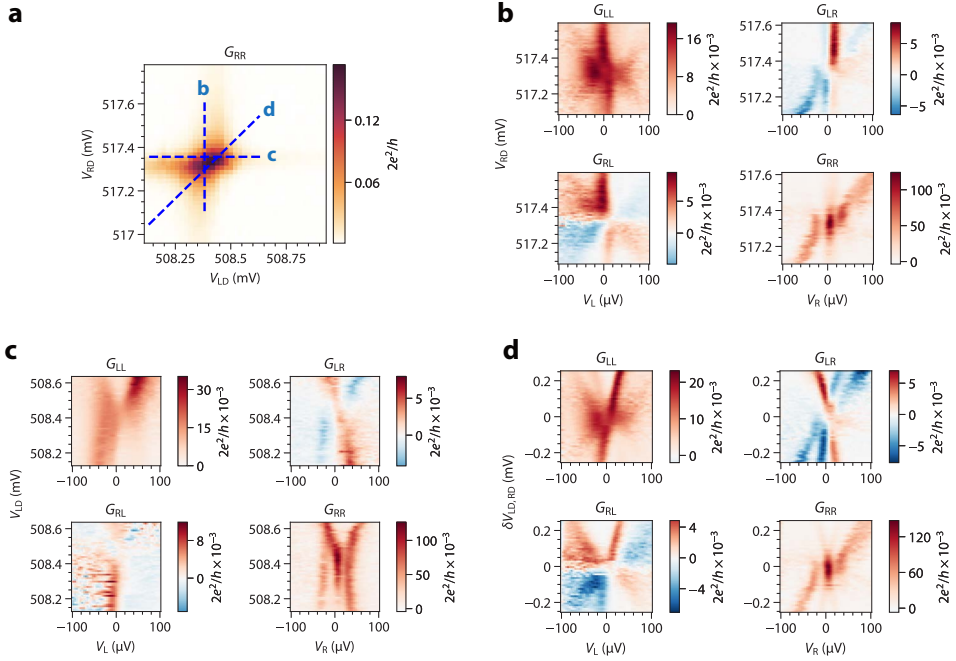
Figure 4.12: **Device B spectrum vs gates. a.** Charge stability diagram measured via G_{RR} of another $t = \Delta$ sweet spot of Device B, at $V_{PG} = 993\,$mV. Dashed lines mark the gate voltage paths the corresponding panels are taken along. **b-d.** Conductance matrices when varying V_{RD} (b), V_{LD} (c), and the two gates simultaneously (d), similar to Fig. 4.3 in the main text. The sticking zero-bias conductance peak feature when only one QD potential is varied around the sweet spot is clearly reproduced in G_{RR} of panel b. The quadratic peak splitting profile when both QD potentials are varied by the same amount is also reproduced in panel d. The left N contact of this device was broken and a distant lead belonging to another device on the same nanowire was used instead. This and gate jumps in V_{RD} complicate interpretation of other panels.
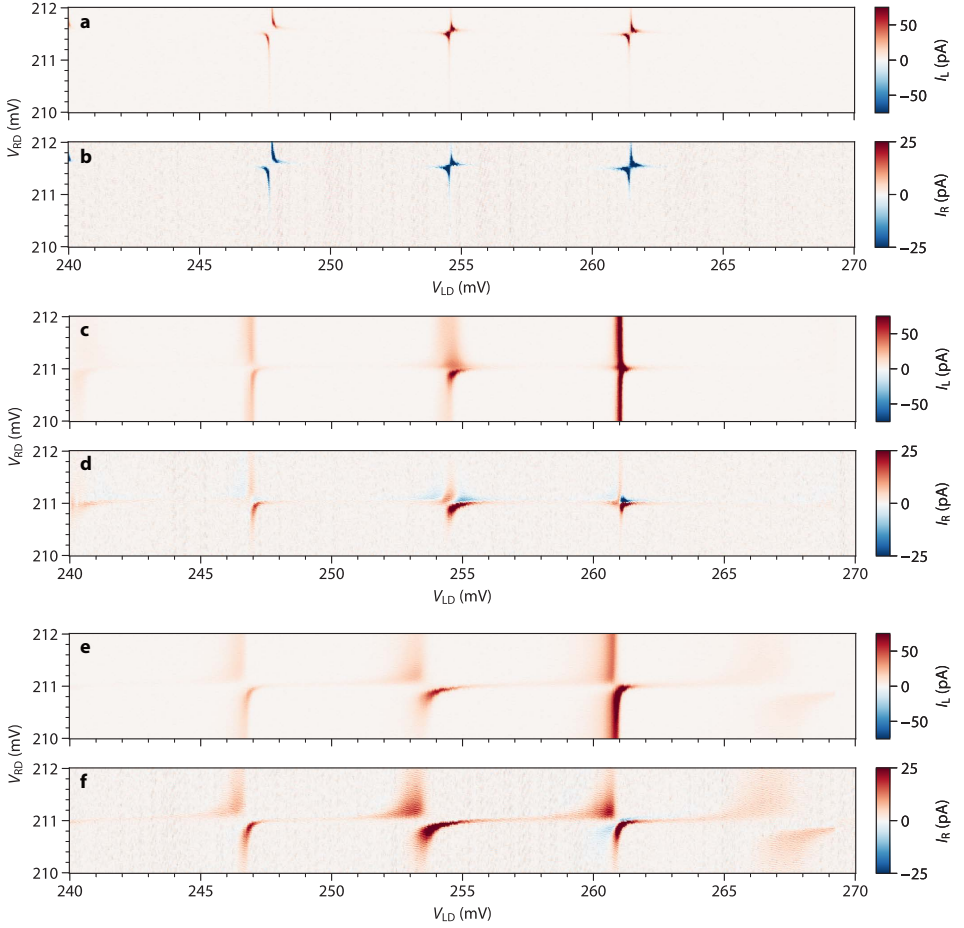
Figure 4.13: **CAR- and ECT-induced interactions across multiple QD resonances. a-b.** local (I_L) and nonlocal (I_R) currents as a function of V_{LD} and V_{RD} measured with $V_{PG} = 200\,\text{mV}$ and fixed V_L. All resonances show an ECT-dominated structure and a negative correlation between the local and the nonlocal currents. **c-d.** local (I_L) and nonlocal (I_R) currents as a function of V_{LD} and V_{RD} measured with $V_{PG} = 218\,\text{mV}$ and fixed V_L. Some resonances show the structure associated with the $t = \Delta$ sweet spot, showing both positive and negative correlations between the local and nonlocal currents. **e-f.** local (I_L) and nonlocal (I_R) currents as a function of V_{LD} and V_{RD} measured with $V_{PG} = 200\,\text{mV}$ and fixed V_L. All orbitals show a CAR-dominated structure and a positive correlation between the local and the nonlocal currents. All measurements were conducted with $V_L = 10\,\mu\text{V}$, $V_R = 0$ and $B = 100\,\text{mT}$.

4
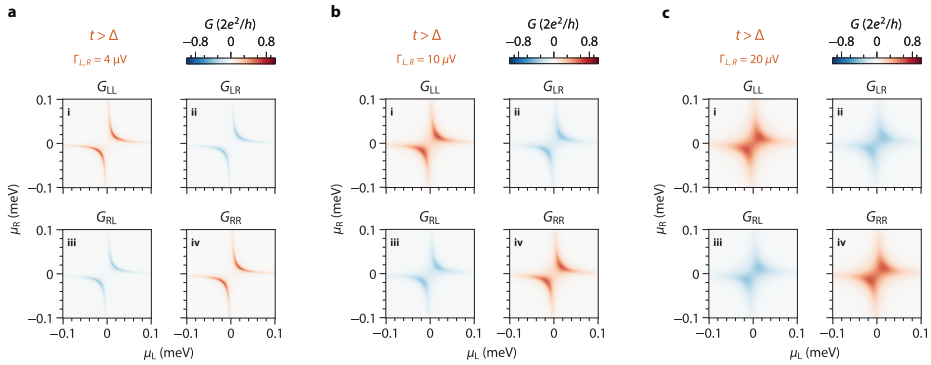
Figure 4.14: **Theoretical effect of tunnel broadening on the charge stability diagrams.** In some charge stability diagrams where level-repulsion is weak, e.g., Fig. 4.2a and Fig. 4.8, some residual conductance is visible even when $\mu_{LD} = \mu_{RD} = 0$. This creates the visual feature of the two conductance curves appearing to "touch" each other at the center. In the main text, we argued this is due to level broadening. Here, we plot the numerically simulated charge stability diagrams at zero temperature under various dot-lead tunnel coupling strengths. We use coupling strengths $t = 20\mu V, \Delta = 10\mu V$ as an example. From panel a to c, increasing the tunnel coupling and, thereby, level broadening reproduces this observed feature. When the level broadening is comparable to the excitation energy, $|t - \Delta|$, finite conductance can take place at zero bias. This feature is absent in, e.g., Fig. 4.2c, where $|t - \Delta|$ is greater than the level broadening.

5

CROSSED ANDREEV REFLECTION AND ELASTIC CO-TUNNELING IN THREE QUANTUM DOTS COUPLED BY SUPERCONDUCTORS

The formation of a topological superconducting phase in a quantum-dot-based Kitaev chain requires nearest neighbor crossed Andreev reflection and elastic co-tunneling. Here we report on a hybrid InSb nanowire in a three-site Kitaev chain geometry — the smallest system with well-defined bulk and edge — where two superconductor-semiconductor hybrids separate three quantum dots. We demonstrate pairwise crossed Andreev reflection and elastic co-tunneling between both pairs of neighboring dots and show sequential tunneling processes involving all three quantum dots. These results are the next step towards the realization of topological superconductivity in long Kitaev chain devices with many coupled quantum dots.

5.1. INTRODUCTION

The Kitaev chain was proposed over two decades ago as a platform that supports unique non-local excitations known as Majorana bound states (Kitaev, 2001). Proposals (Sau and Das Sarma, 2012; Leijnse and Flensberg, 2012a; Fulga et al., 2013) for the realization of such a Kitaev chain rely on creating an array of spin-polarized quantum dots (QDs) where neighboring QDs are coupled via two mechanisms: elastic co-tunneling (ECT) and crossed Andreev reflection (CAR). ECT involves the hopping of a single electron between two QDs. In CAR, two electrons from neighboring QDs simultaneously enter a superconductor to form a Cooper pair, or, in reversed order, two electrons forming a Cooper pair are split into two QDs (Recher et al., 2001; Lesovik et al., 2001; Sauret et al., 2004). Experiments have so far focused on chains consisting of two QDs, showing both CAR and ECT in such systems (Hofstetter et al., 2009, 2011; Herrmann et al., 2010; Wei and Chandrasekhar, 2010; Das et al., 2012; Schindele et al., 2012, 2014; Tan et al., 2015; Gramich et al., 2017; Baba et al., 2018; Scherübl et al., 2020; Ranni et al., 2021; G. Wang et al., 2022a; Q. Wang et al., 2023) and even strongly coupling the QDs to form a minimal Kitaev chain (Dvir et al., 2023). Longer QD chains, necessary for the formation of a topological phase, have so far not been realized.

In this work, we report on the fabrication of a three-site device and its characterization at zero magnetic field, where no isolated Majorana states are expected, but all the elements of a Kitaev chain Hamiltonian can already be tested. We show CAR and ECT between each pair of neighboring QDs and show that transport across the entire device is possible through sequential events of CAR and ECT. By measuring the currents on all of the terminals of our device, we identify all the possible CAR and ECT combinations.

5.2. DEVICE STRUCTURE

In Fig. 5.1a we show a scanning electron micrograph of device A. This device consists of an InSb nanowire placed on top of an array of 11 finger gates separated by a thin dielectric. Two superconducting Al contacts (marked S_1 and S_2) are evaporated on top of the nanowire using the shadow-wall lithography technique (Heedt et al., 2021; Mazur et al., 2022). Both sides of the device are further contacted by two normal Cr/Au probes (marked N_L and N_R). Every contact is connected to an independent voltage source (V_L, V_{S1}, V_{S2}, V_R) and current meter (I_L, I_{S1}, I_{S2}, I_R). The two finger gates underneath the semiconductor-superconductor hybrid segments control their chemical potential, while the other 9 gates form QDs on each of the three bare InSb sections. The QD chemical potentials μ_1, μ_2 and μ_3, are controlled by the gate voltages V_{QD1}, V_{QD2} and V_{QD3} respectively (Fig. 5.1b). See Supplementary Information for further nanofabrication details and gate settings.

5.3. RESULTS

5.3.1. DEVICE CHARACTERIZATION

Discrete Andreev bound states (ABSs) in a hybrid semiconductor-superconductor segment, separating two QDs, can efficiently mediate CAR and ECT between them (Fülöp
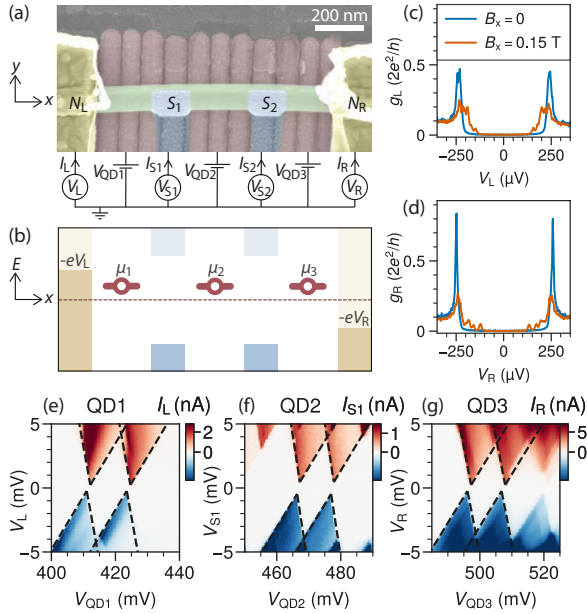
Figure 5.1: **a.** False-colored scanning electron micrograph of the device. An InSb nanowire (green) is deposited on top of 11 finger gates (red) and it is contacted with two superconducting leads S_1 and S_2 (blue) and two normal leads N_L and N_R (yellow). Every contact is connected to a corresponding voltage bias source and current meter. **b.** Illustrative energy diagram. Brown symbols represent QD energy levels when occupied by an electron. **c., d.** Spectroscopy of the hybrid segments. $g_L \equiv \frac{dI_L}{dV_L}$ and $g_R \equiv \frac{dI_R}{dV_R}$ are obtained by numerical differentiation of the DC currents measured from the left and the right normal leads respectively. Gate settings are reported in Supplementary Information (Fig. 5.7, 5.8 and 5.9). **e., f., g.** Coulomb diamond characterization of QD_1 (panel e), QD_2 (panel f), QD_3 (panel g). Fitting to a constant interaction model (Hanson et al., 2007) yields charging energies of 4, 3.5, 3.3 mV and lever arms of 0.32, 0.33, 0.31 for QD_1, QD_2, and QD_3 respectively.

et al., 2015; Liu et al., 2022; Bordin et al., 2023). We find such discrete states by controlling the two finger gates underneath contacts S_1 and S_2. Figs. 5.1c and 5.1d show the spectra measured on the first and the second hybrid respectively, by using the finger gates separating the superconducting and normal contacts as tunneling barriers (van Driel et al., 2023). In the absence of an external magnetic field, both hybrid segments show a hard superconducting gap. A closer inspection of the gate dependence (see Fig. 5.8) shows that ABSs are present at energies close to the energy gap. At 150 mT, the ABSs are more visible in the spectrum. The remainder of the experiment was conducted at zero magnetic field and at fixed values of the hybrid gates.

In Figs. 5.1e-g we characterize QDs 1-3 respectively. QD_1 is characterized by applying a voltage bias to N_L and measuring the corresponding current while keeping all other contacts grounded. For QD_2 the voltage bias is applied to S_1 and for QD_3 to N_R. During the characterization of a given QD, the other QDs are kept off-resonance. The observed Coulomb diamond structure allows us to estimate the charging energy of all QDs to be between 3 and 4 mV and the lever arm of the underlying gates to be ≈ 0.3. We note the presence of a superconducting gap in the spectrum.

5.3.2. PAIRWISE CAR AND ECT BETWEEN NEIGHBORING QDS
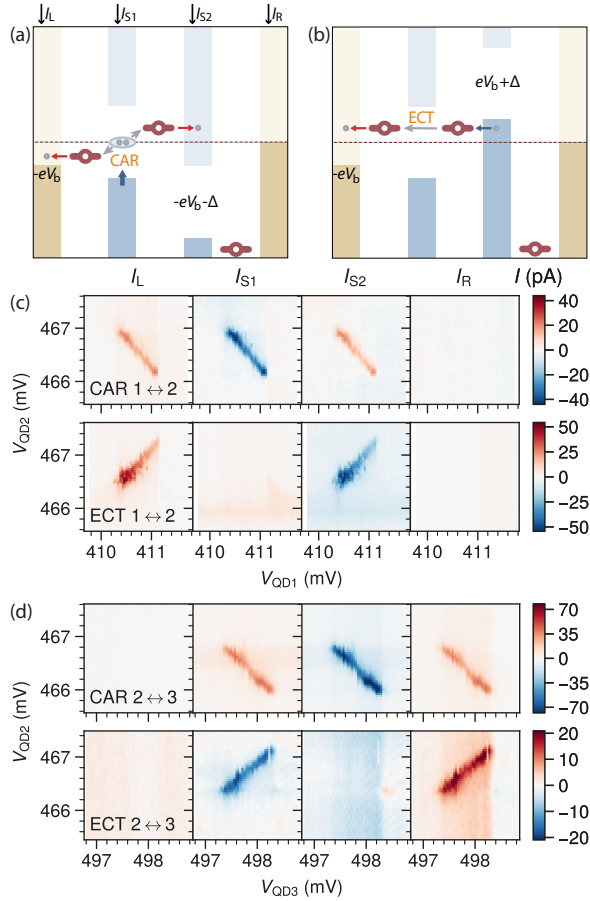
Figure 5.2: **a., b.** Schematic diagrams of CAR and ECT processes between QD_1 and QD_2. CAR is measured by applying V_b on N_L and $V_b + \Delta/e$ on S_2 (panel a). ECT is measured by applying V_b on N_L and $-V_b - \Delta/e$ on S_2 (panel b). **c.** CAR and ECT between QD_1 and QD_2. The currents I_L, I_{S1}, I_{S2}, and I_R are measured as a function of V_{QD1} and V_{QD2}. $V_L = V_b = 150\,\mu V$, while $V_{S2} = V_b + \Delta/e = 380\,\mu V$ (top row) or $V_{S2} = -380\,\mu V$ (bottom row). **d.** CAR and ECT between QD_2 and QD_3. The currents through the leads as a function of V_{QD2} and V_{QD3} are measured with $V_{S1} = 380\,\mu V$ in the top row and $V_{S1} = -380\,\mu V$ in the bottom row, while $V_R = 150\,\mu V$.

We begin by demonstrating CAR and ECT processes between pairs of neighboring QDs. Fig. 5.2a shows schematically how CAR between QD_1 and QD_2 is measured while QD_3 is kept off-resonance such that it does not participate in the transport. CAR involves current flowing from a superconductor into the neighboring leads (or vice-versa). In recent works, CAR was measured setting symmetric voltage biases, V_b, on two normal leads on both sides of the hybrid segment (Wang et al., 2022a; Bordin et al., 2023; Wang et al., 2023). Here, to account for the presence of the superconducting gap in S_2 ($\Delta \approx$ 230 μeV), we apply a bias of $V_b + \Delta/e$ to the superconducting leads. In this configuration, CAR can be sustained as long as $\mu_1 = -\mu_2$ and the two chemical potentials are in the bias

window $-|eV_b| < \mu_1, \mu_2 < |eV_b|$ (Wang et al., 2022a). ECT can be measured in an anti-symmetric bias configuration. Due to the presence of the superconducting gap, such a configuration similarly requires adding Δ to the bias on S_2, as shown schematically in Fig. 5.2b.

Fig. 5.2c shows the currents through all leads measured in the bias configuration that allows for CAR (top row) and ECT (bottom row) as a function of V_{QD1} and V_{QD2}. In the top row, we find that the currents I_L, I_{S1}, and I_{S2} are largest along a diagonal line consistent with $\mu_1 = -\mu_2$. Moreover, I_L and I_{S2} are positive and nearly equal, draining to the ground only through S_1. These observations signal the presence of CAR between QD_1 and QD_2. The bottom row is measured in a bias configuration that supports ECT. The measurements show finite I_L and I_{S2} currents with maxima along a diagonal compatible with $\mu_1 = \mu_2$. In this case, I_L and I_{S2} have opposite signs, and almost no current flows through S_1, signaling the presence of ECT.

Analogously, we measure CAR (and ECT) signatures between QD_2 and QD_3 by applying effectively symmetric (and antisymmetric) biases V_{S1} and V_R (Fig. 5.2d). We also notice finite currents $< 10\,\mathrm{pA}$ that depend only on the value of V_{QD3}. We interpret this as a sign of local Andreev reflection (LAR) not being completely suppressed by the charging energy of QD_3 (see also Fig. 5.9).

The results shown in Fig. 5.2 demonstrate both CAR and ECT — the crucial ingredients of a Kitaev chain — between every pair of QDs. We exploited here the freedom to bias each superconductor independently. This freedom might not always be accessible, e.g., in a Kitaev chain design with the superconductors connected in a loop. In the following, we discuss the signatures of CAR and ECT when both superconducting leads are grounded.

5.3.3. TWO-TERMINAL CAR AND ECT PROCESSES

We set $V_{S1} = V_{S2} = 0$, and begin by discussing CAR and ECT processes between QD_2 and QD_3 while keeping QD_1 off-resonance. We observe three transport mechanisms involving only leads S_2 and N_R.
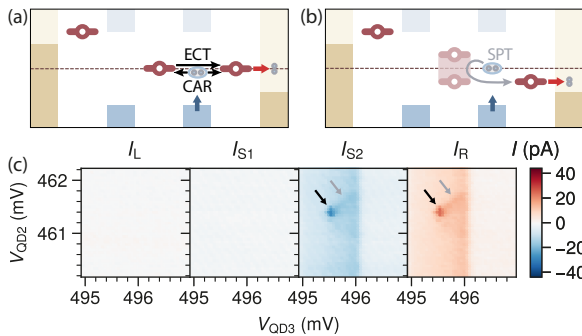
Figure 5.3: **a.** Schematic illustration of the resonant CAR and ECT tunneling. When $\mu_2 = \mu_3 = 0$ both CAR and ECT are allowed between QD_2 and QD_3, allowing a complete transport cycle to transfer a Cooper pair between N_R and S_2. **b.** Schematic illustration of the Shiba-assisted local pair tunneling (SPT). **c.** Current through the device as a function of V_{QD2} and V_{QD3}, with $V_{QD1} = 414.1\,\mathrm{mV}$, equivalent to $\mu_1 \approx 230\,\mu\mathrm{eV}$.

The first transport mechanism, already mentioned above, is LAR, which gives rise to a signal that depends only on the chemical potential of QD_3.

The second transport mechanism takes place when $\mu_2 = \mu_3 = eV_{S2} = 0$, as depicted in Fig. 5.3a. In this alignment, both CAR and ECT are allowed. A Cooper pair can be transmitted from S_2 to N_R by sequential CAR and ECT processes. First, a Cooper pair is split from S_2 to QD_2 and QD_3. Then, the electron in QD_3 is drained to N_R, allowing ECT to shuttle the other electron from QD_2 to QD_3, which is finally drained as well. Because of the resonant condition on the chemical potentials, this process appears as a single spot in the measurements shown in Fig. 5.3c (black arrow).

When $\mu_2 \neq 0$, the resonant CAR-ECT process is not allowed anymore; however, a third transport mechanism can be observed. The grey arrow in Fig. 5.3c highlights a faint line showing local transport from S_2 to N_R that is enhanced by QD_2 alignment. We observe current flow when μ_3 is between 0 and $-eV_R$ and the chemical potentials of QD_2 and QD_3 are either aligned or anti-aligned. Following literature, this process may be interpreted as "Shiba-assisted local pair tunneling" (SPT) (Scherübl et al., 2020, 2022), which is depicted schematically in Fig. 5.3b. Further details of such process and additional data are discussed in Supplementary Information (Fig. 5.11).

5.3.4. THREE-DOT SEQUENTIAL CAR AND ECT
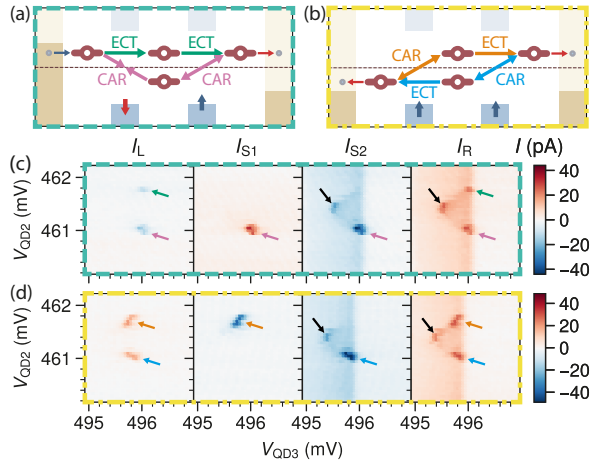
Figure 5.4: **a.** Schematic illustration of sequential ECT processes (with $\mu_1 = \mu_2 = \mu_3$, green) and sequential CAR processes (with $\mu_1 = -\mu_2 = \mu_3$, pink). **b.** Schematic illustration of CAR followed by ECT (with $-\mu_1 = \mu_2 = \mu_3$, orange) and ECT followed by CAR (with $\mu_1 = \mu_2 = -\mu_3$, blue). **c.** Current through the device as a function of V_{QD2} and V_{QD3}, with $V_R = -V_L = 150\,\mu V$ and $V_{QD1} = 413.8\,mV$, equivalent to $\mu_1 \approx 130\,\mu eV$. **d.** Current through the device as a function of V_{QD2} and V_{QD3}, with $V_R = V_L = 150\,\mu V$ and $V_{QD1} = 413\,mV$, equivalent to $\mu_1 \approx -100\,\mu eV$. Note that the arrow colors in panels c and d correspond to the process colors in panels a and b, while the black arrow corresponds to the resonant CAR and ECT process shown in Fig. 5.3a,c.

When setting $|\mu_1| < |eV_L|$, QD_1 can participate in transport, enabling sequential CAR and ECT processes involving all three QDs. Fig. 5.4a shows schematically such processes with antisymmetric bias settings ($V_L = -V_R$). In this configuration, electrons incoming from N_L can be transferred all the way to N_R, in two ways. Sequential ECT events (green

arrows) can first transfer an electron from QD_1 to QD_2 and then from QD_2 to QD_3, provided that the QD chemical potentials are all aligned ($\mu_1 = \mu_2 = \mu_3$). Alternatively, if the QD chemical potentials are anti-aligned ($\mu_1 = -\mu_2 = \mu_3$), sequential CAR events can first form a Cooper pair into S_1 and then split a Cooper pair from S_2, resulting in a net transfer of one electron from QD_1 to QD_3 (pink arrows). Equivalently, this sequential CAR process can be seen as an electron from QD_1 being converted into a hole in QD_2 and converted back to an electron into QD_3.

Fig. 5.4c shows measured currents as a function of V_{QD2} and V_{QD3} for fixed $V_R = -V_L$. We observe both the two-QD processes discussed above (see black arrows) and the three-QD processes discussed here. Sequential ECT processes appear as a single spot in only I_L and I_R, when μ_2 and μ_3 are aligned with μ_1 (marked by the green arrow). The sequence involving two CAR processes (marked by the pink arrow) appears as a spot in the currents measured on all leads when $\mu_3 = \mu_1$ and $\mu_2 = -\mu_1$. The currents alter in sign at every lead, corresponding to Cooper pair formation in S_1 followed by Cooper pair splitting in S_2. We note that also the amount of measured current is consistent with CAR, showing in the superconducting leads twice the amount of current registered in the normal leads.

Under symmetric bias conditions, current is sustained when both leads N_L and N_R drain electrons (see Fig. 5.4b). The two sequences involving all QDs in agreement with this condition are CAR followed by ECT and the opposite, ECT followed by CAR. The first, marked by the orange arrow in Fig. 5.4d, it is seen in the current appearing when $\mu_3 \approx \mu_2 \approx -\mu_1$ in I_L and I_R. This feature further appears in I_{S1} but not in I_{S2}, since CAR between QD_1 and QD_2 drains current to the ground through S_1, whereas ECT between QD_2 and QD_3 drains no such current to ground via S_2. The opposite sequence, marked by the blue arrow, takes place with $\mu_3 \approx -\mu_2 \approx -\mu_1$ and shows similar behavior. We emphasize that this coupling between all three sites gives rise to a non-local transport feature. For example, we observe in Fig. 5.4c,d that I_L is strongly modulated by QD_3, two sites away.
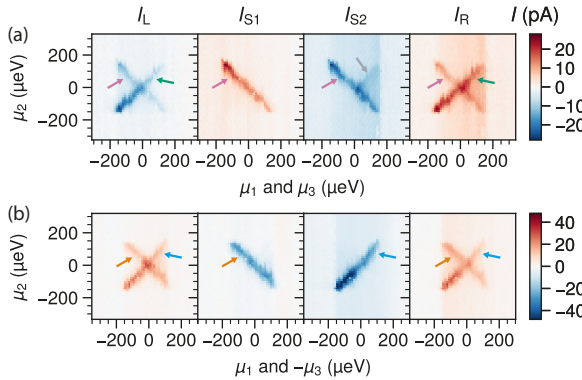
Figure 5.5: **a.** Current through the device as a function of μ_2 and jointly μ_1 and μ_3, which are set to equal values, measured with antisymmetric bias configuration. **b.** Current through the device as a function of μ_2 and jointly μ_1 and μ_3, which are set to opposite values, measured with symmetric bias configuration. Note that the color of the arrows corresponds to the color of the processes in Fig. 5.4 (and 5.3 for the grey arrow).

These observations are consistent with CAR and ECT in the energy alignment of the QDs, in the signs, and in the amounts of the measured currents, for every voltage bias combination (see additional data in the linked repository). So far, we have shown CAR and ECT signatures from two different points of view: pairwise in Fig. 5.2 and sequential at fixed QD_1 in Fig. 5.4. In Fig. 5.5, we add a third one, noticing that both sequential ECT processes and sequential CAR processes always require $\mu_1 = \mu_3$, whereas CAR followed by ECT and ECT followed by CAR require $\mu_1 = -\mu_3$. In Fig. 5.5, we measure the currents through the devices while tuning the QDs to follow these constraints. Fig. 5.5a was measured by setting $V_R = -V_L = 150\mu V$. V_{QD1} and V_{QD3} were swept together, imposing $\mu_1 = \mu_3$ for the full measurement (see Fig. 5.10 in Supplementary Information for details regarding the tuning of chemical potential). Fig. 5.5a features two diagonal lines. The positive-slope diagonal, compatible with $\mu_1 = \mu_2 = \mu_3$, is prominent in panels I_L and I_R only, allowing us to attribute it to sequential ECT processes. The negative-slope diagonal, compatible with $\mu_1 = -\mu_2 = \mu_3$, appears in all panels and is associated with sequential CAR processes. The measurements in Fig. 5.5b were conducted with $V_R = V_L = 150\mu V$. Here, V_{QD1} and V_{QD3} are varied together, while imposing $\mu_1 = -\mu_3$. Similarly to the previous scenario, measured currents feature a positive-slope diagonal alongside a negative-slope one. Here, the positive-slope diagonal involves I_{S2} as expected for ECT followed by CAR. The negative-slope diagonal involves I_{S1} instead, as required by CAR followed by ECT.

In summary, the results of Fig. 5.4 and 5.5 show how all four possible compositions of CAR and ECT mediate transport through the entire device.

5.4. CONCLUSION

We have fabricated and measured an InSb-Al device with three QDs separated by semiconductor-superconductor hybrids, showing the signatures of CAR and ECT between all pairs of neighboring QDs. We have further demonstrated control over sequential CAR and ECT processes involving all QDs by tuning the biases applied to the normal leads and the chemical potential of the QDs. Our measurements demonstrate the operation of all the known requirements to extend the Kitaev chain physics to longer multi-site chains. To enable the formation of a three-site Kitaev chain in such devices, future work will focus on fine-tuning the interdot couplings at a finite magnetic field to balance the pairwise CAR and ECT ratios to observe the emergence of Majorana Bound States at the chain ends. Finally, we note that the scope of the experiments presented here further demonstrates a general platform enabling long-range entanglement in condensed matter systems (Choi et al., 2000; Recher et al., 2001). For instance, we note that three sequential CAR events involving four QDs realize a simple entanglement swapping scheme (Bennett et al., 1993; Żukowski et al., 1993).

AUTHOR CONTRIBUTIONS

AB, XL, JCW, and DvD fabricated the devices. AB and XL performed the electrical measurements with help from QW and SLDtH. AB and TD designed the experiment and analyzed the data. TD and LPK supervised the project. AB, TD, and LPK prepared the manuscript with input from all authors.

DATA AVAILABILITY

All raw data in the publication and the analysis code used to generate figures are available at https://doi.org/10.5281/zenodo.8021184. In the same repository, we share in addition a complete dataset of three-dimensional current measurements as a function of V_{QD1}, V_{QD2} and V_{QD3} for all combinations of symmetric and anti-symmetric biases ($V_b = \pm V_L = \pm V_R$). We share a similar dataset for a second device as well (see also Fig. 5.12 in Supplementary Information). We include GIF animations for better visualization.

5

5.5. SUPPLEMENTARY INFORMATION

5.5.1. NANOFABRICATION DETAILS

The device is fabricated by depositing an InSb nanowire with a micromanipulator on top of a keyboard of 11 pre-patterned Ti/Pd gates. Nanowire and gates are separated by a double-layer dielectric deposited with ALD: 10 nm of Al_2O_3 followed by 10 nm of HfO_2. Two superconducting Al contacts S_1 and S_2 are deposited with the shadow-wall lithography technique (Heedt et al., 2021). The Al is deposited at a temperature of 140 K and a rate of 0.05 Å/s, alternating the deposition angle between 45° and 15° with respect to the substrate. This produces a uniform Al coating, 9 nm thick, on three over six facets of the nanowire, which has a hexagonal cross-section (Badawy et al., 2019). Without breaking the vacuum, the Al is covered by 7 nm of Al_2O_3. Finally, two normal Cr/Au contacts N_L and N_R are deposited at the two edges of the nanowire. Prior to Al deposition, the native nanowire oxide is removed with a gentle H cleaning (Heedt et al., 2021); prior to Cr/Au deposition, the oxide is removed with Ar milling.

5.5.2. SETUP DISCUSSION
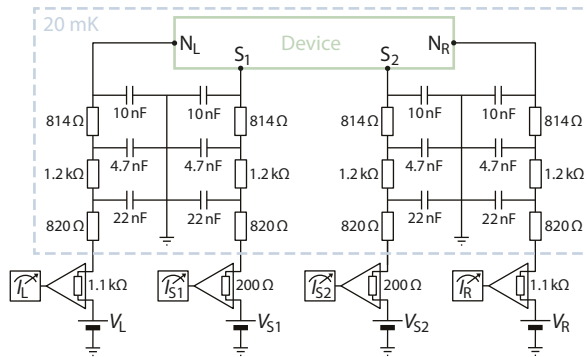
Figure 5.6: Illustrative diagram of the measurement circuit. The total series resistance ($R_s \approx 4\,k\Omega$ for the normal lead lines and $R_s \approx 3\,k\Omega$ for the superconducting ones) is small compared to the typical device resistance ($R_{QD} \sim 1\,M\Omega$, see Fig. 5.9).

Electrical transport measurements are carried out in a dry dilution refrigerator with a base temperature of 20 mK, and electron temperature of ≈ 25 mK measured with a metallic N-S tunnel junction thermometer. Electrical lines are filtered at the mixing chamber plate with low-pass RC-filters (< 40 MHz, see Fig. 5.6), low-pass π-filters (< 100 MHz to < 1 GHz) and low-pass Cu-powder-filters (< 1 GHz). More details can be found in de Moor (2019, chapter 3)

As pointed out in the main text, every contact of the four-terminal device is connected to an independent voltage source (V_L, V_{S1}, V_{S2}, V_R) and current meter (I_L, I_{S1}, I_{S2}, I_R). Due to Kirchoff's law, a minimal setup requires only 3 voltage differences and 3 current meters. We choose to set up 4 for symmetry reasons. Moreover, such a redundant setup allows checking that the sum of all currents is compatible with the noise floor, ruling out potential leakage currents to the gates.

Through the main text, the voltage biases on the normal leads are set to $\pm V_b = \pm 150\,\mu V$. This value is smaller than the energy of the lowest ABS and large enough to have an appreciable bias window $|eV_b|$ for the QD chemical potentials.

Finger gate settings

We denote the voltages applied to the 11 finger gates with V_{1L}, V_{QD1}, V_{1R}, V_{H1}, V_{2L}, V_{QD2}, V_{2R}, V_{H2}, V_{3L}, V_{QD3}, V_{3R} from left to right. We set the hybrid gates V_{H1} and V_{H2} such that both hybrids hold Andreev bound states (ABSs). Fig. 5.7 shows bias spectroscopy of the two hybrids at $B_x = 0.2\,T$ (x is the direction along the length of the nanowire), where ABSs are easier to see due to their high g-factor ~ 20 (Wang et al., 2022a). ABSs appear for $V_{H1} > 0.3\,V$ and for $V_{H2} > 0.2\,V$.
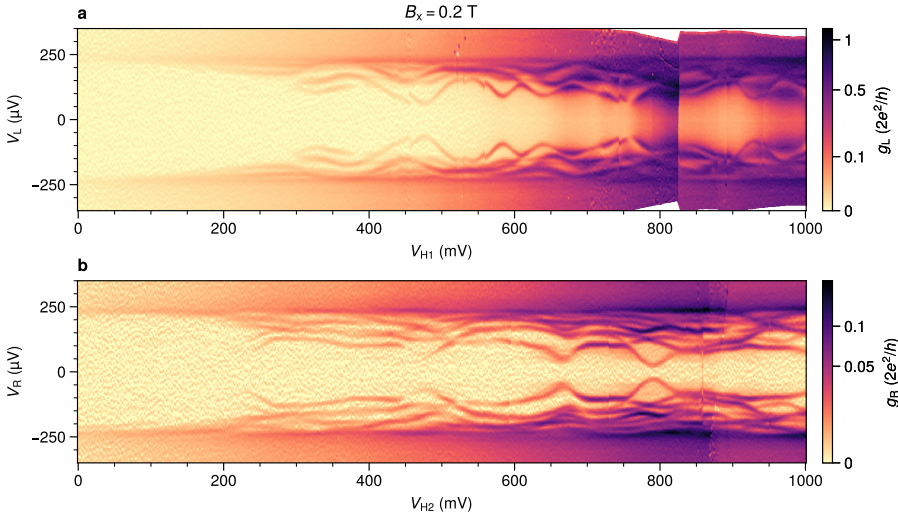
Figure 5.7: **a.** Tunneling spectroscopy of the first hybrid as a function of V_{H1}. **b.** Tunneling spectroscopy of the second hybrid as a function of V_{H2}. For both panels, $B_x = 0.2\,T$, $V_{1L} = V_{QD1} = 0.5\,V$, $V_{1R} = -0.15\,V$, $V_{2L} = V_{QD2} = V_{2R} = 0$, $V_{3L} \approx -0.1\,V$, $V_{QD3} = V_{3R} = 0.5\,V$. $g_L \equiv \frac{dI_L}{dV_L}$ and $g_R \equiv \frac{dI_R}{dV_R}$ are calculated by taking the numerical derivative after applying a Savitzky-Golay filter of window length 3 and polynomial order 1. V_L, V_R, g_L, g_R take into account a series resistance $R_s = 7\,k\Omega$ due to the dilution refrigerator lines and measurement electronics.
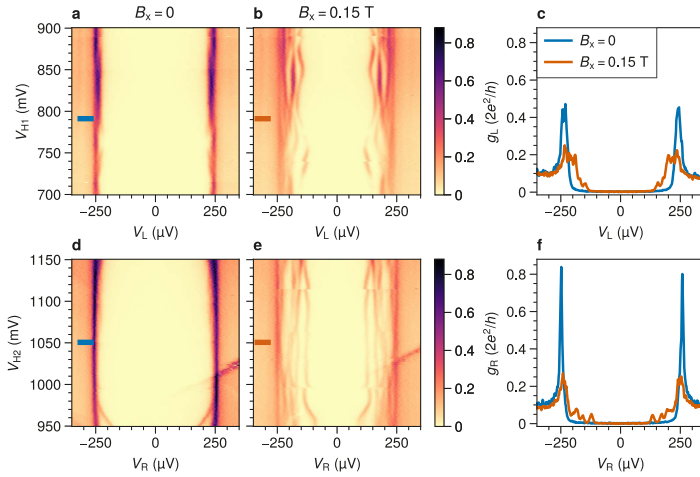
Figure 5.8: a., b., c. Tunneling spectroscopy of the first hybrid. We fix $V_{H1} = 0.79$ V for all other figures (with small changes within 0.05 V, see the linked repository for further details). **d., e., f.** Tunneling spectroscopy of the second hybrid. $V_{H2} = 1.05$ V for all other figures. In all panels, $V_{1L} = 0.5$ V, $V_{QD1} = 0.4$ V, $V_{1R} = -0.14$ V, $V_{2L} = -0.02$ V, $V_{QD2} = 0.472$ V, $V_{2R} = -0.015$ V, $V_{3L} = -0.055$ V, $V_{QD3} = 0.49$ V, $V_{3R} = 0.5$ V. g_L and g_R are calculated by taking the numerical derivative after applying a Savitzky-Golay filter of window length 3 and polynomial order 1. V_L, V_R, g_L, g_R take into account a series resistance $R_s = 7$ kΩ. Panels **c.** and **f.** report the same data of Fig. 5.1c,d.

Since ECT followed by local Andreev reflection can mimic CAR (Schindele et al., 2014), we set the gates in order to minimize local Andreev reflection while keeping a detectable CAR signal. In order to do so, the hybrid gates are fine-tuned to the values of Fig. 5.8, where both ECT and CAR signals are strong (see Fig. 5.2 in the main text), while the tunneling barriers defining the quantum dots are kept as high as possible in order to suppress local Andreev reflection. Typical barrier gate voltages are reported in Fig. 5.9. Numbers might vary a little from Fig. to Fig. (within 0.01 V), all values are available in the linked repository.
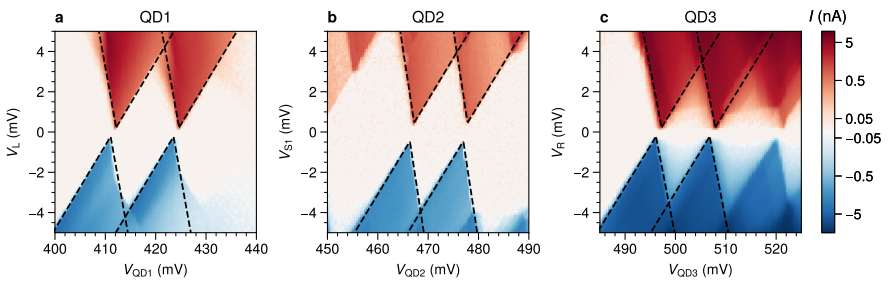
Figure 5.9: a., b., c. Coulomb diamonds for QDs 1-3. It is the same data reported in the main text in Fig. 5.1e-g but with a logarithmic colorbar scale in order to visualize small currents inside the Coulomb-blockaded regions. A linear interpolation between −0.03 and +0.03 avoids the logarithm divergence for small values. All Coulomb diamonds are very sharp, a signature of high tunneling barriers. Only QD$_3$, the QD where we measured the strongest local Andreev reflection current, shows some current leaking inside the Coulomb blockade diamond. Tunneling gates are set to $V_{1L} = -0.123$ V, $V_{1R} = -0.14$ V, $V_{2L} = -0.02$ V, $V_{2R} = -0.015$ V, $V_{3L} = -0.053$ V, $V_{3R} = -0.395$ V.

In Fig. 5.5 of the main text, the chemical potentials of QD_1 and QD_3 are set to be either equal (Fig. 5.5a) or opposite (Fig. 5.5b). Both situations require careful calibration. Fig. 5.10 shows how V_{QD1} and V_{QD3} can be finely tuned in order to set $\mu_1 = -\mu_3$ (the $\mu_1 = \mu_3$ case is analogous). The chemical potentials are related to the gate voltages via $\mu_1 = \alpha_1(V_{QD1} - V_1)$ and $\mu_3 = \alpha_3(V_{QD3} - V_3)$, where $\alpha_1 = 0.32$ and $\alpha_3 = 0.31$ are the lever arms and $V_1 \approx 412\,\mathrm{mV}$ and $V_3 \approx 497\,\mathrm{mV}$ are offsets. These values are extracted from the Coulomb diamonds of Fig. 5.1. Assuming equal lever arms, $\mu_1 = -\mu_3$ if $(V_{QD1} - V_1) = -(V_{QD3} - V_3)$, which means $V_{QD1} + V_{QD3} = \mathrm{constant} \equiv V_+$. Fig. 5.10 shows the measured currents as the value of V_+ is varied in small steps until the condition $\mu_1 = -\mu_3$ is reached.
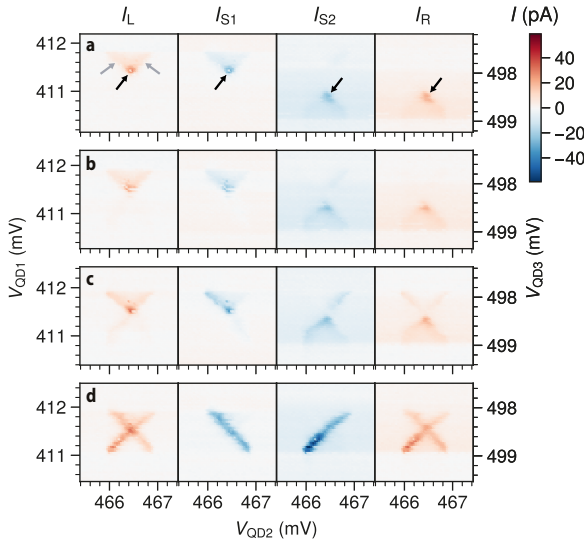
Figure 5.10: $\mu_1 = -\mu_3$ tuning example. **a., b., c., d.** Sequence of current measurements as a function of V_{QD1} and V_{QD2} with $V_{QD1} = -V_{QD3} + V_+$. V_+ is varied in steps of 0.2 mV from $V_+ = 909.4\,\mathrm{mV}$ (panel a) to $V_+ = 910.0\,\mathrm{mV}$ (panel d). Grey arrows highlight local pair tunneling (see Fig. 5.3) while black arrows highlight the resonant CAR and ECT processes happening on the left when $\mu_1 = \mu_2 = 0$ (panels I_L and I_{S1}) and on the right when $\mu_2 = \mu_3 = 0$ (panels I_{S2} and I_R). As V_+ increases, the left and right resonant CAR and ECT current spots get closer and closer until they align in panel d, where $\mu_1 = \mu_2 = \mu_3 = 0$ at the center of the cross.

5.6. EXTENDED DATA

5.6.1. SHIBA-ASSISTED LOCAL PAIR TUNNELING

A small but finite LAR in QD_2 can lead to the formation of a Yu-Shiba-Rusinov state (Yu, 1965; Shiba, 1968; Rusinov, 1969; Bauer et al., 2007; Meng et al., 2009; Lee et al., 2013), which has an electron and a hole part. Shiba-assisted local pair tunneling can occur when QD_3 is resonant with either the electron or the hole part of the Yu-Shiba-Rusinov state on QD_2. This process should then appear as two current features observing $|\mu_2| = |\mu_3|$, one with a positive slope and the other with a negative slope in the measurement. Contrary to the LAR taking place in QD_3, for the SPT the electron-hole conversion occurs in QD_2. As a result, the current flows only when μ_3 is between 0 and $-eV_R$.

To better appreciate this feature, we report here the same measurement of Fig. 5.3 next to another measurement with opposite bias on N_R and with QD_2 slightly more coupled to the right superconductor. Fig. 5.11a reports the same data of Fig. 5.3c, where V_R is positive, while Fig. 5.11b shows a similar measurement but with negative V_R. For better contrast, we repeat below both panels the same data after subtraction of the LAR current (Fig. 5.11c,d). We observe a V-shaped signal, compatible with the $|\mu_2| = |\mu_3|$ condition. The orientation of the V-shape depends on the bias sign, it extends from $\mu_3 \approx 0$ to $\mu_3 \approx -eV_R$.
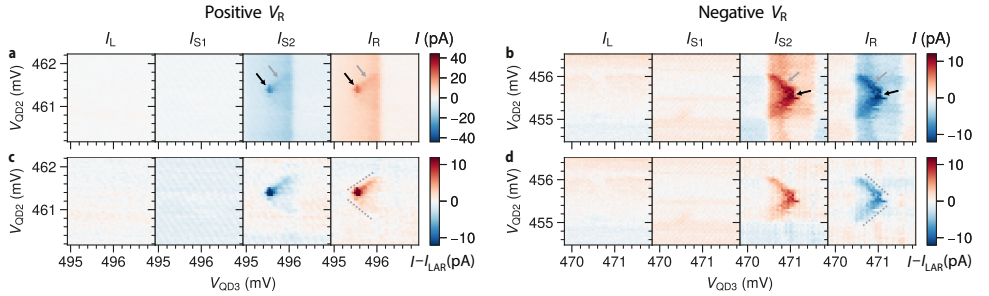
Figure 5.11: **a.** Same data of Fig. 5.3c. $V_R = 150\,\mu V$ and $V_{2R} = -0.02\,V$. **b.** Current through the device as a function of V_{QD2} and V_{QD3}, with $V_{QD1} = 423.95\,mV$, equivalent to $\mu_1 \approx 230\,\mu eV$. The other gates are set to $V_{1L} = -0.13\,V$, $V_{1R} = -0.14\,V$, $V_{H1} = 0.7\,V$, $V_{2L} = -0.01\,V$, $V_{2R} = 0.01\,V$, $V_{H2} = 0.8\,V$, $V_{3L} = -0.08\,V$, $V_{3R} = -0.4\,V$. $V_R = -150\,\mu V$. Here, QD_2 is slightly more coupled to the right superconductor than in panel a. Consistently with the SPT interpretation, the V-shaped current signature of the process is more visible. **c, d.** Same data of panels a and b but with subtracted LAR, which is extracted from the average of the top and bottom linecuts at fixed V_{QD2}. Grey dashed lines highlight the V-shaped signature of SPT. Grey lines are intentionally offset from resonance condition to not obscure data visibility.

5.6.2. SECOND DEVICE

In Fig. 5.12 we report signatures of sequential CAR and ECT measured in a second device. Additional data is shared in the linked repository, including three-dimensional current measurements as a function of V_{QD1}, V_{QD2} and V_{QD3} with V_L and V_R set in all possible symmetric and anti-symmetric configurations (with $V_b = 100\,\mu V$). We include GIF images for data visualization.
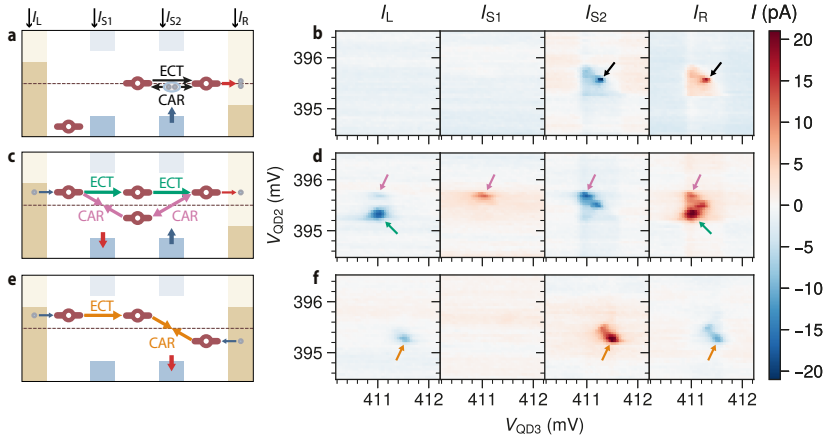
Figure 5.12: Signatures of sequential CAR and ECT processes in a second device. **a.** Schematic illustration of resonant CAR and ECT tunneling. **b.** Current through the device as a function of V_{QD2} and V_{QD3}, with μ_1 out of the bias window ($V_{QD1} = 294.65\,mV$). **c.** Schematic illustration of sequential ECT and sequential CAR processes. **d.** Current through the device as a function of V_{QD2} and V_{QD3}, with μ_1 within the bias window ($V_{QD1} = 295.15\,mV$), measured with an antisymmetric bias configuration **e.** Schematic illustration of ECT followed by CAR. **f.** Current through the device as a function of V_{QD2} and V_{QD3}, with μ_1 within the bias window ($V_{QD1} = 295.15\,mV$), measured with a symmetric bias configuration. The arrow colors are chosen as in the main text. In panels b, d, f, a constant background current is subtracted in every I panel for better visibility; see the code in the linked repository for further details.

6

SIGNATURES OF MAJORANA PROTECTION IN A THREE-SITE KITAEV CHAIN

Majorana zero modes (MZMs) are non-Abelian excitations predicted to emerge at the edges of topological superconductors. One proposal for realizing a topological superconductor in one dimension involves a chain of spinless fermions, coupled through p-wave superconducting pairing and electron hopping. This concept is also known as the Kitaev chain. A minimal two-site Kitaev chain has recently been experimentally realized using quantum dots (QDs) coupled through a superconductor. In such a minimal chain, MZMs are quadratically protected against global perturbations of the QD electrochemical potentials. However, they are not protected from perturbations of the inter-QD couplings. In this work, we demonstrate that extending the chain to three sites offers greater protection than the two-site configuration. The enhanced protection is evidenced by the stability of the zero-energy modes, which is robust against variations in both the coupling amplitudes and the electrochemical potential variations in the constituent QDs. While our device offers all the desired control of the couplings it does not allow for superconducting phase control. The experimental observations are in good agreement with numerical simulated conductances with phase averaging. This work pioneers the development of longer Kitaev chains, a milestone towards topological protection in QD-based chains.

6.1. INTRODUCTION

The pursuit of topological superconductivity is driven by its potential for decoherence-free quantum computing (Kitaev, 2003; Nayak et al., 2008) and high fidelity quantum gates. Topological superconductor hosts zero-energy subgap states, called Majorana zero-modes (MZMs). Majorana zero modes stand apart from bosons and fermions as they are predicted to exhibit non-Abelian exchange statistics. The act of braiding, or exchanging the order of these particles, alters their wavefunction properties. Braiding is a bedrock of topological quantum computation. Topological superconductors, however, are difficult to find in nature and, thus, it is appealing to engineer such systems in the laboratory. For more than a decade the field of topological superconductivity has seen many systems emerging as potential realizations of this new state of matter. These include proximitized Rashba nanowires (Lutchyn et al., 2010; Oreg et al., 2010; Prada et al., 2020), chains of magnetic atoms on superconductors (Nadj-Perge et al., 2014), 2D van der Waals based stacks (Kezilebieke et al., 2020), phase-biased Josephson junctions (Pientka et al., 2017; Fornieri et al., 2019; Ren et al., 2019), iron based superconductors (Zhang et al., 2018) and more (Vaitiekėnas et al., 2020; Banerjee et al., 2023). Recently, a compelling alternative has been pioneered, using two quantum dots coupled through superconductors to form a minimal Kitaev chain (Kitaev, 2001; Sau and Das Sarma, 2012; Dvir et al., 2023; ten Haaf et al., 2024a). Even shortest, two-site Kitaev chain hosts a pair of MZMs (Leijnse and Flensberg, 2012a). These MZMs, however, lack topological protection and have been referred to as Poor Man's Majoranas (PMMs). In this work, we show an experimental realization of a three-site chain, where emerging Majorana zero-modes are protected against perturbations of their couplings as well as improved stability against chemical potential variations. This achievement also demonstrates the ability of these systems to scale up to longer chains and shows the onset of topological protection.

6.2. COUPLING QUANTUM DOTS

In order to engineer a three-site Kitaev chain Hamiltonian Kitaev (2001); Sau and Das Sarma (2012)

$$H = \sum_{n=1}^{3} \mu_n c_n^\dagger c_n + \sum_{n=1}^{2} \left(t_n c_n^\dagger c_{n+1} + \Delta_n c_n^\dagger c_{n+1}^\dagger + h.c. \right), \qquad (6.1)$$

where $c_n^\dagger$ and c_n are the fermionic creation and annihilation operators, we need control over the onsite energies μ_n, the hopping terms t_n and the pairing terms Δ_n. In our semiconducting nanowire device, shown in Fig. 6.1a-b, three quantum dots are defined by an array of bottom gates, with V_{QD1}, V_{QD2} and V_{QD3} controlling the electrochemical potentials μ_n of every QD. The hopping term t_n is realized by elastic co-tunneling (ECT) between the dots, whereas Δ_n is achieved through the crossed Andreev reflection (CAR) (Sau and Das Sarma, 2012), which splits Cooper pairs into two adjacent quantum dots (Hofstetter et al., 2009, 2011; Herrmann et al., 2010; Ranni et al., 2021). Schematics of these two processes are depicted in Fig. 6.1b-c. To lift the spin degeneracy, as prescribed by the Hamiltonian of Eq. 6.1, we apply a magnetic field parallel to the nanowire axis ($B_x = 200\,mT$). This leads to spin-polarization of the quantum dots (Fig. 6.6). Nevertheless, CAR and ECT are allowed for all spin configurations, due to spin-orbit interaction

(Wang et al., 2022a, 2023). Tunneling spectroscopy of our semiconductor–superconductor hybrid segments (referred to as *hybrids* further in the text) is also performed at a finite field and is presented in the Supplementary Information (Fig. 6.7). In our previous work (Bordin et al., 2024b), we confirmed the presence of $t_{1,2}$ and $\Delta_{1,2}$ by detecting ECT and CAR across two hybrid segments with weakly coupled quantum dots. Here, we target strong couplings: $t_n, \Delta_n \gg k_B T$, where k_B is the Boltzmann constant and T the temperature.
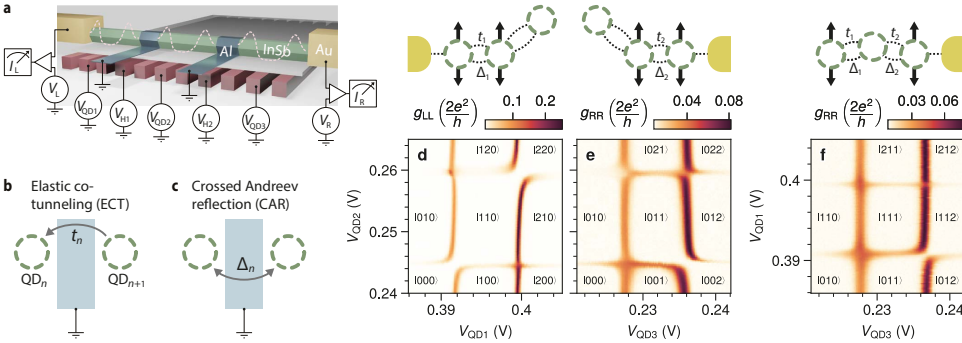
Figure 6.1: **a.** Illustrative diagram of the device. A semiconducting InSb nanowire (green) is placed on an array of eleven gates (pink), and contacted by two Al (blue) and two Cr/Au (yellow) leads. The gates, separated from each other and from the nanowire by a thin dielectric, form a potential landscape defining three QDs, controlled by the plunger gate voltages V_{QD1}, V_{QD2}, V_{QD3}. The QDs are connected by two hybrid semiconducting-superconducting sections controlled by V_{H1} and V_{H2}. The superconductors are separately grounded through room temperature electronics, while the left and right normal probes are connected to corresponding voltage sources (V_L, V_R) and current meters (I_L, I_R). Differential conductances $\left(g_L \equiv \frac{dI_L}{dV_L}, g_R \equiv \frac{dI_R}{dV_R}\right)$ are measured with standard lockin techniques. A scanning electron micrograph of the device is shown in Fig. 6.13. **b-c.** Schematic illustrations of ECT and CAR processes. **d-f.** QD–QD charge stability diagrams (where $|n_1, n_2, n_3\rangle$ indicate the effective charge occupations). Zero-bias conductance is measured across two charge degeneracy points for every pair of QDs. (We attribute the finite background conductance of $\approx 15\,mG_0$ on the left and $\approx 8\,mG_0$ on the right to finite capacitive response to lockin excitations of the dilution refrigerator lines, such background remains constant throughout the manuscript). Avoided crossings indicate strong coupling between each pair; while crossings signal that couplings between the dots are equalized (Dvir et al., 2023). In panel c, QD_3 is kept off-resonance, in panel d, QD_1 is kept off-resonance, while, in panel e, QD_2 is set close to resonance, as the schematics above indicate.

Indeed, the minimum value among t_n and Δ_n determines the amplitude of the topological gap in a long Kitaev chain (Sau and Das Sarma, 2012; Fulga et al., 2013). To couple the QDs we rely on the Andreev Bound States (ABSs) populating the hybrids (Liu et al., 2022; Bordin et al., 2023; Zatelli et al., 2024). Measuring the zero-bias conductance on the left and the right of the device $\left(g_L \equiv \frac{dI_L}{dV_L}, g_R \equiv \frac{dI_R}{dV_R}\right)$, we optimize the coupling site by site, as shown in the Supplementary Information (Fig. 6.8), until we see the appearance of several avoided crossings in the charge stability diagrams of Fig. 6.1c-e. Panels c and d show avoided crossings between QD_1 and QD_2 and between QD_2 and QD_3 respectively.

Remarkably, the coupling between neighboring QDs is strong enough to mediate interaction even between the outer QDs (panel e). We note that the coupling between QD_1 and QD_3 is mediated by the middle QD as it is suppressed if QD_2 is moved off-resonance (see Fig. 6.10).

6.3. TUNING 2-SITE KITAEV CHAINS

After demonstrating strong coupling between the quantum dots, the next goal is to demonstrate the tunability of the chain. Ideally, ECT and CAR amplitudes should be balanced pairwise, setting:

$$\begin{cases} t_1 = \Delta_1 \\ t_2 = \Delta_2 \end{cases} \tag{6.2}$$

We begin by illustrating in Fig. 6.2 how each condition of Eq. 6.2 can be individually met, with the constraint of keeping constant voltages on the three central gates forming QD_2. In the measurements of the left column of Fig. 6.2, QD_3 is kept off-resonance, such that the low-energy behavior of the chain is effectively two sites. When $t_1 = \Delta_1$, we observe level crossing instead of repulsion in Fig. 6.2a (Dvir et al., 2023). The spectrum at the center, shown in Fig. 6.2c, shows a zero-bias conductance peak corresponding to a Poor Man's Majorana mode (PMM) (Leijnse and Flensberg, 2012a), with excitation gap
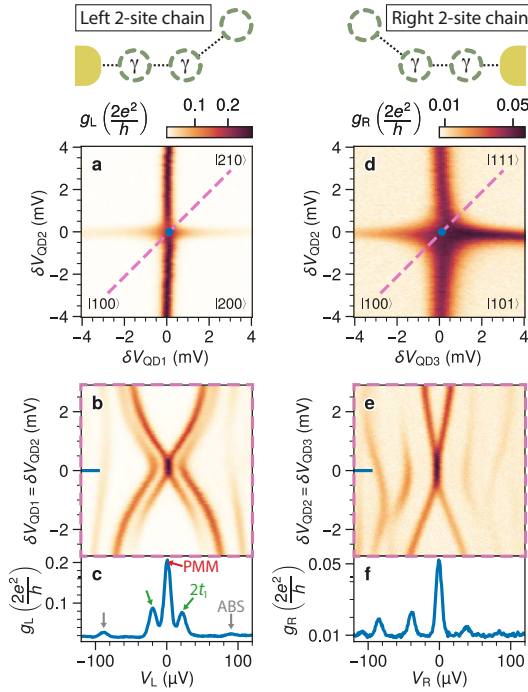
Figure 6.2: **Two-site Kitaev chains tuned on both ends of the device.** In the left column QD_1 and QD_2 are on resonance while QD_3 is being kept off-resonance as depicted in the schematic ($\delta V_{QD3} = -5\,\text{mV}$). With $\delta V_{QD1/2/3}$ we indicate the deviations from the crossing points, here happening at $V_{QD1} = 0.3995\,\text{V}$, $V_{QD2} = 0.2445\,\text{V}$ and $V_{QD3} = 0.2275\,\text{V}$ **a.** QD_1–QD_2 charge stability diagram at a sweet spot where $t_1 = \Delta_1$. **b.** Conductance spectroscopy as a function of simultaneous detuning of QD_1 and QD_2. **c.** Line-cut depicting spectrum at $\delta V_{QD1} = \delta V_{QD2} = 0\,\text{V}$ illustrating a zero-bias peak (red arrow) and a gap of $\sim 20\,\mu\text{eV}$ (green arrows). An ABS is visible at a higher bias (grey arrows). Right column: QD_2 and QD_3 are kept on resonance, while QD_1 is kept off-resonance as depicted in the schematic ($\delta V_{QD1} = -4\,\text{mV}$). **d.** QD_2–QD_3 charge stability diagram at a $t_2 = \Delta_2$ sweet spot. **e.** Conductance spectroscopy as a function of simultaneous detuning of QD_2 and QD_3. **f.** Line-cut depicting spectrum at $\delta V_{QD2} = \delta V_{QD3} = 0\,\text{V}$, illustrating a zero-bias peak and a gap of $\sim 40\,\mu\text{eV}$.

being $2t_1 = 2\Delta_1 \approx 20\mu eV$. As pointed out in Leijnse and Flensberg (2012a), if μ_1 and μ_2 are detuned from 0, then the PMMs split quadratically from zero energy, as shown in Fig. 6.2b. Similarly, the right column of Fig. 6.2 studies the case where QD_1 is kept off-resonance and the PMM pair appears on the right side of the device when $t_2 = \Delta_2$. We note that the gap of the right PMM pair is $\approx 40\mu eV$, twice as much compared to the left PMM pair. This is achieved with a higher degree of hybridization between the ABSs of the right hybrid and the neighboring quantum dots (Fig. 6.9), resulting in higher coupling strengths as well as lower QD lever arms (Zatelli et al., 2024). Although it is possible to tune the amplitudes of t_n and Δ_n to be all equal, we choose to focus on the scenario where they are equal only pairwise. This approach allows us to identify spectral features arising from different coupling values in the chain.

6.4. THE THREE-SITE CHAIN

Having satisfied the pairwise condition of Eq. 6.2, we tune into the three-site Kitaev chain regime by setting all QDs on resonance. Fig. 6.3 shows the spectrum of such a system, tunnel-probed from the left and the right (first and second row, respectively), as a function of the detuning of every QD (first, second, and third column).

The first observation is zero-bias conductance peaks manifesting on both ends of the device, remaining stable against the detuning of any constituent QD. Furthermore, spectroscopies from the left and the right reveal identical gate dispersions of the excited states, albeit with different intensities. Excited states originating from the left two sites are expected to couple more strongly to the left lead, while excited states originating from the right pair are expected to couple more strongly to the right one. Indeed, we identify excited states corresponding to $2t_1 = 2\Delta_1 \approx 20\mu eV$, marked by blue arrows in Fig. 6.3(a,c). Such states disperse only as a function of V_{QD1} and V_{QD2} and have higher g_L, signaling a higher local density of states. For the right side of the device, similar reasoning applies to the states marked by green arrows in Fig. 6.3(d,f), from which we estimate $2t_2 = 2\Delta_2 \approx 60\mu eV$.
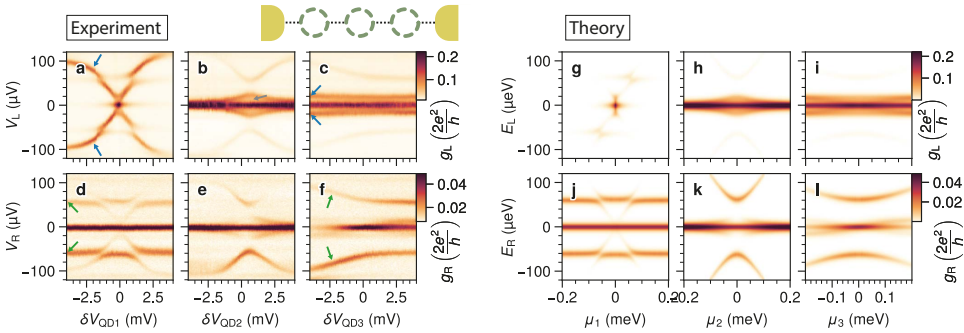
Figure 6.3: **a-c.** Conductance spectroscopy from the left lead, as a function of the detuning of individual quantum dots δV_{QD_n} constituting the chain. By looking at the excited states when QD_3 is off-resonance, we can estimate the left couplings to be $2t_1 = 2\Delta_1 \approx 20\mu eV$ (blue arrows in panel c). **d-f.** Analogously, this section illustrates conductance spectroscopy from the right lead. When QD_1 is off-resonance we can estimate the left couplings to be $2t_2 = 2\Delta_2 \approx 60\mu eV$ (green arrows in panel d). **g-l.** Each panel depicted here presents the results of numerical simulations corresponding to measurements presented in panels a to f.

Importantly, we observe a finite conductance between the first excited state and the zero-bias peak (grey arrow in Fig. 6.3b). While we have successfully equalized the amplitudes of the coupling parameters, another significant parameter to consider is the phase difference between them. In the Kitaev chain Hamiltonian (Eq. 6.1), the terms t_n and Δ_n are complex numbers, each with a distinct, non-trivial phase: $t_n = |t_n|e^{i\phi_{n,t}}$ and $\Delta_n = |\Delta_n|e^{i\phi_{n,\Delta}}$.

In the context of a two-site Kitaev chain, the consideration of these phases is redundant as they can be absorbed into the quantum dot modes via a gauge transformation (Sau and Das Sarma, 2012). The scenario changes, however, with a three-site Kitaev chain, where only three out of the four phases can be similarly absorbed, leaving one phase as an independent parameter. In our system, the phase difference originates from the superconducting leads, which then translates into the phase difference between Δ_1 and Δ_2, as explained in the Supplementary Information. To understand the spectroscopic results presented in Fig. 6.3, we offer the following interpretation. Conceptually, the device's central part is a Josephson junction, which doesn't exhibit any measurable supercurrent when the device is tuned in a three-site chain configuration (see Fig. 6.11). As a result, the junction behaves ohmically and can support an infinitesimal voltage difference. According to the second Josephson relation (Tinkham, 2004), finite voltage bias in Josephson junctions induces phase precession: $\frac{d\phi}{dt} = \frac{2eV}{\hbar}$. In our experiment, the voltage bias between the two superconducting leads cannot be set to zero with arbitrary precision due to voltage divider effects, thermal fluctuations, finite equipment resolution, and noise levels. We estimate the voltage difference to be on the order of $\delta V \sim 1\,\mu V$ (see Supplementary Information). The corresponding phase difference precesses with periods of $T_\phi = \frac{h}{2e\delta V} \sim 2$ ns. This is a very small time scale relative to the DC measurement time (~ 1 s). We thus assume that the spectra obtained for a three-site chain are uniformly averaged over possible phase differences. Fig. 6.3g-i shows the average simulated conductance of 50 phase selections uniformly distributed from 0 to 2π. Here, the system of Eq. (6.1) is coupled to external normal leads and the differential conductances are calculated using the scattering matrix method (see Supplementary Information for more details). Within our interpretation, the zero-bias conductance peaks are still induced by Majorana zero modes. In particular, the Majoranas that should appear in a three-site Kitaev chain with zero phase difference would remain at zero energy regardless of the phase uncertainty. However, a major effect of the superconducting phase deviation is the change in the size of the energy gap, ranging from its maximum value $2t$ at 0-phase to 0 at π-phase. Our theoretical model reproduces the features observed in the experiment accurately, despite having only a few parameters. As opposed to a spinful model treating the ABSs in the hybrids explicitly (Tsintzis et al., 2024; Liu et al., 2023), the effective spinless model we are considering here only requires the fitting of the coupling to the leads $\Gamma_{L/R}$; all other model parameters are estimated from independent measurements (see Supplementary Information). We note that these observations have been replicated also on another nanowire device with similar values of t_n and Δ_n, as presented in Fig. 6.12.

6.5. INCREASED PROTECTION
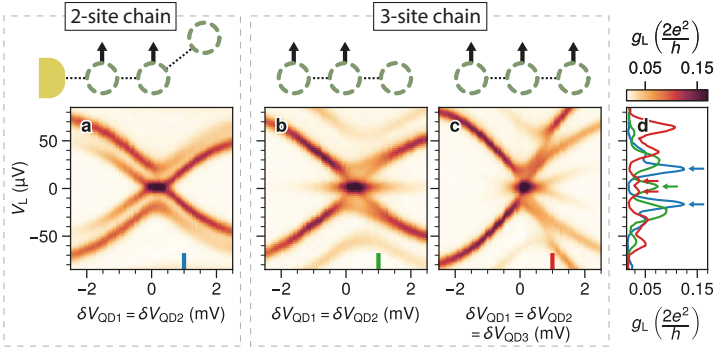
Figure 6.4: **Stability of a zero-energy state against electrochemical potential variations.** Left conductance spectroscopy of the device in a 2-site chain configuration (panel a) and three-site chain configuration (panels b and c). Theory simulations are reported in Fig. 6.14. **a.** Spectrum of a two-site chain at the left of the device (as Fig. 6.2c) showing the splitting of Poor Man's Majorana modes as a function of simultaneous detuning of QD_1 and QD_2. QD_3 is off-resonance at $\delta V_{QD3} = -5\,\text{mV}$. **b.** A three site chain configuration where $\delta V_{QD3} = 0\,\text{V}$. The zero-bias conductance peak persists over the full scanned range. See Fig. 6.16 for similar measurements as a function of the detuning of any pair of QDs. **c.** Three site chain spectrum as a function of simultaneous detuning δV of $QD_{1,2,3}$. A visible splitting is observed once all the dots are detuned by $\delta V = 1\,\text{mV}$. **d.** Line-cuts of previous panels taken at $\delta V = 1\,\text{mV}$ for a 2-site chain (blue) and a three-site one (green and red). The arrows highlight the splitting of the zero-bias peak.

Fig. 6.4 compares the robustness of two- and three-site chains against electrochemical potential variations. As shown in Fig. 6.2, detuning both QDs of two-site chains leads to the splitting of the Majorana modes. In panels a and b of Fig. 6.4 we compare such a scenario with the detuning of the same two QDs in a three-site chain. Apart from V_{QD3}, all the gate settings are identical, but the spectrum measured from the left probe shows for the three-site chain a stable zero-bias peak.

To split the zero energy modes of three-site chains, all QDs need to be detuned, as shown in panel c, and even in this case they disperse slower compared to the two-site scenario. As we demonstrate in the Supplementary Information (Eq. 6.14), if all electrochemical potentials of a three-site chain are detuned, the zero modes should split cubically. See Fig. 6.14 in the Supplementary Information for theoretical simulations, Fig. 6.15 for a comparison with the right two-site chain and Fig. 6.16 showing the stability of three-site chain Majorana modes against the detuning of any pair of QDs.

Finally, Fig. 6.5 compares the robustness of two- and three-site chains when leaving the pairwise sweet-spot condition of Eq. 6.2. As opposed to electrochemical potential detuning, two-site chains have no protection against tunnel coupling deviations: perturbing either t or Δ results in a linear splitting of the zero modes (Leijnse and Flensberg, 2012a; Dvir et al., 2023; Zatelli et al., 2024). Here we reproduce such a result in panel a of Fig. 6.5. When QD_3 is off-resonance, the zero bias peak of the left two-site chain is split as soon as the V_{H1} controlling the t_1 and Δ_1 ratio is detuned from the sweet-spot value (pink arrow). However, if we repeat the same measurement for the three-site Kitaev chain after bringing QD_3 back on resonance, the zero-bias conductance peak persists over the

entire V_{H1} range (Fig. 6.5b), indicating tolerance to tunnel coupling deviations. We note that the V_{H1} range of Fig. 6.5 is large enough to pass through a gate jump (blue arrow), which we find reproducible across multiple scans. While gate jumps can greatly affect the spectrum of 2-site chains, we find that a 3-site one is robust against them. Since the zero-bias peak persists, the gate jump clearly visible in panel a becomes barely noticeable in Fig. 6.5b. Finally, we stress that the stability of a zero-bias peak in a two-site chain can be larger than presented in Fig. 6.5a. For instance, when the dispersion of t and Δ as a function of V_H are similar (Bordin et al., 2023), the region with $t \approx \Delta$ will be extended. An example of such a scenario is presented in the Fig. 6.18.
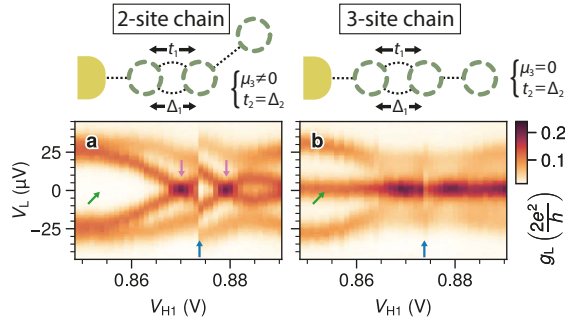
Figure 6.5: **Comparison of stability against variation of t and Δ in a two- and three-site Kitaev chain. a.** Conductance spectroscopy of a two-site chain as a function of V_{H1}, which controls the magnitude of t_1 and Δ_1. QD_3 is kept off-resonance. **b.** QD_3 is brought into resonance with the other two quantum dots in order to measure the spectrum of a three-site chain. Here, the zero-bias conductance peak persists over the entire V_{H1} range > 40 mV. A blue arrow indicates a reproducible gate jump observed in this parameter region. See also Figs. 6.17, 6.18 and 6.20 for a higher resolution scan, a symmetric study of the right side and theoretical simulations.

The results presented in Figures 6.4 and 6.5 demonstrate the enhanced protection of three-site chain Majorana zero modes compared to two-site chain ones. In particular, MZMs in three site chains are resilient against perturbations in the couplings t_n and Δ_n (Fig. 6.5), which is expected to be the main limiting factor of coherence of Poor Man's Majorana-based qubits. The coherence time of a qubit made of 2-site Kitaev chains was previously predicted to be ~ 10 ns (Zatelli et al., 2024). Based on the parameters extracted from the current experiment, in the Supplementary Information we estimate a qubit coherence time for a three-site Kitaev chain at $\phi = 0$ to be around ~ 1 μs (we remark that the coherence time of three-site Kitaev chains without phase control is limited by the time scale of phase evolution T_ϕ due to Landau-Zener (Knapp et al., 2016) transitions near gap closing). This two orders of magnitude improvement provides further motivation for developing devices with phase control. By increasing the number of sites, the protection of MZMs against perturbations of μ_n, t_n, and Δ_n is expected to increase further (Sau and Das Sarma, 2012). In particular, we estimate that a 5-site chain would be enough for a target qubit lifetime of ~ 1 ms (Fig. 6.21). Here we stress that while extending the chain length always leads to a quantitative enhancement in protection, the transition from two to three sites introduces also two qualitative differences, which become ev-

ident by looking at the leading perturbation terms of the Kitaev Hamiltonian (6.1) for $\phi = 0$, $(t_n - \Delta_n) \approx 0$ and $\mu_n \approx 0$ for all n:

$$[\text{2-site chain}] \quad (t - \Delta) + \frac{\mu_1 \mu_2}{2t} \tag{6.3}$$

$$[\text{3-site chain}] \quad \frac{(t_1 - \Delta_1)\mu_3}{2t_2} + \frac{\mu_1(t_2 - \Delta_2)}{2t_1} + \frac{\mu_1 \mu_2 \mu_3}{(2t_1)(2t_2)} + \frac{(t_1 - \Delta_1)\mu_2(t_2 - \Delta_2)}{(2t_1)(2t_2)} \tag{6.4}$$

First, looking at the numerators of equations 6.3 and 6.4, 2-site chain Majoranas can split with a single perturbation $(t - \Delta)$, while three-site chains are the smallest ones where no single-parameter perturbation, by itself, can couple the two edge Majorana modes: all terms are a product of at least two factors. Secondly, looking at the denominators, two-site chains are not protected by the $2t$ gap. With three sites, instead, all perturbation terms have the $2t_{1/2}$ gap at the denominator.

This onset of topology, given by the additional QD acting as the "bulk" gap of the chain, motivates new research directions, including longer chains, qubit experiments (Pino et al., 2024; Tsintzis et al., 2024; Spethmann et al., 2022) and the pursuit of new material combinations which could provide larger gap (Kanne et al., 2021; Pendharkar et al., 2021; Mazur et al., 2022).

6.6. CONCLUSION

In this study, we have realized a strongly coupled three-quantum-dot chain engineered via coherent coupling of the constituent dots through CAR and ECT processes. Our devices have demonstrated the capability to host two adjacent two-site Kitaev chains. Additionally, we illustrate that when the three dots are on resonance, the system exhibits the spectrum expected for a three-site Kitaev chain, averaged across all possible phase differences. The setup permits the investigation of the MZM stability to variations in the electrochemical potential, as well as influences from CAR and ECT. This achievement addresses a key limitation of two-site Kitaev chains, where the finite overlap of MZM wavefunctions is considered a primary decoherence In conclusion, extending Kitaev chains improves stability against μ_n, t_n and Δ_n, appreciated even without the phase control, the next step towards qubit experiments.

6

AUTHOR CONTRIBUTIONS

AB, JCW, DvD, and GPM fabricated the device, AB, GPM, TD, FZ, and TVC measured the devices and analyzed the data with help from SLDtH, YW, GW, and NvL. GB, SG, and EPAMB performed nanowire synthesis. CXL and MW performed the numerical simulations. AB and TD initiated and designed the early phase of the project. GPM and LPK supervised the experiments presented in this manuscript. AB, GPM, CXL, and LPK prepared the manuscript with input from all authors.

DATA AVAILABILITY

All raw data in the publication and the analysis code used to generate figures are available at https://doi.org/10.5281/zenodo.10709983.

6

6.7. SUPPLEMENTARY INFORMATION

6.7.1. THEORETICAL MODEL AND SIMULATION

The Hamiltonian of a three-site Kitaev chain is

$$
\begin{aligned}
H_{K3} = {} & \mu_1 n_1 + \mu_2 n_2 + \mu_3 n_3 + t_1(c_2^\dagger c_1 + c_1^\dagger c_2) + t_2(c_3^\dagger c_2 + c_2^\dagger c_3) \\
& + \Delta_1(c_2^\dagger c_1^\dagger + c_1 c_2) + \Delta_2(e^{i\phi} c_3^\dagger c_2^\dagger + e^{-i\phi} c_2 c_3).
\end{aligned}
\tag{6.5}
$$

Here c_i is the annihilation operator of the orbital in dot i, $n_i = c_i^\dagger c_i$ is the occupancy, μ_i is the orbital energy relative to the superconductor Fermi energy. t_i and Δ_i are the normal and superconducting tunnelings between dots i and $i+1$, and ϕ is the phase difference between the two superconducting leads. Physically, t's and Δ's are the ECT and CAR amplitudes mediated by the subgap Andreev bound states in the hybrid segments. In the Nambu basis, the above Hamiltonian can be written as

$$
H = \frac{1}{2}\Psi^\dagger \cdot h_{BdG} \cdot \Psi,
$$

$$
\Psi = (c_1, c_2, c_3, c_1^\dagger, c_2^\dagger, c_3^\dagger)^T,
$$

$$
h_{BdG} = \begin{pmatrix}
\mu_1 & t_1 & 0 & 0 & -\Delta_1 & 0 \\
t_1 & \mu_2 & t_2 & \Delta_1 & 0 & -\Delta_2 e^{i\phi} \\
0 & t_2 & \mu_3 & 0 & \Delta_2 e^{i\phi} & 0 \\
0 & \Delta_1 & 0 & -\mu_1 & -t_1 & 0 \\
-\Delta_1 & 0 & \Delta_2 e^{-i\phi} & -t_1 & -\mu_2 & -t_2 \\
0 & -\Delta_2 e^{-i\phi} & 0 & 0 & -t_2 & -\mu_3
\end{pmatrix}.
\tag{6.6}
$$

When the system is coupled to normal leads, the scattering matrix describing the transmission and reflection amplitudes between modes in the leads can be expressed by the Weidenmuller formula

$$
S(\omega) = 1 - iW^\dagger \left(\omega - h_{BdG} + \frac{i}{2}WW^\dagger\right)^{-1} W
\tag{6.7}
$$

where the tunnel matrix W is defined as

$$
W = \mathrm{diag}\left(\sqrt{\Gamma_L}, 0, \sqrt{\Gamma_R}, -\sqrt{\Gamma_L}, 0, -\sqrt{\Gamma_R}\right),
\tag{6.8}
$$

with $\Gamma_{L/R}$ being the dot-lead coupling strength on the left and right ends respectively. At zero temperature, the differential conductance is expressed as

$$
G_{ij}^{(0)}(\omega) \equiv dI_i/dV_j = \delta_{ij} - \left|S_{ij}^{ee}(\omega)\right|^2 + \left|S_{ij}^{he}(\omega)\right|^2
\tag{6.9}
$$

in unit of e^2/h. Here $i, j = 1, 2, 3$, and ω denotes the bias energy in the leads. The finite-temperature conductance is obtained by a convolution between the zero-temperature one and the derivative of the Fermi distribution

$$
G_{ij}^T(\omega) = \int_{-\infty}^{+\infty} dE \frac{G_{ij}^{(0)}(E)}{4k_B T \cosh^2[(E-\omega)/2k_B T]}.
\tag{6.10}
$$

In performing the numerical simulations, we choose the coupling strengths to be $t_1 = \Delta_1 = 10\ \mu eV$, $t_2 = \Delta_2 = 30\ \mu eV$ based on the positions of the excited states shown in Fig. 6.3. The electron temperature in the normal leads, $T \sim 35\,\mathrm{mK}$, corresponds to a broadening $k_B T \sim 3\mu eV$. The strengths of the lead-dot couplings are chosen to be $\Gamma_L = 1.5\mu eV$, $\Gamma_R = 0.3\mu eV$, such that the conductance values obtained in the numerical simulations are close to those in the experimental measurements. Moreover, to capture the effects of lever arms strength differences in the three dots, we choose $\delta\mu_1 = \delta\mu, \delta\mu_2 = \delta\mu, \delta\mu_3 = 0.3\,\delta\mu$. Crucially, we notice that in the particular experimental devices studied in this work, since the voltage bias between the two superconducting leads cannot be set to zero precisely, $0.1\,\mu V \lesssim \delta V \lesssim 1\,\mu V$, the phase difference precesses with periods of $2\,\mathrm{ns} \lesssim T_\phi \sim \frac{h}{2e\delta V} \lesssim 20\,\mathrm{ns}$. On the other hand, the lifetime of an electron spent in a quantum dot is at the order of $\tau_e \sim \hbar/\Gamma \sim 1\,\mathrm{ns}$. This is the time scale of a single event of electron tunneling giving electric current, which would take a random value of phase difference ϕ since τ_e is smaller than or of similar order as the period of the phase winding T_ϕ. On the other hand, both τ_e and T_ϕ are a very small time scale relative to the DC current measurement time ($\sim 1\,\mathrm{s}$). Therefore, any particular data point collected in the conductance measurement is an average over $\sim 10^9$ tunneling events with different possible phases. Theoretically, we capture this effect by performing a phase average on the differential conductance as follows

$$\langle G_{ij}^T(\omega)\rangle_\phi \equiv \int_0^{2\pi} \frac{d\phi}{2\pi} G_{ij}^T(\omega, \phi). \tag{6.11}$$

The numerically calculated conductances shown in the main text are obtained by averaging over 50 values of phases evenly distributed between 0 and 2π.

ENHANCED PROTECTION

For the Majorana zero modes at the sweet spot of an N-site Kitaev chain ($t_i = \Delta_i, \mu_i = 0$), its energy deviation against onsite chemical potential fluctuation can be expressed as

$$\delta E_{K_N} \equiv E_{odd,gs} - E_{even,gs} = \mu_N \prod_{i=1}^{N-1} \frac{\mu_i}{2t_i}, \tag{6.12}$$

where $t_i = \Delta_i$ are the strengths of the normal and superconducting couplings between sites i and $i+1$. In particular, for a two-site Kitaev chain, the energy deviation is

$$\delta E_{K_2} = \frac{\mu_1 \mu_2}{2t} = C_{K_2} \cdot \tilde{\mu}^2, \tag{6.13}$$

where $\mu_i = \mu$ and $\tilde{\mu} = \mu/(\mu eV)$ is dimensionless. Note that for a two-site Kitaev chain, the protection is quadratic. Here, the unit of C_{K_2} is μeV, the physical meaning of which is the energy deviation when both dot orbitals are away from the fermi energy by 1 μeV. Using the values obtained in the measurements, i.e., $t_1 = 15\ \mu eV$ and $t_2 = 30\ \mu eV$, we estimate that $C_2 = 3.33 \times 10^{-2}$ and 1.66×10^{-2} for the left and right pairs of PMM, respectively. For an extended three-site Kitaev chain, the energy deviation becomes

$$\delta E_{K_3} = \frac{\mu_1 \mu_2 \mu_3}{4t_1 t_2} = C_{K_3} \cdot \tilde{\mu}^3, \tag{6.14}$$

which is a cubic protection. Now $C_{K_3} = 5.55 \times 10^{-4}$, which is smaller than C_{K_2} by two orders of magnitudes, indicating a significantly enhanced degree of protection in the three-site Kitaev chain than its two-site version. Moreover, we illustrate the physical meaning of "exponential protection" in scaling up a Kitaev chain. Without loss of generality, assuming homogeneity of the model parameters ($t_i = \Delta_i = t \equiv E_g/2$ with E_g being the energy gap), we have

$$\delta E_{K_N} = \mu_N \prod_{i=1}^{N-1} \frac{\mu_i}{2t_i} = \frac{\mu^N}{E_g^{N-1}} = E_g \left(\frac{\mu}{E_g}\right)^N = E_g \exp\{-N \log(E_g/\mu)\}. \tag{6.15}$$

Physically, it means that when the onsite energies of all the N dots are detuned from zero by the same amount $\mu \ll E_g$, the energy splitting of the Majorana zero modes will decrease exponentially fast with the increasing number of sites at a rate of $\log(E_g/\mu)$.

DERIVATION OF THE EFFECTIVE THREE-SITE KITAEV CHAIN MODEL

In this section, we derive the effective Hamiltonian of a three-site Kitaev chain from a more microscopic level. For the three quantum dots, in the presence of large Zeeman spin splitting and Coulomb interaction, we can approximate it to a single spin-polarized orbital as below:

$$H_{Di} = \mu_i(n_{i\uparrow} + n_{i\downarrow}) + 2E_Z n_{i\uparrow} + U_D n_{i\uparrow} n_{i\downarrow} \approx \mu_i n_{i\downarrow}, \tag{6.16}$$

for $i = 1, 2, 3$ and $\mu_i \approx 0$. Here in the derivation, we focus on the spin-down orbitals in all dots, but the analysis holds for other spin polarizations as well. On the other hand, the hybrid segment hosts subgap Andreev Bound States, of which the Hamiltonian is

$$H_{Aj} = \mu_j(n_{j\uparrow} + n_{j\downarrow}) + |\Delta_j^{\text{ind}}|(e^{i\phi_j} c_{j\uparrow}^\dagger c_{j\downarrow}^\dagger + e^{-i\phi_j} c_{j\downarrow} c_{j\uparrow}) \tag{6.17}$$

where $j = L, R$, and $|\Delta_j^{\text{ind}}|$ is the magnitude of the induced gap, and ϕ_j is the superconducting phase. The coupling between the dot and the hybrid is described by the following tunnel Hamiltonian

$$H_{tunn} = \sum_{i=1,2} \sum_{\sigma=\uparrow,\downarrow} \left(w c_{i\sigma}^\dagger d_{i\sigma} + \sigma w_{so} c_{i\bar{\sigma}}^\dagger d_{i\sigma} + w d_{i+1\sigma}^\dagger c_{i\sigma} + \sigma w_{so} d_{i+1\bar{\sigma}}^\dagger c_{i\sigma}\right) + h.c., \tag{6.18}$$

where w and w_{so} are the tunneling amplitudes for spin-conserving and spin-flipping processes. As shown in Ref. (Liu et al., 2022), in the tunneling regime, i.e., $w, w_{so} \ll |\Delta^{\text{ind}}|$, the Andreev bound states in the hybrid will mediate normal and superconducting couplings of quantum dots via elastic cotunneling and crossed Andreev reflection processes, giving

$$t_1 = (w^2 - w_{so}^2) \frac{u_L^2 - v_L^2}{E_{AL}},$$

$$\Delta_1 = w w_{so} \frac{2u_L v_L}{E_{AL}} e^{i\phi_L},$$

$$t_2 = (w^2 - w_{so}^2) \frac{u_R^2 - v_R^2}{E_{AR}},$$

$$\Delta_2 = w w_{so} \frac{2u_R v_R}{E_{AR}} e^{i\phi_R}, \tag{6.19}$$

where u_j, v_j are the BCS coherence factors of the ABS, and $E_{Aj} = \sqrt{\mu_j^2 + (\Delta_j^{\text{ind}})^2}$ is the excitation energy. Thereby, by varying the chemical potential of the ABS, we can obtain the sweet spot by balancing the normal and superconducting coupling strengths ($|t_i| = |\Delta_i|$). Furthermore, by performing a gauge transformation on the dot orbitals, we can remove the possible phases in three couplings in Eq. (6.19), and obtain

$$
\begin{aligned}
t_1 &\to |t_1|, \quad \Delta_1 \to |\Delta_1|, \\
t_2 &\to |t_2|, \quad \Delta_2 \to |\Delta_2| e^{i\phi}, \\
\phi &= \phi_R - \phi_L + \arg(t_1) + \arg(t_2).
\end{aligned}
\tag{6.20}
$$

That is, the effect of the phase difference between the two superconducting leads is now completely absorbed in a single parameter ϕ. We therefore justify the use of the effective Hamiltonian in Eq. (6.5) as the low-energy description of the dot-hybrid array. We emphasize that in performing numerical simulations of dot energy detuning, as shown in Figs. 6.3 and 6.4, the couplings between dots are just denoted by t_j, Δ_j, while when considering the effect of voltage change in the hybrid segment for Fig. 6.20e-f, we reintroduce the effect of ABS using Eq. (6.19) for the couplings in order to capture the μ_A dependence features.

ESTIMATION OF DEPHASING RATE FOR THE KITAEV CHAIN QUBIT

In this subsection, we perform a numerical estimation of the dephasing time of different types of Kitaev chain qubits, similar to Zatelli et al. (2024) in spirit. In particular, we consider three different types of Kitaev chain qubits: two-site Kitaev chain with weak and strong dot-hybrid coupling, and three-site Kitaev chain with a fixed phase difference $\phi = 0$. A qubit consists of two copies of Kitaev chains, H_K^A and H_K^B, respectively. Without loss of generality, we focus on the subspace of total parity even, and therefore the two qubit states are defined as $|0\rangle = |e_A, e_B\rangle$ and $|1\rangle = |o_A, o_B\rangle$, where $|o\rangle$ and $|e\rangle$ denote the odd- and even-parity ground states in each chain and $|e_A, e_B\rangle \equiv |e\rangle_A \otimes |e\rangle_B$ is the tensor state. Note that here we do not consider inter-chain coupling, which depends on the device details that have not been implemented so far, thus going beyond the scope of this work. Therefore our estimation only provides an upper limit of the dephasing time in a Majorana qubit. Furthermore, we assume that charge noise within a Kitaev chain is the main source of decoherence in the device we consider here. As such, the energy difference between the two qubit states would fluctuate, giving rise to a dephasing rate $1/T_2^* \sim \delta E / \hbar$ where δE is the characteristic energy splitting of $E_{oo} - E_{ee}$.

Generally, charge noise is dominated by fluctuations of charge impurities in the environment. However, as shown in Scarlino et al. (2022), the charge impurity fluctuations can be equivalently described by fluctuations in the gate voltages. Theoretically, the voltage fluctuations enter the Kitaev-chain Hamiltonian as follows:

$$
\begin{aligned}
\delta \mu_i &= \alpha_i \cdot \delta V_i, \\
\delta t_j &= \frac{\partial t_j}{\partial V_{H_j}} \cdot \delta V_j,
\end{aligned}
\tag{6.21}
$$

with α_i being the lever arm of the i-th quantum dot. In the second formula, the derivative is extracted from a single pair of PMM (Fig. 6.5a). We emphasize that the fluctuations

Device parameters	QD-PMM	YSR-PMM	Kitaev-3 ($\phi = 0$)
α_{QD} [e]	0.3	0.04	0.04
$\partial t / \partial V_H$ [e]	5×10^{-3}	5×10^{-3}	5×10^{-3}
t, Δ [μeV]	10	40	10(left), 30(right)
$1/T_2^*$ [MHz] (μ noises)	~ 900	~ 4	~ 0.1
$1/T_2^*$ [MHz] (t noises)	~ 100	~ 100	0
$1/T_2^*$ [MHz] (all noises)	~ 900	~ 100	~ 2

Table 6.1: Estimation of dephasing rate for different types of Kitaev chain qubits, assuming charge noise to be the only source of noises.

of t_j and Δ_j are correlated because both of them are induced by the ABS in the hybrid, which is controlled by a single electrostatic gate.

Here as a first-order approximation, we assume that the fluctuations are on t_j while Δ_j remains constant. Charge noise is also known as slow-varying in time, and thus can be well described quasi-static disorder approximation [Phys. Rev. B 109, 125410 (2024)]. We generate 5000 different disorder realizations of the set of gate voltages. Moreover, we assume two chains in a qubit are subject to independent sources of charge noises and thus we can calculate their energy splitting individually and the energy splitting of the qubit states is just the sum as $E_{oo} - E_{ee} = (E_o^A - E_e^A) + (E_o^B - E_e^B)$. Finally, we take the standard deviation of $\langle E_{oo} - E_{ee} \rangle_{std}$, which eventually gives the dephasing rate.

The voltage fluctuations obey Gaussian distribution with mean zero and standard deviation $\delta V \sim 10\mu$eV, as discussed in a similar experimental device (Zatelli et al., 2024). In our models of Kitaev chains, we consider independent fluctuation sources in dots, and in the hybrid segment. Our analysis considers three distinct scenarios: dephasing due to dot energies only, hybrid coupling only, and both of them. The device parameters used in our numerical simulations and the results of the estimations are summarized in Table 6.1. In Fig. 6.21, we show how dephasing time T_2^* scales with the number of chain sites. For a fair comparison, we now choose the model parameters (e.g. $t_i = \Delta_i = 20\mu$eV and lever arms $\alpha_D = 0.04e$) to be identical for all N.

6

6.7.2. NANOFABRICATION AND SETUP

Our hybrid nanowire devices have been fabricated by means of the shadow-wall lithography technique thoroughly described in Heedt et al. (2021). Specific details are described in the *Device structure* paragraph of (Bordin et al., 2024b) and its Supplementary Information, which reports a detailed description of the dilution refrigerator setup as well.

6.7.3. TUNING PROCEDURES

STRONG COUPLING

We report here the tuning protocol we follow to achieve strong coupling between all QD pairs. First, we form QDs that are weakly coupled as in Bordin et al. (2024b). Weakly coupled QDs have high tunneling barriers and sharp Coulomb diamonds since the broadening due to a finite lifetime is smaller than the broadening due to temperature. Secondly, we start to couple the QDs more and more by progressively lowering the tunneling barriers between them. Since, in our system, the coupling between QDs is mediated by ABSs (Liu et al., 2022; Bordin et al., 2023), to optimize the barrier height we look at QD-ABS charge stability diagrams (Zatelli et al., 2024). To optimize, for instance, the right tunneling barrier of QD_1, we measure the zero-bias conductance g_L as a function of V_{QD1} and V_{H1}. As long as QD_1 resonances are not affected by V_{H1}, the tunneling barrier is too high. So we lower the tunneling barrier by increasing the corresponding bottom gate voltage and measure the QD_1-ABS charge stability diagram again. When the QD resonance lines start to bend as a function of V_{H1}, then QD_1 and the ABS start to hybridize, indicating the onset of strong coupling. We repeat this procedure four times, once for every tunneling barrier in between the QDs, as Fig. 6.8 shows. Finally, we check that QD-QD charge stability diagrams show avoided crossings as in Fig. 6.1, indicating a strong coupling between each pair of QDs.

We note that our device doesn't have a normal-metal probe directly connected to QD_2. Therefore, we start by tuning the middle QD while the outer ones are not yet formed. When there is a single tunneling barrier separating, for instance, the right hybrid and the right probe, it is possible to perform tunneling spectroscopy of the right hybrid as Fig. 6.7b shows; and it is also possible to probe QD_2 as long as the right bias V_R is kept below the ABS energies. A possible electron transport mechanism from the right probe to QD_2 is co-tunneling via the ABS, or even direct tunneling if the QD_2 is hybridized with the ABS (Bennebroek Evertsz', 2023). Regardless of the specific mechanism, QD_2 can be probed from the right normal-metal lead, as panels b and c of Fig. 6.8 demonstrate. After tuning the tunneling barriers of QD_2 with the procedure described above, we form QD_1 and QD_3 and tune their inner barriers in the same way, as can be seen in panels a and d of Fig. 6.8. The outer tunneling barriers, i.e. the left barrier of QD_1 and the right barrier of QD_3, are kept high to ensure a low coupling to the normal leads.

POOR MAN'S MAJORANA SWEET-SPOTS

After achieving strong coupling between the QDs, the system needs to be tuned to the pairwise sweet-spot condition of Eq. 6.2. The procedure is similar to what is presented in Dvir et al. (2023). The balance between CAR and ECT is found by looking at the direction of the avoided crossings in the QD-QD charge stability diagrams. We note that

if the QDs are strongly coupled to the ABSs as in Zatelli et al. (2024), CAR and ECT are not well-defined anymore but need to be generalized to even-like and odd-like pairings. Here we stick to the CAR/ECT nomenclature for clarity and reference further readings for the generalized concepts (Zatelli et al., 2024; Liu et al., 2023). An avoided crossing along the positive diagonal indicates CAR dominance and an avoided crossing along the negative diagonal indicates ECT dominance. We select a QD_1-QD_2 charge degeneracy point where it is possible to range from CAR dominance to ECT dominance by varying V_{H1} (Bordin et al., 2023). Similarly, we select a QD_2-QD_3 charge degeneracy point where it is possible to range from CAR dominance to ECT dominance by varying V_{H2}, with the added constraint that the QD_2 resonance must be the same for both choices. This is an important point: to be able to combine the tuning of the left and right QD pairs into a three-site chain, the gate settings of QD_2 must be exactly the same for both pairs. To achieve this, we tune the left pair and the right pair iteratively, converging to a pairwise sweet-spot condition that shares the gate settings of QD_2. For this reason, Fig. 6.2 and Fig. 6.3 share the same settings for all 11 bottom gates, apart, obviously, from $QD_{1,2,3}$ depending on the panel. We note a discrepancy between the estimation of $t_2 = \Delta_2$, which is $\sim 40\,\mu eV$ for Fig. 6.2 and $\sim 60\,\mu eV$ for Fig. 6.3. We attribute such discrepancy to a small charge jump for the right tunneling gate of QD_2 between the two measurements.

When CAR and ECT are balanced for both pairs, the charge stability diagrams show crossings instead of avoided crossings and the spectrum measured at the charge degeneracy points show zero-bias peaks (Fig. 6.2). Away from such sweet spots, the zero-bias peaks are split, as Fig. 6.5a, Fig. 6.17a and Fig. 6.18a show.

Calibration of the voltage difference between the superconducting leads

The superconducting leads of our device are separately grounded via room-temperature electronics. This facilitates the tuning and characterization of QD_2 as shown in ref. (Bordin et al., 2024b). For a precise calibration of the voltage offset between the two superconducting leads, we tune the device to sustain a finite supercurrent (see Fig. 6.11b for an example). With zero voltage drop across the device, a small voltage offset V_{offset} between the room-temperature grounds drops entirely through the resistances of the source and drain DC lines in the dilution refrigerator, $\approx 3\,k\Omega$ each, yielding of total series resistance $R_s \approx 6\,k\Omega$. Connecting a voltage source V_{S1} and a current meter I_{S1} to the first superconducting lead, we can calibrate the offset between the grounds using $V_{S1} - V_{offset} = R_s \cdot I_{S1}$. As long as there is a measurable I_{S1}, this procedure is insensitive to the actual R_s value and is limited only by the resolution of the voltage source. Of course, even if this procedure can be very precise (see also the vertical axis of Fig. 6.11b to appreciate our voltage resolution), we can expect our calibration to drift over time. This can be due, for example, to fluctuations in the room temperature and $1/f$ noise of the electronics equipment. Therefore, we measure the offset with the same precise procedure after a few days and assess how much it can drift. For the first device, such offset was always lower than $1\,\mu V$ and typically closer to $\sim 0.1\,\mu V$. For the second device, concerning only Fig. 6.12 and 6.11, the offset calibration was less rigorous, for Fig. 6.12 we estimate an offset of $\sim 1\,\mu V$. Lastly, we note that a finite voltage applied to the left or right normal-metal leads (V_L or V_R) might lead to an effective voltage difference between the two superconducting leads due to a voltage divider effect (Martinez et al., 2021); we calculate the impact of such effect on the voltage offset between the superconductors to be $\sim 0.1\,\mu V$.

MEASURING THE SPECTRUM AS A FUNCTION OF V_{H1}

To measure the two- and three-site chain spectrum as a function of V_{H1} (Fig. 6.5), we follow the same procedure outlined for two-site chains in ref. (Zatelli et al., 2024). For every V_{H1} set-point, we perform a sequence of three measurements:

1. We set QD_3 off-resonance and measure the V_{QD1}–V_{QD2} charge stability diagram. From the center of the corresponding crossing (when $t_1 = \Delta_1$) or avoided-crossing ($t_1 \neq \Delta_1$), we extract the $\delta V_{QD1} = \delta V_{QD2} = 0$ charge degeneracy point.

2. We measure the two-site chain spectrum at the charge degeneracy point.

3. Finally, we set QD_3 back on-resonance and measure the three-site chain spectrum at the charge degeneracy point.

6

6.8. EXTENDED DATA
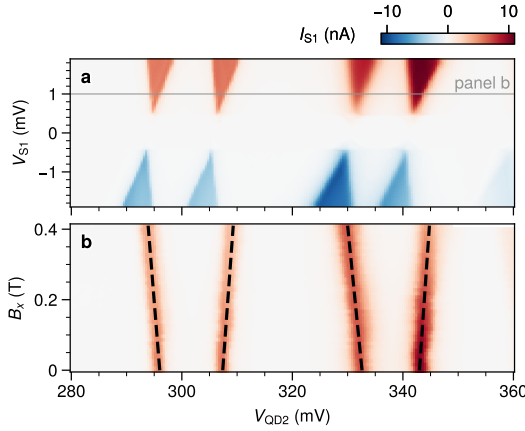
Figure 6.6: **QD spin polarization.** From the QD_2 Coulomb diamonds shown in panel **a**, spanning two orbitals, we extract respectively charging energies of 3.3 and 2.5 meV and lever arms of 0.28 and 0.23. Using such lever arms, we can fit the g-factor from the B_x dependence at $V_{S1} = 1$ mV shown in panel **b**. The black dashed lines yield $g = 45 \pm 7$, on par with our previous measurements (Wang et al., 2022a). With magnetic field $B = B_x = 200$ mT, this gives a Zeeman splitting $E_Z = g\mu_B B = 0.5$ meV, which is much bigger than our temperature broadening (few μeV) and our interdot couplings t_n and Δ_n. If the QDs are strongly hybridized with the ABSs, then the g-factor is renormalized to lower values. Then, a lower bound to the QD g-factor is set by the ABS one, which is ~ 20, as estimated below in Fig. 6.7 and in Ref. (Dvir et al., 2023) (a direct g-factor measurement of strongly hybridized QDs is reported in Ref. (Zatelli et al., 2024)). This gives a lower bound $E_Z > 0.2$ meV for all our QDs. We note that the Zeeman splitting might vary from dot to dot, but as long as $E_Z \gg k_B T, t_n, \Delta_n$, the QDs are well polarized. Finally, two further independent checks are consistent with a high Zeeman energy: first, the QD spectra shown in Fig. 6.9 show isolated lines for all the QD resonances used for the experiment, secondly, the PMM spectra measured when detuning individual QDs, reported in the linked repository, do not show the extra features predicted for low Zeeman energy (Bozkurt et al., 2024; ten Haaf et al., 2024a).
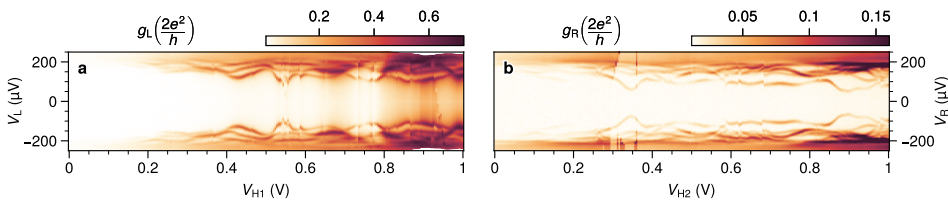
Figure 6.7: **ABS spectroscopy. a.** Spectroscopy of the left hybrid. **b.** Spectroscopy of the right hybrid. Both panels are measured at a fixed external magnetic field roughly parallel to the nanowire $B_x = 200$ mT and exhibit ABSs populating the spectrum. We chose a magnetic field intensity that is large enough to polarize the dots ($\gtrsim 100$ mT) but small enough for the ABSs not to close the gap ($\lesssim 300$ mT). From the ABS energy, we estimate the ABS g-factor to be ~ 20. Both measurements are corrected for a dilution refrigerator line resistance of 7 kΩ.
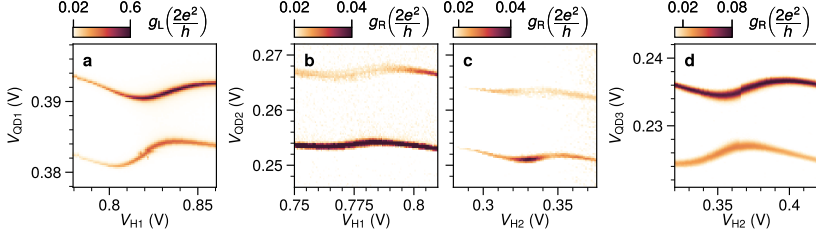
Figure 6.8: QD-ABS charge stability diagrams. a. Left zero-bias conductance as a function of V_{QD1} and V_{H1}. **b, c, d.** Right zero-bias conductance as a function of V_{QD2} and V_{H1} (panel c), V_{QD2} and V_{H2} (panel c), V_{QD3} and V_{H2} (panel d). All panels show how a pair of QD resonances is modulated by the neighboring hybrid gates, indicating QD-ABS hybridization (Zatelli et al., 2024). Panels b and c are measured before forming a QD on the right; here there is a single tunneling barrier separating the right normal lead and the right hybrid so that it is possible to perform spectroscopy of QD_2 from the right normal lead as long as the right bias V_R is smaller than the superconducting gap (Bennebroek Evertsz', 2023).
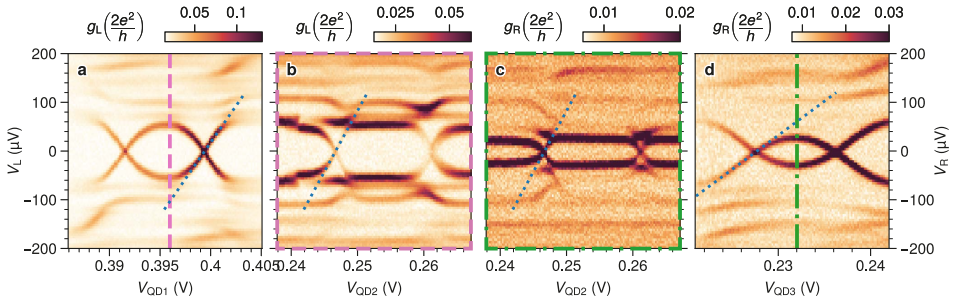
Figure 6.9: QD spectroscopy. a. QD_1 spectroscopy. The QD state appears as an eye shape, while the ABSs of the left hybrid are visible at higher energies (Zatelli et al., 2024). **b.** QD_2 spectroscopy taken from the left probe. Here QD_1 is kept in the middle of the pair of charge degeneracy points shown in panel a: $V_{QD1} = 0.396$ V. QD_1 states appear as persistent lines at $\approx \pm 60\,\mu$V and mix with the ABS and QD_2 spectra. **c.** QD_2 spectroscopy taken from the right probe. Here $V_{QD3} = 0.232$ V. QD_3 states appear as persistent lines at $\approx \pm 25\,\mu$V and mix with the ABS and QD_2 spectra. Both panels show zero energy crossings at ≈ 0.246 and ≈ 0.2615 V, which we attribute to QD_2 charge transitions. **d.** QD_3 spectroscopy. We note that the eye shape is smaller compared to QD_1, which implies a lower lever arm. The lever arms α_n are extracted for all QDs from the slopes of the fitted blue dotted lines; here we find $\alpha_1 = 0.03$, $\alpha_2 = 0.025$ and $\alpha_3 = 0.014$.
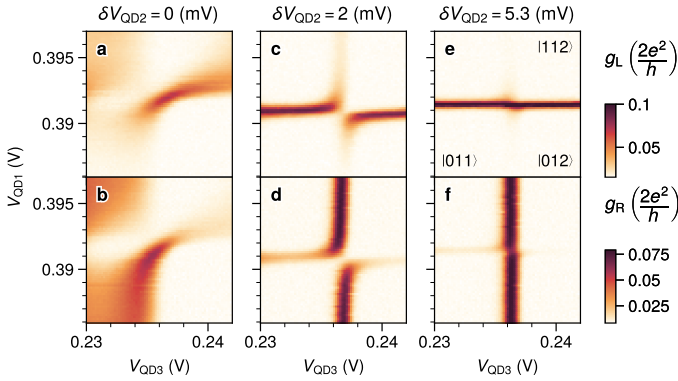
Figure 6.10: **Impact of** QD_2 **on the coupling between the outer dots. a-b.** QD_1–QD_3 charge stability diagrams measured from the left probe (panel a) and the right one (panel b). At the center of the avoided crossing, all QDs are on resonance. **c-d.** Same measurements of panels a and b, but with QD_2 2 mV off-resonance. **e-f.** Here QD_2 is 5.3 mV off-resonance. The more QD_2 is detuned, the smaller the QD_1–QD_3 avoided crossings are. In panels e and f, the avoided crossings are barely noticeable, indicating suppression of the coupling between the outer dots. Finally, we note that not only the size of the avoided crossings but also the amount of conductance indicates suppression of the QD_1–QD_3 coupling: in panel e, the vertical conductance line representing the QD_3 charge transition is barely visible; while in panel f it is the horizontal line corresponding to the QD_1 transition to be suppressed.
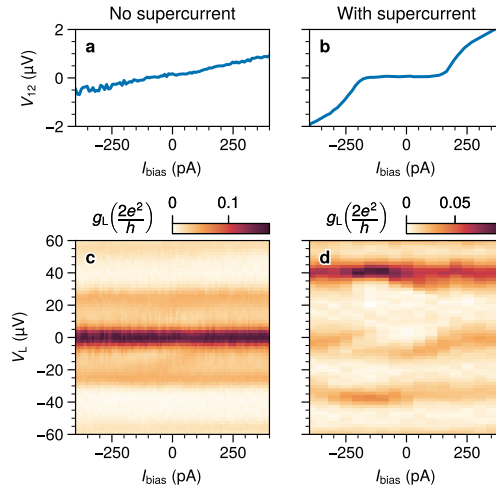
Figure 6.11: **a, b.** I-V curves without and with a measurable supercurrent. The voltage V_{12} between the two superconductors is measured as a function of the current bias I_{bias} between them. See the code in the shared repository for measurement details. **c, d.** Left spectroscopy of a three-site chain as a function of I_{bias}, without and with a measurable supercurrent. To avoid complications due to supercurrent, in all the measurements reported in this manuscript (apart from Fig. 6.11b,d) the tunneling barriers forming QD_2 are kept high enough to suppress the supercurrent. In the left column of this figure, we check that such settings show a linear I-V curve and that the I_{bias} doesn't affect the three-site chain spectrum. To prove that our device can carry supercurrent and this might affect the spectrum of a three-site chain, we lower the QD_2 tunneling barriers and measure what is presented in panels b and d. A detailed investigation of the effects of supercurrent is beyond the scope of this manuscript and is left for follow-up works.
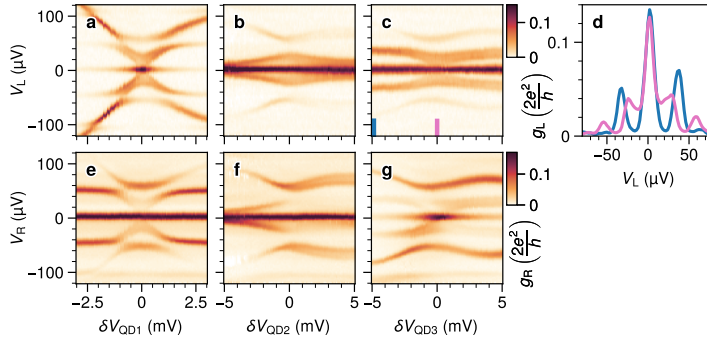
Figure 6.12: **Second device. a-c, e-g.** Left and right tunneling spectroscopy of a second device tuned to the double sweet-spot condition of Eq. 6.2. Here, $t_1 = \Delta_1 \approx 25\,\mu\text{eV}$ and $t_2 = \Delta_2 \approx 50\,\mu\text{eV}$. Such coupling strengths are tuned on purpose to values similar to the ones measured for the device in the main text. The remarkable similarity between this figure and panels a-f of Fig. 3 evidences the determinism and reproducibility of our tuning procedure across multiple devices. This device's QDs, ECT and CAR are characterized at zero external magnetic field in ref. (Bordin et al., 2024b). **d.** Linecuts of panel c at $\delta V_{QD3} = -5\,\text{mV}$ (blue) and $0\,\text{mV}$ (pink) showing that when all QDs are on resonance there is no gap in the conductance (pink line) due to fast phase precession.
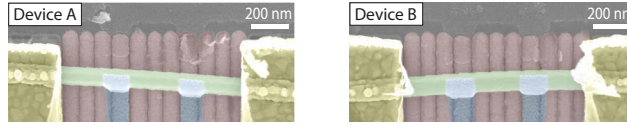
Figure 6.13: **False-colored scanning electron microscope images of both devices.** InSb nanowires (green) are deposited on top of an array of bottom gates (pink) and contacted by superconductors (blue) and normal metals (yellow). The fabrication details are reported in ref. (Bordin et al., 2024b).
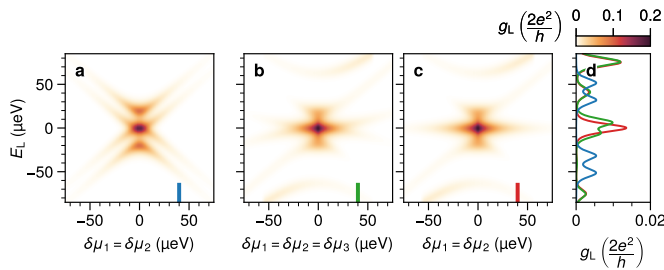
Figure 6.14: **a-d.** Theoretical simulation of Fig. 4 data with the spinless model of Eq. 6.1. All panels report the average conductance of 50 simulations with different phases on Δ_2. The phase choices are uniformly distributed between 0 and 2π. Panel d displays linecuts at $\mu = 40\,\mu\text{eV}$.
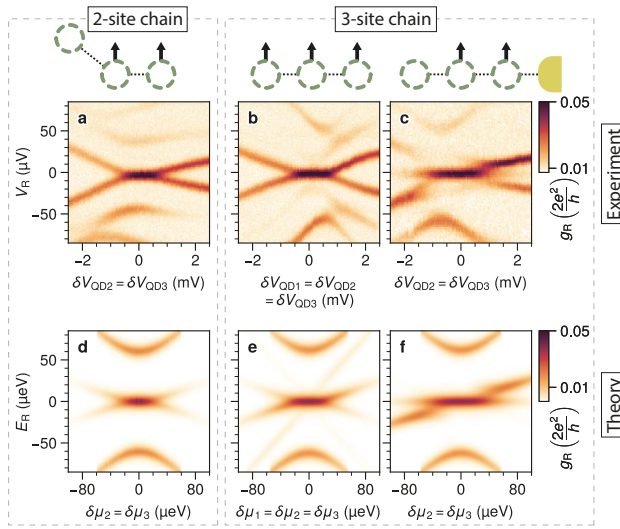
Figure 6.15: **Zero-bias peak stability against variations of the chemical potential. a-c.** Tunneling spectroscopy measured from the right side of the device. **a** Two-site Kitaev chain located on the right side of the device, with the leftmost dot being off-resonance. **b** A three-site Kitaev chain device. Stability of the zero-bias peak against detuning of all constituent quantum dots. The range of voltage variation for stable zero-bias conductance peak is now enhanced relative to the two-site device. **c.** Conductance spectrum for a three-site Kitaev chain when detuning two quantum dots on the right side. In this scenario, the zero-bias conductance peak persists against dot detuning. **d-f.** Theoretical simulations of each detuning scenario with phase averaging. It shows good consistency with the experimental measurements.

6
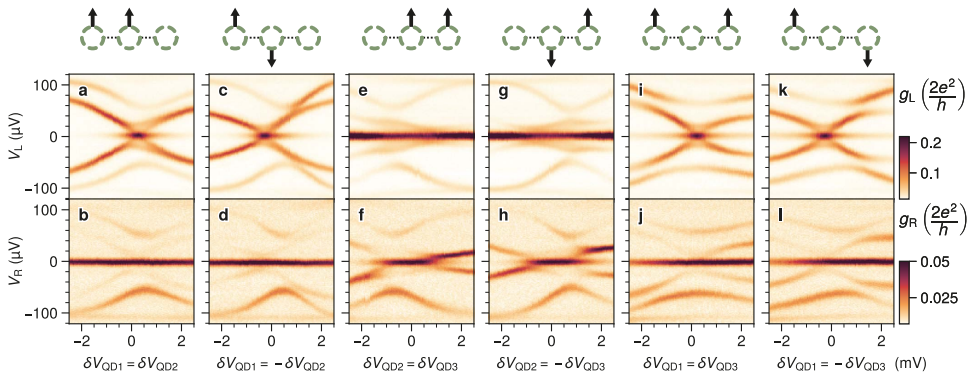
Figure 6.16: **Zero bias peak persistence of a three-site chain while detuning any pair of QDs. a-l.** Tunnelling spectroscopy from the left probe (top row) and the right one (bottom row). **a, b.** Symmetric detuning of QD_1 and QD_2. **c, d.** Anti-symmetric detuning of QD_1 and QD_2. **e-l.** Symmetric and anti-symmetric detuning of any other pair of QDs. All panels show a persistent zero-bias conductance peak over the full detuning range.
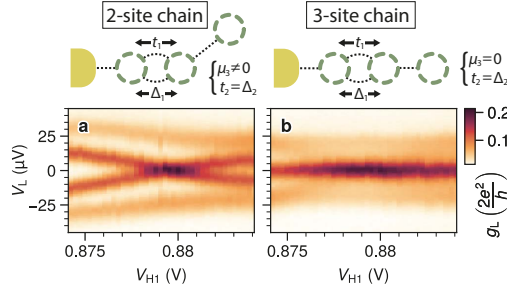
Figure 6.17: **a, b.** Tunneling spectroscopy of a 2-site chain (panel a) and 3-site chain (panel b) as a function of V_{H1}. This measurement is a repetition of what is presented in Fig. 6.5 of the main text but with higher resolution and only around the $V_{H1} \approx 0.88$ V sweet-spot. $\delta V_{QD3} = -4$ mV in panel a and 0 mV in panel b.
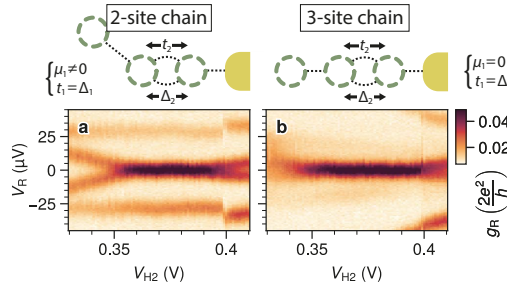
Figure 6.18: **a, b.**. Right tunneling spectroscopy of a 2-site chain (panel a) and 3-site chain (panel b) as a function of V_{H2}. $\delta V_{QD1} = -4$ mV in panel a and 0 mV in panel b. We note that the zero-bias conductance peak of panel a is more stable compared to the one of Fig. 6.5a, we speculate that this is due to accidental similar dispersion of t_2 and Δ_2 as a function of V_{H2} (see also Fig. 6.19). Nevertheless, the 3-site zero-bias conductance peak of panel b is more persistent. We note that such peak broadens and its intensity fades at the edges of the scan, which may indicate the onset of splitting. This can be a result of imperfect centering of V_{QD1} at $\mu = 0$.
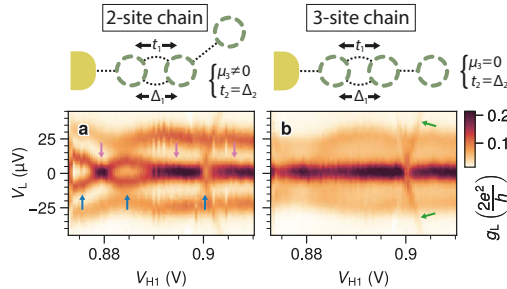
Figure 6.19: **a, b.** Left tunneling spectroscopy of a 2-site chain (panel a) and 3-site chain (panel b) as in Fig. 6.5 and 6.17 but for a different V_{H1} range. Here we can appreciate that even two-site chains can have improved the zero-bias conductance peak stability: the pink arrows highlight three sweet-spot regions, two of which have a more stable zero-bias peak. This can be due, for instance, to accidentally similar dispersion of t_1 and Δ_1 as a function of V_{H1}, which can, in principle, be optimized using the external magnetic field direction (Bordin et al., 2023). However, this requires careful tuning or searching to avoid non-sweet-spot regions, highlighted here with blue arrows. The 3-site chain has instead a stable zero-bias peak over the full range (panel b). We also note, for both panels, the presence of a spurious resonance (green arrows) likely due to an accidental dot near the left probe.
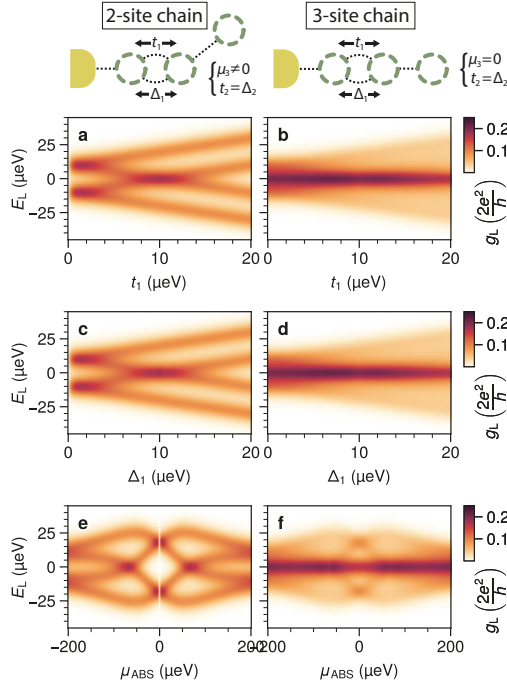
Figure 6.20: **a, b.**. Conductance simulation with t_1 varied from 0 to 20 μeV for a 2-site chain (panel a) and a 3-site chain (panel b) exactly as Fig. 5c,d. $\Delta_1 = 10$ μeV. **c, d.**. Conductance simulations as a function of Δ_1. $t_1 = 10$ μeV. The result is identical to the panels above where t_1 was varied instead. **e, f.**. Conductance simulations in a more realistic scenario, where t_1 and Δ_1 are varied simultaneously as if there were a single ABS mediating them (Liu et al., 2022; Bordin et al., 2023). In all scenarios, the left column – corresponding to 2-site chains – exhibits zero energy crossings, while the right column – corresponding to 3-site chains – shows persistent zero-bias peaks over the full range. For 3-site chain simulations, the conductance is averaged over 50 phase values of Δ_2, uniformly distributed from 0 to 2π.
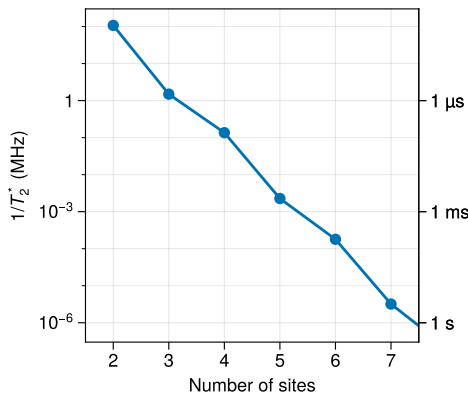
Figure 6.21: **Qubit coherence times as a function of the number of sites, assuming charge noise to be the only source of noise.** For a fair comparison, we assume homogeneity in the Hamiltonian parameters: $t = \Delta = 20$ μeV, $\alpha_D = 0.04$, $\partial t / \partial V_H = 5 \times 10^{-3}$.

7

IMPACT OF ANDREEV BOUND STATES WITHIN THE LEADS OF A QUANTUM DOT JOSEPHSON JUNCTION

Detection and control of Andreev Bound States (ABSs) localized at semiconductor-superconductor interfaces are essential for their use in quantum applications. Here we investigate the impact of ABSs on the supercurrent through a Josephson junction containing a quantum dot (QD). Additional normal-metal tunneling probes on both sides of the junction unveil the ABSs residing at the semi-superconductor interfaces. Such knowledge provides an ingredient missing in previous studies, improving the connection between theory and experimental data. By varying the ABS energies using electrostatic gates, we show control of the switching current, with the ability to alter it by more than an order of magnitude. Finally, the large degree of ABS tunability allows us to realize a three-site Andreev molecule in which the central QD is screened by both ABSs. This system is studied simultaneously using both supercurrent and spectroscopy.

7.1. Introduction

Quantum dots (QDs) confine electrons into orbitals with discrete energies, similar to individual atoms (Kouwenhoven et al., 2001). They find countless applications as sensors (Lu et al., 2003; Zhu et al., 2015), light sources (Michler et al., 2000; García de Arquer et al., 2021) or qubits (Hanson et al., 2007; Burkard et al., 2023). Superconductors, on the other hand, feature an attractive pairing between electrons, condensing them into a sea of Cooper pairs (Tinkham, 2004). One consequence of this pairing is the ability to carry supercurrent: zero-resistance transport of electron pairs. Supercurrent can flow even if two superconducting leads are connected by a thin insulating material or a weak link. Such a system is known as a Josephson junction and forms the core component behind superconducting qubits (Clarke and Wilhelm, 2008; Kjaergaard et al., 2020) and superconducting diodes (Ando et al., 2020).

Using semiconducting QDs as weak links in Josephson junctions combines the precise orbital tunability of QDs with the quantum coherent properties of superconductors, resulting in substantial control over the supercurrent (Jarillo-Herrero et al., 2006; van Dam et al., 2006; Jørgensen et al., 2007; Katsaros et al., 2010; Szombati et al., 2016) and facilitating cQED operation (Bargerbos et al., 2022, 2023a). Intriguingly, QDs can also hybridize with a superconductor. For example, when hosting an odd number of electrons a QD acts as a localized spin 1/2, which becomes screened by quasiparticles at stronger coupling, resulting in a spinless Yu-Shiba-Rusinov ground state (Maurand et al., 2012; Lee et al., 2012; Pillet et al., 2013; Jellinggaard et al., 2016). Control of this interaction allows for tuning of both the ground state composition and the spectrum; an interesting lever for Andreev Spin Qubits (Padurariu and Nazarov, 2010; Hays et al., 2021; Pita-Vidal et al., 2023, 2024b), Kitaev chains (Dvir et al., 2023; Tsintzis et al., 2022; ten Haaf et al., 2024a) and the creation of larger superconducting molecules (Deacon et al., 2015; Probst et al., 2016; Bouman et al., 2020; Estrada Saldaña et al., 2020). However, typical devices are prone to the formation of accidental QDs or localized ABSs due to defects or impurities (Pan and Das Sarma, 2020; Prada et al., 2020; Valentini et al., 2021). Such states are hard to characterize and control and are generally detrimental to device operation. Conversely, recent works have shown that gate-controlled ABSs are useful for tuning the coupling between sites in minimal Kitaev chains (Liu et al., 2022; Bordin et al., 2023; Zatelli et al., 2024; Liu et al., 2024a), spurring further interest into measuring and manipulating them.

In this work, we investigate – theoretically and experimentally – the impact of ABSs on a QD-based Josephson junction, and distinguish its features from a S-QD-S junction. We show how gate-tuning of ABSs affects both the size and gate symmetries of the critical current; an important quantity for e.g. Andreev Spin Qubits, whose readout signal is proportional to it (Pita-Vidal et al., 2023, 2024b). Furthermore, we study the influence of the QD-ABS tunnel coupling on the spin screening of the odd-parity doublet state, by comparing measurements of zero-bias conductance and critical current. In this manner, we realize an ABS-QD-ABS Andreev trimer where the screening of the central QD is facilitated by ABSs in both leads, highlighting their potential use in realizing larger chains and artificial molecules.

7.2. DEVICE
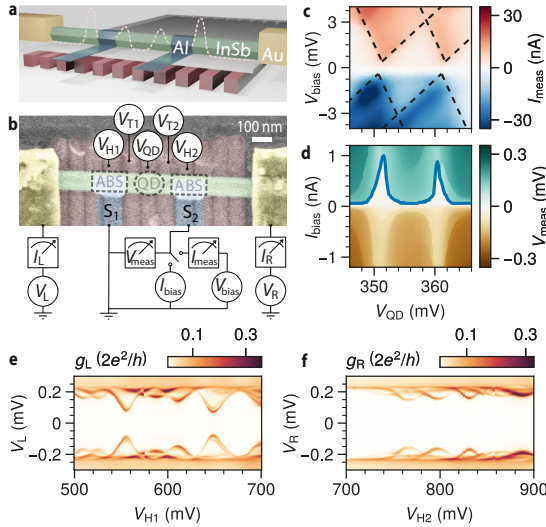
Figure 7.1: **a.** Illustration of the device. **b.** Schematic of the measurement setup on a false-colored scanning electron micrograph of the reported device. **c.** I_{meas} as a function of V_{QD} and V_{bias} showing a single Coulomb diamond. The dashed lines correspond to a QD model with charging energy $U = 2.7$ meV and lever arm $\alpha = 0.26$. **d.** V_{meas} as a function of V_{QD} and I_{bias}. The blue line identifies the switching current, I_{sw}, where the Josephson junction transitions from a superconducting to a resistive regime. **e, f.** Examples of typical tunneling spectroscopy measurements (from a previous cooldown of the same device) of the left and right hybrids respectively; $g_L \equiv \frac{dI_L}{dV_L}$ and $g_R \equiv \frac{dI_R}{dV_R}$ are measured with standard lockin techniques.

A tunable Josephson junction can be realized by contacting a semiconducting nanowire with two superconducting leads (van Dam et al., 2006; Lee et al., 2012; Pillet et al., 2013; Estrada Saldaña et al., 2018). In this work, two Al contacts are deposited on an InSb nanowire using the shadow-wall lithography technique (Heedt et al., 2021), creating two superconducting-semiconducting hybrid segments. In addition, we introduce one Au normal contact at each end of the device. Below the nanowire, separated by a thin dielectric, an array of bottom gates defines an electrostatic potential along the device, as Fig. 7.1a illustrates. The three gates between the hybrid segments form a QD; its chemical potential is controlled by V_{QD} while the barriers are tuned by V_{T1} and V_{T2}. Two additional outer barriers separate each hybrid from the external normal contacts, turning them into tunneling probes.

The device is loaded in a dilution refrigerator with a base temperature of ~15 mK. Both normal contacts are connected to corresponding voltage sources and current meters (V_L, I_L and V_R, I_R). The Josephson junction in the middle of our device is connected to a flexible circuit that enables setting either a voltage bias or a current bias across the junction. Fig. 7.1b shows that while the left Al contact is always grounded, the right one is connected to a switch between either a voltage source with a current meter (V_{bias}, I_{meas}) or a current source with a voltage meter (I_{bias}, V_{meas}). See the Supplementary Information for further nanofabrication and circuit details (Fig. 7.9).

Panel c of Fig. 7.1 reports a voltage bias measurement characterizing the QD's Coulomb blockade diamonds. In panel d, instead, we apply a current bias and observe a $V_{meas} = 0$ region, which is identified as the DC supercurrent regime. The transition from zero to finite voltage is marked by a blue line, with the associated current bias values denoted as I_{sw}, the switching current. An explanation of how I_{sw} is extracted is presented in Fig. 7.10. As previously demonstrated in literature, $I_{sw}(V_{QD})$ depends sensitively on the QD gate voltage. The device behaves like a supercurrent transistor: I_{sw} is maximal at the QD charge degeneracies, where the parity transitions between even and odd, while it is suppressed whenever the QD is off-resonance (Jarillo-Herrero et al., 2006; van Dam et al., 2006).

The novelty of our device is highlighted in panels e and f of Fig. 7.1, which show examples of tunneling spectroscopy measurements performed from the left and the right normal probes, yielding differential conductance g_L and g_R respectively. Both hybrid segments feature ABSs that disperse as a function of the gate voltages V_{H1} and V_{H2}. To understand their implications, we introduce in the following section a minimal three-site model, considering a single ABS on the left, a single QD orbital in the center, and a single ABS on the right.

7.3. Model

The left and right ABSs are modeled as single levels with negligible charging energy ($U_{ABS} = 0$) coupled to BCS superconductors by couplings $\Gamma_{L/R}$ in the atomic limit (Bauer et al., 2007). Both ABSs are tunnel coupled to a central QD with a large charging energy, $U = 10\Delta$, where Δ represents the energy of the superconducting gap. This system is described by the following Hamiltonian:

$$H = H_{ABS} + H_D + H_T \tag{7.1}$$

$$H_{ABS} = \sum_{j=L/R} \left[\xi_j n_j + \Gamma_j d_{j\uparrow}^\dagger d_{j\downarrow}^\dagger + \text{h.c.} \right] \tag{7.2}$$

$$H_D = \frac{U}{2} (n - n_C)^2 \tag{7.3}$$

$$H_T = \sum_{j=L/R} \sum_{\sigma=\uparrow/\downarrow} t_j d_{C\sigma}^\dagger d_{j\sigma} + \text{h.c.} \tag{7.4}$$

Here, $\xi_{L/R}$ are the single-level energies, with $n_{L/R}$ and $d_{L/R\sigma}^\dagger$ denoting the corresponding number and creation operator. These result in ABS excitation energies $E_{L/R} = \sqrt{\xi_{L/R}^2 + \Gamma_{L/R}^2}$ and particle-hole coherence factors $u_{L/R}^2 = \frac{1}{2}\left(1 + \frac{\xi_{L/R}}{E_{L/R}}\right)$ and $v_{L/R}^2 = 1 - u_{L/R}^2$ (Bauer et al., 2007). The central QD is described by a typical Anderson model with creation operators $d_{C\sigma}^\dagger$, the number operator $n = d_{C\uparrow}^\dagger d_{C\uparrow} + d_{C\downarrow}^\dagger d_{C\downarrow}$ and the number n_C describing the electrochemical potential controlled by V_{QD}. Lastly, the QD is tunnel coupled to the ABSs by couplings $t_{L/R} = |t_{L/R}| \exp\left[i\phi_{L/R}\right]$, with the phase drop across the junction characterized by the difference $\phi = \phi_L - \phi_R$. A sketch of the model is depicted in Fig. 7.2a. This model neglects both the detailed structure of the ABSs, e.g. multiple orbitals, and any screening of the QD due to a direct coupling to the BCS density of states (Pillet et al., 2013; Lee et al., 2013), capturing only the screening stemming from the coupling to ABSs. Consequently,

the validity of the model is limited to where ABSs are tuned close to their energy minima. More details can be found in the Supplementary Information. Theory plots in this manuscript are produced with numerical diagonalization of Eq. 7.1, capturing QD-ABS hybridization and its dependence on $u_{L/R}$, $v_{L/R}$ and n_C, for all coupling regimes. Here, we define the junctions critical current as, $I_c = \max_\phi [I(\phi)]$, following typical conventions, which in plots is obtained numerically.
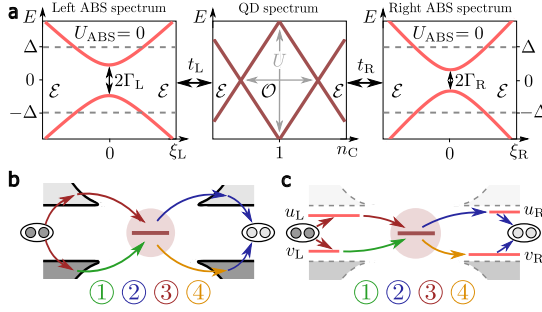
Figure 7.2: **a.** Schematic of the ABS-QD-ABS model depicting the decoupled ($t_{L/R} = 0$) electronic spectrum of each component. The scale Δ illustrates the position of the BCS continuum neglected in the model, while the QD spectrum is shown in scale of U. Symbols $\mathcal{E}$ and $\mathcal{O}$ indicate even and odd ground state parity respectively. Smaller sketches resembling this schematic are used in the following figures to indicate gate settings. **b-c.** Sketches of 4th order cotunneling contributions to the critical current, I_c, for a S-QD-S model (**b**) and an ABS-QD-ABS model (**c**). The numbers below indicate the ordering of the dominant 4th order process for an empty QD, $n = 0$.

For low ABS-QD coupling, intuition on the behavior of I_c can be obtained from the lowest (4th) order perturbation theory in $t_{L/R}$. This yields qualitatively similar I_c curves to a weakly coupled QD junction with BCS leads: QD parity transitions ($n_C = 0.5$ or 1.5) result in peaks of I_c accompanied by a switch from a 0 to a π phase (van Dam et al., 2006; Martín-Rodero and Levy Yeyati, 2011). However, the supercurrent through an S-QD-S junction involves virtual occupation of the BCS continuum, while the supercurrent through an ABS-QD-ABS junction instead relies on the occupation of the ABSs (Fig. 7.2b-c). In the $U \gg \Delta$ limit, the peak I_c is given by:

$$\text{S-QD-S} \qquad I_{c,peak} \approx \frac{8e}{\hbar} \frac{|t_L|^2 |t_R|^2}{2\Delta^3} (\Delta\rho_L)(\Delta\rho_R) \tag{7.5}$$

$$\text{ABS-QD-ABS} \qquad I_{c,peak} \approx \frac{8e}{\hbar} \frac{|t_L|^2 |t_R|^2}{E_L E_R (E_L + E_R)} \left(\frac{\Gamma_L}{2E_L}\right)\left(\frac{\Gamma_R}{2E_R}\right), \tag{7.6}$$

where $\rho_{L/R}$ denotes the density of states. Here, the factors ($\Delta\rho_{L/R}$) and ($\Gamma_{L/R}/2E_{L/R}$) correspond to $|u_{L/R} v_{L/R}|$, which denote the expectation value of adding or removing a Cooper-pair (Estrada Saldaña et al., 2018). Intuitively, the ABS energies $E_{L/R}$ act as a gap and the additional powers of $E_L E_R$ in denominators stem from the asymmetrical coherence factors when $\xi_{L/R} \neq 0$ (Bennebroek Evertsz', 2023). Further details on the calculations, including more terms and the n_C dependence, are reported in Supplementary Information.

This perturbative approach highlights the difference between S-QD-S and ABS-QD-ABS junctions and inspires the next section. Since both $E_{L/R}$ and the $u_{L/R}$ and $v_{L/R}$ components depend on $\xi_{L/R}$, tunable by $V_{H1/H2}$, their effect on the supercurrent can be tested experimentally.

7.4. SUPERCURRENT CONTROL
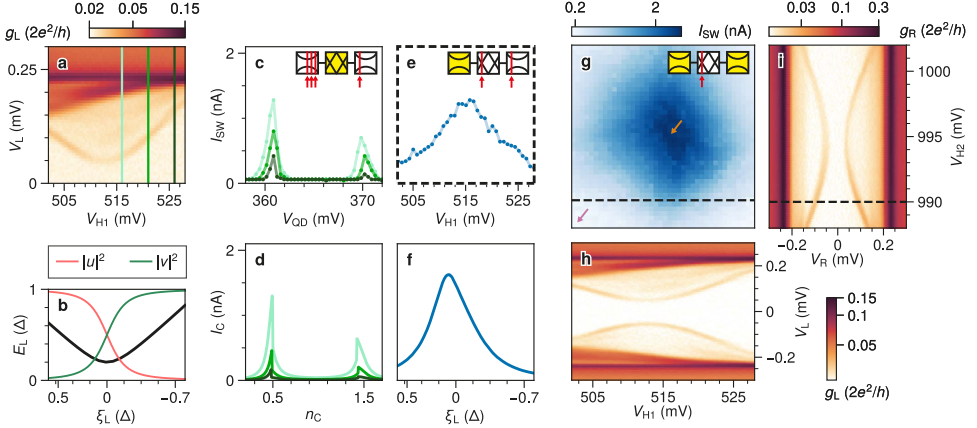
Figure 7.3: **a.** g_L as a function of V_L and V_{H1}, showing the ABS energy dispersion. **b.** ABS energy and square of the particle-hole components u_L and v_L as predicted by the theory model. **c.** I_{sw} as a function of V_{QD} ranging over a single QD orbital and color-coded to the vertical line cuts in panel a. The inset illustrates the chemical potentials of the three sites of our system. When a site is colored yellow, the corresponding chemical potential is varied. Otherwise, a red arrow indicates the fixed position of the chemical potential. **d.** I_c predicted by the theory model. **e.** I_{sw} as a function of V_{H1}, tracing the left QD parity transition in panel c. **f.** Theory I_c as a function of ξ_L, tracing the left QD parity transition in panel d. **g.** I_{sw} as a function of V_{H1} and V_{H2}. The black dashed line indicates the position along V_{H2} at which I_{sw} in panel c and e is measured. See Fig. 7.13 for extra details. **h,i.** Spectra of both hybrids (panel h shows the same data as panel a but including negative V_L values). For both panels, V_{QD} is fixed at 358 mV. All the other figures in the manuscript, excluding Fig. 7.1e,f which were measured in a previous cooldown, make use of the same ABSs shown here.

To test the impact of ABSs on the supercurrent, we focus in Fig. 7.3a on a single ABS weakly coupled to the QD. In panel c, we measure the switching current I_{sw} as a function of V_{QD} at three different positions along V_{H1}, color-coded to the vertical line cuts shown in panel a. We observe an overall increase in I_{sw} as we move closer to the minimum energy of the ABS, which is reproduced by the model in panel d, and which can be understood from the denominator in Eq. (7.6). When comparing theory to experiment we distinguish between measured switching current, I_{sw}, and theoretical critical current, I_c, since I_{sw} might be reduced ($I_{sw} < I_c$) by circuit noise and thermal fluctuations (Tinkham, 2004). In some instances, the employed minimal model predicts I_c to be smaller than the measured I_{sw}. These discrepancies we ascribe to missing critical current contributions from e.g. direct coupling to the BCS states or neighboring QD and ABS orbitals neglected in the model. We stress that all parameters of the model, apart from t_L and t_R, are estimated from independent measurements such as ABS spectroscopy and QD Coulomb diamonds (see Fig. 7.11). The summary of all extracted and fitted model parameters is

reported in the Supplementary Information (Table 1).

So far, we studied the switching current as a function of V_{QD}. To study it instead as a function of V_{H1}, we may track the I_{sw} peak value along one of the QD parity transitions (as detailed in Fig. 7.13c). In Fig. 7.3e we plot I_{sw} (blue) as a function of V_{H1}, tracking the left QD parity transition in Fig. 7.3c. We observe a maximum I_{sw} of 1.28 nA around the ABS minimum energy and a decline in I_{sw} as we move away from this minimum. Notably, I_{sw} is decreased as low as 0.24 nA when E_L approaches Δ, suggesting that most of the supercurrent is mediated via the ABS and not via the BCS continuum. This is supported by the model, which does not include these continuum states and yields a similar decrease in panel f. Finally, we note in panels d and f, that I_c is not symmetric around $n_C = 1$ and $\xi_L = 0$. This feature is visible with the numerical diagonalization of Eq. 7.1 and is not captured by 4th order perturbation theory. We will return to such asymmetries in Fig. 7.8 and in the following section dedicated to stronger couplings (Fig. 7.4).

Thus far, the ABS in the right hybrid was kept at $V_{H2} = 990$ mV. In Fig. 7.3g, we present I_{sw} as a function of both ABS gates. In the corners of panel g, both ABSs are tuned away from their energy minima, resulting in a minimal I_{sw} of 0.12 nA (pink arrow). Along the sides of the panel, a single ABS reaches its energy minimum, resulting in an increase of I_{sw} to ~ 1 nA. In the middle of the panel, both ABSs are positioned at their energy minima, resulting in a maximum enhancement of I_{sw} up to 2.58 nA (orange arrow). Controlling the ABSs, we can modulate I_{sw} by over an order of magnitude.

7.5. ANDREEV TRIMER

After demonstrating switching current control, we turn our attention to the physics of an ABS-QD-ABS molecule. Conceptually, this setup is reminiscent of a S-QD-S junction. However, while the screening states of the S-QD-S junction are of a complicated Kondo-like nature (Martín-Rodero and Levy Yeyati, 2011; Meden, 2019), the ABS-QD-ABS equivalents are simpler. Here, at odd-parity the QD binds to an excited ABS, gaining an exchange energy E_{ex}, of order ~ $|t_{L/R}|^2/U$. If E_{ex} exceeds $E_{L/R}$, then the QD odd-parity ground state is screened and rendered into a molecular singlet state of even parity. To investigate this bonding, we fix the electrochemical potential of the right ABS and study the coupling between the left ABS and the QD by looking at the ABS-QD charge stability diagrams of Fig. 7.4 (the right ABS setpoints are shown in Fig. 7.14). Due to our device geometry, charge stability diagrams can be measured either via tunneling spectroscopy from the normal probes or via supercurrent through our Josephson junction. In the first case, the parity transitions of the QD are identified by zero-bias conductance peaks and, in the second case, by switching current peaks.

We can vary the ABS-QD coupling from weak to strong by tuning V_{T1}. The crossover is characterized by a critical tunnel coupling $t_L^c = \sqrt{U\Gamma_L/6}$ (see the Supplementary Information for a detailed derivation). When the coupling is weak ($t_L \ll t_L^c$, panels a,d) the QD parity transitions are barely shifted along V_{QD} as we sweep V_{H1}. As a result, the odd-parity sector separating the even-parity sectors remains roughly equal in width. In the intermediate coupling case ($t_L \lesssim t_L^c$, panels b,e), the QD parity transitions are visibly modulated and the odd-parity sector is reduced as shown in Fig. 7.4b. In the strong case ($t_L > t_L^c$, panels c,f), the topology of the ABS-QD charge stability diagram is changed (Grove-Rasmussen et al., 2018; Estrada Saldaña et al., 2020): when the ABS is at its energy
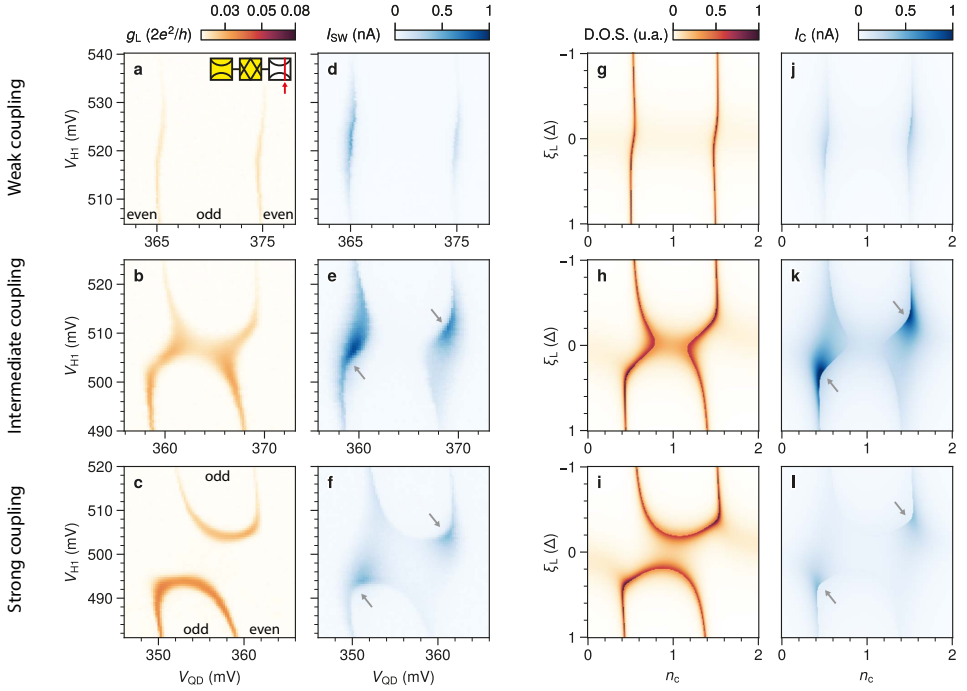
Figure 7.4: **a-c.** Zero-bias conductance g_L as a function of V_{QD} and V_{H1} for weak, intermediate and strong QD-ABS hybridization. The strength is tuned by the tunnel gate voltage $V_{T1} = 210, 220$ and $226\,mV$ for panels a, b and c respectively. The spectrum of the ABSs is reported in Fig. 7.14. **d-f.** 2D maps of the switching current corresponding to the same gate range of panels **a-c**. **g-i.** Theory simulation of the zero-energy density of states using the Lehmann representation at $\phi = 0$ (see Supplementary Information). **j-l.** Simulated critical current using our minimal three-site model. Panels (**g, j**), (**h, k**) and (**i, l**) share the same model parameters.

7

minimum, the system no longer transitions to an odd-parity ground state. All coupling regimes are accurately reproduced by our model in both conductance and supercurrent simulations (panels g-l).

In the weak coupling regime, the switching current could be understood with 4th order perturbation theory; the presence of ABSs quantitatively affects I_c, with $E_{L/R}$ mimicking a smaller Δ. However, in the intermediate and strong coupling regimes, the presence of ABSs leads to a qualitative difference as well: the grey arrows in Fig. 7.4e,f,k,l highlight strong asymmetries in the switching current peak heights. Such asymmetries are due to the u and v components of the ABSs. Approaching e.g. $n_C \sim 0.5$, the ABS-QD hybridization is strongest for an ABS with $|u| \gg |v|$ as then both the ABS and the QD are most easily excited by the addition of an electron. This stronger hybridization results in a higher I_c, as shown also in Fig. 7.7. Switching current peak asymmetries were previously attributed to multiple QD orbitals (van Dam et al., 2006). Here we propose an additional possibility for hybrid devices: asymmetries explained by the coherence factors of subgap ABSs.

7.5.1. SIMULTANEOUS TUNING OF ALL THREE SITES
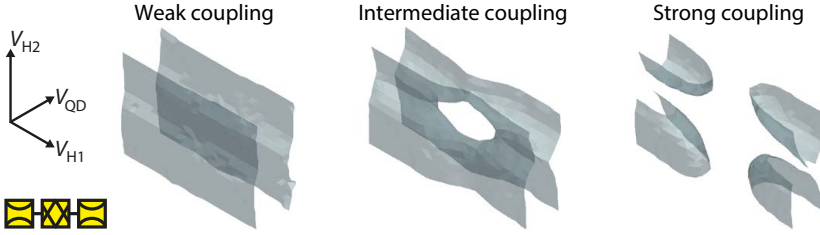
Figure 7.5: Measured 3D charge stability diagrams for weak, intermediate, and strong coupling between the QD and the neighboring ABSs. The blue surfaces delineate the boundaries between even and odd parity. See Fig. 7.12 for the measurement details.

Finally, we turn our attention to the full three-site Andreev molecule by varying the right ABS as well. Fig. 7.5 shows 3D charge stability diagrams extracted from zero-bias conductance measurements (the technique is explained in Fig. 7.12). In the weak coupling regime ($t_L \ll t_L^c$, $t_R \ll t_R^c$), the parity transitions form two parallel planes, isolating an odd-parity region between two even-parity regions; here, varying V_{QD} can always switch the ground state parity, regardless of the ABS tuning, indicating the independence of the three components. In the intermediate coupling regime ($t_L \lesssim t_L^c$, $t_R \lesssim t_R^c$), the situation is different, as can be appreciated by the different topology of the parity transition manifold, which presents a hole connecting the two even-parity regions. In this regime, it is only when both ABSs are simultaneously at their minimum energy that the odd parity sector can be screened to an even parity, indicating $E_{ex} > E_{L/R}$, while a single ABS at minimum energy cannot fully screen the odd parity sector. This shows that the two ABSs can cooperate in the screening of the QD spins, expanding the regions where the system has an even-parity ground state. The even-parity regions expand even further in the strong coupling regime ($t_L > t_L^c$, $t_R > t_R^c$), where the topology of the parity transition manifold is changed once more. Here a single ABS, positioned at its energy minimum, is able to fully screen the odd parity QD state, as observed by the odd-parity domes only being present in the four corners of the diagram where both ABSs are tuned away from their energy minima.

To appreciate the effect on the supercurrent of the parity transitions shown in Fig. 7.5, we focus in Fig. 7.6 on the strong coupling regime. Keeping the QD gate fixed as in panel c, we study the system as a function of both ABS gates. Panel a shows the measured charge stability diagram, while panel b shows the corresponding I_{sw} map. The theory counterpart is presented in panels d and e. These simulations reproduce the experimental features, apart from a discrepancy between I_{sw} and I_c at the center of panels b and e, where both ABSs are tuned to their energy minima. We speculate that this discrepancy stems from the possibility of ground state transitions as a function of phase difference, ϕ. For $\phi = 0$, the two ABSs cooperate in screening the QD. This decreases the odd-parity area shown in panel f, compared to the screening from a single ABS. For $\phi = \pi$, however, the two ABSs compete, expanding the range of the odd-parity ground state (Rozhkov and Arovas, 1999; Pavešić et al., 2024). This results in an area in Fig. 7.6e where the ground state transitions from singlet to doublet as ϕ changes from 0 to π. This area is shown with
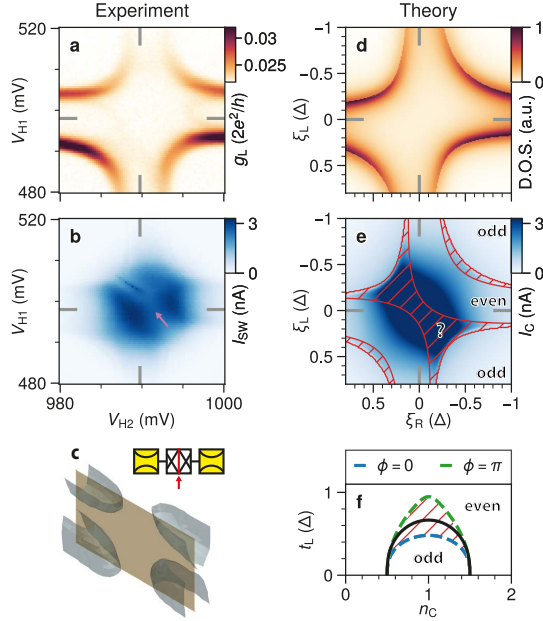
Figure 7.6: **a.** Left zero-bias conductance g_L as a function of V_{H1} and V_{H2} in the strong coupling regime. Grey lines indicate the positions of the energy minima of both ABSs. **b.** A 2D switching current map. In both panel **a** and **b**, V_{QD} is placed between the two QD parity transitions as panel **c** indicates. **d.** Theory simulation of the zero-energy density of states using the Lehmann representation at $\phi = 0$. **e.** Simulated critical current using our minimal three-site model. Panels **d** and **e** share the same model parameters. **f.** A phase space diagram indicating the ground state transitions of the system at $\phi = 0$ (blue) and $\phi = \pi$ (green) for parameters of d and e with $t_L = 0.7$ and $t_R = 0.8$. For comparison, in black the ground state transitions are illustrated assuming a single ABS. The red-shaded areas of panels **e** and **f** indicate the region where $\phi = 0$ and $\phi = \pi$ result in different ground state parities. The question mark indicates that ground state parity is not unique in this region.

red overlays in panels e and f, and qualitatively matches the area of discrepancy between b and e. We recall that our critical current is defined as $I_c = \max_\phi \left[I(\phi) \right]$. If the ground state is unstable as a function of phase, the real device is affected by non-trivial phase dynamics and might switch prematurely to the resistive branch. These phase-induced ground state transitions, appearing solely in the strong coupling regime, are further discussed in the Supplementary Information (Fig. 7.8, 7.16 and 7.17). They are beyond the scope of this manuscript and motivate future works incorporating SQUIDs, which could unveil the interesting phase-dependence of this regime.

7.6. CONCLUSION

In summary, we realized a QD embedded into a Josephson junction with additional side probes revealing neighboring ABSs. These ABSs are shown to be the primary carrier of supercurrent, with measured switching currents matching the predictions of a simple three-site model. This illustrates the crucial role of controlling and detecting localized ABSs in semiconductor-superconductor hybrid devices. Furthermore, by tuning couplings and ABSs we have demonstrated that the system effectively behaves as an Andreev trimer, whose charging diagram can be fully characterized via either supercurrent or normal probe measurements. This additionally exemplifies how ABS tuning can be done via supercurrent in long nanowire-based Kitaev chains, for which the normal probes would be further away from central ABSs (Tsintzis et al., 2024; Miles et al., 2024; Bordin et al., 2024b). Besides that, our study sets the ground for future works on Josephson junction devices with increased complexity, including longer Andreev molecules predicted to modulate the supercurrent non-locally (Kocsis et al., 2024) and complex Andreev spin qubit devices (Pita-Vidal et al., 2024b).

AUTHOR CONTRIBUTIONS

AB, JCW, and DvD fabricated the device. GOS and ALY developed the theoretical model and performed numerical simulations. FJBE and AB performed the electrical measurements with help from GPM and NvL. AB and TD designed the experiment. EPAMB provided the nanowires. LPK supervised the project. AB, FJBE, GOS, ALY, and LPK prepared the manuscript with input from all authors.

DATA AVAILABILITY

All raw data in the publication and the analysis code used to generate figures are available at `https://doi.org/10.5281/zenodo.10711820`. For every dataset, the `exp_name` attribute reports the corresponding gate settings.

7.7. SUPPLEMENTARY INFORMATION

7.7.1. THEORY

MODEL DETAILS

In this section, we elaborate on the theory used in the main text. In general, the coupling of an interacting QD with a superconducting gap leads to the formation of YSR states which, in full treatment, requires techniques able to capture strong interaction, e.g. the Numerical Renormalization Group (NRG) (Bauer et al., 2007). In this paper we instead opt for a minimal model, capturing the dynamics of an ABS coupled to a QD qualitatively. We assume that both the left and right ABS can be described as a non-interacting resonant level ($U_{\mathrm{ABS}} = 0$) coupled to a superconducting lead with gap Δ, shown in eq. (1-4) of the main text. The full Hilbert space of this Hamiltonian is 64×64 and can be numerically diagonalized to obtain measurables. The supercurrent is given by,

$$I(\phi) = \frac{2e}{\hbar} \frac{\partial F(\phi)}{\partial \phi} \stackrel{T=0}{=} \frac{2e}{\hbar} \frac{\partial E_g(\phi)}{\partial \phi} \tag{7.7}$$

with the systems free energy, F, being fully characterized by the ground state energy, $E_g(\phi)$, at zero temperature, $T = 0$, which is the limit used in the main paper. In our device geometry, we don't have active control over the phase, which therefore adjusts itself to satisfy the current-phase relationship $\phi(I_{\mathrm{bias}}, I_c)$. The critical current is given by $I_c = \max_{\phi}\left[I(\phi)\right]$ and, for a sinusoidal current phase relation, is either at $\phi = \pi/2$ or $\phi = 3\pi/2$ for even and odd ground state parity respectively (van Dam et al., 2006).

In the weak coupling limit, $t_{\mathrm{L/R}} \ll U, \Gamma_{\mathrm{L/R}}$, the critical current can also be analytically obtained via 4th order perturbation of the current operator in t_{L} and t_{R} (Novotný et al., 2005; Estrada Saldaña et al., 2018),

$$I_c(n = 0) = \frac{e}{\hbar} \frac{\Gamma_{\mathrm{L}}\Gamma_{\mathrm{R}}|t_{\mathrm{L}}|^2|t_{\mathrm{R}}|^2}{E_{\mathrm{L}}E_{\mathrm{R}}} \Big[\frac{4}{(E_1 - E_0 + E_{\mathrm{L}})(E_2 - E_0)(E_1 - E_0 + E_{\mathrm{R}})} \tag{7.8}$$
$$+ \frac{2}{(E_1 - E_0 + E_{\mathrm{L}})(E_{\mathrm{L}} + E_{\mathrm{R}})(E_1 - E_0 + E_{\mathrm{R}})} \Big],$$

$$I_c(n = 1) = \frac{e}{\hbar} \frac{\Gamma_{\mathrm{L}}\Gamma_{\mathrm{R}}|t_{\mathrm{L}}|^2|t_{\mathrm{R}}|^2}{E_{\mathrm{L}}E_{\mathrm{R}}} \Big[\sum_{k=0,2} \frac{1}{(E_k - E_1 + E_{\mathrm{L}})(E_{\mathrm{L}} + E_{\mathrm{R}})(E_k - E_1 + E_{\mathrm{R}})} \tag{7.9}$$
$$+ \sum_{m=\mathrm{L,R}} \frac{2}{(E_0 - E_1 + E_m)(E_{\mathrm{L}} + E_{\mathrm{R}})(E_2 - E_1 + E_m)} \Big],$$

$$I_c(n = 2) = \frac{e}{\hbar} \frac{\Gamma_{\mathrm{L}}\Gamma_{\mathrm{R}}|t_{\mathrm{L}}|^2|t_{\mathrm{R}}|^2}{E_{\mathrm{L}}E_{\mathrm{R}}} \Big[\frac{4}{(E_1 - E_2 + E_{\mathrm{L}})(E_0 - E_2)(E_1 - E_2 + E_{\mathrm{R}})} \tag{7.10}$$
$$+ \frac{2}{(E_1 - E_2 + E_{\mathrm{L}})(E_{\mathrm{L}} + E_{\mathrm{R}})(E_1 - E_2 + E_{\mathrm{R}})} \Big],$$

where $E_0 = Un_{\mathrm{C}}^2/2$, $E_1 = U(1 - n_{\mathrm{C}})^2/2$, and $E_2 = U(2 - n_{\mathrm{C}})^2$ are the QD eigenenergies. Analytical expressions of 4th or higher order perturbation terms can be obtained using `pymablock` (Araya Day et al., 2023; Araya Day et al., 2024).

Lastly, we evaluate the electron and hole component of the Lehmann representation from the eigenstates of eq. (1-4) of the main text using,

$$G_{je}^R(\omega) = \sum_i \sum_\sigma \frac{|\langle i|d_{j\sigma}^\dagger|g\rangle|^2}{\omega - E_i + E_g + i\eta} \qquad (7.11)$$

$$G_{jh}^R(\omega) = \sum_i \sum_\sigma \frac{|\langle i|d_{j\sigma}|g\rangle|^2}{\omega - E_i + E_g + i\eta} \qquad (7.12)$$

with $|g\rangle$ indicating ground state and the sum of i is over all other excitation's. A broadening, η, has been added for visibility. Using these, the local tunneling density of states (DOS) of site j, as probed by a weakly coupled metallic lead (Domínguez and Yeyati, 2016), is given by,

$$\text{DOS}_j(\omega) = \text{Im}\left[G_{je}(\omega) + G_{jh}(-\omega)\right], \qquad (7.13)$$

which can be compared to measurements of the tunneling DOS using either the left or right metallic lead as a probe. Throughout the paper, we plot the DOS in arbitrary units, as the magnitude depends on unknown quantities such as the initial density of states, etc. In general, we find that the theory matches experimental data to a qualitative degree across most gate settings. An exception occurs in the regimes where one or both ABSs are brought far away from their energy minima, such that $E_{L/R} \approx \xi_{/R} > \Delta$. The primary contribution to both the screening of the QD and supercurrent across it then stems from the gap, which is not captured by the model.

CRITICAL COUPLING $t_{L/R}^c$

In the section "Andreev trimer" we define the boundaries between coupling regimes in terms of $t_{L/R}^c$ which we derive here. In the Hamiltonian of Eq. (1) at $n_C = 1$ (half-filling), and considering $t_L \approx 0$ while neglecting the right ABS, the ground state is given by the odd-parity half-filled QD with spin σ_C and energy $E_{\mathscr{O}} = 0$, denoted $|0_L, \sigma_C\rangle$. The first excited even-parity state (assuming $U/2 \ll E_L$) is given by $|\sigma_L, \sigma_C\rangle$, with σ_L denoting the spin of an excited ABS and energy $E_{\mathscr{E}} = E_L$. Next, using quasi-degenerate perturbation theory we expand to second order in t_L to truncate higher energy states. For the even parity we consider only the lowest energy exchange state, $|S_{\text{ex}}\rangle = \frac{1}{\sqrt{2}}(|\uparrow_L, \downarrow_C\rangle - |\downarrow_L, \uparrow_C\rangle)$. From this, we obtain the following modified energies of the even and odd parity states,

$$E_{\mathscr{O}} = -2\frac{t_L^2}{U + 2E_L}, \qquad E_{\mathscr{E}} = E_L - 8\frac{U t_L^2}{U^2 - 4E_L^2}. \qquad (7.14)$$

Further, assuming $U \gg 2E_L$, we find that a ground state transition occurs at $E_L = 6t_L^2/U$, which yields the critical value $t_{L/R}^c = \sqrt{U\Gamma_{L/R}/6}$ for the particle-hole symmetrical point $E_{L/R} = \Gamma_{L/R}$ used in the main text. This term yields the screening threshold for a single ABS-QD system, while the screening of the joint ABS-QD-ABS system is more complicated, also depending on the $u_{L/R}$, $v_{L/R}$ factors of the ABSs, which do not influence $t_{L/R}^c$.

CRITICAL CURRENT ASYMMETRIES

Next, we discuss various regimes of the model and its impact on experimental interpretation. In Fig. 7.7a, we show I_c at weak coupling such that the 4th order approximation is
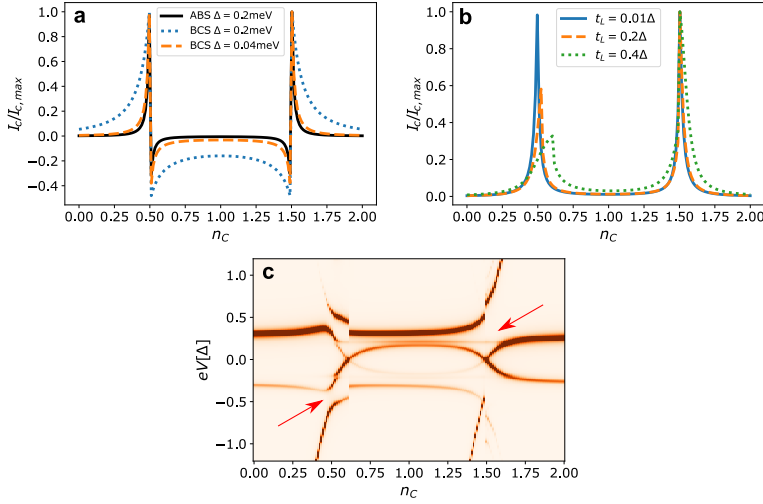
Figure 7.7: **a** Comparison between S-QD-S and ABS-QD-ABS in the low coupling limit, which for ABS is $t_L = t_R = 0.01\Delta$ and for BCS corresponds to coupling rate $\Gamma_{LS} = \Gamma_{RS} = 0.001\Delta$. Furthermore, $U = 2$ meV and $\xi_L = \xi_R = 0.0$ for all plots. Negative I_c indicates π-phase. **b** Highlight of I_c asymmetry at higher t_L for finite detuning, $\xi_L = -0.2\Delta$, with $\Delta = 0.2$ meV, $U = 10\Delta$, $t_R = 0.1\Delta$, and $\xi_R = 0.0$. **c** DOS for identical parameters as **b** with $t_L = 0.4\Delta$ and $\phi = 0$.

valid, and compare it to the standard BCS 4th order result (Estrada Saldaña et al., 2018). In general for both models, if U/Δ is increased I_c becomes more confined around the parity transitions. Choosing $\Delta = \Gamma_L = \Gamma_R$ yields very similar curves between ABS and BCS, supporting that in the low coupling regime the ABSs qualitatively act as reduced gaps. In Fig. 7.7b we show that for finite ABS detuning, $\xi_L = 0.2\Delta$, the critical current is initially symmetric between the two parity transitions for low coupling ($t_L = 0.01\Delta$), but becomes asymmetric as the coupling is increased. This highlights the breakdown of the 4th order expansion, which is always symmetric, and the appearance of QD-ABS hybridization. In Fig. 7.7c we show the DOS for similar parameters and highlight the different sizes of anti-crossings which correlate with the I_c asymmetry. This relates to the coherence factors of the ABSs; for positive ξ_L, the hole component v_L is amplified while at the 2 to 1 QD parity transition the QD is also most easily excited by the removal of an electron. At the 0 to 1 transition, there is a mismatch as the QD is most easily excited by the addition of an electron, and so the hybridization is smaller.

PHASE-INDUCED GROUND-STATE PARITY TRANSITIONS

Finally, we discuss the strong coupling regime shown in Fig. 7.6 of the main text, and the dissimilarity between measured switching current and critical current in proximity to $\xi_L \approx \xi_R \approx 0.0$. In this regime, the current phase relation (CPR) becomes largely non-sinusoidal with ground state transitions occurring as a function of ϕ, as can be seen in Fig. 7.8b-g. This is distinct from other explored regimes for which the CPR is mostly sinusoidal. Here, ground state transitions are apparent in b and c, while d stays singlet for all ϕ and shows a more sinusoidal CPR in g. The skewed CPRs shown in e and f are related
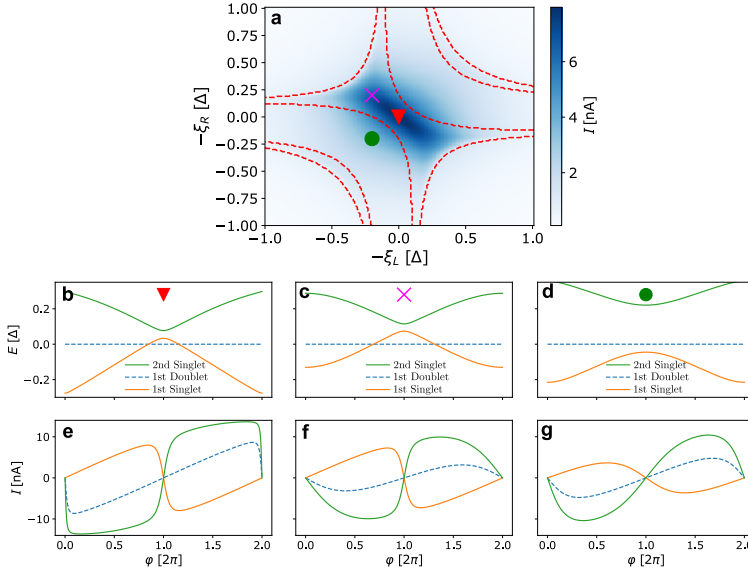
Figure 7.8: **a** Full range I_c plot identical to Fig. 7.6 of the main text. Icons indicate ξ_L and ξ_R settings in plots below. **b-d** State dispersion as a function of ϕ of the three lowest energy states for; **b** $\xi_L = \xi_R = 0.0$, **c** $\xi_L = 0.2\Delta$, $\xi_R = -0.2\Delta$, and **d** $\xi_L = \xi_R = 0.2\Delta$. Full lines indicate singlet parity states, while dashed lines indicate doublet parity. **e-g** Associated CPR of the three states plotted above. Colors indicate state matching state in plots above.

to small anti-crossings between the two lowest singlet states as seen in b and c. All this together leaves some complications in how to interpret the measured switching current as we will now discuss. In a typical Resistively and Capacitively Shunted Junction (RCSJ) model, the supercurrent branch corresponds to a particle at rest in a washboard potential at a finite phase, $\phi = \arcsin(I/I_c)$ with no voltage drop across the junction, $V = 0$ (Tinkham, 2004). Here the washboard is given by the sinusoidal CPR of the ground state, which is assumed to be unchanging. The stability of this branch relates to the possibility of escaping into a running finite voltage state, $V \neq 0$, where the phase, ϕ, evolves with time. For our system, in e.g. Figs. 7.8c,f, the washboard potential would be skewed due to the non-sinusoidal CPR of either the singlet or doublet state (depending on which is occupied) yielding more complicated RCSJ dynamics. In addition, as the not occupied state has lower energy in parts of the CPR, a parity-changing relaxation process can occur as ϕ evolves, resulting in a change of CPR and thus washboard potential. The full dynamics of this system would depend on the singlet to doublet relaxation rate compared to the rate of ϕ change, typically dictated by circuit impedance at GHz frequencies, as well as the circuit details. A full treatment of this is beyond our scope. We simply note a correspondence between the range where model and experiment do not match well and the range where ground state transitions occur as a function of ϕ. This area is marked by red lines in both Fig. 7.6 and Fig. 7.8.

7.7.2. METHODS

NANOFABRICATION

The nanofabrication process is identical to what is reported in ref. (Bordin et al., 2024b). An InSb nanowire is deposited with a micromanipulator on top of pre-patterned bottom gates (3/17 nm of Ti/Pd). We note that while our device has 11 bottom gates as in (Bordin et al., 2024b), only 7 of them are necessary for the experiment of the present manuscript: 3 central gates are used to form a QD, 2 gates – one per hybrid – are used to control the ABSs and 2 more gates are used to form tunneling barriers between the superconducting contacts and the outer normal-metal ones. The remaining 4 gates are not used, they are held at a fixed positive voltage for the full duration of the experiment. This ensures that the corresponding portions of the nanowire are not pinched-off and always conduct.

A bi-layer dielectric deposited with ALD separates the gates from each other and from the nanowire (10/10 nm of Al_2O_3/HfO_2). The superconducting Al contacts are deposited with the shadow-wall lithography technique after removal of the native oxide on the surface of the nanowire via hydrogen cleaning (Heedt et al., 2021). Finally, 10/120 nm of Cr/Au contacts are deposited on the two sides of the device with standard e-beam lithography after the removal of the native oxide with Ar milling.

We note that most choices of thicknesses and materials are not critical. The essential requirements are the creation of a QD in a Josephson junction and the formation of ABSs, which are ubiquitous across diverse platforms (De Franceschi et al., 2010). In our specific material combination, the ABSs are particularly visible thanks to the otherwise hard gap of our InSb-Al hybrids (Heedt et al., 2021), they are isolated from each other thanks to the confining geometry, they can extend far below the Al energy gap thanks to the tunability of our semiconductor (van Loo et al., 2023), and they can be analyzed thanks to the normal-metal probes on either side of our device. We have empirically demonstrated the impact of such ABSs on the supercurrent, emphasizing that it should not be disregarded in any Josephson junction device defined in hybrid materials, including superconductors in combination with InSb, InAs, Si, Ge nanowires and 2DEGs, carbon nanotubes and others.

ELECTRICAL CIRCUIT

The device is placed inside a dilution refrigerator with a base temperature of ≈ 15 mK. It is connected to standard measurement equipment via fridge lines, resulting in an in-series resistance R_F at multiple points in the circuit as illustrated in Fig. 7.9.

The normal leads of the device, N_L and N_R, are connected to independent voltage sources, V_L and V_R, and current meters, I_L and I_R. The use of operational amplifiers results in an additional series resistance R_{OA} added to R_F. In all experiments presented in this work, R_L, R_R and $R_{QD} \gg R_F + R_{OA}$ such that their effect on transport experiments is negligible. We have, therefore, not corrected our data for voltage drops across these circuit resistances. Conductance measurements are performed using lock-in techniques with an AC excitation between 5 and 10 μV.

The superconducting leads, S_1 and S_2, allow for both a voltage and current bias on the Josephson junction. In either configuration, S_1 is grounded and S_2 is driven. Transitioning between setups occurs via a switch as indicated in Fig. 7.9. To prevent a potential
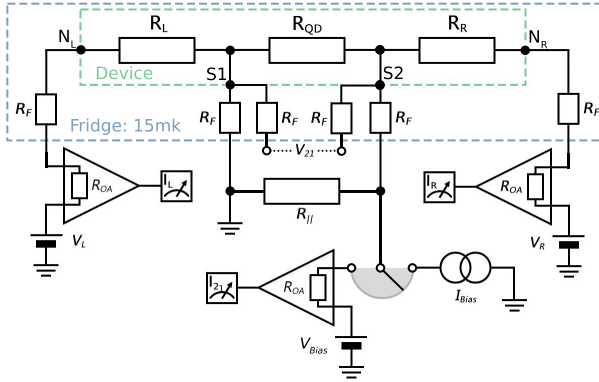
Figure 7.9: The measurement setup. The device is enclosed by the green dashed line. R_{L}, R_{R} and R_{QD} represent the tunneling barriers used for spectroscopy and the formation of the QD. The blue dashed line denotes the part of the circuit placed inside the dilution refrigerator at 15 mK. The device is connected to standard measurement equipment outside the fridge by fridge lines with a resistance R_{F}. The switch allows for the transition between voltage- and current-biased experiments on the Josephson junction. The switch is presented open in this figure.

build-up of large voltages when the switch is open, an additional transport channel is created between S_1 and S_2 via a parallel resistor $R_{||} = 10\,\mathrm{M\Omega}$.

In the voltage bias setup, S_2 is connected to a voltage source V_{bias} and current meter I_{meas}. This setup allows for characterization measurements of the QD in the form of Coulomb diamonds. For these measurements, I_{21} is always corrected for the leakage current flowing through $R_{||}$ and R_{R}. To minimize the leakage current, we aim for $R_{||}$ and $R_{\mathrm{R}} \gg R_{\mathrm{QD}}$.

In the current bias setup, S_2 is connected to a current source I_{bias}. The voltage over the junction V_{21} is measured using a four-probe configuration to circumvent the fridge line resistances as illustrated in Fig. 7.9. It is essential that, whilst in the supercurrent regime, all current flows through the Josephson junction and none through other transport paths such as $R_{||}$ or R_{R} to accurately determine I_{sw}. This is ensured by the fact that $R_{\mathrm{QD}} = 0$ in the supercurrent regime. When the Josephson junction is resistive, this no longer holds and some of the applied current will leak away. We argue that this is not relevant since we are generally only interested in the supercurrent regime of the junction.

CONTACT AND GATE SETTINGS

The voltage biases on the leads (V_{L}, V_{bias}, V_{R}) are varied only during spectroscopy measurements; otherwise, they are kept at 0 V.

The voltages set on the 11 bottom gates are always specified in the `exp_name` attribute of every measurement. If a gate is swept, the initial value is specified. For instance, the gate settings of Fig. 7.1c,d have the following values (in mV):
500, 500, -100, 481 (V_{H1}), 226 (V_{T1}), 345 (V_{QD}, swept), 241 (V_{T2}), 995 (V_{H2}), -117, 700, 700.
The 3 gates on the left and the 3 gates on the right of the device are fixed so that, on each side, the two external ones are always at high voltage and the one closest to the superconductor is forming a tunneling barrier, they are basically never varied (they are

significantly different only for the measurement of Fig. 7.1e,f since they are from a previous cooldown). A label is given only to the 5 gates in the center of the device. V_{H1}, V_{QD}, and V_{H2} control the left ABS, the QD, and the right ABS, respectively. They are continually varied; therefore, most figures highlight in yellow the swept one(s) and in red the set-points of the fixed one(s). Finally, V_{T1} and V_{T2} control the tunnel couplings between the QD and the ABSs. They are never swept; they are varied only to set the ABS-QD hybridization to be either weak, intermediate or strong. There is obviously a sensible cross-talk between neighboring gates so that the raw values of V_{T1} and V_{T2} are not very meaningful out of context; the coupling strength is better assessed from the ABS-QD charge stability diagrams as shown in Fig. 7.4 rather than looking at the raw voltages. On the other side, the cross-talk between next-to-nearest-neighbor gates is negligible due to the efficient screening of electric fields operated by the two superconducting strips on top of the device and by the nearest-neighbor gates at the bottom; so that any experiment that fixes V_{T1} and V_{T2} and sweeps any combination of V_{H1}, V_{QD} and V_{H2} can be performed without invoking virtual gates. See, for instance, Fig. 7.16.

SWITCHING CURRENT EXTRACTION
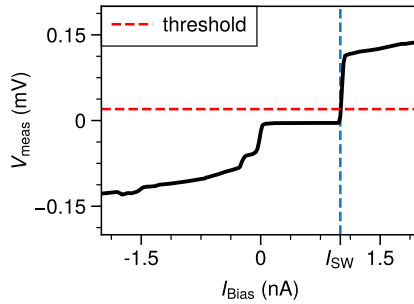
Figure 7.10: An I-V curve of the QD Josephson junction, extracted from Fig. 7.1d. The red dashed line denotes a threshold of 20 μV, placed on V_{meas}. I_{sw} is extracted as the last measured point along I_{bias} below the threshold. Above this threshold, the junction is assumed to be resistive. Due to the sharp transition, this procedure is not sensitive to the threshold choice: we tested multiple values between 10 and 50 μV and observed no appreciable difference in the I_{sw} extracted.

FITTING PROCEDURE

Estimating the theory model parameters relies on a variety of measurements, presented in Fig. 7.11a-c. The Hamiltonian parameters are illustrated in panel g. Both the ABS chemical potential $\xi_{L/R}$ and the coupling between ABS and superconductor $\Gamma_{L/R}$ can be estimated from ABS spectroscopy by comparing panels (b, e) and (c, f). We note that although the same ABSs are used throughout this work, $\Gamma_{L/R}$ may vary slightly from figure to figure since it is sensitive to changes in the potential landscape generated by the gates, see details in the linked repository. Therefore, for every measurement presented in the main text, we monitor the ABS spectroscopy, from which we extract $\Gamma_{L/R}$ and $\xi_{L/R}$. The charging energy can be extracted from Coulomb diamonds presented in Fig. 7.1c, which leaves the couplings between the QD and the ABSs $t_{L/R}$ as the only free parameters. $t_{L/R}$ are estimated based on the best fit to the experiment (panel a).
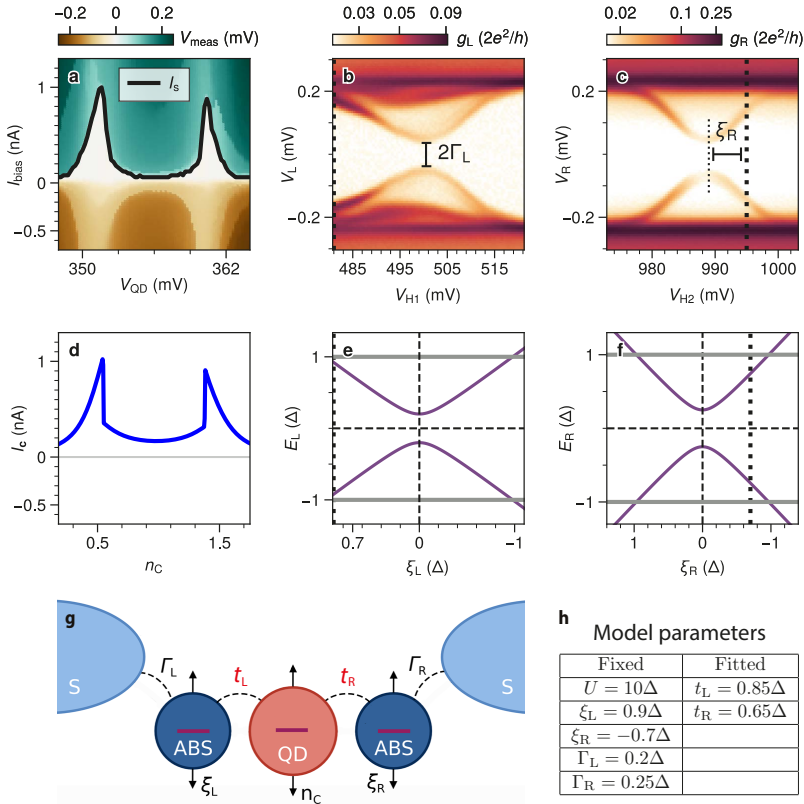
Figure 7.11: **The fitting procedure. a.** V_{meas} as a function of V_{QD} and I_{bias}. V_{meas} is saturated at 250μV. The black line denotes I_{sw}, extracted at a threshold of 20μV. **b, c.** The sub-gap excitation spectra measured from N_L and N_R as a function of V_{H1} and V_{H2} respectively. The dotted lines indicate the positions along V_{H1} and V_{H2} at which the supercurrent measurement of panel c was taken. **d.** A calculation of I_c as a function of n_C, controlling the occupation of the QD. **e, f.** The excitation spectrum of the left and right ABS as a function of ξ_L and ξ_R, simulated by the exact model. Grey horizontal lines indicate the gap edge. The dotted lines denote ξ_L and ξ_R as estimated from the experimental data in panel **b** and **c**. **g.** A schematic of the model, depicting all parameters. **h.** The model parameters used for panel **d**. Fixed parameters are estimated based on ABS spectroscopy and Coulomb diamonds.

Rendering of 3D charge stability diagrams

Every 3D charge stability diagram of Fig. 7.5 is extracted from a series of twenty V_{H1}−V_{QD} 2D zero-bias conductance maps at different V_{H2} set-points, as shown if Fig. 7.12. From every 2D conductance map, we extract the charge degeneracy points with the following algorithm. First, the 2D map is smoothed with a Gaussian filter, then, a Hessian filter highlights the ridges by extracting the minimum eigenvalues of the matrix of second derivatives; for both filters, we use functions of the `scikit-image` python package. Finally, a custom `find_ridge` routine extracts the charge degeneracy points from the filtered 2D map starting from the maxima on the top and bottom edges and following the pixels with maximum values. A representative example of this procedure is shown in the top row of Fig. 7.12. The bottom part of Fig. 7.12 shows the result of the charge degeneracy point extraction on top of all the raw 2D conductance maps of the intermediate coupling regime. Similar plots for the weak and strong regimes are shared in the linked repository. After all charge degeneracy points are extracted, they can be converted into a 3D manifold with a point-cloud-to-mesh conversion function. Specifically, we used the `reconstruct_surface` function of the `pyvista` python package.

All raw data, code, and extracted charge degeneracy points for all coupling regimes are shared in the linked Zenodo repository.

7
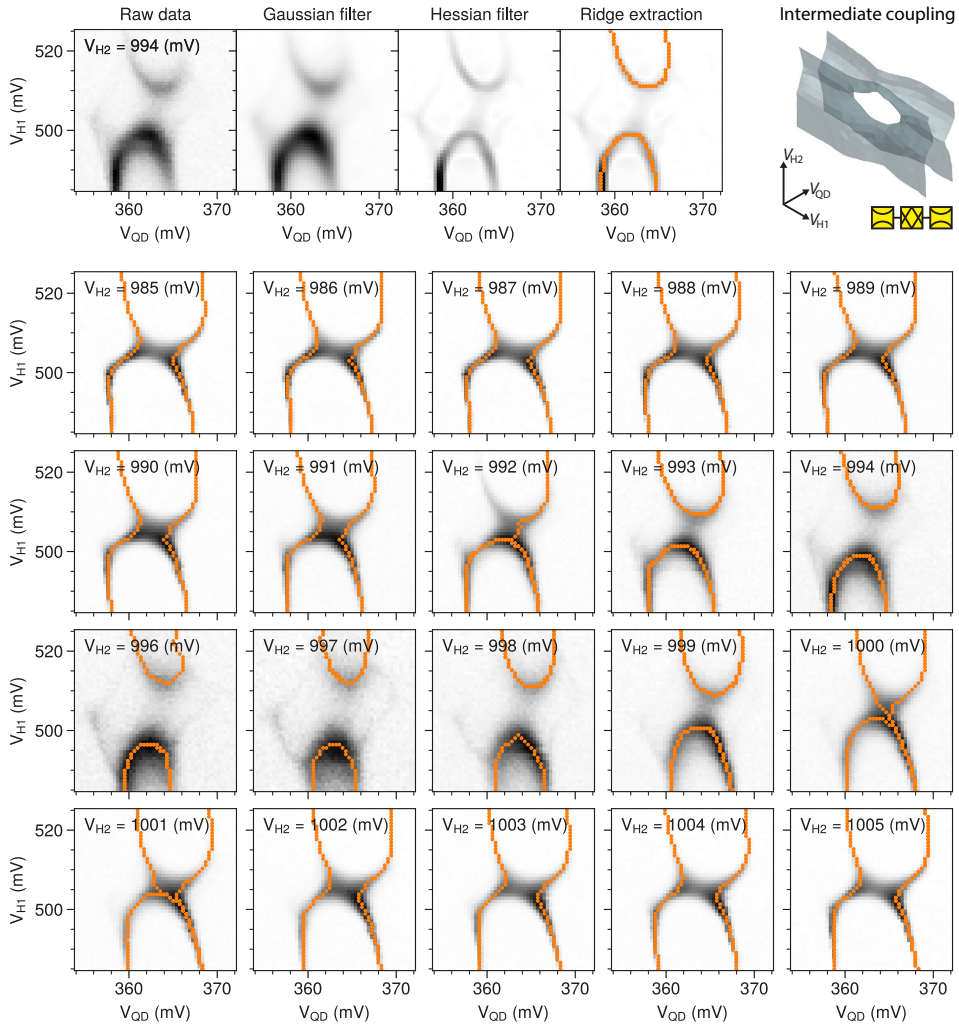
Figure 7.12: **3D charge stability diagram extraction procedure.** The four-panel sequence in the first row shows how the charge degeneracy points are extracted from a zero-bias conductance measurement. First, the raw data is smoothed with a Gaussian filter; then, a Hessian filter highlights the ridges; finally, a custom algorithm extracts the charge degeneracy points starting from the maxima on the top and bottom edges and following the pixels with maximum values. Such process is repeated for the 20 slices at different V_{H2} values shown below; the extracted charge degeneracy points are plotted here on top of the raw conductance data. Eventually, all the charge degeneracy points are converted into the 3D manifold shown in the top-right corner using the `reconstruct_surface` function of the `pyvista` python package. For further details see the Methods and the linked repository.

7.8. EXTENDED DATA
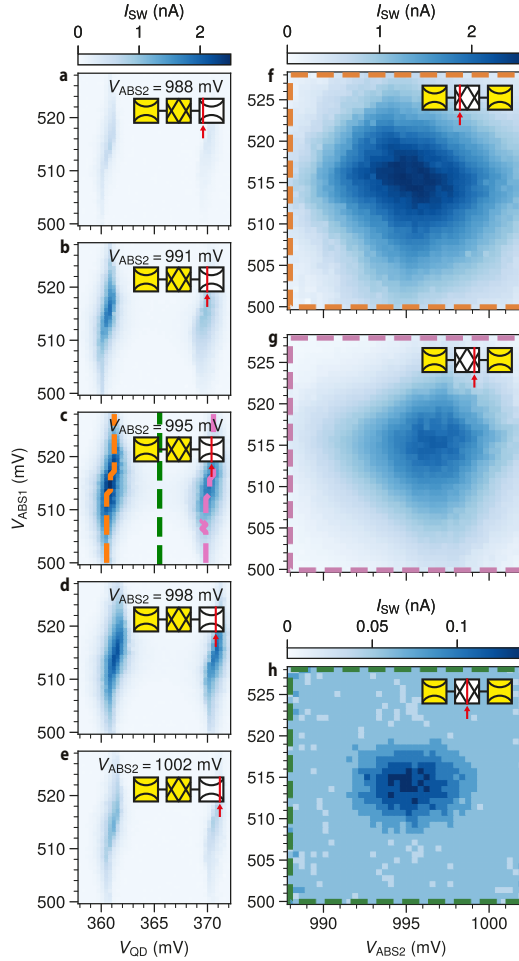
Figure 7.13: **a, b, c, d, e.** 2D maps of I_{sw} as a function of V_{H1} and V_{QD}. These are 5 examples among 40 V_{H1}-V_{QD} maps taken at different V_{H2} set points ranging from 988 to 1002 mV, collectively forming a 3D dataset of I_{sw} as a function of V_{H1}, V_{QD} and V_{H2}. From such dataset, we extract the data plotted in panels **f**, **g**, and **h**. **f, g, h.** 2D maps of I_{sw} as a function of V_{H1} and V_{H2}. In panels **f** and **g**, V_{QD} is placed along the left and right QD resonance respectively, color-coded to superimposed lines in panel **c**. In panel **h**, V_{QD} is placed in between the two QD resonances. Panel **f** reports the same data of Fig. 7.3g.
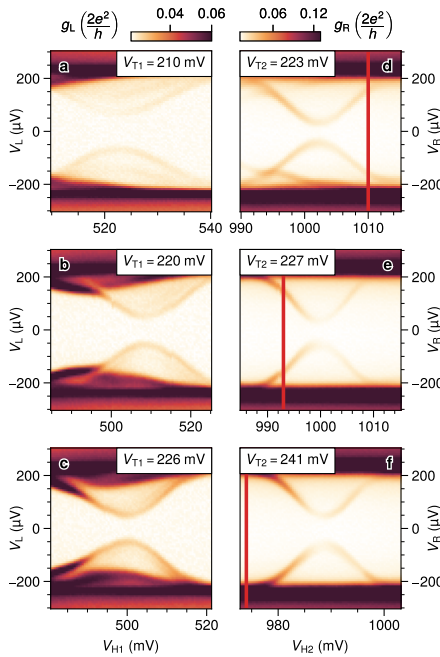
Figure 7.14: **ABS spectra at Fig. 7.4 settings. a-c.** Spectrum of the left ABS for low, intermediate, and strong coupling regimes, respectively. **d-f.** Spectrum of the right ABS for low, intermediate, and strong coupling. The red lines indicate the V_{H2} settings used in Fig. 7.4. For weaker couplings, V_{H2} is set closer to the ABS energy minimum in order to get comparable switching currents over the different coupling regimes; for the strong coupling V_{H2} is set where the ABS energy approaches the superconducting gap.
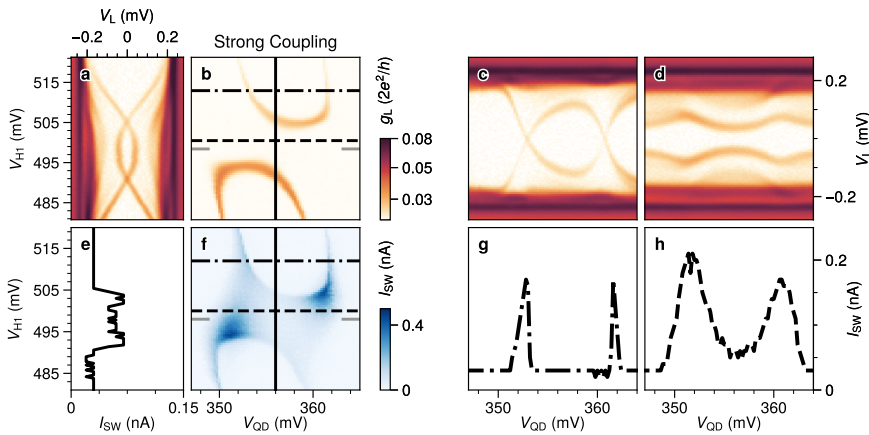
Figure 7.15: **Dissection of the ABS-QD system in the strong coupling regime. a.** Spectroscopy as a function of V_{H1} and measured from N_L. The position of V_{QD} is indicated by the vertical line-cut in panel **b**. **b.** Zero-bias conductance, measured from N_L, as a function of V_{QD} and V_{H1}. **c, d.** Spectroscopy as a function of V_{QD} measured from N_L. Positions along V_{H1} are indicated by horizontal lines in panel **b**. **e.** I_{sw} as measured along the vertical black line of panel **f. f.** I_{sw} as a function of V_{QD} and V_{H1}. The gray inset indicates the minimum energy of the ABS. Dashed lines correspond to panels **g** and **h. g, h.** I_{sw} as measured along the horizontal lines in panel **f**, extracted using a threshold of $30\mu V$.
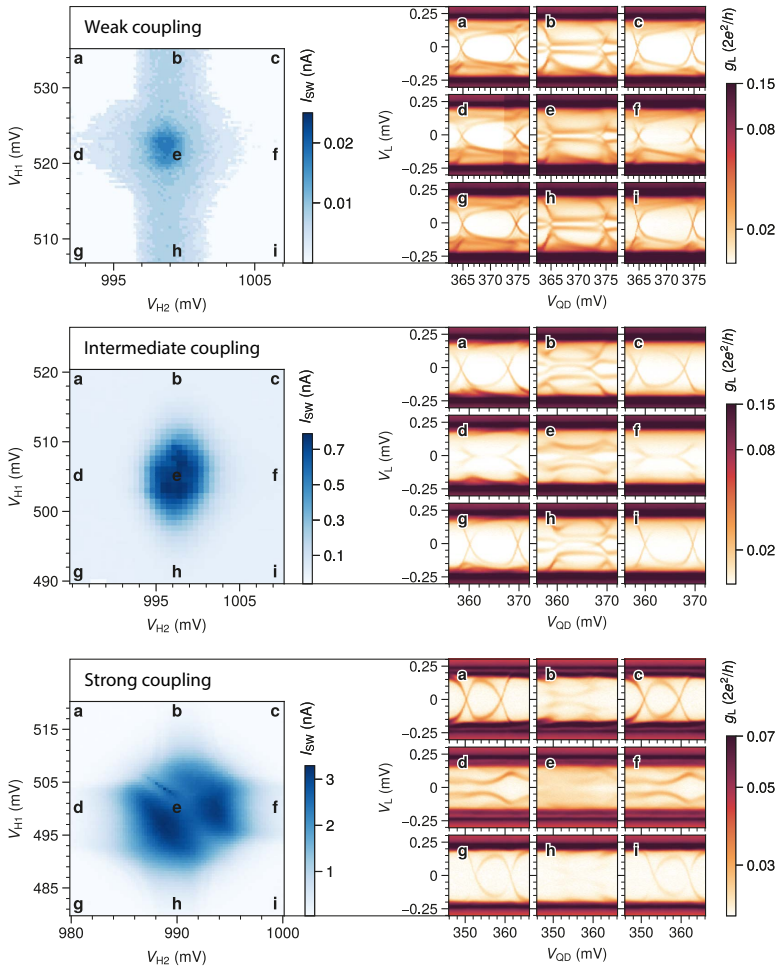
Figure 7.16: **Additional QD spectroscopy measurements.** The left side of the figure shows three I_{sw} maps as a function of both ABS gates in the weak, intermediate, and strong coupling regimes. The strong coupling I_{sw} map is identical to panel **b** of Fig. 7.6, the weak and intermediate I_{sw} maps present additional data not presented in the main text. The QD gate is kept between the two resonances, as in Fig. 7.6. The right side of the figure shows spectroscopy measured from N_L. Each plot corresponds to a different configuration of V_{H1} and V_{H2}, as indicated in the I_{sw} maps. In the weak coupling regime, parity switches are observed for every combination of V_{H1} and V_{H2}. In the intermediate regime, the parity switch no longer occurs when both ABSs are at their energy minima (panel e), resulting in a strong increase in the I_{sw} map on the left. In the strong coupling regime, parity switches only occur when both ABSs are placed far from their energy minima (panels a,c,g,i).
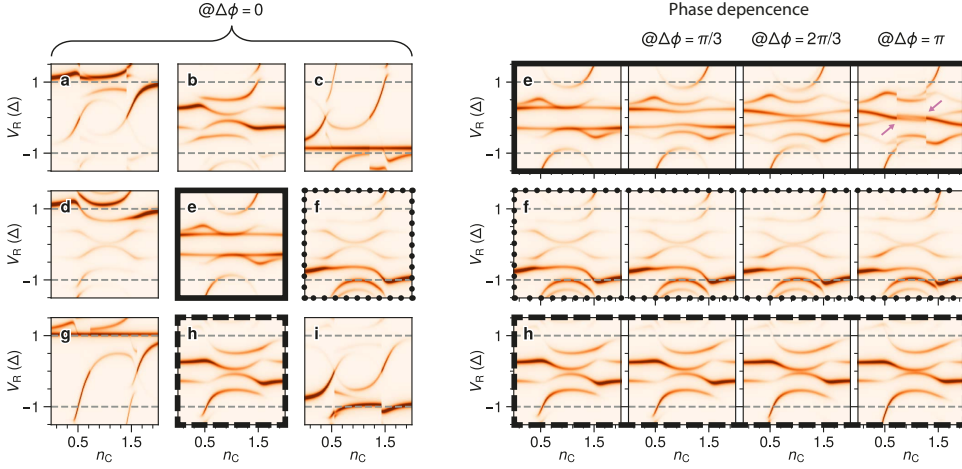
Figure 7.17: **Modulation of the excitation spectrum as a function of phase in the strong coupling regime.** The left side of the figure shows theory simulations of the DOS, at $\phi = 0$, in accordance with the strong coupling data presented in Fig. 7.16. The middle panel, corresponding to both ABSs being at their energy minima and highlighted by a thick black line, is reevaluated at different values of ϕ on the right side of the figure, ranging from $\phi = 0$ to $\phi = \pi$. A modulation of the excitation spectrum is clearly visible in this case. Depending on ϕ, the ground state parity of the system may be even ($\phi = 0, \pi/3, 2\pi/3$) or odd ($\phi = \pi$). The region in V_{H1} vs V_{H2} space where this switching of the ground state parity is possible is indicated in red in Fig. 7.6. The excitation spectrum of panels where one ABS is placed far from its energy minimum is largely unaffected by ϕ, as can be observed from the dotted and dashed panels presented in this figure.

Figure	U	n_C	ξ_L	ξ_R	Γ_L	Γ_R	t_L	t_R
7.3d	10	[0.2, 1.8]	-0.05, -0.35, -0.65	0.37	0.2	0.16	0.2	0.38
7.3f	10	-	[-0.8, 0.6]	0.37	0.2	0.16	0.2	0.38
7.4g,j	10	[0,2]	[-1,1]	-0.7	0.3	0.2	0.3	0.3
7.4h,k	10	[0,2]	[-1,1]	0.5	0.25	0.2	0.6	0.3
7.4i,l	10	[0,2]	[-1,1]	1.3	0.2	0.25	0.7	0.45
7.6	10	1	[-1, 0.8]	[-1, 0.8]	0.25	0.35	0.7	0.8
7.7a	10	[0,2]	0	0	0.001	0.001	0.01	0.01
7.7b,c	10	[0,2]	0.2	0	1	1	0.4	0.1
7.8a	10	1	[-1,1]	[-1,1]	0.25	0.35	0.7	0.8
7.8b	-	-	0	0	-	-	-	-
7.8c	-	-	0.2	-0.2	-	-	-	-
7.8d	-	-	0.2	0.2	-	-	-	-
7.11	10	[0,2]	0.9	-0.7	0.2	0.25	0.85	0.65
7.17	10	[0,2]	-	-	0.3	0.2	0.8	0.75

Table 7.1: A summary of all model parameters used throughout this chapter. All parameters except n_C are in units of $\Delta = 0.2$ meV.

8

OUTLOOK

Quivi è la sapïenza e la possanza
ch'aprì le strade tra 'l cielo e la terra,
onde fu già sì lunga disïanza».

Dante Alighieri, *Paradiso*, XXIII, 37-39

[This is the Wisdom and the Potency
that opened roads between the earth and Heaven,
the paths for which desire had long since waited.]

This chapter begins by discussing ongoing progress in Kitaev chain engineering. Finally, it presents a roadmap to the next goals: a first Majorana qubit and the scaling up of Kitaev chains towards the topological limit.

hapter 6 leaves the reader suspended by an open question: can we control the phase of a three-site Kitaev chain in hybrid nanowires? It is a question with important consequences. Fixing the phase is essential both for maintaining the coherence of a Majorana qubit and for scaling up the chain to many sites. Any π-phase mismatch in a long chain introduces a domain wall, essentially breaking the chain into smaller fragments and, thus, impeding the realization of a robust topological phase. Recently, ten Haaf et al. (2024b) showed how to fix the phase in a Kitaev chain defined in a two-dimensional electron gas device; here, we close the circle by demonstrating phase control in a hybrid nanowire as well.

8.1. PHASE CONTROL

Fixing the relative phase between two superconductors is straightforward: it is sufficient to connect them in a superconducting loop geometry, as shown in the top left picture of figure 8.1. It is not as trivial, though, to link the superconductor phase difference ϕ_{Al} to the three-site Kitaev chain phase difference ϕ. In the case of a single ABS mediating CAR and ECT in each hybrid section, then the link is provided by equations 6.19 and 6.20, yielding

$$\phi = \phi_{Al} + \text{constant} \tag{8.1}$$

where the constant is either 0 or π depending on the chosen sweet-spot (Liu et al., 2024b). If the device is not so ideal, then the constant might assume different values, as suggested by the experimental evidence of ten Haaf et al. (2024b). Nevertheless, ϕ and ϕ_{Al} should still differ only by a fixed constant, which guarantees the ability to set $\phi = 0$ with an appropriate out-of-plane magnetic field B_z. Panels a and b of figure 8.1 show the measured conductance spectra for such a field sweep. In this case, the constant is ≈ 0 and the period is ≈ 7.3 mT, which is compatible with the device loop size.
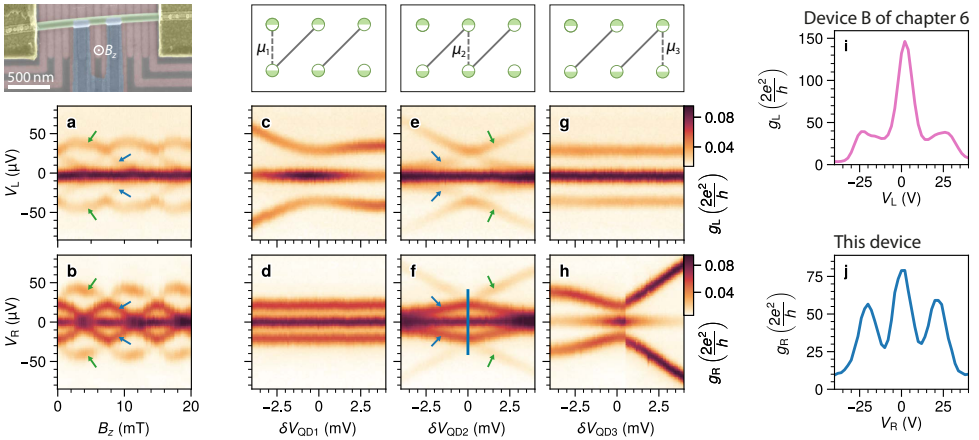
Figure 8.1: **Three-site Kitaev chain with phase control.** Left and right differential conductance of a three-site chain as a function of the out-of-plane magnetic field B_z (panels **a,b**) and the detuning of QD$_1$ (panels **c,d**), QD$_2$ (panels **e,f**), and QD$_3$ (panels **g,h**). Panel **j** shows a linecut of panel f, while panel **i** shows an analogous linecut from a device without a loop (from Figure 6.12). Green and blue arrows highlight the excited states. $B_x = 175$ mT in all panels but j, where it is 220 mT. $B_z = 0$ mT in all panels but a and b. To be published by Bennebroek Evertsz' et al. (2025).

Panels c to h display conductance spectra at $B_z = 0$ as a function of each dot's detuning. Although these spectra resemble earlier measurements of loop-less devices (figures 6.3 and 6.12), we note two important differences. First, the spectrum is gapped: the linecut in panel j reveals three separated peaks, while panel i – from a loop-less device – shows nearly flat conductance on the sides of the zero-bias peak due to fast phase precession (see section 6.4). Second, the two excited states (indicated by blue and green arrows) appear simultaneously only when either the phase or the middle QD is detuned. Both observations are compatible with a three-site Kitaev chain model with fixed phase $\phi = 0$. In particular, observing a single excited state in panels c, d, g, h signals that each normal lead cannot couple to the states on the other side – a symptom of ideal device behavior. It indicates that the tuning of ϕ and μ_2 to 0 is precise and that the Zeeman splitting is large enough that distant states are not sensibly coupled via other spin species at higher energy. Therefore, the ideal, spinless, three-site Kitaev chain model with $\phi = 0$ seems to adequately describe the system. This is further confirmed by the simulations reported in figure 8.2. For such a simple model, the match between theory and experiment is extraordinary.
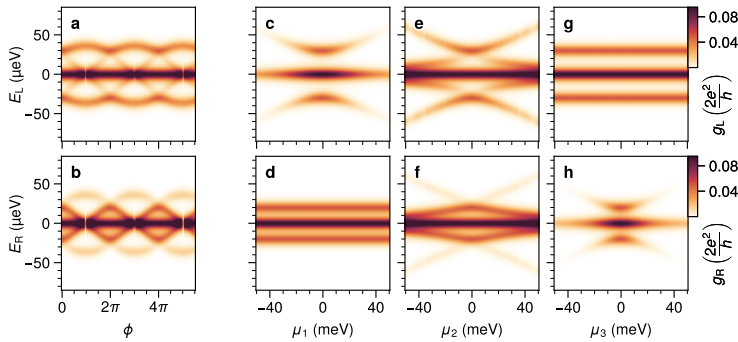
Figure 8.2: **Theoretical simulations of the differential conductance of a three-site Kitaev chain**. The calculation utilizes the scattering matrix approach (Dvir et al., 2023) at finite temperature $k_B T = 3\,\mu eV$ and coupling to the leads $\Gamma_L = \Gamma_R = 0.8\,\mu eV$. $t_1 = \Delta_1 = 15\,\mu eV$, $t_2 = \Delta_2 = 10\,\mu eV$. All the μ_n that are not varied are kept at $0\,\mu eV$. In panels c-h, $\phi = 0$.

The proof of phase control concludes the main quest of this thesis. In summary, we showed how to realize every element of the Kitaev chain Hamiltonian (chapters 2, 3, 5), how to control them (chapter 3), and how to realize two- and three-site Kitaev chains hosting Majorana bound states (chapters 4, 6, and 8). We also demonstrated that three sites offer more protection against perturbations of the parameters (chapter 6), thanks to an energy gap in the middle of the chain (ten Haaf et al., 2024b).

What's next?
The remaining sections of this chapter explore future directions. Ranging from the phenomenology of a Kitaev chain coupled to an additional quantum dot to the architecture of a Majorana qubit and the challenges of scaling up the chain even further.

8.2. ASSESSING MAJORANA QUALITY IN FEW-SITE CHAINS COUPLED TO A QUANTUM DOT

Stating that Majorana bound states are topologically protected means that their energy doesn't split for small perturbations of the Hamiltonian parameters and, at the same time, that local additions to the Hamiltonian do not couple them (Kitaev, 2001). Although not yet topological, partial protection against parameter perturbations in two- and three-site Kitaev chains was demonstrated, showing, in particular, that three-site chains are significantly more robust. It is then compelling, from a fundamental point of view, to test how isolated the Majoranas are by attempting to couple them via additional device elements. It is also important from a practical point of view since the residual coupling of Majorana bound states would limit future qubit performance via dephasing.

A first hint of Majorana isolation in three site chains comes from the lack of multiple excited states in panels c, d, g, h of figure 8.1, discussed above. However, this is neither quantitative nor direct evidence, since the lack of coupling between leads and distant excited states doesn't exclude coupling between distant Majoranas. A direct evidence of Majorana isolation can be obtained by attempting to couple the edge Majoranas via an additional quantum dot located at one end of the chain. This test was studied theoretically by Prada et al. (2017) and Clarke (2017) in the context of Lutchyn-Oreg nanowires and then adapted by Seoane Souto et al. (2023) to minimal Kitaev chains. Hence, it is sometimes referred to as the *Prada-Clarke test*.

Conceptually, the test is simple: it requires an additional quantum dot – "PC" in figure 8.3 – and sweeping one of its levels across zero energy (Deng et al., 2016, 2018). If the PC dot couples to both Majoranas, then it splits their energy. This is possible only if there is a finite overlap between the wavefunctions of the two Majorana bound states; the amount of splitting could be used as a quality measure of the Majorana localization (Prada et al., 2017; Clarke, 2017; Deng et al., 2018; Seoane Souto et al., 2023).
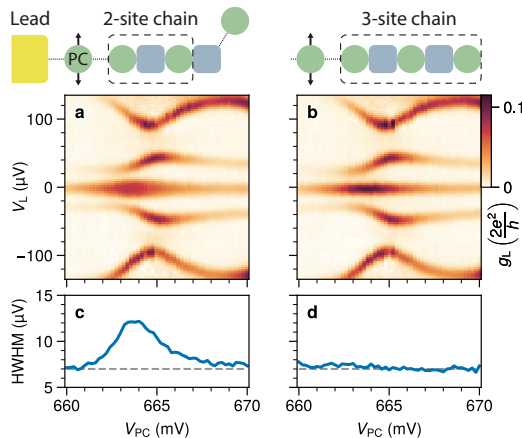
Figure 8.3: **Prada-Clarke test in two- and three-site Kitaev chains**. **a,b.** Conductance spectra of Kitaev chains coupled to an additional dot, as a function of the gate voltage controlling the dot energy. **c, d.** Half width at half maximum of the zero-bias conductance peak of panels a and b, respectively. $B_x = 175$ mT in all panels. Bennebroek Evertsz' et al. (2025).

Figure 8.3 compares the results of a Prada-Clarke test performed on two- and three-site Kitaev chains (left and right columns, respectively). Both chains are defined in the same device and switching between one and the other is executed, as in chapter 6, by setting the third dot of the chain off and on resonance (see schematics above). In particular, the measurements shown in panels a and b are identical in everything but the plunger gate voltage of the rightmost QD, which is set 4.7 mV off-resonance in panel a.

Since the Majorana energy splitting is smaller than the linewidth, we quantify it by tracking the excess of half width at half maximum (HWHM) of the zero-bias conductance peak. When the PC dot is off-resonance, the HWHM is $\approx 7\,\mu$V for both the two- and the three-site chain. Instead, when it's on resonance, the HWHM increases by as much as $\approx 5\,\mu$V for the two-site chain, while there is no visible increase for the three-site chain. Notice that when the PC dot is off-resonance, it effectively behaves as a standard tunneling barrier (Deng et al., 2016). Since no splitting is observed in that limit, we conclude that the splitting observed in panel a is not detectable with standard spectroscopy: the Prada-Clarke test gives access to new information. It also provides a remarkable energy resolution $\lesssim 1\,\mu$V, estimated from the deviations from HWHM = 7 μV in panel b.

The simple Prada-Clarke test of figure 8.3 shows that poor man's Majoranas in this two-site chain are indeed coupled by the additional dot, while there is no detectable coupling in the three-site chain. This demonstrates that scaling up the chain is not only increasing the protection against parameter perturbations (chapter 6) but also isolating Majoranas from local couplers. Piece by piece, we are engineering all the features of topologically protected Majoranas.

True topology arises only in an infinite Kitaev chain, while, for any finite chain, it is important to quantify the Majorana quality in terms of metrics. One metric suggested by Tsintzis et al. (2022) is the so-called *Majorana polarization* (MP), another one, recently proposed by Svensson and Leijnse (2024), is the *local distinguishability* (LD), and finding new metrics is an active field of research. The desired properties of Majorana quality metrics are (1) ease to calculate, (2) ease to measure, (3) prediction power – the ability to connect it to other properties such as qubit coherence time, gate fidelity, and Majorana braiding visibility. The Majorana polarization on the first chain site can be calculated as follows, in the general case of a finite Zeeman splitting:

$$\mathrm{MP}_1 = \frac{\sum_\sigma \left(\langle o|\gamma_{1\sigma}|e\rangle^2 - \langle o|\gamma_{2\sigma}|e\rangle^2 \right)}{\sum_\sigma \left(\langle o|\gamma_{1\sigma}|e\rangle^2 + \langle o|\gamma_{2\sigma}|e\rangle^2 \right)} \tag{8.2}$$

where σ runs through the two spin species, $\gamma_{1\sigma,2\sigma}$ are the Majorana operators in the first site, and $|e\rangle$, $|o\rangle$ are the lowest-energy states with even and odd fermion parity, respectively. An analogous definition can be given for the MP on the last site.[1] The link between the MP, qubit performance, and braiding visibility is studied by Tsintzis et al. (2024), but measuring the MP is not as easy. One proposal to measure the MP relies on coupling two Kitaev chains to a transmon qubit (Pino et al., 2024). A much simpler method is provided by the Prada-Clarke test: Seoane Souto et al. (2023) simulated the correspondence

---

[1] Here we are reporting the MP definition used in Aksenov et al. (2020), Tsintzis et al. (2022), Seoane Souto et al. (2023), and Tsintzis et al. (2024). See Sticlet et al. (2012), Sedlmayr and Bena (2015), Sedlmayr et al. (2016), and Samuelson et al. (2024) for slightly different MP definitions depending on the generality of the context.

between the Majorana splitting induced by the Prada-Clarke dot and the MP of Kitaev chains with limited Zeeman energy.

The poor man's Majorana splitting of figure 8.3a,c is likely due to imperfect device tuning since here the Zeeman energy is very large compared to t, Δ. Therefore, future directions include

- tuning the device as well as possible and using the measured HWHM to set a lower bound to the corresponding MP,

- performing Prada-Clarke tests at different Zeeman energies – to gauge the dependence and find whether the Majorana quality is limited by either imperfect tuning or finite Zeeman,

- relating the splitting induced by the Prada-Clarke dot to other Majorana quality metrics.

In summary, coupling Kitaev chains to an additional quantum dot demonstrates that three-site chain Majoranas can be more isolated than two-site ones (figure 8.3) and provides an accessible experimental tool to quantify the Majorana quality required for qubits and braiding (Seoane Souto et al., 2023; Tsintzis et al., 2024). However, a Prada-Clarke test can only *predict* future qubit properties. To move beyond prediction, we need to realize an actual qubit. Once realized, we might even employ the qubit itself to further investigate the Majorana properties connected to topology, such as protection and isolation.

8

8.3. MAJORANA QUBIT

Creating a first Majorana qubit is not easy. This section outlines the requirements needed to accomplish it and presents a viable architecture. Many steps are needed, ranging from the device nanofabrication to the readout of the qubit state. They are summarized in the following table. Different steps require different experimental capabilities, in particular, some tasks can be performed slowly while others have stringent speed requirements. In the following, we discuss the typical timescale of every step and the constraints that need to be considered to design, build, wire, and operate a viable qubit device.

Step	Process	Timescale
1	Device nanofabrication and cooldown	weeks
2	Device characterization and tuning	months
3	Qubit initialization	μs
4	Qubit manipulation	ns
5	Qubit readout	μs

FABRICATION

The first step is, of course, the nanofabrication of a parity qubit device. This is relatively easy since it relies on the already-developed fabrication techniques used for chapters 3 to 7 (van Loo, 2023, chapter 3) and for the Kitaev chain of sections 8.1 and 8.2. Essentially, a Majorana qubit device requires two of such chains within the same nanowire (see section 2.2.1) This is not an issue since InSb nanowires are long enough to host two chains (they are ~ 10μm long so they could fit two Kitaev chains with as much as ~ 20 sites each) and the gate and contact yield is nearly 100% (for instance, during the experiments of chapters 6 and 7, 4 three-site devices were tested, for a total of 16/16 working contacts and 43/44 working gates). This does not mean that fabricating a qubit device is trivial, since nanofabrication is always unpredictable due to machine misbehavior, but rather that fabricating two Kitaev chains within the same nanowire is essentially as difficult as fabricating one.

Figure 8.4 illustrates the parity qubit design we propose here. If all nanofabrication processes run with no incidents, it requires about 10 days to fabricate, bond, and cooldown in a dilution refrigerator.

TUNING

Tuning a device is more delicate and time-consuming. Characterizing the ABSs, forming the QDs, and tuning the couplings may require several weeks (see appendix C). Part of the tuning can be performed with the DC measurement techniques used in chapter 6, but not all of it. The difficulty lies in forming and characterizing the QDs in the bulk of the device since they are not accessible with local tunneling spectroscopy performed from the normal probes on the sides. To overcome this limitation, we propose two possible techniques:

- Single-lead radio-frequency (RF) reflectometry using an LC resonator attached to the superconductor. Normally, this is performed as in Jung et al. (2012) using a

8

normal-metal lead. For an extensive review, see Vigneau et al. (2023). Using a superconductor is partly different. It requires either adding the parent gap $\Delta_{Al} \approx 200\,\mu V$ to the bias voltage (and relying on finite temperature to poison the otherwise fully filled or fully empty BCS density of states) or destroying superconductivity by either heating the device to $T \gtrsim T_c \approx 1.2\,K$ or applying an out-of-plane field $B_z \gtrsim B_z^c \approx 200\,mT$

- Dispersive gate sensing. This requires an LC resonator attached to the plunger gate of the sensed QD and another electron reservoir attached to the same QD so that that charge can tunnel in and out of it. The minimal system enabling dispersive gate sensing is then a double quantum dot (Colless et al., 2013).

In our laboratory, we are familiar with both techniques (Wang et al., 2022b; de Jong et al., 2021). Therefore, the next goal is implementing either of the two on a Majorana qubit device, to demonstrate its tunability. With single-lead spectroscopy, the QDs should be tuned one by one by setting all other QDs off-resonance, with dispersive gate sensing, the QDs need to be kept on resonance in pairs.

In addition, in the specific case of Kitaev chains, we suggest another available technique combining different elements of the previous two:

- CAR-induced quantum capacitance. Traditional single-lead reflectometry from a gapped superconductor is challenging since single electrons cannot tunnel in and out of a single QD. However, if there are two QDs coupled to a superconductor, then tunneling of electron pairs is enabled by CAR. Therefore, if the energy levels of consecutive QDs are antialigned, a reflectometry signal arises on the superconducting lead. This procedure was originally proposed by Liu et al. (2022) and Wang (2023, chapter 10) as a parity readout technique. It could be used for device tuning as well, as long as pairs of consecutive QDs are kept on resonance, where being on resonance means, in this context, having both QD energies at zero or, in general, antialigned.

8
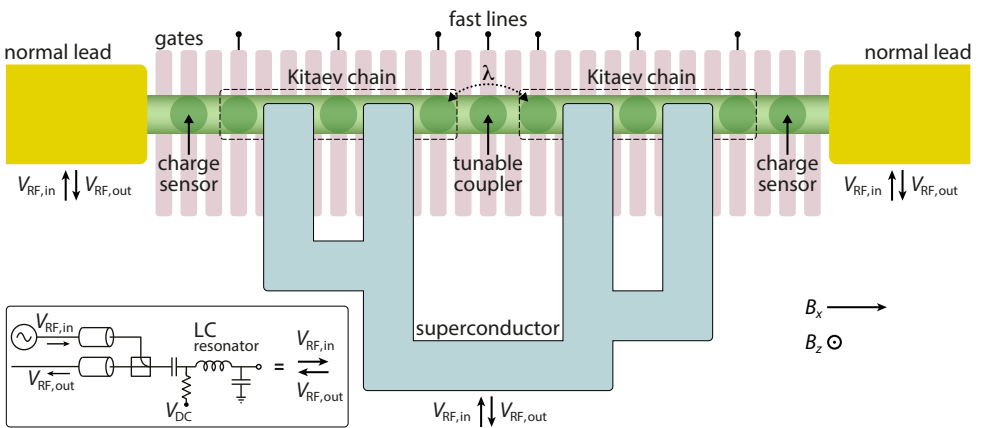
Figure 8.4: **Majorana qubit made with a pair of 3-site Kitaev chains coupled by a central QD.**

There are no stringent speed requirements for the tuning process. Characterizing a device and tuning both Kitaev chains to the sweet spot may take several weeks to a few months. As long as the dilution refrigerator is operational and the device electrostatics are stable enough, time is not a concern. In practice, the gate configuration of our devices can be stable for weeks (see section 6.7.3) and in case of a sudden charge jump it is typically not difficult to rapidly find the sweet spot again.

Instead, qubit operations such as initialization, manipulation, and readout have stringent speed requirements. They are discussed in the next sections. We begin with qubit manipulation, which has the shortest timescale of all.

QUBIT MANIPULATION

For the first proof of principle, we propose to rely on qubit gates that are not protected. Physical or measurement-based braiding proposals typically involve devices that are more complicated than figure 8.4's (Alicea et al., 2011; Plugge et al., 2017; Tsintzis et al., 2024). They will be explored in future works. Here, we rely on the partial protection of few-site Kitaev chains to propose much simpler qubit gates that are not topologically protected. The basic principle is breaking the Majorana protection for short intervals by coupling the Majoranas together. The free evolution induced by Majorana interaction implements the desired gates.

In concrete, we adapt the poor man's Majorana qubit proposals of Tsintzis et al. (2024) and Pan et al. (2024) to generic few-site chains. The low-energy Hamiltonian for such a qubit has the following form (Pan et al., 2024):

$$H_{\text{int}} = \frac{\varepsilon}{2}\sigma_z + \frac{\lambda}{2}\sigma_x \tag{8.3}$$

where ε is the coupling between Majoranas of the same chain, λ is the coupling between adjacent Majoranas from the different chains, and σ_z and σ_x are Pauli matrices on the qubit space (which is either the even or the odd total parity subspace of the non-local fermions stored into such Majorana modes). The intra-chain Majorana coupling ε corresponds to the energy splitting induced by detuning from the Kitaev chain sweet-spot. If every QD of the chain is detuned by $\delta\mu_n$, then $\varepsilon = \delta\mu_N \prod_{n=1}^{N-1} \frac{\delta\mu_n}{2t_n}$ (see section 6.7.1). The inter-chain Majorana coupling λ corresponds to the tunnel coupling between the two chains (Tsintzis et al., 2024). The control of both couplings ε and λ enables all rotations of the qubit Block sphere. For instance, figure 8.5 illustrates the pulse sequences that can be used to measure either Rabi or Ramsey oscillations.

Figure 8.5: **Rabi and Ramsey pulse sequences.**

Referring to the Rabi and Ramsey experiments, the constraints on the couplings, the wiring, and the qubit manipulation speed finally become clear:

- A lower bound on the gate duration is set by the electronics speed. Commercial pulse generators can have a rise time of ~1 ns.

- Correspondingly, the device wiring must accommodate fast pulses. Figure 8.4 device needs at least 4 fast lines: three connected to the QD plunger gates of one Kitaev chain (to control ε) and one more line connected to the gate controlling λ.

- Another lower bound is set by the maximum achievable λ. Since tunnel coupling can easily reach a few μeV, this is typically not a limiting factor: with $\lambda = 1$ μeV, a full qubit rotation is achieved with a square pulse lasting ≈ 4 ns.

- Another lower bound is set by the Kitaev chain energy gap: $\min_n(2t_n)$. To avoid Landau-Zener transitions causing leakage to the excited states, all pulses must be slow enough to be adiabatic. This is typically not a concern for our devices: a gap of ~20 μeV prescribes all ε and λ ramps to last much longer than 0.2 ns. The electronics speed is typically a stricter lower bound.

- On the other side, the upper bound on the qubit manipulation timescale is set by how well ε and λ can be switched off. Residual intra-chain coupling leads to dephasing, while residual inter-chain coupling leads to unwanted qubit rotations. Both are detrimental. In two-site Kitaev chains, ε is zero only upon precise tuning of $t = \Delta$. Zatelli et al. (2024) estimated a ~70 neV noise floor for ε, which leads to an estimated dephasing time of ~10 ns. Thus, we propose to design a Majorana qubit made of three-site Kitaev chains, where the dephasing time is expected to improve up to ~1 μs (chapter 6). Then, to limit unwanted qubit rotations to the same timescale, the residual coupling λ must be switched off to ~1 neV or less. Note that the control of the λ amplitude must span at least two orders of magnitude: the maximum λ must reach ~0.1 μeV to enable qubit gates much faster than the dephasing time, while the minimum λ should be less than ~1 neV. For this reason, we propose to use a quantum dot as a tunable coupler between the two Kitaev chains of the qubit. As shown in figure 5.9, the current through a QD can span more than two orders of magnitude while switching from the charge degeneracy points to the Coulomb blockade region.

- Finally, we recall that a hard upper limit on the qubit manipulation time is set by the quasi-particle poisoning time, i.e. the characteristic timescale for which the parity is conserved in a superconducting system. Since quasi-particle poisoning flips the qubit, it is a limit for T_1. In our systems, the quasi-particle poisoning time is above 1 ms so it is not a concern for a three-site Kitaev chain qubit.

In summary, the design proposed in figure 8.4 offers a viable qubit manipulation window: qubit gates can be as short as several ns while residual couplings limit operations under 1 μs. Gates can be controlled with as little as 4 fast lines, wired with coaxial cables and low-pass filters with a cut-off frequency of ~1 GHz.

Qubit readout

The parity of two-site Kitaev chains can be read out via charge sensing (Tsintzis et al., 2024) or CAR-induced quantum capacitance (Liu et al., 2023). Here, we recommend the former, since it is easier to generalize to few-site Kitaev chains of any length. As proposed by Tsintzis et al., we rely on the tunability of the Majorana protection to read out the parity. Since Majoranas are chargeless, a Kitaev chain tuned to the sweet spot yields no signal, whereas a finite charge sensing signal appears as the chain is tuned out of the sweet spot. This can be achieved by pulsing the plunger gate voltages of all the QDs of one chain. It is the same type of pulse required for a $\frac{\varepsilon}{2}\sigma_z$ gate, so it doesn't add any overhead to the Kitaev chain wiring in terms of fast lines and room temperature electronics. We note that a finite ε leads to dephasing, but this is irrelevant for readout purposes since projecting on the $|0\rangle\langle 0|$ or $|1\rangle\langle 1|$ qubit subspaces is insensitive to the relative phase difference. Instead, what is relevant is the residual inter-chain coupling λ, since it superposes the $|0\rangle$ and $|1\rangle$ qubit states. How well λ can be switched off determines the upper bound on the readout timescale. Reading out in a few µs requires λ to be 1 neV or less.

On the other side, the lower bound on the parity readout timescale is set by the sensitivity of the charge sensor. This is quantified in terms of the signal-to-noise ratio (SNR) depending on the readout time. A charge sensor can be implemented with an additional QD on the side of the chain; the QD is coupled to a normal lead connected to an LC resonator, as shown in figure 8.4. It is important to ensure that the charge sensor is coupled only capacitively to the Kitaev chain: the tunneling barrier between the charge sensor and the first sensed QD of the Kitaev chain must be pinched strongly so that no electrons can tunnel within the qubit operation timescales. Tunneling electrons would flip the qubit, just like quasi-particle poisoning. Charge sensing of a minimal Kitaev chain with an SNR > 1 in $\approx$ 200 µs was demonstrated by van Driel et al. (2024b). A higher SNR$\sqrt{\text{Hz}}$ can be obtained by increasing the signal with a higher-quality-factor resonator or by lowering the noise with an additional amplifier at the coldest plate of the dilution refrigerator (de Jong et al., 2021).

Instead of optimizing the SNR$\sqrt{\text{Hz}}$, an alternative is reducing further the minimal λ. However, it might be challenging to span it by more than four orders of magnitude, from the $\lambda \sim 0.1$ µs needed for fast qubit manipulation to the $\lambda \ll 10$ ps needed for a readout taking ~ 100 µs. A third alternative is relying, once more, on the tunability of the chain by setting $\varepsilon \gg \lambda$. This locks the qubit precession approximately around the z axis. This way, the constraint posed by the residual coupling λ is moved from the readout timescale to the readout fidelity. The readout error would be $\sim \arctan(\lambda/\varepsilon)$. Since ε can be tuned up to ~ 10 µeV (figure 6.4), this technique relaxes enormously the readout requirements for the residual coupling λ. In this scenario, the readout timescale is limited by the quasi-particle poisoning.

Qubit initialization

Since the readout technique discussed above is a projective measurement, the qubit can be initialized by reading it out. Alternatively, it can be initialized by waiting more than the quasi-particle poisoning time after pulsing the QDs of both chains where the quasi-particle population is unbalanced (Tsintzis et al., 2024).

8.4. Scaling-up the Kitaev chain

After realizing the first Majorana qubit, the natural progression is to scale up the chains to improve its performance. Figure 8.6 shows that the expected dephasing time of a Kitaev chain qubit scales exponentially as a function of the chain length. It improves by three orders of magnitude every two additional sites. Based on this prediction, the next crucial target is realising a five-site Kitaev chain, which is the shortest one predicted to outperform the *typical* coherence times of popular solid-state platforms such as spin qubits and superconducting qubits (Stano and Loss, 2022; Kjaergaard et al., 2020). This would be a ground-breaking milestone. It would also stimulate research towards hybrid quantum processors. For instance, spin qubits defined in semiconductor quantum dots have the advantage of allowing fast two-qubit gates, due to their strong inter-QD coupling. However (especially if not isotopically purified), they typically have a shorter coherence time than superconducting qubits. A hybrid quantum processor using spin qubits for fast operations and Kitaev chains as quantum memories could outperform superconducting qubits on multiple metrics. Such a hybrid platform would benefit from the long coherence of Kitaev chains even without implementing topologically protected gates via braiding.

However, Kitaev qubits and hybrid spin-Kitaev qubits become technologically appealing only if the coherence of Kitaev chains can surpass, substantially, *the best* semiconducting spin qubits ever made (Stano and Loss, 2022; Burkard et al., 2023). Therefore, scaling up even further five sites is crucial. This will bring the Majorana research to new grounds since there are other phenomena that would bind the lifetime of longer Kitaev chains. For instance, the quasi-particle poisoning time is a hard limit on the T_1 of a Majorana qubit: finding strategies to increase it is an important and timely research direction, shared with the superconducting qubit community (Wang et al., 2014; Bargerbos et al., 2023b; Connolly et al., 2024). Similarly, the residual inter-chain coupling λ leads
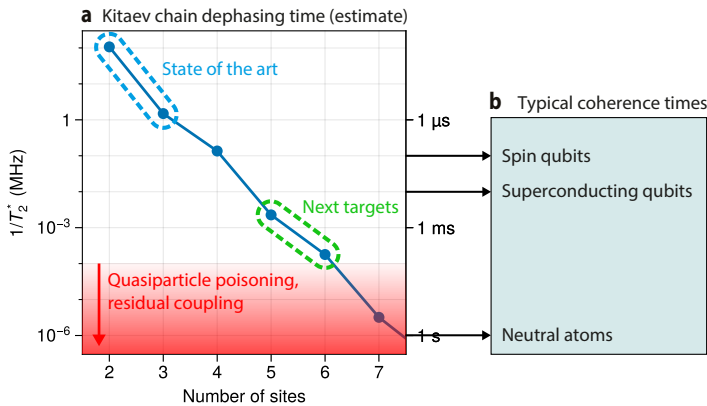
Figure 8.6: **Scaling targets. a.** Estimated T_2^* of a Majorana qubit limited by a finite intra-chain coupling ε due to ~10μV gate noise (blue line). The lifetime T_1 is limited by quasiparticle poisoning and residual inter-chain coupling λ (red shade). **b.** Typical coherence times of selected qubit platforms. We remark that typical timescales shouldn't be compared just as absolute values, but also related to the typical gate duration of each platform (Stano and Loss, 2022; Kjaergaard et al., 2020; Evered et al., 2023). In this context, Kitaev chains can be especially competitive due to relatively long dephasing times *and* relatively fast gates (see section 8.3).

to unwanted qubit flips over the $\frac{h}{\lambda}$ timescale, motivating the development of high-range tunable couplers.

We remark that the interest in scaling up the Kitaev chain extends beyond Majorana qubit performance. First and foremost, scaling up the chain offers the opportunity to study the appearance of topology. This is characterized by increased protection against perturbations and the transition from a discrete spectrum of excited states to a continuous band (Sau and Das Sarma, 2012).

Secondly, the challenge of tuning longer chains forces further investigation of the phase behavior. Kitaev chains with $N > 3$ require more than one superconducting loop, which poses the challenge of tuning all $N-2$ phase differences with a single free parameter: B_z. Up to $N \sim 7$, this is achievable by designing loop sizes of different areas, such that the optimal phase of every loop can be approximated by selecting appropriate multiples of the flux quantum. If the ratios between the loop areas are irrational, this approximation can be, in principle, arbitrarily accurate. In practice, the larger the loop areas, the better the approximation, due to the number of flux quantum multiples that are accessible before a large B_z destroys superconductivity ($B_z \sim 100\,\text{mT}$). This strategy works well for a limited number of loops, after which the required amount of flux quantum multiples becomes exponentially large (for a target phase precision $\delta\phi_n \sim \frac{\pi}{x}$ the required amount of multiples scales as $\sim x^{N-2}$). To scale up further, it is unthinkable to tune all phases with a single parameter B_z: every ϕ_n should be addressed with a dedicated tuning knob. A standard strategy popular in the superconducting qubit community is controlling every loop with a dedicated flux line (Pita-Vidal et al., 2024a), but given the small footprint of Kitaev chain devices, fabricating many flux lines can be challenging and cumbersome. An attractive alternative was recently proposed by Liu et al. (2024b). This relies on the ABS origin of the t_n and Δ_n couplings and the one-dimensionality of the nanowire to tune the relative ϕ_n phases in a fully electrostatic fashion, i.e. acting only on the bottom gate voltages. The device shown in figure 8.7 can be used to test the assumptions and the feasibility of such a protocol.

Finally, scaling up Kitaev chains stimulates the development of new automation techniques. Koch et al. (2023) and van Driel et al. (2024a) pioneered the advent of machine learning to tune the t/Δ balance in minimal Kitaev chains. Now, the dream is to create
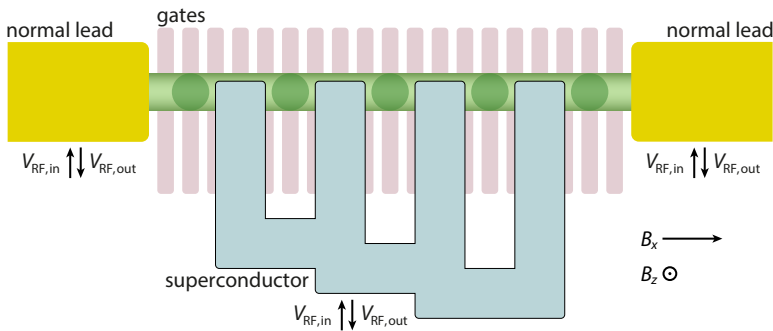
Figure 8.7: **5-site Kitaev chain.**

a fully autonomous algorithm, able to tune a Kitaev chain from scratch, as was recently achieved for spin qubits (Schuff et al., 2024). This requires the autonomous formation of the QDs, the optimization of the inter-dot couplings, and the balance of all the t_n/Δ_n ratios. A device like figure 8.7's is ideal for training such an algorithm: normal-lead spectroscopy (accessing the innermost sites via cotunneling) can be used to understand and label the data, while the algorithm can take as inputs either gate sensing signals or CAR-induced quantum capacitance detected with RF reflectometry on the superconducting lead. An algorithm getting only gate sensing or RF reflectometry signals as the possible inputs is then applicable to Kitaev chains of any length.

8

8.5. CONCLUSION

In essence, this dissertation illustrates the realization of few-site Kitaev chains: it starts with a review of the theory background (chapter 2), it constructs the necessary ingredients (chapters 3 and 5), and demonstrates the capabilities of two- and three-site chains (chapters 4, 6 and 8). In the outlook, we propose three follow-up experiments for the coming years: coupling one chain to an additional quantum dot to quantify the Majorana quality, coupling two three-site chains together to realize a parity qubit, and creating a five-site Kitaev chain to better understand the advent of topology.

Looking ahead, I hope the impact of this work transcends the engineering of Kitaev chains. The Andreev trimer investigation of chapter 7 serves as a simple example of how such efforts can yield unexpected discoveries — an outcome I aspire to see repeated. I wish the nanotechnological capabilities shown here could serve as an inspiration for novel metamaterial concepts and new creative approaches to Hamiltonian engineering. It would be wonderful to see the Kitaev chain eventually become a valuable technology, but my deepest hope lies elsewhere: seeing new students fall in love with this science and bring new ideas. This journey is not all about what we can achieve, but what we can learn, and whom we can inspire.

8

A

ECT DESTRUCTIVE INTERFERENCE

e report here a brief calculation showing why the interference between the two ECT paths is destructive. Considering CAR and ECT as second-order processes, their rate can be calculated using Fermi's golden rule:

$$I \propto \frac{2\pi}{\hbar} \left| \sum_m \frac{\langle f | V | m \rangle \langle m | V | i \rangle}{E_m - E_i} \right|^2 \delta(E_f - E_i) \tag{A.1}$$

where $|i\rangle$, $|m\rangle$ $|f\rangle$ are the initial, intermediate and final states, and E_i, E_m and E_f are their energies. V is a perturbative coupling of the following form:

$$
\begin{aligned}
V = & t_L c_{L\uparrow}^\dagger d_\uparrow + t_R d_\uparrow c_{R\uparrow}^\dagger + t_L c_{L\downarrow}^\dagger d_\downarrow + t_R d_\downarrow c_{R\downarrow}^\dagger \\
& + t_L c_{L\uparrow} d_\uparrow^\dagger + t_R d_\uparrow^\dagger c_{R\uparrow} + t_L c_{L\downarrow} d_\downarrow^\dagger + t_R d_\downarrow^\dagger c_{R\downarrow}
\end{aligned}
\tag{A.2}
$$

where c_L, d and c_R are the annihilation operators for the left QD, the ABS, and the right QD, respectively, and $\uparrow$ and $\downarrow$ label the spin. The terms appearing in V account for all the processes where a particle tunnels from a QD to the ABS or vice-versa: t_L and t_R are the corresponding probability amplitudes for the left and the right respectively.

We label the joint state with the convention $\left| \text{left QD, ABS, right QD} \right\rangle$ (and of course $\left\langle \text{left QD, ABS, right QD} \right|$), where the ABS state can be either the singlet $|S\rangle = u |0\rangle - v |\uparrow\downarrow\rangle$ or one of the two doublet states $|\uparrow\rangle$, $|\downarrow\rangle$. It is crucial to fix an order for the application of the operators and stick to it, because, as it will be clear in the following, the minus sign of the ECT destructive interference arises from the anticommutation rules of the fermionic operators. Here, we choose the same order for simplicity: left QD, ABS, right QD.

$$
\begin{aligned}
|\uparrow, \uparrow, \uparrow\rangle &= c_{L\uparrow}^\dagger d_\uparrow^\dagger c_{R\uparrow}^\dagger |0, 0, 0\rangle \\
|0, \uparrow\downarrow, 0\rangle &= d_\uparrow^\dagger d_\downarrow^\dagger |0, 0, 0\rangle
\end{aligned}
$$

A

With these ingredients, we can calculate ECT and CAR rates. We report the calculation explicitly for $\uparrow\uparrow$ ECT, other processes can be calculated in a very similar way. Inserting Eq. A.2 in Eq. A.1 and preserving only non-zero terms we get

$$I_{\text{ECT}}^{\uparrow\uparrow} \propto \frac{e t_L^2 t_R^2}{\hbar} \left| \frac{V_\uparrow}{E_\uparrow} + \frac{V_\downarrow}{E_\downarrow} \right|^2 \tag{A.3}$$

where

$$
\begin{aligned}
V_\uparrow &= \langle 0,S,\uparrow| \, d_\uparrow c_{R\uparrow}^\dagger \, |0,\uparrow,0\rangle \langle 0,\uparrow,0| \, c_{L\uparrow} d_\uparrow^\dagger \, |\uparrow,S,0\rangle \\
&= \langle 0,S,\uparrow| \, d_\uparrow c_{R\uparrow}^\dagger d_\uparrow^\dagger \, |0,0,0\rangle \langle 0,\uparrow,0| \, c_{L\uparrow} d_\uparrow^\dagger c_{L\uparrow}^\dagger (u - v d_\uparrow^\dagger d_\downarrow^\dagger) \, |0,0,0\rangle \\
&\overset{!}{=} \langle 0,S,\uparrow| \, \boxed{-}\, d_\uparrow d_\uparrow^\dagger c_{R\uparrow}^\dagger \, |0,0,0\rangle \langle 0,\uparrow,0| \, \boxed{-}\, c_{L\uparrow} c_{L\uparrow}^\dagger d_\uparrow^\dagger (u - v d_\uparrow^\dagger d_\downarrow^\dagger) \, |0,0,0\rangle \\
&= (-u)(-u) \\
&= u^2
\end{aligned}
$$

$$
\begin{aligned}
V_\downarrow &= \langle 0,S,\uparrow| \, c_{L\uparrow} d_\uparrow^\dagger \, |\uparrow,\downarrow,\uparrow\rangle \langle \uparrow,\downarrow,\uparrow| \, d_\uparrow c_{R\uparrow}^\dagger \, |\uparrow,S,0\rangle \\
&= \langle 0,S,\uparrow| \, c_{L\uparrow} d_\uparrow^\dagger c_{L\uparrow}^\dagger d_\downarrow^\dagger c_{R\uparrow}^\dagger \, |0,0,0\rangle \langle \uparrow,\downarrow,\uparrow| \, d_\uparrow c_{R\uparrow}^\dagger c_{L\uparrow}^\dagger (u - v d_\uparrow^\dagger d_\downarrow^\dagger) \, |0,0,0\rangle \\
&\overset{!}{=} \langle 0,S,\uparrow| \, \boxed{-}\, c_{L\uparrow} c_{L\uparrow}^\dagger d_\uparrow^\dagger d_\downarrow^\dagger c_{R\uparrow}^\dagger \, |0,0,0\rangle \langle \uparrow,\downarrow,\uparrow| \, \boxed{+}\, c_{L\uparrow}^\dagger d_\uparrow (u - v d_\uparrow^\dagger d_\downarrow^\dagger) c_{R\uparrow}^\dagger \, |0,0,0\rangle \\
&= (+v)(-v) \\
&= -v^2
\end{aligned}
$$

Exclamation points highlight the step where fermionic operators are reordered, yielding the signs highlighted in yellow. The destructive interference of ECT arises as anticipated from the anticommutation relations of the fermionic operators.

B

RECIPES

Most of the nanofabrication techniques used in this thesis were developed by Sebastian Heedt, Marina Quintero-Pérez, Francesco Borsoi, Nick van Loo, and Grzegorz P. Mazur over the last five years. They are beautifully reviewed in van Loo's PhD thesis. Here, we supplement his work by detailing the fabrication procedures and other preparatory steps used for the nanowire devices discussed in this dissertation. We make use of the following TU Delft and Kavli Nanolab equipment:

Nickname	Manufacturer, model, (*role*)	Specifications
EBPG5200	Raith EBPG5200 (*Electron Beam Pattern Generator*)	100 kV acceleration voltage; < 20 nm alignment resolution.
Tepla	PVA TePla 300 (*plasma*)	Pyrex holder with Faraday grid.
QT-AJA	AJA (*evaporator*)	Loaded with Au, Pd, Co, Ti, and Cr; powered by 10 kV Temescal CV-12SLX; equipped with KDC40 ion source in the load-lock, KSC1202 source controller.
MB-AJA	AJA (*evaporator*)	Loaded with Pd, Pt, and Ti; powered by 10 kV Temescal CV-6SLX; equipped with KDC40 ion source in the load-lock, KSC1202 source controller.
UTS	*Evaporator* with a cryopump in the main chamber and the possibility of hydrogen clean in the load-lock	Loaded with Pt, Ti, Al, and AlOx; powered by 10 kV Temescal CV-12SLX; the arm can be rotated, the stage cooled with liquid N_2; no PMMA allowed.
AC Metal	Alliance Concept AC450 (*sputtering system*)	Loaded with Cr, Mo, W, and Co; equipped with 600 W Huttinger RF and 1500 W DC source.
Dicer	Disco Hi-Tec Europe GmbH DAD3220	

Nickname	Manufacturer, model, (*role*)	Specifications
Oxford ALD	Oxford Instruments Flexal (*Atomic Layer Deposition*)	Thermal and plasma-assisted ALD of Al_2O_3 and HfO_2.
CPD	Leica CPD3 (*Critical Point Dryer*)	Super-critical CO_2 drying
Vacuum oven	Binder VD23	
Optical microscope	Olympus BX51 with DP25 camera	Amplification: ocular 10x, objective 5x/10x/20x/50x/100x.
SEM	Hitachi S-4800 (*Scanning Electron Microscope*)	Max resolution: 1 nm at 15 kV, 2 nm at 1 kV; LN_2 cooled plate.
Micromanipulator	Equipped with a Leica optical microscope	Three-axis needle control; moving stage.
Probe station	SUSS MicroTec PM8	
Bonder	F&S Bondtec 5630	Fed with 25 µm thick Al wire.

B.1. SUBSTRATE PREPARATION

The substrate nanofabrication starts with a standard 4-inch wafer. Typically, we use $525 \pm 25\,\mu m$ Si wafers covered with 285 nm of SiO_2. The substrate undergoes four electron-beam lithography (EBL) steps to deposit, in order, *EBL markers, bottom gates, bond-pads,* and *smart-walls.* Below, we list the procedures in detail.

MARKERS

1. **Spin-coating** with PMMA-950-A6 resist at 4000 rpm (rotations per minute). The wafer is then baked on a hot-plate at 180°, for 15 minutes. Before spin-coating, cleaning the wafer with **Tepla** (200 sccm O_2 flow, 600 W power, 5 minutes) can improve the resist adhesion.

2. **EBPG5200** exposure.

3. Resist **development** for 1 minute in an MIBK:IPA solution with 1:3 ratio (*methyl isobutyl ketone* and *isopropanol*), followed by rinsing in pure IPA for 1 minute and then blow drying with N_2.

4. **Tepla** descum with oxygen plasma, with 200 sccm flow, 100 W power, for 1 minute.

5. Metal evaporation in **QT-AJA**: 5 nm of Ti deposited at 0.5 Å/s followed by 65 nm of Pt deposited at 1 Å/s.

6. **Lift-off** in acetone, overnight, followed by 10 minutes in an ultrasonic bath. Keep the sample vertical for the lift-off. Then, rinse in IPA for 1 minute and blow dry with N_2.

7. **Tepla** ashing: 200 sccm O_2 flow, 600 W power, for 5 minutes.

The markers are deposited at a wafer scale, whereas gates, bondpads, and smart-walls are deposited on smaller 18x18 mm pieces. We refer to the following nomenclature:

Nickname	Shape	Dimensions
wafer	round	4-inch diameter
coupon	square	18 mm side
chip	square	9 mm side

At this stage, the wafer is **diced** into coupons, after applying a protective layer of PMMA-950-A4, spun at 4000 rpm and baked at 180° for 5 minutes. For the following EBL steps, we process one or two coupons together, so that the fabrication of 4 or 8 identical chips can be carried in parallel.

GATES

1. **Spin-coating** with PMMA-950-A2 at 4000 rpm, baking at 180° for 15 minutes.

2. **EBPG5200** exposure.

3. **Development**: MIBK:IPA (1:3) for 1 minute, rinsing in pure IPA for 1 minute, and blow drying with N_2.

4. **Tepla** descum: 200 sccm O_2 flow, 100 W power, for 1 minute.

5. **MB-AJA**: 3 nm of Ti deposited at 0.5 Å/s followed by 17 nm of Pd deposited at 1 Å/s.

6. **Lift-off** in acetone, overnight, possibly followed by 5 minutes in an ultrasonic bath at minimum power or by gentle blowing with a pipette. Then, rinse in IPA for 1 minute and blow dry with N_2.

7. **Tepla** ashing: 200 sccm O_2 flow, 600 W power, for 5 minutes. (*optional*)
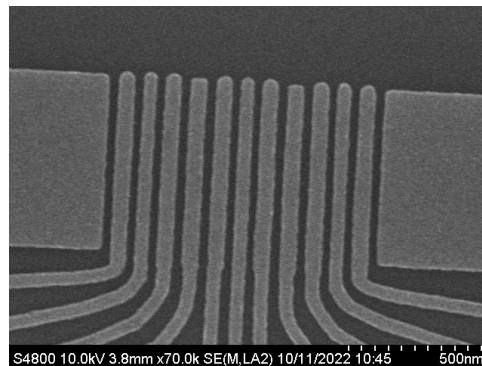
Figure B.1: SEM image of the fine gate structure of a three-site Kitaev chain device.

B

Bond-pads

1. **Spin-coating** with PMMA-950-A6 at 4000 rpm, baking at 180° for 15 minutes.

2. **EBPG5200** exposure.

3. **Development**: MIBK:IPA (1:3) for 1 minute, rinsing in pure IPA for 1 minute, and blow drying with N_2.

4. **Tepla** descum: 200 sccm O_2 flow, 100 W power, for 1 minute. (*optional*)

5. **AC Metal**: W sputtering at 150 W RF power for 150 s. Expected thickness = 50 nm.

6. **Lift-off** in acetone, overnight, possibly followed by 5 minutes in an ultrasonic bath at minimum power or by gentle blowing with a pipette. Then, rinse in IPA for 1 minute and blow dry with N_2.

7. **Tepla** ashing: 200 sccm O_2 flow, 600 W power, for 10 minutes. (*important*)

Then, the whole substrate is covered by a dielectric deposited with **ALD**. Typically, we deposit 20 nm of HfO_2 at 110° (chapters 3 and 4) or a double layer of 10 nm of Al_2O_3 + 10 nm of HfO_2 (chapters 5, 6, and 7).

Smart-Walls

1. **Tepla** cleaning: 200 sccm O_2 flow, 600 W power, for 5 minutes.

2. **Spin-coating** with HSQ FOx25 at 1500 rpm, baking at 180° for 2 minutes. The HSQ is stored in a fridge and must be warmed up to room temperature by waiting at least 5 minutes before usage. To minimize the chances of forming cracks on the resist film, the HSQ should be sprayed with a pipette on the whole coupon and spun immediately.

3. **EBPG5200** exposure.

4. **Development**: Microposit MF321 for 5 minutes at 50°. The coupon is held vertically, with a magnet spinning at 250 rpm to stir the liquid. Rinsing is performed in two steps: first, the coupon is transferred to water to stop the development, then it is transferred to IPA. Both transfers must be performed carefully, holding the coupon horizontally, and without breaking the surface tension of the liquid droplet on the substrate.

5. Since blow-drying with N_2 might damage thin smart-wall structures, the substrate is dried in the **CPD**. If all smart-walls are relatively thick (> 300 nm) then blow-drying with N_2 is fine.

6. **Tepla** cleaning: 200 sccm O_2 flow, 600 W power, for 5 minutes.

Finally, each coupon is **cleaved** into four identical chips.

General remarks:

- Just before spin-coating, cleaning the wafer with **Tepla** (200 sccm O_2 flow, 600 W power, 5 minutes) improves the resist adhesion.

- After development, it is wise to inspect the resist with an **optical microscope**.

- For the **lift-off**, two hours are typically sufficient to dissolve the PMMA in acetone at room temperature, it is even faster in warm acetone. After the PMMA is completely dissolved, delicate pipetting or sonication can help to lift-off the residual metal film.

- **SEM** imaging of the fine structures can be done only in the absence of PMMA or HSQ. It is possible to image the smart-walls after depositing a thin metallic layer on top. In general, SEM inspection dopes the substrate so it is better to avoid it for the chips that are going to be used later on.

B.2. NANOWIRE CONTACTING

A key feature of our fabrication procedure is a clear separation between what is prepared before the incorporation of the nanowire and what is added after. The primary reason for such a division is the strict thermal budget of hybrid InSb-Al nanowires: if their temperature surpasses $\sim 40°$, the interface degrades. This is a severe constraint for cleanroom processes, so the more that can be done before the nanowire is deposited the better. A secondary yet powerful benefit of splitting the fabrication in two is the addition of a checkpoint: when the substrate preparation is finished, SEM inspection of one of the chips verifies the quality of the entire batch.

NANOWIRE DEPOSITION

As soon as the substrates are prepared and can be trusted, the fabrication resumes on one of the chips with the incorporation of the nanowire. This is deposited with a needle controlled by a **micromanipulator**, under an optical microscope. After the nanowire lands on the substrate, it can be pushed next to the smart-walls with the needle itself, as shown in van Loo (2023, chapter 3). Since every chip contains a few copies of identical devices, this process is repeated for every device.

SUPERCONDUCTING CONTACTS

The chip is loaded into the **UTS** load-lock and pumped overnight. Then, the stage is heated to 550 K for outgassing and kept at that temperature for 2 or 3 hours. At the same temperature, the *hydrogen cleaning* of the surface is started: H_2 is injected into the load-lock at a 2 sccm flow to reach a pressure of 6.2×10^{-5} mbar. A W filament heated to ~ 2000 K creates H^* radicals which react with the surface oxide of the InSb nanowire, cleaning it (Haworth et al., 2000; Tessler et al., 2006; Webb et al., 2015). During the H cleaning, the stage is held at a 120° angle for 30 minutes and at a 30° angle for another 30 minutes, to target an approximately uniform cleaning of all the exposed facets of the nanowire. After H cleaning, the stage is loaded into the main chamber and cooled down to 138 K using liquid N_2, letting it thermalize for 1 hour. Finally, Al is deposited at a

~3 Å/min rate while keeping the stage at alternating angles: 45°, 15°, 45°, 15°, 45°, 15°.
2 or 3 nm of Al are deposited at each angle each time for a total thickness ranging from
5 to 17 nm, depending also on the nanowire facet. The nanowire is finally capped with
7.5 nm of Al_2O_3 deposited at 45° and another 7.5 nm at 15° to prevent uncontrolled oxi-
dation of the Al when the nanowire is eventually exposed to air.[1]

Normal contacts

1. **Spin-coating** with PMMA-950-A6 at 4000 rpm, vacuum baking at room tempera-
   ture for 3 hours in the **vacuum oven**.

2. **EBPG5200** exposure.

3. **Development**: MIBK:IPA (1:3) for 1 minute, rinsing in pure IPA for 1 minute, and
   blow drying with N_2.

4. **Tepla** descum: 200 sccm O_2 flow, 100 W power, for 1 minute.

5. **MB-AJA**: the surface oxide is removed with Ar milling. After pumping the load-lock
   under 1 µTorr, Ar is injected with a flow of ~10 sccm to reach a load-lock pressure of
   ~1 mTorr. A Kaufmann KDC40 ion source ionizes, accelerates, and finally neutral-
   izes the Ar to bombard the sample. We Ar mill in two rounds of 15 or 20 s, separated
   by one minute of cooldown time, with ~6 cathode V, 5.75 cathode A, 40 discharge
   V, 0.06 discharge A, 600 beam V, ~10 beam A, 89 accelerator V, ~2.9 accelerator mA,
   ~10 emission mA, ~7 neutralizer V, ~10 neutralizer A. After milling, the sample is
   transferred to QT-AJA for Cr/Au deposition.[2]

6. **QT-AJA**: 10 nm of Cr deposited at 0.5 Å/s followed by ~120 nm of Au deposited at
   1.5 Å/s.

7. **Lift-off** in acetone, overnight, followed by gentle blowing with a pipette. Then,
   rinse in IPA for 1 minute and blow dry with N_2.

8. **SEM** inspection of the final chip. (*optional*)

9. Measure of the resistance between Au contacts at the **probe station**. (*optional*)

---

[1] The UTS is the most technical machine among the ones listed here. In fact, hydrogen cleaning and Al deposi-
tion are the only processes described in this appendix that I couldn't perform myself. They were executed by
either Grzegorz P. Mazur or Jan Cornelis Wolff.

[2] During the transfer from MB-AJA to QT-AJA, the sample is exposed to air for a few seconds. It would be ideal
to deposit Cr/Au right after milling – without breaking the vacuum – but this was not possible: the Ar milling
in QT-AJA was defective (leading to blow-up of nanowires due to electrostatic discharges, it is still unknown
why this was happening in QT-AJA and not in MB-AJA), while MB-AJA didn't have any Cr or Au for deposition
(and we were not allowed to add it to the pockets). Nevertheless, the *ex-situ* process described above is able
to give good ohmic contacts. This creates the suspicion that the main role of milling is not the removal of the
nanowire oxide but rather the creation of metallic In droplets on the surface.
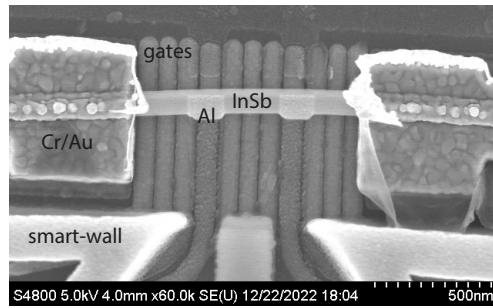
Figure B.2: SEM image of a three-site Kitaev chain device after contact deposition.

Bonding

Finally, The chip is glued on a printed circuit board (PCB) using GE varnish. Based on the SEM inspection (and possibly on the room temperature resistance), one or two devices are selected for cryogenic measurements. They are wired using the Bondtec **bonder**.

a Device   **b** Chip   **c** PCB
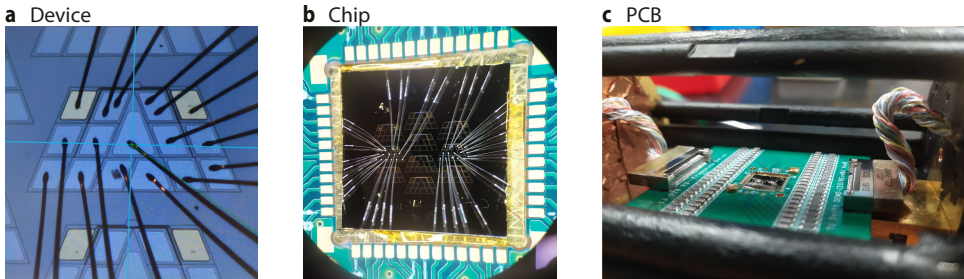
Figure B.3: **a** Optical microscope image of a bonded device. **b** Image through a lens of a full chip with two bonded devices. **c** Image of the PCB inserted into the puck to be loaded into a dilution refrigerator.

C

HOW TO TUNE A KITAEV CHAIN

ere we report a brief and practical tutorial on how to tune a Kitaev chain from scratch. This appendix revisits the structure of the second part of chapter 2, replacing theoretical concepts with real measurements on InSb-Al hybrid nanowires.[1] The steps of the tuning process are outlined in the following checklist:

C.1. PINCHOFFS

First of all, check whether all the gates are responsive. For every bare semiconducting section, set all gates to a voltage that keeps the semiconducting channel in the conducting regime and then try to pinch-off the current with individual gates.
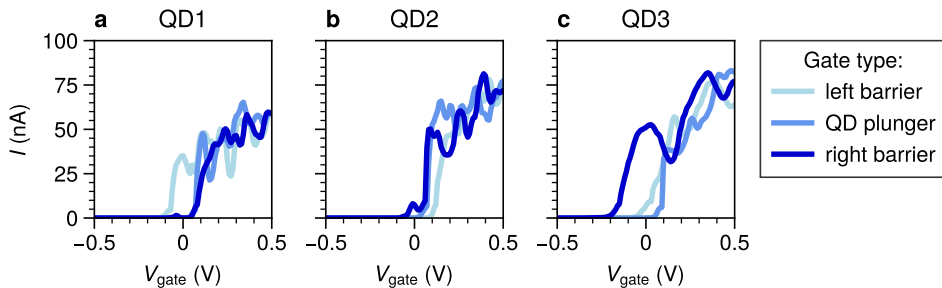
Figure C.1: **Pinch-off curves** for the three gates controlling each QD of a three-site chain device. $V_{bias} = 1\,mV$. The semiconducting InSb channel is conducting for $V_{gate} \sim 0.5\,V$ and insulating for $V_{gate} \sim -0.5\,V$ (with a 10 nm of Al_2O_3 + 10 nm of HfO_2 dielectric separating the InSb nanowire from the gates).

---

[1] In the following, different figures may come from different devices. They are meant to show the most representative example of each tuning step rather than a consistent tuning of the same device. For the tuning of a single device see the `Kitaev3 > raw_data > databases-and-notebooks > devA-notebook-*.pdf` files in https://zenodo.org/records/10709983.

C.2. Hybrid spectra

Then, perform tunneling spectroscopy of the hybrids at zero and finite magnetic field. This checks that the hybrid gates are responsive as well and locates the ABSs. For the following tuning steps, it is useful to avoid low-energy ABSs, since their energy would limit the Kitaev chain gap.[2] It is also important to make sure that the ABSs couple to both sides of the hybrid section. This can be verified by observing the same spectrum from both sides of the hybrid, as reported in the Supplementary Information of Wang et al. (2023), or by measuring a finite non-local conductance, as shown in figure 3.1.
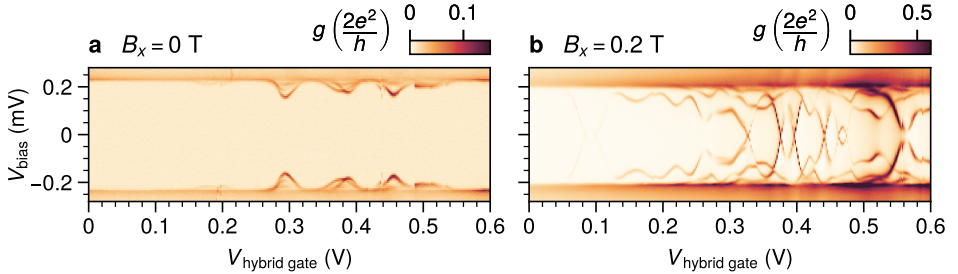
Figure C.2: **Examples of tunneling spectroscopy of one InSb-Al hybrid at zero and finite magnetic field** (the two examples are from the same device but with slightly different gate settings). In panel **a**, only a few ABSs have an energy that is significantly lower than the Al gap ($\approx 230\,\mu V$). At finite field (panel **b**), the ABS energies are reduced according to $E_{ABS} = E_{ABS}^{@B=0} - g\mu_B B/2$ with a g-factor ranging from 10 to 40. This lies between the Al g-factor (≈ 2) and the InSb g-factor (≈ 45). Typically, ABSs at low $V_{hybrid\ gate}$ are more superconducting-like and have a relatively low g-factor, whereas high-$V_{hybrid\ gate}$ ABSs are more semiconducting-like and have a higher g-factor. In the example of panel b, none of the ABSs with $V_{hybrid\ gate} < 0.3\,V$ reach zero energy at $B_x = 0.2\,T$, while some of the others do.

C.3. Form QDs
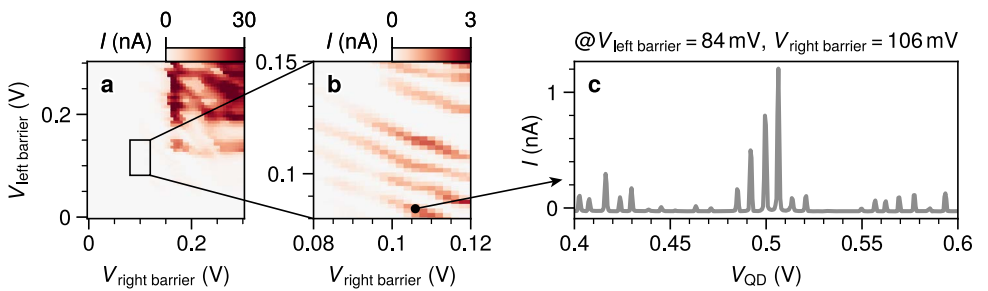
Figure C.3: **QD formation. a.** Corner plot having the barrier gate voltages on the two axes. $V_{QD} = 0.6\,V$, $V_{bias} = 1\,mV$. **b.** Zoom into the tunneling regime. **c.** Coulomb peaks (here, $V_{bias} = 0.5\,mV$).

---

[2] In principle, zero-energy ABSs could be used to define a "Shiba" chain emulating the Kitaev chain Hamiltonian (Fulga et al., 2013). However, tuning a Shiba chain comes with theoretical (Miles et al., 2024) and experimental complications (Wu et al., 2021; van Driel et al., 2024b). Such a scenario is beyond the scope of this appendix.

The formation of a QD starts from the *corner plot* illustrated in figure C.3a: while keeping the QD plunger gate in the conducting regime, both tunnel gates are swept. In this example, both the left and the right tunnel gates switch from the tunneling to the conducting regime around ∼ 150 mV. A zoom into the tunneling regime (panel b) shows sets of parallel lines, indicating the appearance of QD resonant levels. Panel c shows how the QD plunger gate controls the corresponding Coulomb peaks. Eventually, the QD is characterized by measuring the Coulomb diamonds (figure C.4b) and checking the spin polarization with increasing magnetic field (figure C.4c).
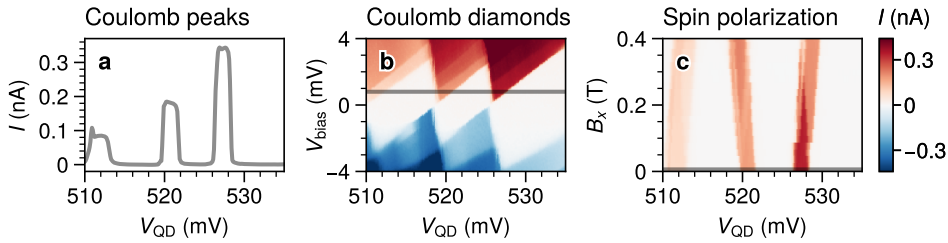
Figure C.4: **QD characterization.** $V_{bias} = 0.8$ mV in panels a and c. From panel b, we extract the lever arm $\alpha \sim 0.3$, the charging energy $E_c \sim 2$ mV, and the typical level spacing $\Delta E_n \sim 1$ mV; from panel c we extract the g-factor ∼ 40. The g-factor can be estimated either from the slope of the resonances or from the extension of the dark-red triangle. Such a triangle is dark precisely because two spin species are available within the bias range above the gap $\left(V_{bias} - \Delta_{Al}\right)$.

C.4. OPTIMIZE QD BARRIERS

After the QDs are formed, fine-tuning the tunneling barriers is key. The barriers separating the QDs from the normal-metal probes can be as high as possible, to have the QD lifetime much smaller than the thermal broadening $\Gamma \ll k_B T$. This scenario is optimal for tunneling spectroscopy since the linewidth is not limited by the QD lifetime. On the other side, the barriers separating the QDs from the hybrid sections shouldn't be too in-
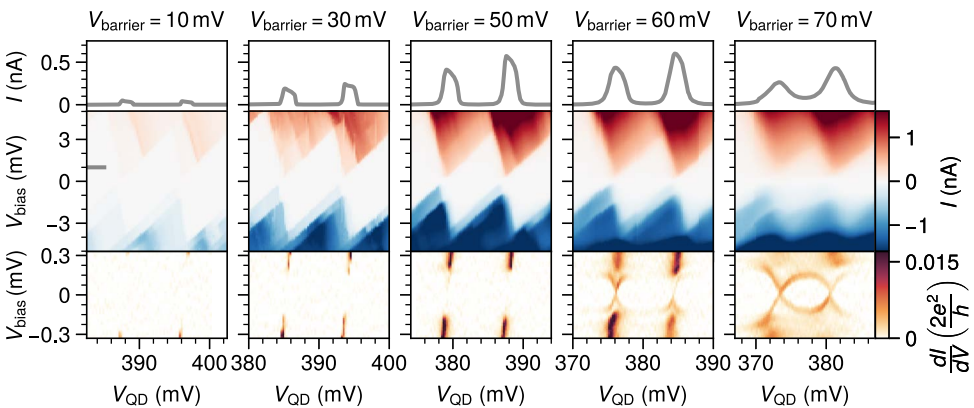
Figure C.5: **Impact of the barrier between a QD and a hybrid segment.** First row: Coulomb peaks. Second row: Coulomb diamonds. Third row: sub-gap spectrum.

sulating, otherwise, they would limit the Kitaev chain t_n and Δ_n couplings. The status of such barriers can be diagnosed in at least three ways:

- Looking at the Coulomb peaks.
  The top row of figure C.5 shows the evolution of the Coulomb peaks as the barrier gate voltage is increased. Here, the peak height stops increasing when $V_{barrier} \geq$ 50 mV, indicating that the current through the QD starts to be limited by the other barrier (to the normal lead). At the same time, from $V_{barrier} \sim 60$ mV on, the peaks get wider and the Coulomb diamonds get more and more blurry, indicating that the QD lifetime (above gap) is set by the QD-hybrid barrier.

- Looking at the QD spectrum (bottom row of figure C.5).
  Below the superconducting gap Δ_{Al}, the spectral lines stay sharp even for relatively high $V_{barrier}$ since the Al gap works effectively as an energy barrier for the QD. Here, a particle-hole symmetric spectrum appears from $V_{barrier} \sim 60$ mV on. In particular, an eye-shaped spectrum is visible at $V_{barrier} = 70$ mV, indicating that the QD is strongly coupled to a superconductor (Lee et al., 2013; Jellinggaard et al., 2016), the smaller the eye, the stronger the coupling. In addition, if the hybrid is populated by ABSs, the direct coupling between the QD and the ABSs can be estimated from the avoided crossings between the QD eye-shape and the ABS spectral lines (Zatelli et al., 2024; Liu et al., 2024a).

- Looking at the QD-ABS charge stability diagrams (figure C.6).
  If a QD and an ABS hybridize, then the QD resonances are modulated by the ABS chemical potential (Grove-Rasmussen et al., 2018). This feature can be used to locate the ABSs in hybrid-gate space (Zatelli et al., 2024). For instance, in panel a of figure C.6, at least four ABSs can be located using this method.
  Strong hybridization can lead to the appearance of dome-like shapes, as in the top of panel c. This scenario should be avoided since it is detrimental to a smooth tuning of the t_n and Δ_n couplings. Note that the QD-ABS hybridization may vary substantially from ABS to ABS.
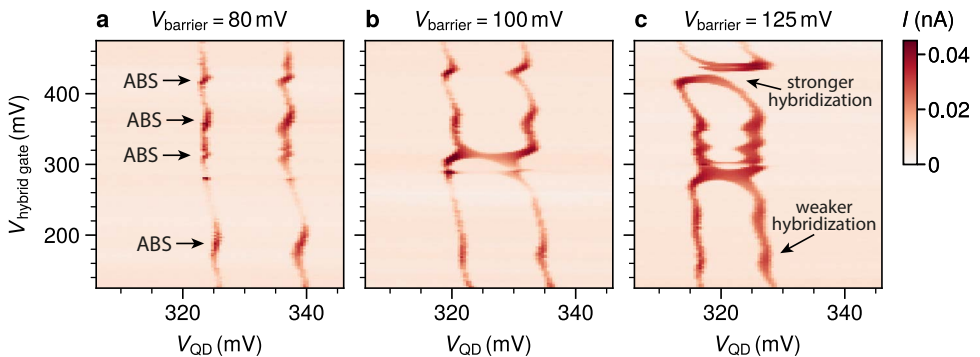
Figure C.6: **QD-ABS charge stability diagrams.** Here, a small $V_{bias} = 50$ μV enables current flow; charge stability diagrams can be measured at zero bias as well by means of lockin conductance (Bordin et al., 2024a).

Here, we would choose an optimum barrier gate voltage of 60 mV or 70 mV for the device of figure C.5 and $V_{\text{barrier}} \sim 80$ mV for the device of figure C.6.

C.5. BALANCE t_n AND Δ_n

After finding ABSs, forming QDs, and optimizing the barriers as described above, observing strong interdot couplings is straightforward. This is manifest in the appearance of avoided crossings in the QD-QD charge stability diagrams, as illustrated in figure C.7. Then, to find a $t = \Delta$ sweet-spot, the procedure is simple: find a $V_{\text{hybrid gate}}$ value with t dominance (avoided crossings opened along the anti-diagonal), find another $V_{\text{hybrid gate}}$ value with Δ dominance (avoided crossings opened along the diagonal), and continuity guarantees to have a sweet-spot at some in-between point. It is sufficient to find these conditions for a single charge degeneracy point. Here, figure C.7 shows a particularly ideal scenario, where the t and Δ dominance (panels a and c, respectively) happen for *all* four charge degeneracy points spanning all possible QD spin combinations. In particular, panel b shows the sweet-spot for the top-left one (up-down spin configuration). At this stage, QD_1 and QD_2 form a minimal Kitaev chain.
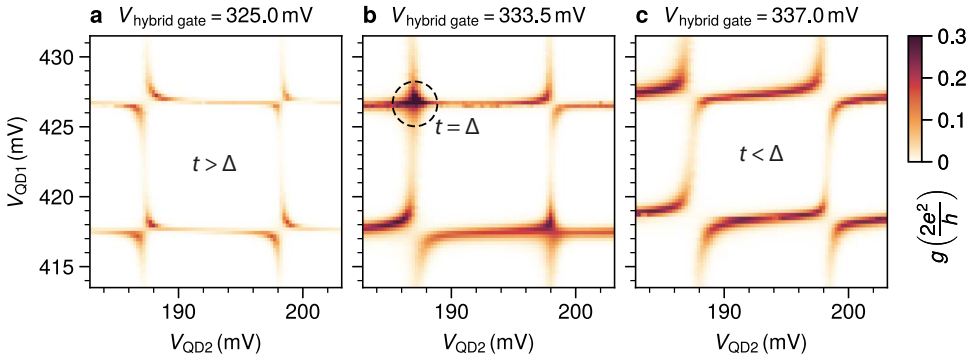
Figure C.7: **QD-QD charge stability diagrams.** From Zatelli et al. (2024).

Tuning a longer Kitaev chain involves repeating this same procedure for all QD pairs, in order: first, form a minimal chain between QD_1 and QD_2, then, set QD_1 off-resonance and balance t_2 and Δ_2 to form a minimal chain between QD_2 and QD_3 – importantly, the QD_2 resonance must be the same used for the first minimal chain – then set QD_2 off-resonance and balance t_3 and Δ_3, and so on. In this inductive procedure, there is one final and key aspect to keep under control: the phase ϕ_n.

C.6. MATCH THE PHASES

For minimal Kitaev chains, the phase is irrelevant, for three-site ones it is sufficient to connect the two superconductors in a loop and apply an out-of-plane field to control the single phase degree of freedom of such a device. Longer chains have more than one phase degree of freedom and require a slightly more elaborated tuning. The simplest solution is addressing each new ϕ_n degree of freedom with the freedom of choosing a corresponding $t_n = \Delta_n$ sweet-spot. Sau and Das Sarma (2012) pointed out, for

one-dimensional Kitaev chains with magnetic field along the chain, that t_n and Δ_n are supposed to be real. Later, Liu et al. (2024b) noted that, if t_n and Δ_n are mediated by ABSs, then either $t_n = +\Delta_n$ or $t_n = -\Delta_n$, depending on the sweet-spot and the spin-configuration of choice. In particular, switching one spin or inverting the u and v components of the ABS should switch the sign. Hence, to tune an arbitrarily long Kitaev chain, it is sufficient to make sure, with appropriate sweet-spot choices, that $t_n = +\Delta_n$ for all n. Here, figure C.8 shows two examples of three-site Kitaev chain sweet-spots where the out-of-plane field B_z sweeps the phase. In the first, $\phi \approx 0$ at $B_z = 0$, while $\phi \approx \pi$ in the second. The target for arbitrarily long chains is choosing the sweet-spots such that, for all n, $\phi_n \approx 0$ at $B_z = 0$, so that no out-of-plane field is needed to tune the chain.
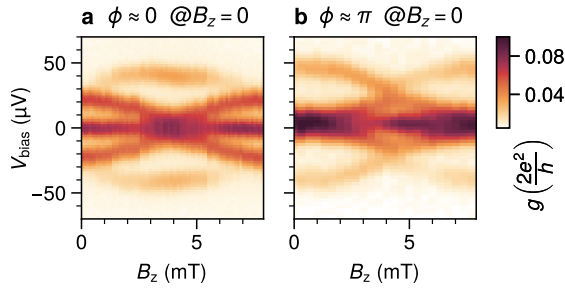
Figure C.8: Three-site Kitaev chain spectrum as a function of the out-of-plane field B_z having $\phi \approx 0$ (panel a) or $\phi \approx \pi$ (panel b) at $B_z = 0$.

BIBLIOGRAPHY

S. Aaronson and L. Chen. Complexity-theoretic foundations of quantum supremacy experiments. In *Proceedings of the 32nd Computational Complexity Conference*, CCC '17, Dagstuhl, DEU, 2017. Schloss Dagstuhl–Leibniz-Zentrum fuer Informatik. ISBN 9783959770408. [Cited on page 5].

R. Acharya, D. A. Abanin, L. Aghababaie-Beni, I. Aleiner, T. I. Andersen, M. Ansmann, F. Arute, K. Arya, A. Asfaw, N. Astrakhantsev, J. Atalaya, R. Babbush, D. Bacon, B. Ballard, J. C. Bardin, J. Bausch, A. Bengtsson, A. Bilmes, S. Blackwell, S. Boixo, G. Bortoli, A. Bourassa, J. Bovaird, L. Brill, M. Broughton, D. A. Browne, B. Buchea, B. B. Buckley, D. A. Buell, T. Burger, B. Burkett, N. Bushnell, A. Cabrera, J. Campero, H.-S. Chang, Y. Chen, Z. Chen, B. Chiaro, D. Chik, C. Chou, J. Claes, A. Y. Cleland, J. Cogan, R. Collins, P. Conner, W. Courtney, A. L. Crook, B. Curtin, S. Das, A. Davies, L. De Lorenzo, D. M. Debroy, S. Demura, M. Devoret, A. Di Paolo, P. Donohoe, I. Drozdov, A. Dunsworth, C. Earle, T. Edlich, A. Eickbusch, A. M. Elbag, M. Elzouka, C. Erickson, L. Faoro, E. Farhi, V. S. Ferreira, L. F. Burgos, E. Forati, A. G. Fowler, B. Foxen, S. Ganjam, G. Garcia, R. Gasca, E. Genois, W. Giang, C. Gidney, D. Gilboa, R. Gosula, A. G. Dau, D. Graumann, A. Greene, J. A. Gross, S. Habegger, J. Hall, M. C. Hamilton, M. Hansen, M. P. Harrigan, S. D. Harrington, F. J. H. Heras, S. Heslin, P. Heu, O. Higgott, G. Hill, J. Hilton, G. Holland, S. Hong, H.-Y. Huang, A. Huff, W. J. Huggins, L. B. Ioffe, S. V. Isakov, J. Iveland, E. Jeffrey, Z. Jiang, C. Jones, S. Jordan, C. Joshi, P. Juhas, D. Kafri, H. Kang, A. H. Karamlou, K. Kechedzhi, J. Kelly, T. Khaire, T. Khattar, M. Khezri, S. Kim, P. V. Klimov, A. R. Klots, B. Kobrin, P. Kohli, A. N. Korotkov, F. Kostritsa, R. Kothari, B. Kozlovskii, J. M. Kreikebaum, V. D. Kurilovich, N. Lacroix, D. Landhuis, T. Lange-Dei, B. W. Langley, P. Laptev, K.-M. Lau, L. Le Guevel, J. Ledford, J. Lee, K. Lee, Y. D. Lensky, S. Leon, B. J. Lester, W. Y. Li, Y. Li, A. T. Lill, W. Liu, W. P. Livingston, A. Locharla, E. Lucero, D. Lundahl, A. Lunt, S. Madhuk, F. D. Malone, A. Maloney, S. Mandrà, J. Manyika, L. S. Martin, O. Martin, S. Martin, C. Maxfield, J. R. McClean, M. McEwen, S. Meeks, A. Megrant, X. Mi, K. C. Miao, A. Mieszala, R. Molavi, S. Molina, S. Montazeri, A. Morvan, R. Movassagh, W. Mruczkiewicz, O. Naaman, M. Neeley, C. Neill, A. Nersisyan, H. Neven, M. Newman, J. H. Ng, A. Nguyen, M. Nguyen, C.-H. Ni, M. Y. Niu, T. E. O'Brien, W. D. Oliver, A. Opremcak, K. Ottosson, A. Petukhov, A. Pizzuto, J. Platt, R. Potter, O. Pritchard, L. P. Pryadko, C. Quintana, G. Ramachandran, M. J. Reagor, J. Redding, D. M. Rhodes, G. Roberts, E. Rosenberg, E. Rosenfeld, P. Roushan, N. C. Rubin, N. Saei, D. Sank, K. Sankaragomathi, K. J. Satzinger, H. F. Schurkus, C. Schuster, A. W. Senior, M. J. Shearn, A. Shorter, N. Shutty, V. Shvarts, S. Singh, V. Sivak, J. Skruzny, S. Small, V. Smelyanskiy, W. C. Smith, R. D. Somma, S. Springer, G. Sterling, D. Strain, J. Suchard, A. Szasz, A. Sztein, D. Thor, A. Torres, M. M. Torunbalci, A. Vaishnav, J. Vargas, S. Vdovichev, G. Vidal, B. Villalonga, C. V. Heidweiller, S. Waltman, S. X. Wang, B. Ware, K. Weber, T. Weidel, T. White, K. Wong,

B. W. K. Woo, C. Xing, Z. J. Yao, P. Yeh, B. Ying, J. Yoo, N. Yosri, G. Young, A. Zalcman, Y. Zhang, N. Zhu, and N. Zobrist. Quantum error correction below the surface code threshold. *Nature*, Dec. 2024. ISSN 1476-4687. doi: 10.1038/s41586-024-08449-y. URL http://dx.doi.org/10.1038/s41586-024-08449-y. [Cited on pages 2 and 3].

M. Aghaee, A. Akkala, Z. Alam, R. Ali, A. Alcaraz Ramirez, M. Andrzejczuk, A. E. Antipov, P. Aseev, M. Astafev, B. Bauer, J. Becker, S. Boddapati, F. Boekhout, J. Bommer, T. Bosma, L. Bourdet, S. Boutin, P. Caroff, L. Casparis, M. Cassidy, S. Chatoor, A. W. Christensen, N. Clay, W. S. Cole, F. Corsetti, A. Cui, P. Dalampiras, A. Dokania, G. de Lange, M. de Moor, J. C. Estrada Saldaña, S. Fallahi, Z. H. Fathabad, J. Gamble, G. Gardner, D. Govender, F. Griggio, R. Grigoryan, S. Gronin, J. Gukelberger, E. B. Hansen, S. Heedt, J. Herranz Zamorano, S. Ho, U. L. Holgaard, H. Ingerslev, L. Johansson, J. Jones, R. Kallaher, F. Karimi, T. Karzig, E. King, M. E. Kloster, C. Knapp, D. Kocon, J. Koski, P. Kostamo, P. Krogstrup, M. Kumar, T. Laeven, T. Larsen, K. Li, T. Lindemann, J. Love, R. Lutchyn, M. H. Madsen, M. Manfra, S. Markussen, E. Martinez, R. McNeil, E. Memisevic, T. Morgan, A. Mullally, C. Nayak, J. Nielsen, W. H. P. Nielsen, B. Nijholt, A. Nurmohamed, E. O'Farrell, K. Otani, S. Pauka, K. Petersson, L. Petit, D. I. Pikulin, F. Preiss, M. Quintero-Perez, M. Rajpalke, K. Rasmussen, D. Razmadze, O. Reentila, D. Reilly, R. Rouse, I. Sadovskyy, L. Sainiemi, S. Schreppler, V. Sidorkin, A. Singh, S. Singh, S. Sinha, P. Sohr, T. Stankevič, L. Stek, H. Suominen, J. Suter, V. Svidenko, S. Teicher, M. Temuerhan, N. Thiyagarajah, R. Tholapi, M. Thomas, E. Toomey, S. Upadhyay, I. Urban, S. Vaitiekėnas, K. Van Hoogdalem, D. Van Woerkom, D. V. Viazmitinov, D. Vogel, S. Waddy, J. Watson, J. Weston, G. W. Winkler, C. K. Yang, S. Yau, D. Yi, E. Yucelen, A. Webster, R. Zeisel, and R. Zhao. InAs-Al hybrid devices passing the topological gap protocol. *Physical Review B*, 107(24), June 2023. ISSN 2469-9969. doi: 10.1103/physrevb.107.245423. URL http://dx.doi.org/10.1103/PhysRevB.107.245423. [Cited on page 3].

M. Aghaee, A. A. Ramirez, Z. Alam, R. Ali, M. Andrzejczuk, A. Antipov, M. Astafev, A. Barzegar, B. Bauer, J. Becker, U. K. Bhaskar, A. Bocharov, S. Boddapati, D. Bohn, J. Bommer, L. Bourdet, A. Bousquet, S. Boutin, L. Casparis, B. J. Chapman, S. Chatoor, A. W. Christensen, C. Chua, P. Codd, W. Cole, P. Cooper, F. Corsetti, A. Cui, P. Dalpasso, J. P. Dehollain, G. de Lange, M. de Moor, A. Ekefjärd, T. E. Dandachi, J. C. E. Saldaña, S. Fallahi, L. Galletti, G. Gardner, D. Govender, F. Griggio, R. Grigoryan, S. Grijalva, S. Gronin, J. Gukelberger, M. Hamdast, F. Hamze, E. B. Hansen, S. Heedt, Z. Heidarnia, J. H. Zamorano, S. Ho, L. Holgaard, J. Hornibrook, J. Indrapiromkul, H. Ingerslev, L. Ivancevic, T. Jensen, J. Jhoja, J. Jones, K. V. Kalashnikov, R. Kallaher, R. Kalra, F. Karimi, T. Karzig, E. King, M. E. Kloster, C. Knapp, D. Kocon, J. Koski, P. Kostamo, M. Kumar, T. Laeven, T. Larsen, J. Lee, K. Lee, G. Leum, K. Li, T. Lindemann, M. Looij, J. Love, M. Lucas, R. Lutchyn, M. H. Madsen, N. Madulid, A. Malmros, M. Manfra, D. Mantri, S. B. Markussen, E. Martinez, M. Mattila, R. McNeil, A. B. Mei, R. V. Mishmash, G. Mohandas, C. Mollgaard, T. Morgan, G. Moussa, C. Nayak, J. H. Nielsen, J. M. Nielsen, W. H. P. Nielsen, B. Nijholt, M. Nystrom, E. O'Farrell, T. Ohki, K. Otani, B. P. Wütz, S. Pauka, K. Petersson, L. Petit, D. Pikulin, G. Prawiroatmodjo, F. Preiss, E. P. Morejon, M. Rajpalke, C. Ranta, K. Rasmussen, D. Razmadze, O. Reentila, D. J. Reilly, Y. Ren, K. Reneris, R. Rouse, I. Sadovskyy, L. Sainiemi, I. Sanlorenzo, E. Schmidgall,

C. Sfiligoj, M. B. Shah, K. Simoes, S. Singh, S. Sinha, T. Soerensen, P. Sohr, T. Stankevic, L. Stek, E. Stuppard, H. Suominen, J. Suter, S. Teicher, N. Thiyagarajah, R. Tholapi, M. Thomas, E. Toomey, J. Tracy, M. Turley, S. Upadhyay, I. Urban, K. Van Hoogdalem, D. J. Van Woerkom, D. V. Viazmitinov, D. Vogel, J. Watson, A. Webster, J. Weston, G. W. Winkler, D. Xu, C. K. Yang, E. Yucelen, R. Zeisel, G. Zheng, and J. Zilke. Interferometric Single-Shot Parity Measurement in an InAs-Al Hybrid Device, 2024. URL https://arxiv.org/abs/2401.09549. [Cited on page 3].

D. Aharonov and M. Ben-Or. Fault-tolerant quantum computation with constant error. In *Proceedings of the twenty-ninth annual ACM symposium on Theory of computing - STOC '97*, STOC '97. ACM Press, 1997. doi: 10.1145/258533.258579. URL http://dx.doi.org/10.1145/258533.258579. [Cited on page 23].

S. Ahn, H. Pan, B. Woods, T. D. Stanescu, and S. Das Sarma. Estimating disorder and its adverse effects in semiconductor Majorana nanowires. *Physical Review Materials*, 5 (12), Dec. 2021. ISSN 2475-9953. doi: 10.1103/physrevmaterials.5.124602. URL http://dx.doi.org/10.1103/PhysRevMaterials.5.124602. [Cited on pages 3 and 4].

S. V. Aksenov, A. O. Zlotnikov, and M. S. Shustin. Strong Coulomb interactions in the problem of Majorana modes in a wire of the nontrivial topological class BDI. *Physical Review B*, 101(12), Mar. 2020. ISSN 2469-9969. doi: 10.1103/physrevb.101.125431. URL http://dx.doi.org/10.1103/PhysRevB.101.125431. [Cited on page 163].

S. M. Albrecht, A. P. Higginbotham, M. Madsen, F. Kuemmeth, T. S. Jespersen, J. Nygård, P. Krogstrup, and C. M. Marcus. Exponential protection of zero modes in Majorana islands. *Nature*, 531(7593):206–209, Mar. 2016. ISSN 1476-4687. doi: 10.1038/nature17162. URL http://dx.doi.org/10.1038/nature17162. [Cited on page 3].

J. Alicea. New directions in the pursuit of Majorana fermions in solid state systems. *Reports on Progress in Physics*, 75(7):076501, June 2012. ISSN 1361-6633. doi: 10.1088/0034-4885/75/7/076501. URL http://dx.doi.org/10.1088/0034-4885/75/7/076501. [Cited on pages 3 and 19].

J. Alicea and P. Fendley. Topological Phases with Parafermions: Theory and Blueprints. *Annual Review of Condensed Matter Physics*, 7(1):119–139, Mar. 2016. ISSN 1947-5462. doi: 10.1146/annurev-conmatphys-031115-011336. URL http://dx.doi.org/10.1146/annurev-conmatphys-031115-011336. [Cited on page 24].

J. Alicea, Y. Oreg, G. Refael, F. von Oppen, and M. P. A. Fisher. Non-Abelian statistics and topological quantum information processing in 1D wire networks. *Nature Physics*, 7 (5):412–417, Feb. 2011. ISSN 1745-2481. doi: 10.1038/nphys1915. URL http://dx.doi.org/10.1038/nphys1915. [Cited on pages 10, 20, 21, and 167].

M. Alvarado, A. L. Yeyati, R. Aguado, and R. S. Souto. Interplay between Majorana and Shiba states in a minimal Kitaev chain coupled to a superconductor, 2024. URL https://arxiv.org/abs/2407.07050. [Cited on page 39].

T. I. Andersen, Y. D. Lensky, K. Kechedzhi, I. K. Drozdov, A. Bengtsson, S. Hong, A. Morvan, X. Mi, A. Opremcak, R. Acharya, R. Allen, M. Ansmann, F. Arute, K. Arya, A. Asfaw,

J. Atalaya, R. Babbush, D. Bacon, J. C. Bardin, G. Bortoli, A. Bourassa, J. Bovaird, L. Brill, M. Broughton, B. B. Buckley, D. A. Buell, T. Burger, B. Burkett, N. Bushnell, Z. Chen, B. Chiaro, D. Chik, C. Chou, J. Cogan, R. Collins, P. Conner, W. Courtney, A. L. Crook, B. Curtin, D. M. Debroy, A. Del Toro Barba, S. Demura, A. Dunsworth, D. Eppens, C. Erickson, L. Faoro, E. Farhi, R. Fatemi, V. S. Ferreira, L. F. Burgos, E. Forati, A. G. Fowler, B. Foxen, W. Giang, C. Gidney, D. Gilboa, M. Giustina, R. Gosula, A. G. Dau, J. A. Gross, S. Habegger, M. C. Hamilton, M. Hansen, M. P. Harrigan, S. D. Harrington, P. Heu, J. Hilton, M. R. Hoffmann, T. Huang, A. Huff, W. J. Huggins, L. B. Ioffe, S. V. Isakov, J. Iveland, E. Jeffrey, Z. Jiang, C. Jones, P. Juhas, D. Kafri, T. Khattar, M. Khezri, M. Kieferová, S. Kim, A. Kitaev, P. V. Klimov, A. R. Klots, A. N. Korotkov, F. Kostritsa, J. M. Kreikebaum, D. Landhuis, P. Laptev, K.-M. Lau, L. Laws, J. Lee, K. W. Lee, B. J. Lester, A. T. Lill, W. Liu, A. Locharla, E. Lucero, F. D. Malone, O. Martin, J. R. McClean, T. McCourt, M. McEwen, K. C. Miao, A. Mieszala, M. Mohseni, S. Montazeri, E. Mount, R. Movassagh, W. Mruczkiewicz, O. Naaman, M. Neeley, C. Neill, A. Nersisyan, M. Newman, J. H. Ng, A. Nguyen, M. Nguyen, M. Y. Niu, T. E. O'Brien, S. Omonije, A. Petukhov, R. Potter, L. P. Pryadko, C. Quintana, C. Rocque, N. C. Rubin, N. Saei, D. Sank, K. Sankaragomathi, K. J. Satzinger, H. F. Schurkus, C. Schuster, M. J. Shearn, A. Shorter, N. Shutty, V. Shvarts, J. Skruzny, W. C. Smith, R. Somma, G. Sterling, D. Strain, M. Szalay, A. Torres, G. Vidal, B. Villalonga, C. V. Heidweiller, T. White, B. W. K. Woo, C. Xing, Z. J. Yao, P. Yeh, J. Yoo, G. Young, A. Zalcman, Y. Zhang, N. Zhu, N. Zobrist, H. Neven, S. Boixo, A. Megrant, J. Kelly, Y. Chen, V. Smelyanskiy, E.-A. Kim, I. Aleiner, and P. Roushan. Non-Abelian braiding of graph vertices in a superconducting processor. *Nature*, 618 (7964):264–269, May 2023. ISSN 1476-4687. doi: 10.1038/s41586-023-05954-4. URL http://dx.doi.org/10.1038/s41586-023-05954-4. [Cited on page 3].

P. W. Anderson. Localized Magnetic States in Metals. *Physical Review*, 124(1):41–53, Oct. 1961. ISSN 0031-899X. doi: 10.1103/physrev.124.41. URL http://dx.doi.org/10.1103/PhysRev.124.41. [Cited on page 34].

F. Ando, Y. Miyasaka, T. Li, J. Ishizuka, T. Arakawa, Y. Shiota, T. Moriyama, Y. Yanase, and T. Ono. Observation of superconducting diode effect. *Nature*, 584(7821):373–376, Aug. 2020. ISSN 1476-4687. doi: 10.1038/s41586-020-2590-4. URL http://dx.doi.org/10.1038/s41586-020-2590-4. [Cited on page 134].

A. F. Andreev. The Thermal Conductivity of the Intermediate State in Superconductors. *Soviet Physics JETP*, 19(5), Nov. 1964. URL http://www.jetp.ras.ru/cgi-bin/dn/e_019_05_1228.pdf. [Cited on page 32].

A. E. Antipov, A. Bargerbos, G. W. Winkler, B. Bauer, E. Rossi, and R. M. Lutchyn. Effects of Gate-Induced Electric Fields on Semiconductor Majorana Nanowires. *Physical Review X*, 8(3), Aug. 2018. ISSN 2160-3308. doi: 10.1103/physrevx.8.031041. URL http://dx.doi.org/10.1103/PhysRevX.8.031041. [Cited on page 35].

I. Araya Day, S. Miles, D. Varjas, and A. R. Akhmerov. Pymablock, 6 2023. [Cited on page 144].

I. Araya Day, S. Miles, H. K. Kerstens, D. Varjas, and A. R. Akhmerov. Pymablock: an

algorithm and a package for quasi-degenerate perturbation theory, 2024. URL https://arxiv.org/abs/2404.03728. [Cited on page 144].

P. Aseev, A. Fursina, F. Boekhout, F. Krizek, J. E. Sestoft, F. Borsoi, S. Heedt, G. Wang, L. Binci, S. Martí-Sánchez, T. Swoboda, R. Koops, E. Uccelli, J. Arbiol, P. Krogstrup, L. P. Kouwenhoven, and P. Caroff. Selectivity Map for Molecular Beam Epitaxy of Advanced III–V Quantum Nanowire Networks. *Nano Letters*, 19(1):218–227, Dec. 2018. ISSN 1530-6992. doi: 10.1021/acs.nanolett.8b03733. URL http://dx.doi.org/10.1021/acs.nanolett.8b03733. [Cited on page 3].

S. Baba, C. Jünger, S. Matsuo, A. Baumgartner, Y. Sato, H. Kamata, K. Li, S. Jeppesen, L. Samuelson, H. Q. Xu, C. Schönenberger, and S. Tarucha. Cooper-pair splitting in two parallel InAs nanowires. *New Journal of Physics*, 20(6):063021, June 2018. ISSN 1367-2630. doi: 10.1088/1367-2630/aac74e. URL http://dx.doi.org/10.1088/1367-2630/aac74e. [Cited on page 92].

G. Badawy, S. Gazibegovic, F. Borsoi, S. Heedt, C.-A. Wang, S. Koelling, M. A. Verheijen, L. P. Kouwenhoven, and E. P. A. M. Bakkers. High Mobility Stemless InSb Nanowires. *Nano Letters*, 19(6):3575–3582, May 2019. ISSN 1530-6992. doi: 10.1021/acs.nanolett.9b00545. URL http://dx.doi.org/10.1021/acs.nanolett.9b00545. [Cited on pages 3 and 100].

A. Banerjee, O. Lesser, M. A. Rahman, H.-R. Wang, M.-R. Li, A. Kringhøj, A. M. Whiticar, A. C. C. Drachmann, C. Thomas, T. Wang, M. J. Manfra, E. Berg, Y. Oreg, A. Stern, and C. M. Marcus. Signatures of a topological phase transition in a planar Josephson junction. *Physical Review B*, 107(24), June 2023. ISSN 2469-9969. doi: 10.1103/physrevb.107.245304. URL http://dx.doi.org/10.1103/PhysRevB.107.245304. [Cited on page 108].

J. Bardeen, L. N. Cooper, and J. R. Schrieffer. Theory of Superconductivity. *Physical Review*, 108(5):1175–1204, Dec. 1957. ISSN 0031-899X. doi: 10.1103/physrev.108.1175. URL http://dx.doi.org/10.1103/PhysRev.108.1175. [Cited on page 30].

A. Bargerbos, M. Pita-Vidal, R. Žitko, J. Ávila, L. J. Splitthoff, L. Grünhaupt, J. J. Wesdorp, C. K. Andersen, Y. Liu, L. P. Kouwenhoven, R. Aguado, A. Kou, and B. van Heck. Singlet-Doublet Transitions of a Quantum Dot Josephson Junction Detected in a Transmon Circuit. *PRX Quantum*, 3(3), July 2022. ISSN 2691-3399. doi: 10.1103/prxquantum.3.030311. URL http://dx.doi.org/10.1103/PRXQuantum.3.030311. [Cited on page 134].

A. Bargerbos, M. Pita-Vidal, R. Žitko, L. J. Splitthoff, L. Grünhaupt, J. J. Wesdorp, Y. Liu, L. P. Kouwenhoven, R. Aguado, C. K. Andersen, A. Kou, and B. van Heck. Spectroscopy of Spin-Split Andreev Levels in a Quantum Dot with Superconducting Leads. *Physical Review Letters*, 131(9), Aug. 2023a. ISSN 1079-7114. doi: 10.1103/physrevlett.131.097001. URL http://dx.doi.org/10.1103/PhysRevLett.131.097001. [Cited on page 134].

A. Bargerbos, L. J. Splitthoff, M. Pita-Vidal, J. J. Wesdorp, Y. Liu, P. Krogstrup, L. P. Kouwenhoven, C. K. Andersen, and L. Grünhaupt. Mitigation of Quasiparticle Loss in Superconducting Qubits by Phonon Scattering. *Physical Review Applied*, 19(2), Feb. 2023b. ISSN 2331-7019. doi: 10.1103/physrevapplied.19.024014. URL http://dx.doi.org/10.1103/PhysRevApplied.19.024014. [Cited on page 170].

J. Bauer, A. Oguri, and A. C. Hewson. Spectral properties of locally correlated electrons in a Bardeen–Cooper–Schrieffer superconductor. *Journal of Physics: Condensed Matter*, 19(48):486211, Nov. 2007. ISSN 1361-648X. doi: 10.1088/0953-8984/19/48/486211. URL http://dx.doi.org/10.1088/0953-8984/19/48/486211. [Cited on pages 34, 35, 45, 46, 53, 104, 136, and 144].

D. Beckmann and H. v. Löhneysen. Experimental Evidence for Crossed Andreev Reflection. In *AIP Conference Proceedings*, volume 850, page 875–876. AIP, 2006. doi: 10.1063/1.2354983. URL http://dx.doi.org/10.1063/1.2354983. [Cited on page 70].

D. Beckmann, H. B. Weber, and H. v. Löhneysen. Evidence for Crossed Andreev Reflection in Superconductor-Ferromagnet Hybrid Structures. *Physical Review Letters*, 93 (19), Nov. 2004. ISSN 1079-7114. doi: 10.1103/physrevlett.93.197003. URL http://dx.doi.org/10.1103/PhysRevLett.93.197003. [Cited on page 42].

C. Beenakker. Search for Majorana Fermions in Superconductors. *Annual Review of Condensed Matter Physics*, 4(1):113–136, Apr. 2013. ISSN 1947-5462. doi: 10.1146/annurev-conmatphys-030212-184337. URL http://dx.doi.org/10.1146/annurev-conmatphys-030212-184337. [Cited on page 3].

J. Benestad, A. Tsintzis, R. S. Souto, M. Leijnse, E. van Nieuwenburg, and J. Danon. Machine-learned tuning of artificial Kitaev chains from tunneling spectroscopy measurements. *Physical Review B*, 110(7), Aug. 2024. ISSN 2469-9969. doi: 10.1103/physrevb.110.075402. URL http://dx.doi.org/10.1103/PhysRevB.110.075402. [Cited on page 39].

F. Bennebroek Evertsz'. Supercurrent modulation by Andreev bound states in a quantum dot Josephson junction. Master's thesis, Delft University of Technology, 2023. [Cited on pages 122, 126, and 137].

F. J. Bennebroek Evertsz', A. Bordin, B. S. J. Roovers, J. D. Torres Luna, N. van Loo, R. Seoane Souto, F. Zatelli, and L. P. Kouwenhoven. . *In preparation*, 2025. [Cited on pages 160 and 162].

C. H. Bennett, G. Brassard, C. Crépeau, R. Jozsa, A. Peres, and W. K. Wootters. Teleporting an unknown quantum state via dual classical and Einstein-Podolsky-Rosen channels. *Physical Review Letters*, 70(13):1895–1899, Mar. 1993. ISSN 0031-9007. doi: 10.1103/physrevlett.70.1895. URL http://dx.doi.org/10.1103/PhysRevLett.70.1895. [Cited on page 98].

E. Bernstein and U. Vazirani. Quantum complexity theory. In *Proceedings of the twenty-fifth annual ACM symposium on Theory of computing - STOC '93*, STOC '93, page

11–20. ACM Press, 1993. doi: 10.1145/167088.167097. URL http://dx.doi.org/10.1145/167088.167097. [Cited on page 5].

N. N. Bogoljubov. On a new method in the theory of superconductivity. *Il Nuovo Cimento*, 7(6):794–805, Mar. 1958. ISSN 1827-6121. doi: 10.1007/bf02745585. URL http://dx.doi.org/10.1007/BF02745585. [Cited on pages 30 and 31].

J. D. Bommer, H. Zhang, O. Gül, B. Nijholt, M. Wimmer, F. N. Rybakov, J. Garaud, D. Rodic, E. Babaev, M. Troyer, D. Car, S. R. Plissard, E. P. Bakkers, K. Watanabe, T. Taniguchi, and L. P. Kouwenhoven. Spin-Orbit Protection of Induced Superconductivity in Majorana Nanowires. *Physical Review Letters*, 122(18), May 2019. ISSN 1079-7114. doi: 10.1103/physrevlett.122.187702. URL http://dx.doi.org/10.1103/PhysRevLett.122.187702. [Cited on page 63].

P. Bonderson, M. Freedman, and C. Nayak. Measurement-Only Topological Quantum Computation. *Physical Review Letters*, 101(1), June 2008. ISSN 1079-7114. doi: 10.1103/physrevlett.101.010501. URL http://dx.doi.org/10.1103/PhysRevLett.101.010501. [Cited on page 21].

A. Bordin, G. Wang, C.-X. Liu, S. L. ten Haaf, N. van Loo, G. P. Mazur, D. Xu, D. van Driel, F. Zatelli, S. Gazibegovic, G. Badawy, E. P. Bakkers, M. Wimmer, L. P. Kouwenhoven, and T. Dvir. Tunable Crossed Andreev Reflection and Elastic Cotunneling in Hybrid Nanowires. *Physical Review X*, 13(3), Sept. 2023. ISSN 2160-3308. doi: 10.1103/physrevx.13.031031. URL http://dx.doi.org/10.1103/PhysRevX.13.031031. [Cited on pages 37, 69, 76, 93, 94, 109, 114, 122, 123, 130, 131, and 134].

A. Bordin, F. J. Bennebroek Evertsz', G. O. Steffensen, T. Dvir, G. P. Mazur, D. van Driel, N. van Loo, J. C. Wolff, E. P. A. M. Bakkers, A. L. Yeyati, and L. P. Kouwenhoven. Supercurrent through an Andreev trimer, 2024a. URL https://arxiv.org/abs/2402.19284. [Cited on page 188].

A. Bordin, X. Li, D. van Driel, J. C. Wolff, Q. Wang, S. L. ten Haaf, G. Wang, N. van Loo, L. P. Kouwenhoven, and T. Dvir. Crossed Andreev Reflection and Elastic Cotunneling in Three Quantum Dots Coupled by Superconductors. *Physical Review Letters*, 132(5), Feb. 2024b. ISSN 1079-7114. doi: 10.1103/physrevlett.132.056602. URL http://dx.doi.org/10.1103/PhysRevLett.132.056602. [Cited on pages 109, 122, 123, 128, 143, and 148].

A. Bordoloi, V. Zannier, L. Sorba, C. Schönenberger, and A. Baumgartner. Spin cross-correlation experiments in an electron entangler. *Nature*, 612(7940):454–458, Nov. 2022. ISSN 1476-4687. doi: 10.1038/s41586-022-05436-z. URL http://dx.doi.org/10.1038/s41586-022-05436-z. [Cited on page 38].

P. Boross and A. Pályi. Braiding-based quantum control of a Majorana qubit built from quantum dots. *Physical Review B*, 109(12), Mar. 2024. ISSN 2469-9969. doi: 10.1103/physrevb.109.125410. URL http://dx.doi.org/10.1103/PhysRevB.109.125410. [Cited on page 39].

P. Boross, J. K. Asbóth, G. Széchenyi, L. Oroszlány, and A. Pályi. Poor man's topological quantum gate based on the Su-Schrieffer-Heeger model. *Physical Review B*, 100(4), July 2019. ISSN 2469-9969. doi: 10.1103/physrevb.100.045414. URL http://dx.doi.org/10.1103/PhysRevB.100.045414. [Cited on page 39].

F. Borsoi, G. P. Mazur, N. van Loo, M. P. Nowak, L. Bourdet, K. Li, S. Korneychuk, A. Fursina, J. Wang, V. Levajac, E. Memisevic, G. Badawy, S. Gazibegovic, K. van Hoogdalem, E. P. A. M. Bakkers, L. P. Kouwenhoven, S. Heedt, and M. Quintero-Pérez. Single-Shot Fabrication of Semiconducting–Superconducting Nanowire Devices. *Advanced Functional Materials*, 31(34), June 2021. ISSN 1616-3028. doi: 10.1002/adfm.202102388. URL http://dx.doi.org/10.1002/adfm.202102388. [Cited on pages 44, 56, and 75].

D. Bouman, R. J. J. van Gulik, G. Steffensen, D. Pataki, P. Boross, P. Krogstrup, J. Nygård, J. Paaske, A. Pályi, and A. Geresdi. Triplet-blockaded Josephson supercurrent in double quantum dots. *Physical Review B*, 102(22), Dec. 2020. ISSN 2469-9969. doi: 10.1103/physrevb.102.220505. URL http://dx.doi.org/10.1103/PhysRevB.102.220505. [Cited on page 134].

A. M. Bozkurt, S. Miles, S. L. D. t. Haaf, C.-X. Liu, F. Hassler, and M. Wimmer. Interaction-induced strong zero modes in short quantum dot chains with time-reversal symmetry, 2024. URL https://arxiv.org/abs/2405.14940. [Cited on pages 39 and 125].

S. Bravyi. Universal quantum computation with the $\nu = 5/2$ fractional quantum Hall state. *Physical Review A*, 73(4), Apr. 2006. ISSN 1094-1622. doi: 10.1103/physreva.73.042313. URL http://dx.doi.org/10.1103/PhysRevA.73.042313. [Cited on page 23].

S. Bravyi and A. Kitaev. Universal quantum computation with ideal Clifford gates and noisy ancillas. *Physical Review A*, 71(2), Feb. 2005. ISSN 1094-1622. doi: 10.1103/physreva.71.022316. URL http://dx.doi.org/10.1103/PhysRevA.71.022316. [Cited on page 23].

S. B. Bravyi and A. Y. Kitaev. Fermionic Quantum Computation. *Annals of Physics*, 298 (1):210–226, May 2002. ISSN 0003-4916. doi: 10.1006/aphy.2002.6254. URL http://dx.doi.org/10.1006/aphy.2002.6254. [Cited on page 18].

G. Burkard, T. D. Ladd, A. Pan, J. M. Nichol, and J. R. Petta. Semiconductor spin qubits. *Reviews of Modern Physics*, 95(2), June 2023. ISSN 1539-0756. doi: 10.1103/revmodphys.95.025003. URL http://dx.doi.org/10.1103/RevModPhys.95.025003. [Cited on pages 134 and 170].

J. Cayao and R. Aguado. Non-Hermitian minimal Kitaev chains, 2024. URL https://arxiv.org/abs/2406.18974. [Cited on page 39].

W. Chang, S. M. Albrecht, T. S. Jespersen, F. Kuemmeth, P. Krogstrup, J. Nygård, and C. M. Marcus. Hard gap in epitaxial semiconductor–superconductor nanowires. *Nature Nanotechnology*, 10(3):232–236, Jan. 2015. ISSN 1748-3395. doi: 10.1038/nnano.2014.306. URL http://dx.doi.org/10.1038/nnano.2014.306. [Cited on page 3].

C.-K. Chiu, J. C. Teo, A. P. Schnyder, and S. Ryu. Classification of topological quantum matter with symmetries. *Reviews of Modern Physics*, 88(3), Aug. 2016. ISSN 1539-0756. doi: 10.1103/revmodphys.88.035005. URL http://dx.doi.org/10.1103/RevModPhys.88.035005. [Cited on page 24].

M.-S. Choi, C. Bruder, and D. Loss. Spin-dependent Josephson current through double quantum dots and measurement of entangled electron states. *Physical Review B*, 62(20):13569–13572, Nov. 2000. ISSN 1095-3795. doi: 10.1103/physrevb.62.13569. URL http://dx.doi.org/10.1103/PhysRevB.62.13569. [Cited on pages 42, 68, and 98].

D. J. Clarke. Experimentally accessible topological quality factor for wires with zero energy modes. *Physical Review B*, 96(20), Nov. 2017. ISSN 2469-9969. doi: 10.1103/physrevb.96.201109. URL http://dx.doi.org/10.1103/PhysRevB.96.201109. [Cited on page 162].

J. Clarke and F. K. Wilhelm. Superconducting quantum bits. *Nature*, 453(7198):1031–1042, June 2008. ISSN 1476-4687. doi: 10.1038/nature07128. URL http://dx.doi.org/10.1038/nature07128. [Cited on page 134].

J. I. Colless, A. C. Mahoney, J. M. Hornibrook, A. C. Doherty, H. Lu, A. C. Gossard, and D. J. Reilly. Dispersive Readout of a Few-Electron Double Quantum Dot with Fast rf Gate Sensors. *Physical Review Letters*, 110(4), Jan. 2013. ISSN 1079-7114. doi: 10.1103/physrevlett.110.046805. URL http://dx.doi.org/10.1103/PhysRevLett.110.046805. [Cited on page 166].

T. Connolly, P. D. Kurilovich, S. Diamond, H. Nho, C. G. Bøttcher, L. I. Glazman, V. Fatemi, and M. H. Devoret. Coexistence of Nonequilibrium Density and Equilibrium Energy Distribution of Quasiparticles in a Superconducting Qubit. *Physical Review Letters*, 132(21), May 2024. ISSN 1079-7114. doi: 10.1103/physrevlett.132.217001. URL http://dx.doi.org/10.1103/PhysRevLett.132.217001. [Cited on page 170].

L. N. Cooper. Bound Electron Pairs in a Degenerate Fermi Gas. *Physical Review*, 104(4):1189–1190, Nov. 1956. ISSN 0031-899X. doi: 10.1103/physrev.104.1189. URL http://dx.doi.org/10.1103/PhysRev.104.1189. [Cited on page 30].

J. Danon, A. B. Hellenes, E. B. Hansen, L. Casparis, A. P. Higginbotham, and K. Flensberg. Nonlocal Conductance Spectroscopy of Andreev Bound States: Symmetry Relations and BCS Charges. *Physical Review Letters*, 124(3), Jan. 2020. ISSN 1079-7114. doi: 10.1103/physrevlett.124.036801. URL http://dx.doi.org/10.1103/PhysRevLett.124.036801. [Cited on pages 42, 47, and 71].

A. Das, Y. Ronen, M. Heiblum, D. Mahalu, A. V. Kretinin, and H. Shtrikman. High-efficiency Cooper pair splitting demonstrated by two-particle conductance resonance and positive noise cross-correlation. *Nature Communications*, 3(1), Nov. 2012. ISSN 2041-1723. doi: 10.1038/ncomms2169. URL http://dx.doi.org/10.1038/ncomms2169. [Cited on pages 42, 65, and 92].

S. Datta. *Quantum Transport: Atom to Transistor*. Cambridge University Press, 2005. ISBN 9781139164313. doi: 10.1017/cbo9781139164313. URL http://dx.doi.org/10.1017/CBO9781139164313. [Cited on page 78].

S. De Franceschi, L. Kouwenhoven, C. Schönenberger, and W. Wernsdorfer. Hybrid superconductor–quantum dot devices. *Nature Nanotechnology*, 5(10):703–711, Sept. 2010. ISSN 1748-3395. doi: 10.1038/nnano.2010.173. URL http://dx.doi.org/10.1038/nnano.2010.173. [Cited on page 148].

D. de Jong, C. G. Prosko, D. M. A. Waardenburg, L. Han, F. K. Malinowski, P. Krogstrup, L. P. Kouwenhoven, J. V. Koski, and W. Pfaff. Rapid Microwave-Only Characterization and Readout of Quantum Dots Using Multiplexed Gigahertz-Frequency Resonators. *Physical Review Applied*, 16(1), July 2021. ISSN 2331-7019. doi: 10.1103/physrevapplied.16.014007. URL http://dx.doi.org/10.1103/PhysRevApplied.16.014007. [Cited on pages 166 and 169].

M. de Moor. *Quantum transport in nanowire networks*. PhD thesis, Delft University of Technology, 2019. URL http://resolver.tudelft.nl/uuid:59e7cafc-2345-44e0-8f26-4370288898a3. [Cited on page 100].

R. S. Deacon, A. Oiwa, J. Sailer, S. Baba, Y. Kanai, K. Shibata, K. Hirakawa, and S. Tarucha. Cooper pair splitting in parallel quantum dot Josephson junctions. *Nature Communications*, 6(1), July 2015. ISSN 2041-1723. doi: 10.1038/ncomms8446. URL http://dx.doi.org/10.1038/ncomms8446. [Cited on page 134].

M. T. Deng, S. Vaitiekėnas, E. B. Hansen, J. Danon, M. Leijnse, K. Flensberg, J. Nygård, P. Krogstrup, and C. M. Marcus. Majorana bound state in a coupled quantum-dot hybrid-nanowire system. *Science*, 354(6319):1557–1562, Dec. 2016. ISSN 1095-9203. doi: 10.1126/science.aaf3961. URL http://dx.doi.org/10.1126/science.aaf3961. [Cited on pages 3, 66, 162, and 163].

M.-T. Deng, S. Vaitiekėnas, E. Prada, P. San-Jose, J. Nygård, P. Krogstrup, R. Aguado, and C. M. Marcus. Nonlocality of Majorana modes in hybrid nanowires. *Physical Review B*, 98(8), Aug. 2018. ISSN 2469-9969. doi: 10.1103/physrevb.98.085125. URL http://dx.doi.org/10.1103/PhysRevB.98.085125. [Cited on page 162].

E. Dennis, A. Kitaev, A. Landahl, and J. Preskill. Topological quantum memory. *Journal of Mathematical Physics*, 43(9):4452–4505, Sept. 2002. ISSN 1089-7658. doi: 10.1063/1.1499754. URL http://dx.doi.org/10.1063/1.1499754. [Cited on page 3].

D. P. DiVincenzo. Topics in quantum computers. In *Mesoscopic electron transport*, pages 657–677. Springer, 1997. [Cited on page 17].

D. P. DiVincenzo. The Physical Implementation of Quantum Computation. *Fortschritte der Physik*, 48(9–11):771–783, Sept. 2000. ISSN 1521-3978. doi: 10.1002/1521-3978(200009)48:9/11<771::aid-prop771>3.0.co;2-e. URL http://dx.doi.org/10.1002/1521-3978(200009)48:9/11<771::AID-PROP771>3.0.CO;2-E. [Cited on page 17].

F. Domínguez and A. L. Yeyati. Quantum interference in a Cooper pair splitter: The three sites model. *Physica E: Low-dimensional Systems and Nanostructures*, 75:322–329, Jan. 2016. ISSN 1386-9477. doi: 10.1016/j.physe.2015.09.040. URL http://dx.doi.org/10.1016/j.physe.2015.09.040. [Cited on pages 45 and 145].

T. Dvir, G. Wang, N. van Loo, C.-X. Liu, G. P. Mazur, A. Bordin, S. L. D. ten Haaf, J.-Y. Wang, D. van Driel, F. Zatelli, X. Li, F. K. Malinowski, S. Gazibegovic, G. Badawy, E. P. A. M. Bakkers, M. Wimmer, and L. P. Kouwenhoven. Realization of a minimal Kitaev chain in coupled quantum dots. *Nature*, 614(7948):445–450, Feb. 2023. ISSN 1476-4687. doi: 10.1038/s41586-022-05585-1. URL http://dx.doi.org/10.1038/s41586-022-05585-1. [Cited on pages 42, 44, 51, 52, 92, 108, 109, 110, 113, 122, 125, 134, and 161].

M. C. Escher. Knots, Aug. 1965. URL https://www.escherinhetpaleis.nl/. Accessed: 2024-10-16. [Cited on page 2].

J. Estrada Saldaña, A. Vekris, G. Steffensen, R. Žitko, P. Krogstrup, J. Paaske, K. Grove-Rasmussen, and J. Nygård. Supercurrent in a Double Quantum Dot. *Physical Review Letters*, 121(25), Dec. 2018. ISSN 1079-7114. doi: 10.1103/physrevlett.121.257701. URL http://dx.doi.org/10.1103/PhysRevLett.121.257701. [Cited on pages 135, 137, 144, and 146].

J. C. Estrada Saldaña, A. Vekris, R. Žitko, G. Steffensen, P. Krogstrup, J. Paaske, K. Grove-Rasmussen, and J. Nygård. Two-impurity Yu-Shiba-Rusinov states in coupled quantum dots. *Physical Review B*, 102(19), Nov. 2020. ISSN 2469-9969. doi: 10.1103/physrevb.102.195143. URL http://dx.doi.org/10.1103/PhysRevB.102.195143. [Cited on pages 134 and 139].

S. J. Evered, D. Bluvstein, M. Kalinowski, S. Ebadi, T. Manovitz, H. Zhou, S. H. Li, A. A. Geim, T. T. Wang, N. Maskara, H. Levine, G. Semeghini, M. Greiner, V. Vuletić, and M. D. Lukin. High-fidelity parallel entangling gates on a neutral-atom quantum computer. *Nature*, 622(7982):268–272, Oct. 2023. ISSN 1476-4687. doi: 10.1038/s41586-023-06481-y. URL http://dx.doi.org/10.1038/s41586-023-06481-y. [Cited on page 170].

M. Ezawa. Even-odd effect on robustness of Majorana edge states in short Kitaev chains. *Physical Review B*, 109(16), Apr. 2024. ISSN 2469-9969. doi: 10.1103/physrevb.109.l161404. URL http://dx.doi.org/10.1103/PhysRevB.109.L161404. [Cited on page 15].

A. Fornieri, A. M. Whiticar, F. Setiawan, E. Portolés, A. C. C. Drachmann, A. Keselman, S. Gronin, C. Thomas, T. Wang, R. Kallaher, G. C. Gardner, E. Berg, M. J. Manfra, A. Stern, C. M. Marcus, and F. Nichele. Evidence of topological superconductivity in planar Josephson junctions. *Nature*, 569(7754):89–92, Apr. 2019. ISSN 1476-4687. doi: 10.1038/s41586-019-1068-8. URL http://dx.doi.org/10.1038/s41586-019-1068-8. [Cited on pages 66 and 108].

A. G. Fowler, M. Mariantoni, J. M. Martinis, and A. N. Cleland. Surface codes: Towards practical large-scale quantum computation. *Physical Review A*, 86(3), Sept. 2012. ISSN

1094-1622. doi: 10.1103/physreva.86.032324. URL http://dx.doi.org/10.1103/PhysRevA.86.032324. [Cited on page 3].

M. Freedman, A. Kitaev, M. Larsen, and Z. Wang. Topological quantum computation. *Bulletin of the American Mathematical Society*, 40(1):31–38, Oct. 2002. ISSN 1088-9485. doi: 10.1090/s0273-0979-02-00964-3. URL http://dx.doi.org/10.1090/S0273-0979-02-00964-3. [Cited on pages 3 and 21].

M. Freedman, C. Nayak, and K. Walker. Towards universal topological quantum computation in the $\nu = \frac{5}{2}$ fractional quantum Hall state. *Physical Review B*, 73(24), June 2006. ISSN 1550-235X. doi: 10.1103/physrevb.73.245307. URL http://dx.doi.org/10.1103/PhysRevB.73.245307. [Cited on page 23].

H. Fröhlich. Theory of the Superconducting State. I. The Ground State at the Absolute Zero of Temperature. *Physical Review*, 79(5):845–856, Sept. 1950. ISSN 0031-899X. doi: 10.1103/physrev.79.845. URL http://dx.doi.org/10.1103/PhysRev.79.845. [Cited on page 30].

I. C. Fulga, A. Haim, A. R. Akhmerov, and Y. Oreg. Adaptive tuning of Majorana fermions in a quantum dot chain. *New Journal of Physics*, 15(4):045020, Apr. 2013. ISSN 1367-2630. doi: 10.1088/1367-2630/15/4/045020. URL http://dx.doi.org/10.1088/1367-2630/15/4/045020. [Cited on pages 4, 39, 42, 92, 109, and 186].

G. Fülöp, F. Domínguez, S. d'Hollosy, A. Baumgartner, P. Makk, M. Madsen, V. Guzenko, J. Nygård, C. Schönenberger, A. Levy Yeyati, and S. Csonka. Magnetic Field Tuning and Quantum Interference in a Cooper Pair Splitter. *Physical Review Letters*, 115(22), Nov. 2015. ISSN 1079-7114. doi: 10.1103/physrevlett.115.227003. URL http://dx.doi.org/10.1103/PhysRevLett.115.227003. [Cited on pages 42 and 92].

Y. Gao, W. Song, S. Yang, Z. Yu, R. Li, W. Miao, Y. Wang, F. Chen, Z. Geng, L. Yang, Z. Xia, X. Feng, Y. Zang, L. Li, R. Shang, Q.-K. Xue, K. He, and H. Zhang. Hard Superconducting Gap in PbTe Nanowires. *Chinese Physics Letters*, 41(3):038502, Mar. 2024. ISSN 1741-3540. doi: 10.1088/0256-307x/41/3/038502. URL http://dx.doi.org/10.1088/0256-307X/41/3/038502. [Cited on page 3].

F. P. García de Arquer, D. V. Talapin, V. I. Klimov, Y. Arakawa, M. Bayer, and E. H. Sargent. Semiconductor quantum dots: Technological progress and future challenges. *Science*, 373(6555), Aug. 2021. ISSN 1095-9203. doi: 10.1126/science.aaz8541. URL http://dx.doi.org/10.1126/science.aaz8541. [Cited on page 134].

S. Gazibegovic, D. Car, H. Zhang, S. C. Balk, J. A. Logan, M. W. A. de Moor, M. C. Cassidy, R. Schmits, D. Xu, G. Wang, P. Krogstrup, R. L. M. Op het Veld, K. Zuo, Y. Vos, J. Shen, D. Bouman, B. Shojaei, D. Pennachio, J. S. Lee, P. J. van Veldhoven, S. Koelling, M. A. Verheijen, L. P. Kouwenhoven, C. J. Palmstrøm, and E. P. A. M. Bakkers. Retraction Note: Epitaxy of advanced nanowire quantum devices. *Nature*, 604(7907):786–786, Apr. 2022. ISSN 1476-4687. doi: 10.1038/s41586-022-04704-2. URL http://dx.doi.org/10.1038/s41586-022-04704-2. [Cited on page 3].

L. S. Georgiev. Topologically protected gates for quantum computation with non-Abelian anyons in the Pfaffian quantum Hall state. *Physical Review B*, 74(23), Dec. 2006. ISSN 1550-235X. doi: 10.1103/physrevb.74.235112. URL http://dx.doi.org/10.1103/PhysRevB.74.235112. [Cited on page 23].

L. González Rosado, F. Hassler, and G. Catelani. Long-range exchange interaction between spin qubits mediated by a superconducting link at finite magnetic field. *Physical Review B*, 103(3), Jan. 2021. ISSN 2469-9969. doi: 10.1103/physrevb.103.035430. URL http://dx.doi.org/10.1103/PhysRevB.103.035430. [Cited on page 42].

D. Gottesman. *Stabilizer Codes and Quantum Error Correction*. PhD thesis, California Institute of Technology, 1997. URL https://arxiv.org/abs/quant-ph/9705052. [Cited on pages 2, 22, and 23].

J. Gramich, A. Baumgartner, and C. Schönenberger. Andreev bound states probed in three-terminal quantum dots. *Physical Review B*, 96(19), Nov. 2017. ISSN 2469-9969. doi: 10.1103/physrevb.96.195418. URL http://dx.doi.org/10.1103/PhysRevB.96.195418. [Cited on pages 71 and 92].

K. Grove-Rasmussen, H. I. Jørgensen, T. Hayashi, P. E. Lindelof, and T. Fujisawa. A Triple Quantum Dot in a Single-Wall Carbon Nanotube. *Nano Letters*, 8(4):1055–1060, Mar. 2008. ISSN 1530-6992. doi: 10.1021/nl072948y. URL http://dx.doi.org/10.1021/nl072948y. [Cited on page 29].

K. Grove-Rasmussen, G. Steffensen, A. Jellinggaard, M. H. Madsen, R. Žitko, J. Paaske, and J. Nygård. Yu–Shiba–Rusinov screening of spins in double quantum dots. *Nature Communications*, 9(1), June 2018. ISSN 2041-1723. doi: 10.1038/s41467-018-04683-x. URL http://dx.doi.org/10.1038/s41467-018-04683-x. [Cited on pages 139 and 188].

A. Gómez-León, M. Schirò, and O. Dmytruk. High-quality poor man's Majorana bound states from cavity embedding, 2024. URL https://arxiv.org/abs/2407.12088. [Cited on page 39].

R. Hanson, L. P. Kouwenhoven, J. R. Petta, S. Tarucha, and L. M. K. Vandersypen. Spins in few-electron quantum dots. *Reviews of Modern Physics*, 79(4):1217–1265, Oct. 2007. ISSN 1539-0756. doi: 10.1103/revmodphys.79.1217. URL http://dx.doi.org/10.1103/RevModPhys.79.1217. [Cited on pages 25, 48, 76, 93, and 134].

F. Hassler, G. Catelani, and H. Bluhm. Exchange interaction of two spin qubits mediated by a superconductor. *Physical Review B*, 92(23), Dec. 2015. ISSN 1550-235X. doi: 10.1103/physrevb.92.235401. URL http://dx.doi.org/10.1103/PhysRevB.92.235401. [Cited on page 42].

L. Haworth, J. Lu, D. Westwood, and J. MacDonald. Atomic hydrogen cleaning, nitriding and annealing InSb (100). *Applied Surface Science*, 166(1–4):253–258, Oct. 2000. ISSN 0169-4332. doi: 10.1016/s0169-4332(00)00425-6. URL http://dx.doi.org/10.1016/S0169-4332(00)00425-6. [Cited on page 181].

M. Hays, V. Fatemi, D. Bouman, J. Cerrillo, S. Diamond, K. Serniak, T. Connolly, P. Krogstrup, J. Nygård, A. Levy Yeyati, A. Geresdi, and M. H. Devoret. Coherent manipulation of an Andreev spin qubit. *Science*, 373(6553):430–433, July 2021. ISSN 1095-9203. doi: 10.1126/science.abf0345. URL http://dx.doi.org/10.1126/science.abf0345. [Cited on page 134].

S. Heedt, M. Quintero-Pérez, F. Borsoi, A. Fursina, N. van Loo, G. P. Mazur, M. P. Nowak, M. Ammerlaan, K. Li, S. Korneychuk, J. Shen, M. A. Y. van de Poll, G. Badawy, S. Gazibegovic, N. de Jong, P. Aseev, K. van Hoogdalem, E. P. A. M. Bakkers, and L. P. Kouwenhoven. Shadow-wall lithography of ballistic superconductor–semiconductor quantum devices. *Nature Communications*, 12(1), Aug. 2021. ISSN 2041-1723. doi: 10.1038/s41467-021-25100-w. URL http://dx.doi.org/10.1038/s41467-021-25100-w. [Cited on pages 3, 44, 56, 75, 92, 100, 122, 135, and 148].

L. G. Herrmann, F. Portier, P. Roche, A. L. Yeyati, T. Kontos, and C. Strunk. Carbon Nanotubes as Cooper-Pair Beam Splitters. *Physical Review Letters*, 104(2), Jan. 2010. ISSN 1079-7114. doi: 10.1103/physrevlett.104.026801. URL http://dx.doi.org/10.1103/PhysRevLett.104.026801. [Cited on pages 65, 92, and 108].

R. Hess, H. F. Legg, D. Loss, and J. Klinovaja. Trivial Andreev Band Mimicking Topological Bulk Gap Reopening in the Nonlocal Conductance of Long Rashba Nanowires. *Physical Review Letters*, 130(20), May 2023. ISSN 1079-7114. doi: 10.1103/physrevlett.130.207001. URL http://dx.doi.org/10.1103/PhysRevLett.130.207001. [Cited on page 3].

A. Hofmann, V. Maisi, T. Krähenmann, C. Reichl, W. Wegscheider, K. Ensslin, and T. Ihn. Anisotropy and Suppression of Spin-Orbit Interaction in a GaAs Double Quantum Dot. *Physical Review Letters*, 119(17), Oct. 2017. ISSN 1079-7114. doi: 10.1103/physrevlett.119.176807. URL http://dx.doi.org/10.1103/PhysRevLett.119.176807. [Cited on page 51].

L. Hofstetter, S. Csonka, J. Nygård, and C. Schönenberger. Cooper pair splitter realized in a two-quantum-dot Y-junction. *Nature*, 461(7266):960–963, Oct. 2009. ISSN 1476-4687. doi: 10.1038/nature08432. URL http://dx.doi.org/10.1038/nature08432. [Cited on pages 42, 65, 92, and 108].

L. Hofstetter, S. Csonka, A. Baumgartner, G. Fülöp, S. d'Hollosy, J. Nygård, and C. Schönenberger. Finite-Bias Cooper Pair Splitting. *Physical Review Letters*, 107(13), Sept. 2011. ISSN 1079-7114. doi: 10.1103/physrevlett.107.136801. URL http://dx.doi.org/10.1103/PhysRevLett.107.136801. [Cited on pages 42, 44, 92, and 108].

D. A. Ivanov. Non-Abelian Statistics of Half-Quantum Vortices in p-Wave Superconductors. *Physical Review Letters*, 86(2):268–271, Jan. 2001. ISSN 1079-7114. doi: 10.1103/physrevlett.86.268. URL http://dx.doi.org/10.1103/PhysRevLett.86.268. [Cited on page 19].

M. Jardine, J. Stenger, Y. Jiang, E. J. de Jong, W. Wang, A. C. Bleszynski Jayich, and S. Frolov. Integrating micromagnets and hybrid nanowires for topological quantum computing.

SciPost Physics, 11(5), Nov. 2021. ISSN 2542-4653. doi: 10.21468/scipostphys.11.5.090. URL http://dx.doi.org/10.21468/SciPostPhys.11.5.090. [Cited on page 38].

P. Jarillo-Herrero, J. A. van Dam, and L. P. Kouwenhoven. Quantum supercurrent transistors in carbon nanotubes. *Nature*, 439(7079):953–956, Feb. 2006. ISSN 1476-4687. doi: 10.1038/nature04550. URL http://dx.doi.org/10.1038/nature04550. [Cited on pages 134 and 136].

A. Jellinggaard, K. Grove-Rasmussen, M. H. Madsen, and J. Nygård. Tuning Yu-Shiba-Rusinov states in a quantum dot. *Physical Review B*, 94(6), Aug. 2016. ISSN 2469-9969. doi: 10.1103/physrevb.94.064520. URL http://dx.doi.org/10.1103/PhysRevB.94.064520. [Cited on pages 134 and 188].

Y. Jiang, S. Yang, L. Li, W. Song, W. Miao, B. Tong, Z. Geng, Y. Gao, R. Li, F. Chen, Q. Zhang, F. Meng, L. Gu, K. Zhu, Y. Zang, R. Shang, Z. Cao, X. Feng, Q.-K. Xue, D. E. Liu, H. Zhang, and K. He. Selective area epitaxy of PbTe-Pb hybrid nanowires on a lattice-matched substrate. *Physical Review Materials*, 6(3), Mar. 2022. ISSN 2475-9953. doi: 10.1103/physrevmaterials.6.034205. URL http://dx.doi.org/10.1103/PhysRevMaterials.6.034205. [Cited on page 3].

B. Josephson. Possible new effects in superconductive tunnelling. *Physics Letters*, 1(7): 251–253, July 1962. ISSN 0031-9163. doi: 10.1016/0031-9163(62)91369-0. URL http://dx.doi.org/10.1016/0031-9163(62)91369-0. [Cited on page 32].

M. Jung, M. D. Schroer, K. D. Petersson, and J. R. Petta. Radio frequency charge sensing in InAs nanowire double quantum dots. *Applied Physics Letters*, 100(25), June 2012. ISSN 1077-3118. doi: 10.1063/1.4729469. URL http://dx.doi.org/10.1063/1.4729469. [Cited on page 165].

H. I. Jørgensen, T. Novotný, K. Grove-Rasmussen, K. Flensberg, and P. E. Lindelof. Critical Current 0-π Transition in Designed Josephson Quantum Dot Junctions. *Nano Letters*, 7(8):2441–2445, July 2007. ISSN 1530-6992. doi: 10.1021/nl071152w. URL http://dx.doi.org/10.1021/nl071152w. [Cited on page 134].

T. Kanne, M. Marnauza, D. Olsteins, D. J. Carrad, J. E. Sestoft, J. de Bruijckere, L. Zeng, E. Johnson, E. Olsson, K. Grove-Rasmussen, and J. Nygård. Epitaxial Pb on InAs nanowires for quantum devices. *Nature Nanotechnology*, 16(7):776–781, May 2021. ISSN 1748-3395. doi: 10.1038/s41565-021-00900-9. URL http://dx.doi.org/10.1038/s41565-021-00900-9. [Cited on page 115].

T. Karzig, C. Knapp, R. M. Lutchyn, P. Bonderson, M. B. Hastings, C. Nayak, J. Alicea, K. Flensberg, S. Plugge, Y. Oreg, C. M. Marcus, and M. H. Freedman. Scalable designs for quasiparticle-poisoning-protected topological quantum computation with Majorana zero modes. *Physical Review B*, 95(23), June 2017. ISSN 2469-9969. doi: 10.1103/physrevb.95.235305. URL http://dx.doi.org/10.1103/PhysRevB.95.235305. [Cited on page 23].

G. Katsaros, P. Spathis, M. Stoffel, F. Fournel, M. Mongillo, V. Bouchiat, F. Lefloch, A. Rastelli, O. G. Schmidt, and S. De Franceschi. Hybrid superconductor–semiconductor devices made from self-assembled SiGe nanocrystals on silicon. *Nature Nanotechnology*, 5(6):458–464, May 2010. ISSN 1748-3395. doi: 10.1038/nnano. 2010.84. URL http://dx.doi.org/10.1038/nnano.2010.84. [Cited on page 134].

Kavli Nanolab. URL https://www.tudelft.nl/tnw/over-faculteit/afdelingen/quantum-nanoscience/kavli-nanolab-delft. Accessed: 2024-11-25. [Cited on page 177].

G. Kells, D. Meidan, and P. W. Brouwer. Near-zero-energy end states in topologically trivial spin-orbit coupled superconducting nanowires with a smooth confinement. *Physical Review B*, 86(10), Sept. 2012. ISSN 1550-235X. doi: 10.1103/physrevb.86.100503. URL http://dx.doi.org/10.1103/PhysRevB.86.100503. [Cited on page 66].

S. Kezilebieke, M. N. Huda, V. Vaňo, M. Aapro, S. C. Ganguli, O. J. Silveira, S. Głodzik, A. S. Foster, T. Ojanen, and P. Liljeroth. Topological superconductivity in a van der Waals heterostructure. *Nature*, 588(7838):424–428, Dec. 2020. ISSN 1476-4687. doi: 10.1038/s41586-020-2989-y. URL http://dx.doi.org/10.1038/s41586-020-2989-y. [Cited on page 108].

A. Kitaev. Fault-tolerant quantum computation by anyons. *Annals of Physics*, 303(1): 2–30, Jan. 2003. ISSN 0003-4916. doi: 10.1016/s0003-4916(02)00018-0. URL http://dx.doi.org/10.1016/S0003-4916(02)00018-0. [Cited on pages 2, 3, 19, 66, and 108].

A. Y. Kitaev. Fault-tolerant quantum computation by anyons, 1997. URL https://arxiv.org/abs/quant-ph/9707021. [Cited on page 2].

A. Y. Kitaev. Unpaired Majorana fermions in quantum wires. *Physics-Uspekhi*, 44(10S): 131–136, Oct. 2001. ISSN 1468-4780. doi: 10.1070/1063-7869/44/10s/s29. URL http://dx.doi.org/10.1070/1063-7869/44/10s/s29. [Cited on pages 2, 3, 8, 10, 13, 16, 38, 39, 42, 65, 66, 68, 92, 108, and 162].

M. Kjaergaard, M. E. Schwartz, J. Braumüller, P. Krantz, J. I.-J. Wang, S. Gustavsson, and W. D. Oliver. Superconducting Qubits: Current State of Play. *Annual Review of Condensed Matter Physics*, 11(1):369–395, Mar. 2020. ISSN 1947-5462. doi: 10. 1146/annurev-conmatphys-031119-050605. URL http://dx.doi.org/10.1146/annurev-conmatphys-031119-050605. [Cited on pages 19, 134, and 170].

C. Knapp, M. Zaletel, D. E. Liu, M. Cheng, P. Bonderson, and C. Nayak. The Nature and Correction of Diabatic Errors in Anyon Braiding. *Physical Review X*, 6(4), Oct. 2016. ISSN 2160-3308. doi: 10.1103/physrevx.6.041003. URL http://dx.doi.org/10.1103/PhysRevX.6.041003. [Cited on page 114].

E. Knill, R. Laflamme, and W. H. Zurek. Resilient Quantum Computation. *Science*, 279 (5349):342–345, Jan. 1998. ISSN 1095-9203. doi: 10.1126/science.279.5349.342. URL http://dx.doi.org/10.1126/science.279.5349.342. [Cited on page 23].

R. Koch, D. van Driel, A. Bordin, J. L. Lado, and E. Greplova. Adversarial Hamiltonian learning of quantum dots in a minimal Kitaev chain. *Physical Review Applied*, 20(4), Oct. 2023. ISSN 2331-7019. doi: 10.1103/physrevapplied.20.044081. URL http://dx.doi.org/10.1103/PhysRevApplied.20.044081. [Cited on pages 39 and 171].

M. Kocsis, Z. Scherübl, G. Fülöp, P. Makk, and S. Csonka. Strong nonlocal tuning of the current-phase relation of a quantum dot based Andreev molecule. *Physical Review B*, 109(24), June 2024. ISSN 2469-9969. doi: 10.1103/physrevb.109.245133. URL http://dx.doi.org/10.1103/PhysRevB.109.245133. [Cited on pages 39 and 143].

L. Kouwenhoven. Perspective on Majorana bound-states in hybrid superconductor-semiconductor nanowires. *Modern Physics Letters B*, Nov. 2024. ISSN 1793-6640. doi: 10.1142/s0217984925400020. URL http://dx.doi.org/10.1142/S0217984925400020. [Cited on page 3].

L. P. Kouwenhoven, C. M. Marcus, P. L. McEuen, S. Tarucha, R. M. Westervelt, and N. S. Wingreen. *Electron Transport in Quantum Dots*, page 105–214. Springer Netherlands, 1997. ISBN 9789401588393. doi: 10.1007/978-94-015-8839-3_4. URL http://dx.doi.org/10.1007/978-94-015-8839-3_4. [Cited on page 25].

L. P. Kouwenhoven, D. G. Austing, and S. Tarucha. Few-electron quantum dots. *Reports on Progress in Physics*, 64(6):701–736, May 2001. ISSN 1361-6633. doi: 10.1088/0034-4885/64/6/201. URL http://dx.doi.org/10.1088/0034-4885/64/6/201. [Cited on pages 25, 80, and 134].

O. Kürtössy, Z. Scherübl, G. Fülöp, I. E. Lukács, T. Kanne, J. Nygård, P. Makk, and S. Csonka. Parallel InAs nanowires for Cooper pair splitters with Coulomb repulsion. *npj Quantum Materials*, 7(1), Sept. 2022. ISSN 2397-4648. doi: 10.1038/s41535-022-00497-9. URL http://dx.doi.org/10.1038/s41535-022-00497-9. [Cited on page 39].

E. J. H. Lee, X. Jiang, R. Aguado, G. Katsaros, C. M. Lieber, and S. De Franceschi. Zero-Bias Anomaly in a Nanowire Quantum Dot Coupled to Superconductors. *Physical Review Letters*, 109(18), Oct. 2012. ISSN 1079-7114. doi: 10.1103/physrevlett.109.186802. URL http://dx.doi.org/10.1103/PhysRevLett.109.186802. [Cited on pages 134 and 135].

E. J. H. Lee, X. Jiang, M. Houzet, R. Aguado, C. M. Lieber, and S. De Franceschi. Spin-resolved Andreev levels and parity crossings in hybrid superconductor–semiconductor nanostructures. *Nature Nanotechnology*, 9(1):79–84, Dec. 2013. ISSN 1748-3395. doi: 10.1038/nnano.2013.267. URL http://dx.doi.org/10.1038/nnano.2013.267. [Cited on pages 33, 34, 35, 42, 48, 104, 136, and 188].

M. Leijnse and K. Flensberg. Parity qubits and poor man's Majorana bound states in double quantum dots. *Physical Review B*, 86(13), Oct. 2012a. ISSN 1550-235X. doi: 10.1103/physrevb.86.134528. URL http://dx.doi.org/10.1103/PhysRevB.86.134528. [Cited on pages 4, 11, 12, 38, 39, 42, 51, 65, 66, 68, 70, 71, 72, 73, 77, 78, 92, 108, 110, 111, and 113].

M. Leijnse and K. Flensberg. Introduction to topological superconductivity and Majorana fermions. *Semiconductor Science and Technology*, 27(12):124003, Nov. 2012b. ISSN 1361-6641. doi: 10.1088/0268-1242/27/12/124003. URL http://dx.doi.org/10.1088/0268-1242/27/12/124003. [Cited on pages 3, 18, and 20].

M. Leijnse and K. Flensberg. Coupling Spin Qubits via Superconductors. *Physical Review Letters*, 111(6), Aug. 2013. ISSN 1079-7114. doi: 10.1103/physrevlett.111.060501. URL http://dx.doi.org/10.1103/PhysRevLett.111.060501. [Cited on page 42].

J. M. Leinaas and J. Myrheim. On the theory of identical particles. *Il Nuovo Cimento B Series 11*, 37(1):1–23, Jan. 1977. ISSN 1826-9877. doi: 10.1007/bf02727953. URL http://dx.doi.org/10.1007/BF02727953. [Cited on page 20].

G. Lesovik, T. Martin, and G. Blatter. Electronic entanglement in the vicinity of a superconductor. *The European Physical Journal B*, 24(3):287–290, Dec. 2001. ISSN 1434-6028. doi: 10.1007/s10051-001-8675-4. URL http://dx.doi.org/10.1007/s10051-001-8675-4. [Cited on page 92].

N. Leumer, M. Marganska, B. Muralidharan, and M. Grifoni. Exact eigenvectors and eigenvalues of the finite Kitaev chain and its topological properties. *Journal of Physics: Condensed Matter*, 32(44):445502, Aug. 2020. ISSN 1361-648X. doi: 10.1088/1361-648x/ab8bf9. URL http://dx.doi.org/10.1088/1361-648X/ab8bf9. [Cited on page 15].

D. Litinski and F. von Oppen. Quantum computing with Majorana fermion codes. *Physical Review B*, 97(20), May 2018. ISSN 2469-9969. doi: 10.1103/physrevb.97.205404. URL http://dx.doi.org/10.1103/PhysRevB.97.205404. [Cited on page 23].

C.-X. Liu, J. D. Sau, T. D. Stanescu, and S. Das Sarma. Andreev bound states versus Majorana bound states in quantum dot-nanowire-superconductor hybrid structures: Trivial versus topological zero-bias conductance peaks. *Physical Review B*, 96(7), Aug. 2017. ISSN 2469-9969. doi: 10.1103/physrevb.96.075161. URL http://dx.doi.org/10.1103/PhysRevB.96.075161. [Cited on page 66].

C.-X. Liu, G. Wang, T. Dvir, and M. Wimmer. Tunable Superconducting Coupling of Quantum Dots via Andreev Bound States in Semiconductor-Superconductor Nanowires. *Physical Review Letters*, 129(26), Dec. 2022. ISSN 1079-7114. doi: 10.1103/physrevlett.129.267701. URL http://dx.doi.org/10.1103/PhysRevLett.129.267701. [Cited on pages 37, 39, 42, 45, 47, 49, 51, 53, 54, 55, 68, 69, 76, 78, 93, 109, 119, 122, 131, 134, and 166].

C.-X. Liu, H. Pan, F. Setiawan, M. Wimmer, and J. D. Sau. Fusion protocol for Majorana modes in coupled quantum dots. *Physical Review B*, 108(8), Aug. 2023. ISSN 2469-9969. doi: 10.1103/physrevb.108.085437. URL http://dx.doi.org/10.1103/PhysRevB.108.085437. [Cited on pages 39, 112, 123, and 169].

C.-X. Liu, A. M. Bozkurt, F. Zatelli, S. L. D. ten Haaf, T. Dvir, and M. Wimmer. Enhancing the excitation gap of a quantum-dot-based Kitaev chain. *Communications Physics*, 7

(1), July 2024a. ISSN 2399-3650. doi: 10.1038/s42005-024-01715-5. URL http://dx.doi.org/10.1038/s42005-024-01715-5. [Cited on pages 39, 134, and 188].

C.-X. Liu, S. Miles, A. Bordin, S. L. D. t. Haaf, A. M. Bozkurt, and M. Wimmer. Protocol for scaling up a sign-ordered Kitaev chain without magnetic flux control, 2024b. URL https://arxiv.org/abs/2407.04630. [Cited on pages 37, 39, 160, 171, and 190].

Z.-H. Liu, C. Zeng, and H. Q. Xu. Coupling of quantum-dot states via elastic cotunneling and crossed Andreev reflection in a minimal Kitaev chain. *Physical Review B*, 110(11), Sept. 2024c. ISSN 2469-9969. doi: 10.1103/physrevb.110.115302. URL http://dx.doi.org/10.1103/PhysRevB.110.115302. [Cited on page 39].

S. Lloyd. Unconventional Quantum Computing Devices. In *Unconventional models of computation*, pages 52–58. Springer Science & Business Media, 1998. [Cited on page 18].

W. Lu, Z. Ji, L. Pfeiffer, K. W. West, and A. J. Rimberg. Real-time detection of electron tunnelling in a quantum dot. *Nature*, 423(6938):422–425, May 2003. ISSN 1476-4687. doi: 10.1038/nature01642. URL http://dx.doi.org/10.1038/nature01642. [Cited on page 134].

M. Luethi, H. F. Legg, D. Loss, and J. Klinovaja. From perfect to imperfect poor man's Majoranas in minimal Kitaev chains, 2024a. URL https://arxiv.org/abs/2408.03071. [Cited on page 39].

M. Luethi, H. F. Legg, D. Loss, and J. Klinovaja. The fate of poor man's Majoranas in the long Kitaev chain limit, 2024b. URL https://arxiv.org/abs/2408.10030. [Cited on page 39].

R. M. Lutchyn, J. D. Sau, and S. Das Sarma. Majorana Fermions and a Topological Phase Transition in Semiconductor-Superconductor Heterostructures. *Physical Review Letters*, 105(7), Aug. 2010. ISSN 1079-7114. doi: 10.1103/physrevlett.105.077001. URL http://dx.doi.org/10.1103/PhysRevLett.105.077001. [Cited on pages 3, 4, 10, and 108].

E. Majorana. Teoria simmetrica dell'elettrone e del positrone. *Il Nuovo Cimento*, 14(4): 171–184, Apr. 1937. ISSN 1827-6121. doi: 10.1007/bf02961314. URL http://dx.doi.org/10.1007/BF02961314. [Cited on pages 3 and 9].

E. A. Martinez, A. Pöschl, E. B. Hansen, M. A. Y. van de Poll, S. Vaitiekėnas, A. P. Higginbotham, and L. Casparis. Measurement circuit effects in three-terminal electrical transport measurements, 2021. URL https://arxiv.org/abs/2104.02671. [Cited on pages 75 and 123].

A. Martín-Rodero and A. Levy Yeyati. Josephson and Andreev transport through quantum dots. *Advances in Physics*, 60(6):899–958, Dec. 2011. ISSN 1460-6976. doi: 10.1080/00018732.2011.624266. URL http://dx.doi.org/10.1080/00018732.2011.624266. [Cited on pages 137 and 139].

R. Maurand, T. Meng, E. Bonet, S. Florens, L. Marty, and W. Wernsdorfer. First-Order 0-π Quantum Phase Transition in the Kondo Regime of a Superconducting Carbon-Nanotube Quantum Dot. *Physical Review X*, 2(1), Feb. 2012. ISSN 2160-3308. doi: 10.1103/physrevx.2.011009. URL http://dx.doi.org/10.1103/PhysRevX.2.011009. [Cited on page 134].

G. P. Mazur, N. van Loo, J. Wang, T. Dvir, G. Wang, A. Khindanov, S. Korneychuk, F. Borsoi, R. C. Dekker, G. Badawy, P. Vinke, S. Gazibegovic, E. P. A. M. Bakkers, M. Q. Pérez, S. Heedt, and L. P. Kouwenhoven. Spin-Mixing Enhanced Proximity Effect in Aluminum-Based Superconductor–Semiconductor Hybrids. *Advanced Materials*, 34 (33), July 2022. ISSN 1521-4095. doi: 10.1002/adma.202202034. URL http://dx.doi.org/10.1002/adma.202202034. [Cited on pages 49, 56, 63, 75, 80, 92, and 115].

V. Meden. The Anderson–Josephson quantum dot—a theory perspective. *Journal of Physics: Condensed Matter*, 31(16):163001, Feb. 2019. ISSN 1361-648X. doi: 10.1088/1361-648x/aafd6a. URL http://dx.doi.org/10.1088/1361-648X/aafd6a. [Cited on page 139].

T. Meng, S. Florens, and P. Simon. Self-consistent description of Andreev bound states in Josephson quantum dot devices. *Physical Review B*, 79(22), June 2009. ISSN 1550-235X. doi: 10.1103/physrevb.79.224521. URL http://dx.doi.org/10.1103/PhysRevB.79.224521. [Cited on pages 34, 35, and 104].

X. Mi, M. Sonner, M. Y. Niu, K. W. Lee, B. Foxen, R. Acharya, I. Aleiner, T. I. Andersen, F. Arute, K. Arya, A. Asfaw, J. Atalaya, J. C. Bardin, J. Basso, A. Bengtsson, G. Bortoli, A. Bourassa, L. Brill, M. Broughton, B. B. Buckley, D. A. Buell, B. Burkett, N. Bushnell, Z. Chen, B. Chiaro, R. Collins, P. Conner, W. Courtney, A. L. Crook, D. M. Debroy, S. Demura, A. Dunsworth, D. Eppens, C. Erickson, L. Faoro, E. Farhi, R. Fatemi, L. Flores, E. Forati, A. G. Fowler, W. Giang, C. Gidney, D. Gilboa, M. Giustina, A. G. Dau, J. A. Gross, S. Habegger, M. P. Harrigan, M. Hoffmann, S. Hong, T. Huang, A. Huff, W. J. Huggins, L. B. Ioffe, S. V. Isakov, J. Iveland, E. Jeffrey, Z. Jiang, C. Jones, D. Kafri, K. Kechedzhi, T. Khattar, S. Kim, A. Y. Kitaev, P. V. Klimov, A. R. Klots, A. N. Korotkov, F. Kostritsa, J. M. Kreikebaum, D. Landhuis, P. Laptev, K.-M. Lau, J. Lee, L. Laws, W. Liu, A. Locharla, O. Martin, J. R. McClean, M. McEwen, B. Meurer Costa, K. C. Miao, M. Mohseni, S. Montazeri, A. Morvan, E. Mount, W. Mruczkiewicz, O. Naaman, M. Neeley, C. Neill, M. Newman, T. E. O'Brien, A. Opremcak, A. Petukhov, R. Potter, C. Quintana, N. C. Rubin, N. Saei, D. Sank, K. Sankaragomathi, K. J. Satzinger, C. Schuster, M. J. Shearn, V. Shvarts, D. Strain, Y. Su, M. Szalay, G. Vidal, B. Villalonga, C. Vollgraff-Heidweiller, T. White, Z. Yao, P. Yeh, J. Yoo, A. Zalcman, Y. Zhang, N. Zhu, H. Neven, D. Bacon, J. Hilton, E. Lucero, R. Babbush, S. Boixo, A. Megrant, Y. Chen, J. Kelly, V. Smelyanskiy, D. A. Abanin, and P. Roushan. Noise-resilient edge modes on a chain of superconducting qubits. *Science*, 378(6621):785–790, Nov. 2022. ISSN 1095-9203. doi: 10.1126/science.abq5769. URL http://dx.doi.org/10.1126/science.abq5769. [Cited on page 3].

P. Michler, A. Kiraz, C. Becher, W. V. Schoenfeld, P. M. Petroff, L. Zhang, E. Hu, and A. Imamoglu. A Quantum Dot Single-Photon Turnstile Device. *Science*, 290(5500):

2282–2285, Dec. 2000. ISSN 1095-9203. doi: 10.1126/science.290.5500.2282. URL http://dx.doi.org/10.1126/science.290.5500.2282. [Cited on page 134].

S. Miles, D. van Driel, M. Wimmer, and C.-X. Liu. Kitaev chain in an alternating quantum dot-Andreev bound state array. *Physical Review B*, 110(2), July 2024. ISSN 2469-9969. doi: 10.1103/physrevb.110.024520. URL http://dx.doi.org/10.1103/PhysRevB.110.024520. [Cited on pages 39, 143, and 186].

V. Mourik, K. Zuo, S. M. Frolov, S. R. Plissard, E. P. A. M. Bakkers, and L. P. Kouwenhoven. Signatures of Majorana Fermions in Hybrid Superconductor-Semiconductor Nanowire Devices. *Science*, 336(6084):1003–1007, May 2012. ISSN 1095-9203. doi: 10.1126/science.1222360. URL http://dx.doi.org/10.1126/science.1222360. [Cited on pages 3 and 66].

J. Mu, S. Huang, Z.-H. Liu, W. Li, J.-Y. Wang, D. Pan, G.-Y. Huang, Y. Chen, J. Zhao, and H. Q. Xu. A highly tunable quadruple quantum dot in a narrow bandgap semiconductor InAs nanowire. *Nanoscale*, 13(7):3983–3990, 2021. ISSN 2040-3372. doi: 10.1039/d0nr08655j. URL http://dx.doi.org/10.1039/D0NR08655J. [Cited on page 29].

G. Ménard, G. Anselmetti, E. Martinez, D. Puglia, F. Malinowski, J. Lee, S. Choi, M. Pendharkar, C. Palmstrøm, K. Flensberg, C. Marcus, L. Casparis, and A. Higginbotham. Conductance-Matrix Symmetries of a Three-Terminal Hybrid Device. *Physical Review Letters*, 124(3), Jan. 2020. ISSN 1079-7114. doi: 10.1103/physrevlett.124.036802. URL http://dx.doi.org/10.1103/PhysRevLett.124.036802. [Cited on pages 42, 47, 48, 71, and 80].

S. Nadj-Perge, V. S. Pribiag, J. W. G. van den Berg, K. Zuo, S. R. Plissard, E. P. A. M. Bakkers, S. M. Frolov, and L. P. Kouwenhoven. Spectroscopy of Spin-Orbit Quantum Bits in Indium Antimonide Nanowires. *Physical Review Letters*, 108(16), Apr. 2012. ISSN 1079-7114. doi: 10.1103/physrevlett.108.166801. URL http://dx.doi.org/10.1103/PhysRevLett.108.166801. [Cited on page 28].

S. Nadj-Perge, I. K. Drozdov, J. Li, H. Chen, S. Jeon, J. Seo, A. H. MacDonald, B. A. Bernevig, and A. Yazdani. Observation of Majorana fermions in ferromagnetic atomic chains on a superconductor. *Science*, 346(6209):602–607, Oct. 2014. ISSN 1095-9203. doi: 10.1126/science.1259327. URL http://dx.doi.org/10.1126/science.1259327. [Cited on page 108].

C. Nayak, S. H. Simon, A. Stern, M. Freedman, and S. Das Sarma. Non-Abelian anyons and topological quantum computation. *Reviews of Modern Physics*, 80(3):1083–1159, Sept. 2008. ISSN 1539-0756. doi: 10.1103/revmodphys.80.1083. URL http://dx.doi.org/10.1103/RevModPhys.80.1083. [Cited on pages 3, 18, 21, 24, 66, and 108].

M. A. Nielsen and I. L. Chuang. *Quantum computation and quantum information*. Cambridge university press, 2010. [Cited on pages 2, 17, 18, and 22].

M. Nitsch, L. Maffi, V. V. Baran, R. S. Souto, J. Paaske, M. Leijnse, and M. Burrello. The poor man's Majorana tetron, 2024. URL https://arxiv.org/abs/2411.11981. [Cited on page 39].

T. Novotný, A. Rossini, and K. Flensberg. Josephson current through a molecular transistor in a dissipative environment. *Physical Review B*, 72(22), Dec. 2005. ISSN 1550-235X. doi: 10.1103/physrevb.72.224502. URL http://dx.doi.org/10.1103/PhysRevB.72.224502. [Cited on page 144].

Y. Oreg, G. Refael, and F. von Oppen. Helical Liquids and Majorana Bound States in Quantum Wires. *Physical Review Letters*, 105(17), Oct. 2010. ISSN 1079-7114. doi: 10.1103/physrevlett.105.177002. URL http://dx.doi.org/10.1103/PhysRevLett.105.177002. [Cited on pages 3, 4, 10, and 108].

C. Padurariu and Y. V. Nazarov. Theoretical proposal for superconducting spin qubits. *Physical Review B*, 81(14), Apr. 2010. ISSN 1550-235X. doi: 10.1103/physrevb.81.144519. URL http://dx.doi.org/10.1103/PhysRevB.81.144519. [Cited on page 134].

H. Pan and S. Das Sarma. Physical mechanisms for zero-bias conductance peaks in Majorana nanowires. *Physical Review Research*, 2(1), Mar. 2020. ISSN 2643-1564. doi: 10.1103/physrevresearch.2.013377. URL http://dx.doi.org/10.1103/PhysRevResearch.2.013377. [Cited on pages 3, 66, and 134].

H. Pan and S. Das Sarma. Disorder effects on Majorana zero modes: Kitaev chain versus semiconductor nanowire. *Physical Review B*, 103(22), June 2021. ISSN 2469-9969. doi: 10.1103/physrevb.103.224505. URL http://dx.doi.org/10.1103/PhysRevB.103.224505. [Cited on page 73].

H. Pan, S. D. Sarma, and C.-X. Liu. Rabi and Ramsey oscillations of a Majorana qubit in a quantum dot-superconductor array, 2024. URL https://arxiv.org/abs/2407.16750. [Cited on pages 39 and 167].

L. Pavešić, R. Aguado, and R. Žitko. Strong-coupling theory of quantum-dot Josephson junctions: Role of a residual quasiparticle. *Physical Review B*, 109(12), Mar. 2024. ISSN 2469-9969. doi: 10.1103/physrevb.109.125131. URL http://dx.doi.org/10.1103/PhysRevB.109.125131. [Cited on page 141].

M. Pendharkar, B. Zhang, H. Wu, A. Zarassi, P. Zhang, C. P. Dempsey, J. S. Lee, S. D. Harrington, G. Badawy, S. Gazibegovic, R. L. M. Op het Veld, M. Rossi, J. Jung, A.-H. Chen, M. A. Verheijen, M. Hocevar, E. P. A. M. Bakkers, C. J. Palmstrøm, and S. M. Frolov. Parity-preserving and magnetic field–resilient superconductivity in InSb nanowires with Sn shells. *Science*, 372(6541):508–511, Apr. 2021. ISSN 1095-9203. doi: 10.1126/science.aba5211. URL http://dx.doi.org/10.1126/science.aba5211. [Cited on page 115].

F. Pientka, A. Keselman, E. Berg, A. Yacoby, A. Stern, and B. I. Halperin. Topological Superconductivity in a Planar Josephson Junction. *Physical Review X*, 7(2), May 2017. ISSN 2160-3308. doi: 10.1103/physrevx.7.021032. URL http://dx.doi.org/10.1103/PhysRevX.7.021032. [Cited on page 108].

D. I. Pikulin, J. P. Dahlhaus, M. Wimmer, H. Schomerus, and C. W. J. Beenakker. A zero-voltage conductance peak from weak antilocalization in a Majorana nanowire.

New Journal of Physics, 14(12):125011, Dec. 2012. ISSN 1367-2630. doi: 10.1088/ 1367-2630/14/12/125011. URL http://dx.doi.org/10.1088/1367-2630/14/12/ 125011. [Cited on page 66].

J.-D. Pillet, P. Joyez, R. Žitko, and M. F. Goffman. Tunneling spectroscopy of a single quantum dot coupled to a superconductor: From Kondo ridge to Andreev bound states. *Physical Review B*, 88(4), July 2013. ISSN 1550-235X. doi: 10.1103/physrevb.88.045101. URL http://dx.doi.org/10.1103/PhysRevB.88.045101. [Cited on pages 134, 135, and 136].

D. M. Pino, R. S. Souto, and R. Aguado. Minimal Kitaev-transmon qubit based on double quantum dots. *Physical Review B*, 109(7), Feb. 2024. ISSN 2469-9969. doi: 10.1103/ physrevb.109.075101. URL http://dx.doi.org/10.1103/PhysRevB.109.075101. [Cited on pages 39, 115, and 163].

M. Pita-Vidal, A. Bargerbos, R. Žitko, L. J. Splitthoff, L. Grünhaupt, J. J. Wesdorp, Y. Liu, L. P. Kouwenhoven, R. Aguado, B. van Heck, A. Kou, and C. K. Andersen. Direct manipulation of a superconducting spin qubit strongly coupled to a transmon qubit. *Nature Physics*, 19(8):1110–1115, May 2023. ISSN 1745-2481. doi: 10.1038/ s41567-023-02071-x. URL http://dx.doi.org/10.1038/s41567-023-02071-x. [Cited on page 134].

M. Pita-Vidal, J. J. Wesdorp, and C. K. Andersen. Blueprint for all-to-all connected superconducting spin qubits, 2024a. URL https://arxiv.org/abs/2405.09988. [Cited on page 171].

M. Pita-Vidal, J. J. Wesdorp, L. J. Splitthoff, A. Bargerbos, Y. Liu, L. P. Kouwenhoven, and C. K. Andersen. Strong tunable coupling between two distant superconducting spin qubits. *Nature Physics*, 20(7):1158–1163, May 2024b. ISSN 1745-2481. doi: 10.1038/ s41567-024-02497-x. URL http://dx.doi.org/10.1038/s41567-024-02497-x. [Cited on pages 134 and 143].

S. Plugge, L. A. Landau, E. Sela, A. Altland, K. Flensberg, and R. Egger. Roadmap to Majorana surface codes. *Physical Review B*, 94(17), Nov. 2016. ISSN 2469-9969. doi: 10.1103/physrevb.94.174514. URL http://dx.doi.org/10.1103/PhysRevB. 94.174514. [Cited on page 23].

S. Plugge, A. Rasmussen, R. Egger, and K. Flensberg. Majorana box qubits. *New Journal of Physics*, 19(1):012001, Jan. 2017. ISSN 1367-2630. doi: 10.1088/1367-2630/ aa54e1. URL http://dx.doi.org/10.1088/1367-2630/aa54e1. [Cited on pages 23 and 167].

A. Pöschl, A. Danilenko, D. Sabonis, K. Kristjuhan, T. Lindemann, C. Thomas, M. J. Manfra, and C. M. Marcus. Nonlocal conductance spectroscopy of Andreev bound states in gate-defined InAs/Al nanowires. *Physical Review B*, 106(24), Dec. 2022. ISSN 2469-9969. doi: 10.1103/physrevb.106.l241301. URL http://dx.doi.org/10.1103/ PhysRevB.106.L241301. [Cited on page 48].

E. Prada, P. San-Jose, and R. Aguado. Transport spectroscopy of NS nanowire junctions with Majorana fermions. *Physical Review B*, 86(18), Nov. 2012. ISSN 1550-235X. doi: 10.1103/physrevb.86.180503. URL http://dx.doi.org/10.1103/PhysRevB.86.180503. [Cited on page 66].

E. Prada, R. Aguado, and P. San-Jose. Measuring Majorana nonlocality and spin structure with a quantum dot. *Physical Review B*, 96(8), Aug. 2017. ISSN 2469-9969. doi: 10.1103/physrevb.96.085418. URL http://dx.doi.org/10.1103/PhysRevB.96.085418. [Cited on page 162].

E. Prada, P. San-Jose, M. W. A. de Moor, A. Geresdi, E. J. H. Lee, J. Klinovaja, D. Loss, J. Nygård, R. Aguado, and L. P. Kouwenhoven. From Andreev to Majorana bound states in hybrid superconductor–semiconductor nanowires. *Nature Reviews Physics*, 2(10): 575–594, Sept. 2020. ISSN 2522-5820. doi: 10.1038/s42254-020-0228-y. URL http://dx.doi.org/10.1038/s42254-020-0228-y. [Cited on pages 3, 108, and 134].

B. Probst, F. Domínguez, A. Schroer, A. L. Yeyati, and P. Recher. Signatures of nonlocal Cooper-pair transport and of a singlet-triplet transition in the critical current of a double-quantum-dot Josephson junction. *Physical Review B*, 94(15), Oct. 2016. ISSN 2469-9969. doi: 10.1103/physrevb.94.155445. URL http://dx.doi.org/10.1103/PhysRevB.94.155445. [Cited on page 134].

A. Ranni, F. Brange, E. T. Mannila, C. Flindt, and V. F. Maisi. Real-time observation of Cooper pair splitting showing strong non-local correlations. *Nature Communications*, 12(1), Nov. 2021. ISSN 2041-1723. doi: 10.1038/s41467-021-26627-8. URL http://dx.doi.org/10.1038/s41467-021-26627-8. [Cited on pages 92 and 108].

R. Raussendorf and J. Harrington. Fault-Tolerant Quantum Computation with High Threshold in Two Dimensions. *Physical Review Letters*, 98(19), May 2007. ISSN 1079-7114. doi: 10.1103/physrevlett.98.190504. URL http://dx.doi.org/10.1103/PhysRevLett.98.190504. [Cited on page 23].

P. Recher, E. V. Sukhorukov, and D. Loss. Andreev tunneling, Coulomb blockade, and resonant transport of nonlocal spin-entangled electrons. *Physical Review B*, 63(16), Apr. 2001. ISSN 1095-3795. doi: 10.1103/physrevb.63.165314. URL http://dx.doi.org/10.1103/PhysRevB.63.165314. [Cited on pages 42, 65, 66, 92, and 98].

H. Ren, F. Pientka, S. Hart, A. T. Pierce, M. Kosowsky, L. Lunczer, R. Schlereth, B. Scharf, E. M. Hankiewicz, L. W. Molenkamp, B. I. Halperin, and A. Yacoby. Topological superconductivity in a phase-controlled Josephson junction. *Nature*, 569(7754):93–98, Apr. 2019. ISSN 1476-4687. doi: 10.1038/s41586-019-1148-9. URL http://dx.doi.org/10.1038/s41586-019-1148-9. [Cited on pages 66 and 108].

T. O. Rosdahl, A. Vuik, M. Kjaergaard, and A. R. Akhmerov. Andreev rectifier: A nonlocal conductance signature of topological phase transitions. *Physical Review B*, 97(4), Jan. 2018. ISSN 2469-9969. doi: 10.1103/physrevb.97.045421. URL http://dx.doi.org/10.1103/PhysRevB.97.045421. [Cited on page 45].

A. V. Rozhkov and D. P. Arovas. Josephson Coupling through a Magnetic Impurity. *Physical Review Letters*, 82(13):2788–2791, Mar. 1999. ISSN 1079-7114. doi: 10.1103/physrevlett.82.2788. URL http://dx.doi.org/10.1103/PhysRevLett.82.2788. [Cited on page 141].

A. I. Rusinov. On the theory of gapless superconductivity in alloys containing paramagnetic impurities. *Soviet Physics JETP*, 29(6), Dec. 1969. URL http://jetp.ras.ru/cgi-bin/dn/e_029_06_1101.pdf. [Cited on page 104].

M. Russ. *Quantum information processing in semiconductor quantum dots using single and multi-spin qubits*. PhD thesis, Universität Konstanz, Konstanz, 2019. URL http://nbn-resolving.de/urn:nbn:de:bsz:352-2-1icumgkypxngw1. Accessed: 2024-10-16. [Cited on page 2].

S. Russo, M. Kroug, T. M. Klapwijk, and A. F. Morpurgo. Experimental Observation of Bias-Dependent Nonlocal Andreev Reflection. *Physical Review Letters*, 95(2), July 2005. ISSN 1079-7114. doi: 10.1103/physrevlett.95.027002. URL http://dx.doi.org/10.1103/PhysRevLett.95.027002. [Cited on page 42].

J. J. Sakurai and J. Napolitano. *Modern Quantum Mechanics*. Cambridge University Press, Sept. 2020. ISBN 9781108473224. doi: 10.1017/9781108587280. URL http://dx.doi.org/10.1017/9781108587280. [Cited on page 15].

W. Samuelson, V. Svensson, and M. Leijnse. Minimal quantum dot based Kitaev chain with only local superconducting proximity effect. *Physical Review B*, 109(3), Jan. 2024. ISSN 2469-9969. doi: 10.1103/physrevb.109.035415. URL http://dx.doi.org/10.1103/PhysRevB.109.035415. [Cited on pages 39 and 163].

K. J. Satzinger, Y.-J. Liu, A. Smith, C. Knapp, M. Newman, C. Jones, Z. Chen, C. Quintana, X. Mi, A. Dunsworth, C. Gidney, I. Aleiner, F. Arute, K. Arya, J. Atalaya, R. Babbush, J. C. Bardin, R. Barends, J. Basso, A. Bengtsson, A. Bilmes, M. Broughton, B. B. Buckley, D. A. Buell, B. Burkett, N. Bushnell, B. Chiaro, R. Collins, W. Courtney, S. Demura, A. R. Derk, D. Eppens, C. Erickson, L. Faoro, E. Farhi, A. G. Fowler, B. Foxen, M. Giustina, A. Greene, J. A. Gross, M. P. Harrigan, S. D. Harrington, J. Hilton, S. Hong, T. Huang, W. J. Huggins, L. B. Ioffe, S. V. Isakov, E. Jeffrey, Z. Jiang, D. Kafri, K. Kechedzhi, T. Khattar, S. Kim, P. V. Klimov, A. N. Korotkov, F. Kostritsa, D. Landhuis, P. Laptev, A. Locharla, E. Lucero, O. Martin, J. R. McClean, M. McEwen, K. C. Miao, M. Mohseni, S. Montazeri, W. Mruczkiewicz, J. Mutus, O. Naaman, M. Neeley, C. Neill, M. Y. Niu, T. E. O'Brien, A. Opremcak, B. Pató, A. Petukhov, N. C. Rubin, D. Sank, V. Shvarts, D. Strain, M. Szalay, B. Villalonga, T. C. White, Z. Yao, P. Yeh, J. Yoo, A. Zalcman, H. Neven, S. Boixo, A. Megrant, Y. Chen, J. Kelly, V. Smelyanskiy, A. Kitaev, M. Knap, F. Pollmann, and P. Roushan. Realizing topologically ordered states on a quantum processor. *Science*, 374(6572):1237–1241, Dec. 2021. ISSN 1095-9203. doi: 10.1126/science.abi8378. URL http://dx.doi.org/10.1126/science.abi8378. [Cited on page 3].

J. D. Sau and S. Das Sarma. Realizing a robust practical Majorana chain in a quantum-dot-superconductor linear array. *Nature Communications*, 3(1), July 2012. ISSN 2041-1723. doi: 10.1038/ncomms1966. URL http://dx.doi.org/10.1038/ncomms1966. [Cited on pages 4, 8, 13, 16, 39, 42, 65, 66, 68, 72, 73, 92, 108, 109, 112, 114, 171, and 189].

O. Sauret, D. Feinberg, and T. Martin. Quantum master equations for the superconductor–quantum dot entangler. *Physical Review B*, 70(24), Dec. 2004. ISSN 1550-235X. doi: 10.1103/physrevb.70.245313. URL http://dx.doi.org/10.1103/PhysRevB.70.245313. [Cited on page 92].

P. Scarlino, J. Ungerer, D. van Woerkom, M. Mancini, P. Stano, C. Müller, A. Landig, J. Koski, C. Reichl, W. Wegscheider, T. Ihn, K. Ensslin, and A. Wallraff. In situ Tuning of the Electric-Dipole Strength of a Double-Dot Charge Qubit: Charge-Noise Protection and Ultrastrong Coupling. *Physical Review X*, 12(3), July 2022. ISSN 2160-3308. doi: 10.1103/physrevx.12.031004. URL http://dx.doi.org/10.1103/PhysRevX.12.031004. [Cited on page 120].

Z. Scherübl, G. Fülöp, C. P. Moca, J. Gramich, A. Baumgartner, P. Makk, T. Elalaily, C. Schönenberger, J. Nygård, G. Zaránd, and S. Csonka. Large spatial extension of the zero-energy Yu–Shiba–Rusinov state in a magnetic field. *Nature Communications*, 11(1), Apr. 2020. ISSN 2041-1723. doi: 10.1038/s41467-020-15322-9. URL http://dx.doi.org/10.1038/s41467-020-15322-9. [Cited on pages 92 and 96].

Z. Scherübl, G. Fülöp, J. Gramich, A. Pályi, C. Schönenberger, J. Nygård, and S. Csonka. From Cooper pair splitting to nonlocal spectroscopy of a Shiba state. *Physical Review Research*, 4(2), May 2022. ISSN 2643-1564. doi: 10.1103/physrevresearch.4.023143. URL http://dx.doi.org/10.1103/PhysRevResearch.4.023143. [Cited on page 96].

J. Schindele, A. Baumgartner, and C. Schönenberger. Near-Unity Cooper Pair Splitting Efficiency. *Physical Review Letters*, 109(15), Oct. 2012. ISSN 1079-7114. doi: 10.1103/physrevlett.109.157002. URL http://dx.doi.org/10.1103/PhysRevLett.109.157002. [Cited on pages 42, 65, and 92].

J. Schindele, A. Baumgartner, R. Maurand, M. Weiss, and C. Schönenberger. Nonlocal spectroscopy of Andreev bound states. *Physical Review B*, 89(4), Jan. 2014. ISSN 1550-235X. doi: 10.1103/physrevb.89.045422. URL http://dx.doi.org/10.1103/PhysRevB.89.045422. [Cited on pages 42, 46, 92, and 102].

J. Schuff, M. J. Carballido, M. Kotzagiannidis, J. C. Calvo, M. Caselli, J. Rawling, D. L. Craig, B. van Straaten, B. Severin, F. Fedele, S. Svab, P. C. Kwon, R. S. Eggli, T. Patlatiuk, N. Korda, D. Zumbühl, and N. Ares. Fully autonomous tuning of a spin qubit, 2024. URL https://arxiv.org/abs/2402.03931. [Cited on page 172].

N. Sedlmayr and C. Bena. Visualizing Majorana bound states in one and two dimensions using the generalized Majorana polarization. *Physical Review B*, 92(11), Sept. 2015. ISSN 1550-235X. doi: 10.1103/physrevb.92.115115. URL http://dx.doi.org/10.1103/PhysRevB.92.115115. [Cited on page 163].

N. Sedlmayr, J. M. Aguiar-Hualde, and C. Bena. Majorana bound states in open quasi-one-dimensional and two-dimensional systems with transverse Rashba coupling. *Physical Review B*, 93(15), Apr. 2016. ISSN 2469-9969. doi: 10.1103/physrevb.93.155425. URL http://dx.doi.org/10.1103/PhysRevB.93.155425. [Cited on page 163].

G. Semeghini, H. Levine, A. Keesling, S. Ebadi, T. T. Wang, D. Bluvstein, R. Verresen, H. Pichler, M. Kalinowski, R. Samajdar, A. Omran, S. Sachdev, A. Vishwanath, M. Greiner, V. Vuletić, and M. D. Lukin. Probing topological spin liquids on a programmable quantum simulator. *Science*, 374(6572):1242–1247, Dec. 2021. ISSN 1095-9203. doi: 10.1126/science.abi8794. URL http://dx.doi.org/10.1126/science.abi8794. [Cited on page 3].

R. Seoane Souto, M. Leijnse, and C. Schrade. Josephson Diode Effect in Supercurrent Interferometers. *Physical Review Letters*, 129(26), Dec. 2022. ISSN 1079-7114. doi: 10.1103/physrevlett.129.267702. URL http://dx.doi.org/10.1103/PhysRevLett.129.267702. [Cited on page 5].

R. Seoane Souto, A. Tsintzis, M. Leijnse, and J. Danon. Probing Majorana localization in minimal Kitaev chains through a quantum dot. *Physical Review Research*, 5(4), Nov. 2023. ISSN 2643-1564. doi: 10.1103/physrevresearch.5.043182. URL http://dx.doi.org/10.1103/PhysRevResearch.5.043182. [Cited on pages 39, 162, 163, and 164].

R. Seoane Souto, V. V. Baran, M. Nitsch, L. Maffi, J. Paaske, M. Leijnse, and M. Burrello. Majorana modes in quantum dots coupled via a floating superconducting island, 2024. URL https://arxiv.org/abs/2411.07068. [Cited on page 39].

H. Shiba. Classical Spins in Superconductors. *Progress of Theoretical Physics*, 40(3):435–451, Sept. 1968. ISSN 0033-068X. doi: 10.1143/ptp.40.435. URL http://dx.doi.org/10.1143/PTP.40.435. [Cited on page 104].

P. W. Shor. Scheme for reducing decoherence in quantum computer memory. *Physical Review A*, 52(4):R2493–R2496, Oct. 1995. ISSN 1094-1622. doi: 10.1103/physreva.52.r2493. URL http://dx.doi.org/10.1103/PhysRevA.52.R2493. [Cited on page 2].

F. Siano and R. Egger. Josephson Current through a Nanoscale Magnetic Quantum Dot. *Physical Review Letters*, 93(4), July 2004. ISSN 1079-7114. doi: 10.1103/physrevlett.93.047002. URL http://dx.doi.org/10.1103/PhysRevLett.93.047002. [Cited on page 35].

M. Spethmann, X.-P. Zhang, J. Klinovaja, and D. Loss. Coupled superconducting spin qubits with spin-orbit interaction. *Physical Review B*, 106(11), Sept. 2022. ISSN 2469-9969. doi: 10.1103/physrevb.106.115411. URL http://dx.doi.org/10.1103/PhysRevB.106.115411. [Cited on pages 42 and 115].

M. Spethmann, S. Bosco, A. Hofmann, J. Klinovaja, and D. Loss. High-fidelity two-qubit gates of hybrid superconducting-semiconducting singlet-triplet qubits. *Physical Review B*, 109(8), Feb. 2024. ISSN 2469-9969. doi: 10.1103/physrevb.109.085303. URL http://dx.doi.org/10.1103/PhysRevB.109.085303. [Cited on page 42].

P. Stano and D. Loss. Review of performance metrics of spin qubits in gated semiconducting nanostructures. *Nature Reviews Physics*, 4(10):672–688, Aug. 2022. ISSN 2522-5820. doi: 10.1038/s42254-022-00484-w. URL http://dx.doi.org/10.1038/s42254-022-00484-w. [Cited on pages 18 and 170].

A. M. Steane. Simple quantum error-correcting codes. *Physical Review A*, 54(6): 4741–4751, Dec. 1996. ISSN 1094-1622. doi: 10.1103/physreva.54.4741. URL http://dx.doi.org/10.1103/PhysRevA.54.4741. [Cited on page 2].

D. Sticlet, C. Bena, and P. Simon. Spin and Majorana Polarization in Topological Superconducting Wires. *Physical Review Letters*, 108(9), Mar. 2012. ISSN 1079-7114. doi: 10.1103/physrevlett.108.096802. URL http://dx.doi.org/10.1103/PhysRevLett.108.096802. [Cited on page 163].

V. Svensson and M. Leijnse. Quantum dot based Kitaev chains: Majorana quality measures and scaling with increasing chain length. *Physical Review B*, 110(15), Oct. 2024. ISSN 2469-9969. doi: 10.1103/physrevb.110.155436. URL http://dx.doi.org/10.1103/PhysRevB.110.155436. [Cited on pages 39 and 163].

D. B. Szombati, S. Nadj-Perge, D. Car, S. R. Plissard, E. P. A. M. Bakkers, and L. P. Kouwenhoven. Josephson ϕ_0-junction in nanowire quantum dots. *Nature Physics*, 12(6):568–572, May 2016. ISSN 1745-2481. doi: 10.1038/nphys3742. URL http://dx.doi.org/10.1038/nphys3742. [Cited on page 134].

G. Széchenyi and A. Pályi. Parity-to-charge conversion for readout of topological Majorana qubits. *Physical Review B*, 101(23), June 2020. ISSN 2469-9969. doi: 10.1103/physrevb.101.235441. URL http://dx.doi.org/10.1103/PhysRevB.101.235441. [Cited on page 39].

Z. Tan, D. Cox, T. Nieminen, P. Lähteenmäki, D. Golubev, G. Lesovik, and P. Hakonen. Cooper Pair Splitting by Means of Graphene Quantum Dots. *Physical Review Letters*, 114(9), Mar. 2015. ISSN 1079-7114. doi: 10.1103/physrevlett.114.096602. URL http://dx.doi.org/10.1103/PhysRevLett.114.096602. [Cited on page 92].

S. Tarucha, D. G. Austing, T. Honda, R. J. van der Hage, and L. P. Kouwenhoven. Shell Filling and Spin Effects in a Few Electron Quantum Dot. *Physical Review Letters*, 77 (17):3613–3616, Oct. 1996. ISSN 1079-7114. doi: 10.1103/physrevlett.77.3613. URL http://dx.doi.org/10.1103/PhysRevLett.77.3613. [Cited on page 26].

S. L. D. ten Haaf, Q. Wang, A. M. Bozkurt, C.-X. Liu, I. Kulesh, P. Kim, D. Xiao, C. Thomas, M. J. Manfra, T. Dvir, M. Wimmer, and S. Goswami. A two-site Kitaev chain in a two-dimensional electron gas. *Nature*, 630(8016):329–334, June 2024a. ISSN 1476-4687. doi: 10.1038/s41586-024-07434-9. URL http://dx.doi.org/10.1038/s41586-024-07434-9. [Cited on pages 39, 108, 125, and 134].

S. L. D. ten Haaf, Y. Zhang, Q. Wang, A. Bordin, C.-X. Liu, I. Kulesh, V. P. M. Sietses, C. G. Prosko, D. Xiao, C. Thomas, M. J. Manfra, M. Wimmer, and S. Goswami. Edge and bulk states in a three-site Kitaev chain, 2024b. URL https://arxiv.org/abs/2410.00658. [Cited on pages 39, 160, and 161].

B. M. Terhal. Quantum error correction for quantum memories. *Reviews of Modern Physics*, 87(2):307–346, Apr. 2015. ISSN 1539-0756. doi: 10.1103/revmodphys.87.307. URL http://dx.doi.org/10.1103/RevModPhys.87.307. [Cited on page 2].

R. Tessler, C. Saguy, O. Klin, S. Greenberg, E. Weiss, R. Akhvlediani, R. Edrei, and A. Hoffman. Oxide-free InSb (100) surfaces by molecular hydrogen cleaning. *Applied Physics Letters*, 88(3), Jan. 2006. ISSN 1077-3118. doi: 10.1063/1.2162702. URL http://dx.doi.org/10.1063/1.2162702. [Cited on page 181].

M. Tinkham. *Introduction to superconductivity*. Courier Corporation, 2004. [Cited on pages 30, 31, 32, 112, 134, 138, and 147].

J. D. Torres Luna, A. M. Bozkurt, M. Wimmer, and C.-X. Liu. Flux-tunable Kitaev chain in a quantum dot array. *SciPost Physics Core*, 7(3), Sept. 2024. ISSN 2666-9366. doi: 10.21468/scipostphyscore.7.3.065. URL http://dx.doi.org/10.21468/SciPostPhysCore.7.3.065. [Cited on page 39].

A. Tsintzis, R. S. Souto, and M. Leijnse. Creating and detecting poor man's Majorana bound states in interacting quantum dots. *Physical Review B*, 106(20), Nov. 2022. ISSN 2469-9969. doi: 10.1103/physrevb.106.l201404. URL http://dx.doi.org/10.1103/PhysRevB.106.L201404. [Cited on pages 39, 45, 134, and 163].

A. Tsintzis, R. S. Souto, K. Flensberg, J. Danon, and M. Leijnse. Majorana Qubits and Non-Abelian Physics in Quantum Dot–Based Minimal Kitaev Chains. *PRX Quantum*, 5(1), Feb. 2024. ISSN 2691-3399. doi: 10.1103/prxquantum.5.010323. URL http://dx.doi.org/10.1103/PRXQuantum.5.010323. [Cited on pages 4, 39, 112, 115, 143, 163, 164, 167, and 169].

S. Vaitiekėnas, G. W. Winkler, B. van Heck, T. Karzig, M.-T. Deng, K. Flensberg, L. I. Glazman, C. Nayak, P. Krogstrup, R. M. Lutchyn, and C. M. Marcus. Flux-induced topological superconductivity in full-shell nanowires. *Science*, 367(6485), Mar. 2020. ISSN 1095-9203. doi: 10.1126/science.aav3392. URL http://dx.doi.org/10.1126/science.aav3392. [Cited on pages 66 and 108].

J. G. Valatin. Comments on the theory of superconductivity. *Il Nuovo Cimento*, 7(6): 843–857, Mar. 1958. ISSN 1827-6121. doi: 10.1007/bf02745589. URL http://dx.doi.org/10.1007/BF02745589. [Cited on page 30].

M. Valentini, F. Peñaranda, A. Hofmann, M. Brauns, R. Hauschild, P. Krogstrup, P. San-Jose, E. Prada, R. Aguado, and G. Katsaros. Nontopological zero-bias peaks in full-shell nanowires induced by flux-tunable Andreev states. *Science*, 373(6550):82–88, July 2021. ISSN 1095-9203. doi: 10.1126/science.abf1513. URL http://dx.doi.org/10.1126/science.abf1513. [Cited on page 134].

J. A. van Dam, Y. V. Nazarov, E. P. A. M. Bakkers, S. De Franceschi, and L. P. Kouwenhoven. Supercurrent reversal in quantum dots. *Nature*, 442(7103):667–670, Aug. 2006. ISSN 1476-4687. doi: 10.1038/nature05018. URL http://dx.doi.org/10.1038/nature05018. [Cited on pages 134, 135, 136, 137, 140, and 144].

N. C. van der Vaart, S. F. Godijn, Y. V. Nazarov, C. J. P. M. Harmans, J. E. Mooij, L. W. Molenkamp, and C. T. Foxon. Resonant Tunneling Through Two Discrete Energy States. *Physical Review Letters*, 74(23):4702–4705, June 1995. ISSN 1079-7114. doi: 10.

1103/physrevlett.74.4702. URL http://dx.doi.org/10.1103/PhysRevLett.74.4702. [Cited on page 29].

W. G. van der Wiel, S. De Franceschi, J. M. Elzerman, T. Fujisawa, S. Tarucha, and L. P. Kouwenhoven. Electron transport through double quantum dots. *Reviews of Modern Physics*, 75(1):1–22, Dec. 2002. ISSN 1539-0756. doi: 10.1103/revmodphys.75.1. URL http://dx.doi.org/10.1103/RevModPhys.75.1. [Cited on pages 29 and 67].

D. van Driel, G. Wang, A. Bordin, N. van Loo, F. Zatelli, G. P. Mazur, D. Xu, S. Gazibegovic, G. Badawy, E. P. A. M. Bakkers, L. P. Kouwenhoven, and T. Dvir. Spin-filtered measurements of Andreev bound states in semiconductor-superconductor nanowire devices. *Nature Communications*, 14(1), Oct. 2023. ISSN 2041-1723. doi: 10.1038/s41467-023-42026-7. URL http://dx.doi.org/10.1038/s41467-023-42026-7. [Cited on page 93].

D. van Driel, R. Koch, V. P. M. Sietses, S. L. D. t. Haaf, C.-X. Liu, F. Zatelli, B. Roovers, A. Bordin, N. van Loo, G. Wang, J. C. Wolff, G. P. Mazur, T. Dvir, I. Kulesh, Q. Wang, A. M. Bozkurt, S. Gazibegovic, G. Badawy, E. P. A. M. Bakkers, M. Wimmer, S. Goswami, J. L. Lado, L. P. Kouwenhoven, and E. Greplova. Cross-Platform Autonomous Control of Minimal Kitaev Chains, 2024a. URL https://arxiv.org/abs/2405.04596. [Cited on pages 39 and 171].

D. van Driel, B. Roovers, F. Zatelli, A. Bordin, G. Wang, N. van Loo, J. C. Wolff, G. P. Mazur, S. Gazibegovic, G. Badawy, E. P. Bakkers, L. P. Kouwenhoven, and T. Dvir. Charge Sensing the Parity of an Andreev Molecule. *PRX Quantum*, 5(2), Apr. 2024b. ISSN 2691-3399. doi: 10.1103/prxquantum.5.020301. URL http://dx.doi.org/10.1103/PRXQuantum.5.020301. [Cited on pages 39, 169, and 186].

H. Van Houten, C. W. J. Beenakker, and A. A. M. Staring. *Coulomb-Blockade Oscillations in Semiconductor Nanostructures*, page 167–216. Springer US, 1992. ISBN 9781475721669. doi: 10.1007/978-1-4757-2166-9_5. URL http://dx.doi.org/10.1007/978-1-4757-2166-9_5. [Cited on page 25].

N. van Loo. *Shadow-wall lithography as a novel approach to Majorana devices*. PhD thesis, Delft University of Technology, 2023. URL http://resolver.tudelft.nl/uuid:34bcaaa6-ec2b-44fd-ad25-387236568911. [Cited on pages 165, 177, and 181].

N. van Loo, G. P. Mazur, T. Dvir, G. Wang, R. C. Dekker, J.-Y. Wang, M. Lemang, C. Sfiligoj, A. Bordin, D. van Driel, G. Badawy, S. Gazibegovic, E. P. A. M. Bakkers, and L. P. Kouwenhoven. Electrostatic control of the proximity effect in the bulk of semiconductor-superconductor hybrids. *Nature Communications*, 14(1), June 2023. ISSN 2041-1723. doi: 10.1038/s41467-023-39044-w. URL http://dx.doi.org/10.1038/s41467-023-39044-w. [Cited on page 148].

F. Vigneau, F. Fedele, A. Chatterjee, D. Reilly, F. Kuemmeth, M. F. Gonzalez-Zalba, E. Laird, and N. Ares. Probing quantum devices with radio-frequency reflectometry. *Applied Physics Reviews*, 10(2), Feb. 2023. ISSN 1931-9401. doi: 10.1063/5.0088229. URL http://dx.doi.org/10.1063/5.0088229. [Cited on page 166].

A. Vuik, B. Nijholt, A. Akhmerov, and M. Wimmer. Reproducing topological properties with quasi-Majorana states. *SciPost Physics*, 7(5), Nov. 2019. ISSN 2542-4653. doi: 10.21468/scipostphys.7.5.061. URL http://dx.doi.org/10.21468/SciPostPhys.7.5.061. [Cited on page 66].

C. Wang, Y. Y. Gao, I. M. Pop, U. Vool, C. Axline, T. Brecht, R. W. Heeres, L. Frunzio, M. H. Devoret, G. Catelani, L. I. Glazman, and R. J. Schoelkopf. Measurement and control of quasiparticle dynamics in a superconducting qubit. *Nature Communications*, 5(1), Dec. 2014. ISSN 2041-1723. doi: 10.1038/ncomms6836. URL http://dx.doi.org/10.1038/ncomms6836. [Cited on page 170].

G. Wang. *Quantum Dots Coupled to Superconductors*. PhD thesis, Delft University of Technology, 2023. URL http://resolver.tudelft.nl/uuid:b86bec0b-0f27-4fac-90ae-7ad4bcac407a. [Cited on page 166].

G. Wang, T. Dvir, G. P. Mazur, C.-X. Liu, N. van Loo, S. L. D. ten Haaf, A. Bordin, S. Gazibegovic, G. Badawy, E. P. A. M. Bakkers, M. Wimmer, and L. P. Kouwenhoven. Singlet and triplet Cooper pair splitting in hybrid superconducting nanowires. *Nature*, 612 (7940):448–453, Nov. 2022a. ISSN 1476-4687. doi: 10.1038/s41586-022-05352-2. URL http://dx.doi.org/10.1038/s41586-022-05352-2. [Cited on pages 38, 39, 42, 43, 44, 45, 48, 49, 51, 57, 59, 68, 69, 92, 94, 95, 101, 109, and 125].

J.-Y. Wang, G.-Y. Huang, S. Huang, J. Xue, D. Pan, J. Zhao, and H. Xu. Anisotropic Pauli Spin-Blockade Effect and Spin–Orbit Interaction Field in an InAs Nanowire Double Quantum Dot. *Nano Letters*, 18(8):4741–4747, July 2018. ISSN 1530-6992. doi: 10.1021/acs.nanolett.8b01153. URL http://dx.doi.org/10.1021/acs.nanolett.8b01153. [Cited on page 51].

J.-Y. Wang, N. van Loo, G. P. Mazur, V. Levajac, F. K. Malinowski, M. Lemang, F. Borsoi, G. Badawy, S. Gazibegovic, E. P. A. M. Bakkers, M. Quintero-Pérez, S. Heedt, and L. P. Kouwenhoven. Parametric exploration of zero-energy modes in three-terminal InSb-Al nanowire devices. *Physical Review B*, 106(7), Aug. 2022b. ISSN 2469-9969. doi: 10.1103/physrevb.106.075306. URL http://dx.doi.org/10.1103/PhysRevB.106.075306. [Cited on page 166].

Q. Wang, S. L. D. ten Haaf, I. Kulesh, D. Xiao, C. Thomas, M. J. Manfra, and S. Goswami. Triplet correlations in Cooper pair splitters realized in a two-dimensional electron gas. *Nature Communications*, 14(1), Aug. 2023. ISSN 2041-1723. doi: 10.1038/s41467-023-40551-z. URL http://dx.doi.org/10.1038/s41467-023-40551-z. [Cited on pages 38, 39, 42, 57, 92, 94, 109, and 186].

J. L. Webb, J. Knutsson, M. Hjort, S. Gorji Ghalamestani, K. A. Dick, R. Timm, and A. Mikkelsen. Electrical and Surface Properties of InAs/InSb Nanowires Cleaned by Atomic Hydrogen. *Nano Letters*, 15(8):4865–4875, July 2015. ISSN 1530-6992. doi: 10.1021/acs.nanolett.5b00282. URL http://dx.doi.org/10.1021/acs.nanolett.5b00282. [Cited on page 181].

J. Wei and V. Chandrasekhar. Positive noise cross-correlation in hybrid superconducting and normal-metal three-terminal devices. *Nature Physics*, 6(7):494–498, May 2010.

ISSN 1745-2481. doi: 10.1038/nphys1669. URL http://dx.doi.org/10.1038/nphys1669. [Cited on page 92].

F. Wilczek. Quantum Mechanics of Fractional-Spin Particles. *Physical Review Letters*, 49(14):957–959, Oct. 1982. ISSN 0031-9007. doi: 10.1103/physrevlett.49.957. URL http://dx.doi.org/10.1103/PhysRevLett.49.957. [Cited on page 20].

B. D. Woods, S. Das Sarma, and T. D. Stanescu. Charge-Impurity Effects in Hybrid Majorana Nanowires. *Physical Review Applied*, 16(5), Nov. 2021. ISSN 2331-7019. doi: 10.1103/physrevapplied.16.054053. URL http://dx.doi.org/10.1103/PhysRevApplied.16.054053. [Cited on page 3].

H. Wu, P. Zhang, J. P. T. Stenger, Z. Su, J. Chen, G. Badawy, S. Gazibegovic, E. P. A. M. Bakkers, and S. M. Frolov. Triple Andreev dot chains in semiconductor nanowires, 2021. URL https://arxiv.org/abs/2105.08636. [Cited on page 186].

L. Yu. Bound state in superconductors with paramagnetic impurities. *Acta Physica Sinica*, 21(1):75, 1965. ISSN 1000-3290. doi: 10.7498/aps.21.75. URL http://dx.doi.org/10.7498/aps.21.75. [Cited on page 104].

D. Zajac, T. Hazard, X. Mi, E. Nielsen, and J. Petta. Scalable Gate Architecture for a One-Dimensional Array of Semiconductor Spin Qubits. *Physical Review Applied*, 6(5), Nov. 2016. ISSN 2331-7019. doi: 10.1103/physrevapplied.6.054013. URL http://dx.doi.org/10.1103/PhysRevApplied.6.054013. [Cited on page 29].

F. Zatelli, D. van Driel, D. Xu, G. Wang, C.-X. Liu, A. Bordin, B. Roovers, G. P. Mazur, N. van Loo, J. C. Wolff, A. M. Bozkurt, G. Badawy, S. Gazibegovic, E. P. A. M. Bakkers, M. Wimmer, L. P. Kouwenhoven, and T. Dvir. Robust poor man's Majorana zero modes using Yu-Shiba-Rusinov states. *Nature Communications*, 15(1), Sept. 2024. ISSN 2041-1723. doi: 10.1038/s41467-024-52066-2. URL http://dx.doi.org/10.1038/s41467-024-52066-2. [Cited on pages 39, 109, 111, 113, 114, 120, 121, 122, 123, 124, 125, 126, 134, 168, 188, and 189].

H. Zhang, C.-X. Liu, S. Gazibegovic, D. Xu, J. A. Logan, G. Wang, N. van Loo, J. D. S. Bommer, M. W. A. de Moor, D. Car, R. L. M. Op het Veld, P. J. van Veldhoven, S. Koelling, M. A. Verheijen, M. Pendharkar, D. J. Pennachio, B. Shojaei, J. S. Lee, C. J. Palmstrøm, E. P. A. M. Bakkers, S. Das Sarma, and L. P. Kouwenhoven. Retraction Note: Quantized Majorana conductance. *Nature*, 591(7851):E30–E30, Mar. 2021. ISSN 1476-4687. doi: 10.1038/s41586-021-03373-x. URL http://dx.doi.org/10.1038/s41586-021-03373-x. [Cited on page 3].

P. Zhang, K. Yaji, T. Hashimoto, Y. Ota, T. Kondo, K. Okazaki, Z. Wang, J. Wen, G. D. Gu, H. Ding, and S. Shin. Observation of topological superconductivity on the surface of an iron-based superconductor. *Science*, 360(6385):182–186, Apr. 2018. ISSN 1095-9203. doi: 10.1126/science.aan4596. URL http://dx.doi.org/10.1126/science.aan4596. [Cited on page 108].

S. Zhu, Y. Song, X. Zhao, J. Shao, J. Zhang, and B. Yang. The photoluminescence mechanism in carbon dots (graphene quantum dots, carbon nanodots, and polymer dots):

current state and future perspective. *Nano Research*, 8(2):355–381, Feb. 2015. ISSN 1998-0000. doi: 10.1007/s12274-014-0644-3. URL http://dx.doi.org/10.1007/s12274-014-0644-3. [Cited on page 134].

M. Żukowski, A. Zeilinger, M. A. Horne, and A. K. Ekert. '"Event-ready-detectors"' Bell experiment via entanglement swapping. *Physical Review Letters*, 71(26):4287–4290, Dec. 1993. ISSN 0031-9007. doi: 10.1103/physrevlett.71.4287. URL http://dx.doi.org/10.1103/PhysRevLett.71.4287. [Cited on page 98].

R. Žitko and L. Pavešić. Yu-Shiba-Rusinov states, BCS-BEC crossover, and exact solution in the flat-band limit. *Physical Review B*, 106(2), July 2022. ISSN 2469-9969. doi: 10.1103/physrevb.106.024513. URL http://dx.doi.org/10.1103/PhysRevB.106.024513. [Cited on page 36].

ACKNOWLEDGEMENTS

uomini fuoro, accesi di quel caldo
che fa nascere i fiori e ' frutti santi.

Dante Alighieri, *Paradiso*, XXII, 47-48

[men who were kindled by that heat which brings
to birth the blessed flowers and blessed fruits.]

This journey is the fruit of an immense tree of people and relationships. I cannot find the words to fully express my deepest gratitude to all of you. **Alexei**, we never met in person, but I am deeply grateful to you for inspiring this research. I'm amazed by how often your name comes about whenever I study something new. It all started 8 years ago when I first got interested in the problem of quantum coin tossing. After weeks of research, I found the solution, provided by Andris Ambainis in about 80 pages of hardcore math. His main reference was a certain "Kitaev idea", cited as personal communication. Then I got interested in the Kitaev materials, then into the surface code… it really seems that for every quantum information topic I pick, if I dig deep enough, I find your name. It really deserves to be in the title of this dissertation.

Leo, thank you for making all of this possible. The environment you created is out of this world. Coming from the limited facilities we have in Italy, experiencing your lab was a shock. After five years of research, I see that your lab, and QuTech as a whole, is not just better than what we have in Italy: it's the best place in the world for condensed matter physicists. Thank you for creating it and for co-founding QuTech. Thank you also for all the experience and the pieces of advice you shared through the years, including "to make big steps" and "listen and fill the gaps". Even more than the words, your example is what inspires me the most: thank you, in particular, for holding on during the difficult two years following the retraction and for eventually coming back to the lab to keep innovating for the rest of your career. **Christian**, you're the best co-promotor I could ever hope for. Always kind, smart, available, and incredibly knowledgeable. How come you always have the right answers to my questions even if your research focus is so different?

Tom, you saved my PhD, and I'm not the first one saying it. You saved the whole group. You're a crazy genius and, at the same time, you're never jealous of your ideas. You gifted them here and there all the time without asking for credit, even if you deserve the most of all. I want to deeply thank you, not just for the success you gifted us but also for the spirit you brought. In the lab, you were always playful and happy as a five-year-old, and in the wider community, you were always open and ready to collaborate as a

great leader. We owe it to you if we are now meeting so much among ourselves and with people in Madrid, Copenhagen, and Lund. We miss you, Tom, when are you coming back? **Greg**, it was a pleasure to collaborate with you on the three-site chain project. You're always smiling, even when you're unsatisfied or complaining. It was great to have you around. I wish you the best for your new Oxford adventure and I promise to bring the pecorino the next time I visit.

I am also grateful to the external committee members, **Ronald**, **Sonia**, **Carlo**, **Georgios**, and **Gary** for evaluating this dissertation. Georgios, thank you also for hosting me at ISTA, it was absolutely amazing.

David and **Bas**, you are the best paranymphs I could wish for. David, you were the youngest and closest colleague when I started my PhD, thank you for sharing the first struggles and the first celebrations with me when I arrived. Thank you also for all the nice breakfasts at the March meeting, I had a great time. Bas, my first master's student, the eldest, it's amazing to see how much you have grown, personally and professionally, over the last four years. You wrote a great master's thesis; I look forward to reading a wonderful PhD thesis as well. Two Dutchmen as paranymphs, a rarity considering the international population of QuTech, demonstrates how welcoming this country's people have been. Thank you.

Xiang and **Florian**, it was a pleasure to supervise you as well. I felt very privileged to receive three master's students in total. I tried to teach you everything I knew, and you came a long way. Xiang, good luck with your career in China. Your determination will bring you far; I'm looking forward to reading about your next adventures. Florian, I'm so happy that you decided to join our lab at the end of the day. We did a great job together, and I hope the collaboration can continue in the future. Thank you also for reminding us that life is not only about physics: enjoy your trip to South America!

Nick, master nanofabricator, thank you for teaching me how to make a perfect substrate and how to deposit nanowires. Thank you also for all the detailed comments on the manuscripts. You quoted: "Not everything we do is great", but your meticulous nature ensures that most of what you do is. **Guan**, we are quite different and we manage to argue basically on everything for no apparent reason, like in most marriages. It was great and I can't wait to do it again. I wish you the best for your Stanford post-doc. **Di**, you are very kind and a very nice person. And extremely resilient. Congratulations again for being the only one who managed to graduate on SAG! I wish you the best at Quantum Motion, looks like a great fit. **Francesco**, I'm so happy that you decided to join us for your PhD. I was afraid you chose Zurich and I tried to lobby as much as I could to convince you and the others to get you here. You're a wonderful colleague. Looking forward to reading your thesis! **Bart**, your precision and determination will bring you far. Interacting with you is great; I can't wait to write our first manuscript together. **Cem**, welcome to the lab. I hope you'll have a great time with us and with the experiments waiting for you. **Thomas**, you were a great addition to the lab, professionally and personally, it's a pity that you stayed for so little. I wish you the best at Imec. **Tijl**, I was really looking forward to working with you as a PhD student. You're a very nice, smart, and kind person, good luck with your next adventure. And thank you for the Leonidas tip; now it's a must for me every time I go to Belgium. **Vincent**, the first master's student of my first master's student. I feel like your grandpa, but you grew so quickly and are about to join us as a

PhD student. I look forward to collaborating with you in new experiments as well as in the football pitch.

I also want to thank all the old PhD students of Leo's that I met when I first arrived. Starting from **Luca**, my master's thesis supervisor. I'll always be grateful to you for teaching me fabrication and lockin measurements, for inviting me to the football pitch and for correcting my thesis even if you had already left the lab. **Francesco**, I still remember my first interview. Thank you for introducing me to the lab. I consider you as an elder brother since I have always followed your steps, from Friuli to Pisa to Delft. Let's see what's next. **Jaap**, you're so funny, I'm missing your irony, and I miss **Pepijn** as well. **Lukas**, I wish we had more time to climb, play, and eat carbonara. You're the hardest-working student I've ever met, fatigue is not a thing for you, is it? Have fun in Göteborg. **Willemijn**, thank you for being my first friend in the lab, you're great. **Arno** and **Marta**, congratulations for your achievements. **Lukas**, thanks for always smiling, and congratulations on your new position. Thanks also to **Vukan**, **Lin**, **Damaz**, **Christian**, **Michael**, and your post-docs **Ji-Yin** and **Filip**. Thanks also to **Daniel** for being always nice and to **Jasper** and **Fokko** for sharing the football pitch.

All the Quantum Warriors deserve special thanks. **Christian**, thank you for welcoming me from day one. **Gustavo**, for inviting us to your place. You have a wonderful family. **Michael**, when are you coming back? And thanks to **Valentin**, **Ema**, **Marteen**, **Thijs**, **Sjoerd**, **Fabrizio**, **Jorge**, **Mark**, **Stefano**, **Arjen**, **Anta**, **Luca**, **Tim**, **Nikos**, **Conor**. Thanks also to all the (relatively) new entries: **Maroto**, **Dario**, **Jared**, **Joao**, **Marius**, **Tom**.

Thanks to **Srijit** for being my mentor in the first PhD years, helping me with the choice between SAG and VLS nanowires. And thanks to your whole group. **Ivan** and **Qing**, I'm looking forward to reading your dissertation and attending your defense. Keep it up! **Yining**, **Wietze**, **Rebecca**, **DJ**, **Sebas**, enjoy your PhD. **Prasanna**, **Ting**, **Nayan**, **Praveen**, **Eoin**, have fun in your next adventure.

Thanks also to all the Quantum Tinkerers. **Chun-Xiao**, collaborating with you is a pleasure. You're always precise, reliable, hard-working, and timely; we couldn't wish for better theory support. Good luck with all the applications! **Michael**, thank you for the comments on all the manuscripts. **Anton**, thank you for your sharp irony, for the insights, and for all the bouldering sessions. **Isidora**, thank you for answering with a smile always and everywhere. Being around you is always fun. Thank you also for the bouldering and the amazing help with pymablock. Congratulations on being one of the best presenters of QuTech; after the whiteboard show, the Dordrecht story, and the 2D slides, what's next? **Sebastian** and **Mert**, thank you for all the insightful interactions and the street basketball, always fun. **Juan**, we just started collaborating and it's already so fruitful, I'm curious to see what the next months are going to bring. Thanks also to **Johanna**, **Rik**, **Kostas**, **Antonio**, and **Tess**.

Anasua, welcome to Qubit Research alongside your newborn group. And thanks also to the Andersen lab for reminding us that qubits do exist: **Figen**, **Siddhart**, **Eugene**, **Martijn**, **Marco**, **Taryn**, **Natasha**, **Jinlun**, **Yen-An**, and **Sara**. Thank you **Delphine** for being always curious and cheerful, **Zahra** for the Aula lunches, **Dave** for the queues, and **Lara** for all the cleanroom encounters. The rest of QuTech is too big to thank everyone explicitly, but I really wish to remember at least **Maia**, **Desa**, **Karina**, **Alberto**, **Luka** with a k, **Giordano**, **Lieven**, **Sebastian**, **Stefano** and the real **Stefano**, **Daniel**, **Pablo**, **Hanifa**, **Uri**,

Sasha, **Chien-An**, **Nicolino**, **Nina**, **Christina**, **Mariagrazia**, **Fenglei** and **Grazia**.

Thanks also to all the external collaborators. **Gorm**, I loved working with you and **Alfredo** on the trimer project. It was an amazing journey, started by chance with a random question at the Kitaev workshop and evolved into ongoing collaborations with Francesco and Nick. Thank you for always answering all of our questions and for being such a nice collaborator. I can't wait to hear your joyful "Hello, hello!" again. **Rubén** and **Ramón**, thank you for all the great discussions. Thank you **Rouven** and **Eliska** for adding the power of machine learning to what we do. And even more, for always being nice and open. Rouven, I'm very happy that you joined the Quantum Warriors as well, and Eliska, I really hope that we will eventually manage to collaborate again after the latest attempt. Thank you also for your feedback on the KIND application. I am also very grateful for the wonderful InSb nanowire supply from Eindhoven: thank you **Erik**, **Ghada**, and **Sasa**. And thank also to the Microsoft collaborators, even if many of you left already: **Cristina**, **Pavel**, **Philippe**, **Gijs**, **Elvedin**, **Amrita**, **Mathilde**, **Sebastian**, **Marina**, **Michiel**, **Jouri**, **Sarat**, **Victor**, **Daan**, **Lieuwe**, **David**.

Thank you **Csilla** for the coordination, **Eleonora** for being always friendly, and **Jenny** for being our mum in the department, you are really great.

Last but not least, I can't be grateful enough to all the technicians. You are the true pillars of QuTech. Thank you **Olaf** and **Jason** for taking care of all the fridges. The lab wouldn't exist without you. Thank you **Mark** and **Jan Cornelis** for setting up and taking care of the UTS. This thesis wouldn't exist otherwise. **Raymond**, I'm deeply grateful to you and your whole electronics team – in particular **Roy**, **Erik**, and the second **Raymond** – for enabling everything we do. If the DC current derivative can be basically as accurate as the lockin signal, and if we can detect such tiny supercurrents, it's all thanks to you and your team. What a testimony of what a life-long passion can achieve. Thanks, Raymond, you are the secret force behind the curtains.

Devo anche ringraziare una marea di amici che mi hanno accompagnato in questi anni. **Doc**, non potevo non cominciare da te, ultimo dei colleghi e primo degli amici. Silenziosamente imprescindibile. Appena arrivato mi hai accolto in casa tua e tra i tuoi amici, grazie di cuore. Ringrazio anche tutti gli altri conquilini per la pazienza infinita e immeritata, e per aver accolto la Lucy e i miei amici ogni volta che sono venuti a trovarmi. Grazie **Ale** per la sopportazione di tutte le mie chiamate, e per l'aiuto immeritato sulle pulizie. Grazie **Vec** per tutti gli abbracci a caso. Grazie **Davide** per le cene condivise. Grazie **Manu** per la tua simpatia irresistibile, ci manchi proprio. Grazie **Fede** per la tua follia, cambi tutto e non cambi mai, sei bella così. **Cocchi**, grazie per la ricetta del salmone, per "i fatti di cronaca" e per aver battezzato il mio giacchino come "il brutto". Ora tutta la mia famiglia lo chiama così. **Beliii!!!** . . . segue abbraccio, e non serve aggiungere altro. **Ema**, ti ringrazio anche qui perché sei molto più di un compagno di calcio. **Davide**, **Irene** e ... siete una bellissima famiglia.

Marie, grazie per il bene che vuoi a me e a Lucy. **Marco**, sembra assurdo che tu sia stato qua solo per tre mesi, grazie per esserci stato e per avermi fatto (ri)trovare un sacco di amici: **Carlo**, **Chicca**, **Alessandra**, **Scaio**, **Giocle** e tutti gli ultimi arrivati **Elena**, **Marco**, **Gianluca**, **Letizia**, **Chiara**, **Paola**, **Brazzo**, **Bobbi**, **Javi**, **Lorenzo**, **Mattia**. E grazie anche a **Carlo**, **Emma**, **Franz**, **Bernadette**, **Michiel**, **Francesco**, **Mirka** e tutti gli altri per avermi sempre accolto e ri-accolto dopo tanto tempo.

Un grande abbraccio anche a tutti gli amici lontani ma vicini, a cominciare da **Ema**, **Forna**, **Pol**, **Teo**, **Pietro** e **Leti**, **Sonia**, **Lucina**. Ci siete stati sempre, pur vivendo in un altro stato. E grazie anche a tutti quelli che ho conosciuto negli ultimi anni per "colpa" della Lucy.

Ringrazio di cuore anche tutti i miei compagni di Normale, in questa tesi c'è tanto di quello che ho imparato con voi e da voi: **Jack**, **Hoch**, **Bob**, **Andre**, **Vale**, **Ale**, **Marco**, **Begli**, **Capo**. E quelli che ho ritrovato qui in Olanda: **Elia**, **Gimmy** e **Veronica**. Un grande abbraccio anche a **Benedetta**, **Guaro**, **Giorgio**, **Rhydon**, **Dani** e **Anna**, **Giulio** e **Marta** e tutta la prole.

Tanso, che bello poterti ringraziare anche qui, da quando ci siamo conosciuti è un continuo tira e molla che spero non finisca mai. Tanti complimenti anche a tutto il team di Olivia. **Fede**, è divertentissimo lavorare con te, non dimenticarti che ogni tanto bisogna fare anche le cose noiose, ma non smettere mai di sparare nuove idee. Prima o poi ce la farai a fare uno spin-off, ancora dentro Olivia si spera. **Paolo**, sei una roccia, meno male che ci sei tu a tenere assieme tutti i mattoni. E **Lore**, meno male che c'eri tu a controllare che noi pazzi non andassimo troppo fuori di testa.

Infine, devo tantissimo a tutta la mia famiglia. A cominciare dai nonni **Walter** e **Luciana**, **Antonio**, **Elisabetta** e la zia **Pierina**, grazie a tutti per avermi sempre voluto bene incondizionatamente. Ringrazio tanto gli zii **Lorenzo** e **Luisa**, **Carlo** e **Giovanna**, per essere sempre attenti e cari, e i cuginetti che ormai sono cresciuti un bel po': **Alessia**, **Matteo** e **Maria**. Ricordo ancora di quando mi guardavate dal basso in alto come il cugino grande, ora sono io a guardare entusiasta dove state arrivando.

Sara, anche tu non sei più una bambina, non ci sono ancora abituato, ma è proprio bello vederti crescere. Non dimenticarti mai della spavalderia che ti fece prendere lo scuolabus già dal primo giorno di scuola e dell'attesa con cui hai pianificato il tuo primo pigiama party. Farai strada! Non vedo l'ora di vedere come fiorirai ancora di più. **Luca**, meno male che ci sei tu. Capirsi al volo senza neanche aprire bocca é una senzazione inspiegabile. Grazie per continuare a nerdare con me ogni volta che possiamo, di ingegneria, di fisica, o di qualsiasi cosa. In più, é stato incredibile vederti crescere così tanto in questi ultimi anni, il rapporto che hai coi tuoi amici, vecchi e nuovi, è qualcosa di speciale. **Nina**, sei una grande. Complimenti per l'esempio di tenacia che hai dato a tutti noi: da un liceo molto tosto e un primo anno di università difficile – al punto da mettere in dubbio di poter arrivare in fondo – hai fregato tutti laureandoti in pari e con *matrícula de honor*. Che roccia, non dubitare mai più! Ancor di più, grazie per essere la nostra sorellona. C'è un motivo se veniamo tutti da te quando abbiamo bisogno di aiuto o di un consiglio. **Mamma**, grazie per avermi amato sempre, immeritatamente e incondizionatamente. Anche quando brontoli: è particolarmente tenero quando ci dai una mano controvoglia, lì si vede tantissimo quanto ci vuoi bene. Sei proprio una grande, grazie Mamma! Io e Papà ci saremmo persi senza di te, grazie per essere venuta a salvarci ed essere rimasta per sempre. **Papà**, grazie per tutto. Anche per il naso e l'allergia. E soprattutto grazie per ricordarci sempre che la vita è una figata, nonostante tutte le (apparenti?) "sfighe" che possono capitare. *L'essenziale è invisibile agli occhi.*

Cara **Lucy**, la mia nuova famiglia incomincia con te. Sei il regalo più grande di tutti, per cui desidero ringraziare profondamente te e **Chi** ci ha fatto incontrare. TQ.

Muchísimas gracias a los mejores **Yayos** del mundo. Gracias por ser siempre tan acogedores. Y gracias a todos los primos que comparten esta suerte conmigo, empezando por **Juan** y **Carlos**, los "peques" que ya casi son más altos que yo. Que disfrutéis todo lo que podáis del nuevo trabajo y del tiempo en la universidad. Gracias a **Pablo**, que no para de pasárselo bien en cualquier sitio y con cualquier compañía. A **Dani**, que recuerdo siempre en un cuarto especial de mi corazón, gracias, Dani, por compartir un poco de ciencia, un poco de Otelo y un poco de cualquier otro juego conmigo. Y **Alba**, que ya se casa. Enhorabuena, querida prima.

Muchísimas gracias a todos los tíos. Gracias, **Eva**, por quererme muchísimo, estar siempre tan contenta de verme y acoger tan bien a Lucía. Gracias, **Alberto**, por interesarte en todo lo que hago y enseñarme todo lo que haces tú con esa pasión increíble. Gracias, **Luis**, por quererme tanto, sin que yo lo merezca. Muchísimas gracias por venir hasta Italia el día de mi primera graduación y por todas las excursiones estupendas. Para ti, *Cáritas* no es un trabajo, es una forma de vivir. Gracias, **Inma**, por el diario de mamá y por asegurarte siempre de que disfrutamos a tope todos los días que pasamos en España.

En fin, gracias, **Mamá**, por esta vida maravillosa que me regalaste. Te echo de menos. Gracias por todo lo que has hecho y todo lo que sigues haciendo por mí y por todos nosotros.

Curriculum Vitæ

Alberto BORDIN

12-04-1995   Born in London, UK

EDUCATION

2009–2014   High School
                   Liceo Scientifico G. Bertoni, Udine, Italy

2014-2017   BSc in Physics
                   University of Pisa, Italy
                   Thesis supervisor: Dr. O. Morsch

2017-2019   MSc in Condensed Matter Physics
                   University of Pisa, Italy
                   Thesis supervisors: Prof. A. Tredicucci
                                         Prof. dr. ir. L. P. Kouwenhoven

2014–2019   BSc & MSc in Physics
                   Scuola Normale Superiore, Pisa, Italy

2020-2025   PhD in Physics
                   Delft University of Technology, The Netherlands
                   Promotor: Prof. dr. ir. L. P. Kouwenhoven
                   Co-promotor: Dr. C. K. Andersen

PROFESSIONAL EXPERIENCE

2020–2023   Co-founder and backend developer of Olivia (AIVESP s.r.l.)

AWARDS

2014   Silver medal at the Italian Mathematics Olympiad

LIST OF PUBLICATIONS

📖   Included as a chapter of this thesis
*   Equal contribution

JOURNAL PUBLICATIONS AND PREPRINTS

16. *Edge and bulk states in a three-site Kitaev chain*
Sebastiaan L. D. ten Haaf, Yining Zhang, Qingzhen Wang, **Alberto Bordin**, Chun-Xiao Liu, Ivan Kulesh, Vincent P. M. Sietses, Christian G. Prosko, Di Xiao, Candice Thomas, Michael J. Manfra, Michael Wimmer, Srijit Goswami
arXiv:2410.00658 (2024)

15. *Protocol for scaling up a sign-ordered Kitaev chain without magnetic flux control*
Chun-Xiao Liu, Sebastian Miles, **Alberto Bordin**, Sebastiaan L. D. ten Haaf, A. Mert Bozkurt, Michael Wimmer
arXiv:2407.04630 (2024)

14. *Cross-Platform Autonomous Control of Minimal Kitaev Chains*
David van Driel, Rouven Koch, Vincent P. M. Sietses, Sebastiaan L. D. ten Haaf, Chun-Xiao Liu, Francesco Zatelli, Bart Roovers, **Alberto Bordin**, Nick van Loo, Guanzhong Wang, Jan Cornelis Wolff, Grzegorz P. Mazur, Tom Dvir, Ivan Kulesh, Qingzhen Wang, A. Mert Bozkurt, Sasa Gazibegovic, Ghada Badawy, Erik P. A. M. Bakkers, Michael Wimmer, Srijit Goswami, José L. Lado, Leo P. Kouwenhoven, Eliska Greplova
arXiv:2405.04596 (2024)

📖 13. *Supercurrent through an Andreev trimer*
Alberto Bordin*, Florian J. Bennebroek Evertsz'*, Gorm O. Steffensen*, Tom Dvir, Grzegorz P. Mazur, David van Driel, Nick van Loo, Jan Cornelis Wolff, Erik P. A. M. Bakkers, Alfredo Levy Yeyati, Leo P. Kouwenhoven
arXiv:2402.19284 (2024)

📖 12. *Signatures of Majorana protection in a three-site Kitaev chain*
Alberto Bordin*, Chun-Xiao Liu*, Tom Dvir, Francesco Zatelli, Sebastiaan L. D. ten Haaf, David van Driel, Guanzhong Wang, Nick van Loo, Thomas van Caekenberghe, Jan Cornelis Wolff, Yining Zhang, Ghada Badawy, Sasa Gazibegovic, Erik P. A. M. Bakkers, Michael Wimmer, Leo P. Kouwenhoven, Grzegorz P. Mazur
arXiv:2402.19382 (2024)

11. *Charge Sensing the Parity of an Andreev Molecule*
David Van Driel, Bart Roovers, Francesco Zatelli, **Alberto Bordin**, Guanzhong Wang, Nick Van Loo, Jan Cornelis Wolff, Grzegorz P. Mazur, Sasa Gazibegovic, Ghada Badawy, Erik P. A. M. Bakkers, Leo P. Kouwenhoven, Tom Dvir
PRX Quantum, 5.2: 020301 (2024)

10. *Crossed Andreev Reflection and Elastic Cotunneling in Three Quantum Dots Coupled by Superconductors*
Alberto Bordin, Xiang Li, David Van Driel, Jan Cornelis Wolff, Qingzhen Wang, Sebastiaan L. D. Ten Haaf, Guanzhong Wang, Nick Van Loo, Leo P. Kouwenhoven, Tom Dvir
Physical Review Letters, 132.5: 056602 (2024)

9. *Robust poor man's Majorana zero modes using Yu-Shiba-Rusinov states*
Francesco Zatelli*, David van Driel*, Di Xu*, Guanzhong Wang*, Chun-Xiao Liu, **Alberto Bordin**, Bart Roovers, Grzegorz P. Mazur, Nick van Loo, Jan Cornelis Wolff, A. Mert Bozkurt, Ghada Badawy, Sasa Gazibegovic, Erik P. A. M. Bakkers, Michael Wimmer, Leo P. Kouwenhoven, Tom Dvir
Nature Communications, 15.1: 7933 (2024)

8. *Adversarial Hamiltonian learning of quantum dots in a minimal Kitaev chain*
Rouven Koch, David Van Driel, **Alberto Bordin**, José L. Lado, Eliska Greplova
Physical Review Applied, 20.4: 044081 (2023)

7. *Realization of a minimal Kitaev chain in coupled quantum dots*
Tom Dvir*, Guanzhong Wang*, Nick van Loo*, Chun-Xiao Liu, Grzegorz P. Mazur, **Alberto Bordin**, Sebastiaan L. D. ten Haaf, Ji-Yin Wang, David van Driel, Francesco Zatelli, Xiang Li, Filip K. Malinowski, Sasa Gazibegovic, Ghada Badawy, Erik P. A. M. Bakkers, Michael Wimmer, Leo P. Kouwenhoven
Nature, 614.7948: 445-450 (2023)

6. *Tunable Crossed Andreev Reflection and Elastic Cotunneling in Hybrid Nanowires*
Alberto Bordin*, Guanzhong Wang*, Chun-Xiao Liu*, Sebastiaan L. D. ten Haaf, Nick van Loo, Grzegorz P. Mazur, Di Xu, David van Driel, Francesco Zatelli, Sasa Gazibegovic, Ghada Badawy, Erik P. A. M. Bakkers, Michael Wimmer, Leo P. Kouwenhoven, Tom Dvir
Physical Review X, 13.3: 031031 (2023)

5. *Spin-filtered measurements of Andreev bound states in semiconductor-superconductor nanowire devices*
David van Driel*, Guanzhong Wang*, **Alberto Bordin**, Nick van Loo, Francesco Zatelli, Grzegorz P. Mazur, Di Xu, Sasa Gazibegovic, Ghada Badawi, Erik P. A. M. Bakkers, Leo P. Kouwenhoven, Tom Dvir
Nature Communications, 14.1: 6880 (2023)

4. *Subgap spectroscopy along hybrid nanowires by nm-thick tunnel barriers*
Vukan Levajac*, Ji-Yin Wang*, Cristina Sfiligoj, Mathilde Lemang, Jan Cornelis Wolff, **Alberto Bordin**, Ghada Badawy, Sasa Gazibegovic, Erik P. A. M. Bakkers, Leo P. Kouwenhoven
Nature Communications, 14.1: 6647 (2023)

3. *Electrostatic control of the proximity effect in the bulk of semiconductor-superconductor hybrids*
Nick van Loo*, Grzegorz P. Mazur*, Tom Dvir, Guanzhong Wang, Robin C. Dekker, Ji-Yin Wang, Mathilde Lemang, Cristina Sfiligoj, **Alberto Bordin**, David van Driel, Ghada Badawy, Sasa Gazibegovic, Erik P. A. M. Bakkers, Leo P. Kouwenhoven
Nature Communications, 14.1: 3325 (2023)

2. *Singlet and triplet Cooper pair splitting in hybrid superconducting nanowires*
Guanzhong Wang*, Tom Dvir*, Grzegorz P. Mazur*, Chun-Xiao Liu, Nick van Loo, Sebastiaan L. D. ten Haaf, **Alberto Bordin**, Sasa Gazibegovic, Ghada Badawy, Erik P. A. M. Bakkers, Michael Wimmer, Leo P. Kouwenhoven
Nature, 612.7940: 448-453 (2022)

1. *Ballistic InSb nanowires and networks via metal-sown selective area growth*
   Pavel Aseev*, Guanzhong Wang*, Luca Binci*, Amrita Singh, Sara Martí-Sánchez, Marc Botifoll, Lieuwe J. Stek, **Alberto Bordin**, John D. Watson, Frenk Boekhout, Daniel Abel, John Gamble, Kevin van Hoogdalem, Jordi Arbiol, Leo P. Kouwenhoven, Gijs de Lange, Philippe Caroff
   Nano Letters, 19.12: 9102-9111 (2019)

PATENT APPLICATIONS

1. *Gate-based tuning of a chain of quantum dots into a regime hosting Majorana bound states for topological quantum computing*
   Michael Wimmer, Chun-Xiao Liu, Sebastiaan L. D. ten Haaf, **Alberto Bordin**
   Patent pending.